ESRF HIGHLIGHTS 2010

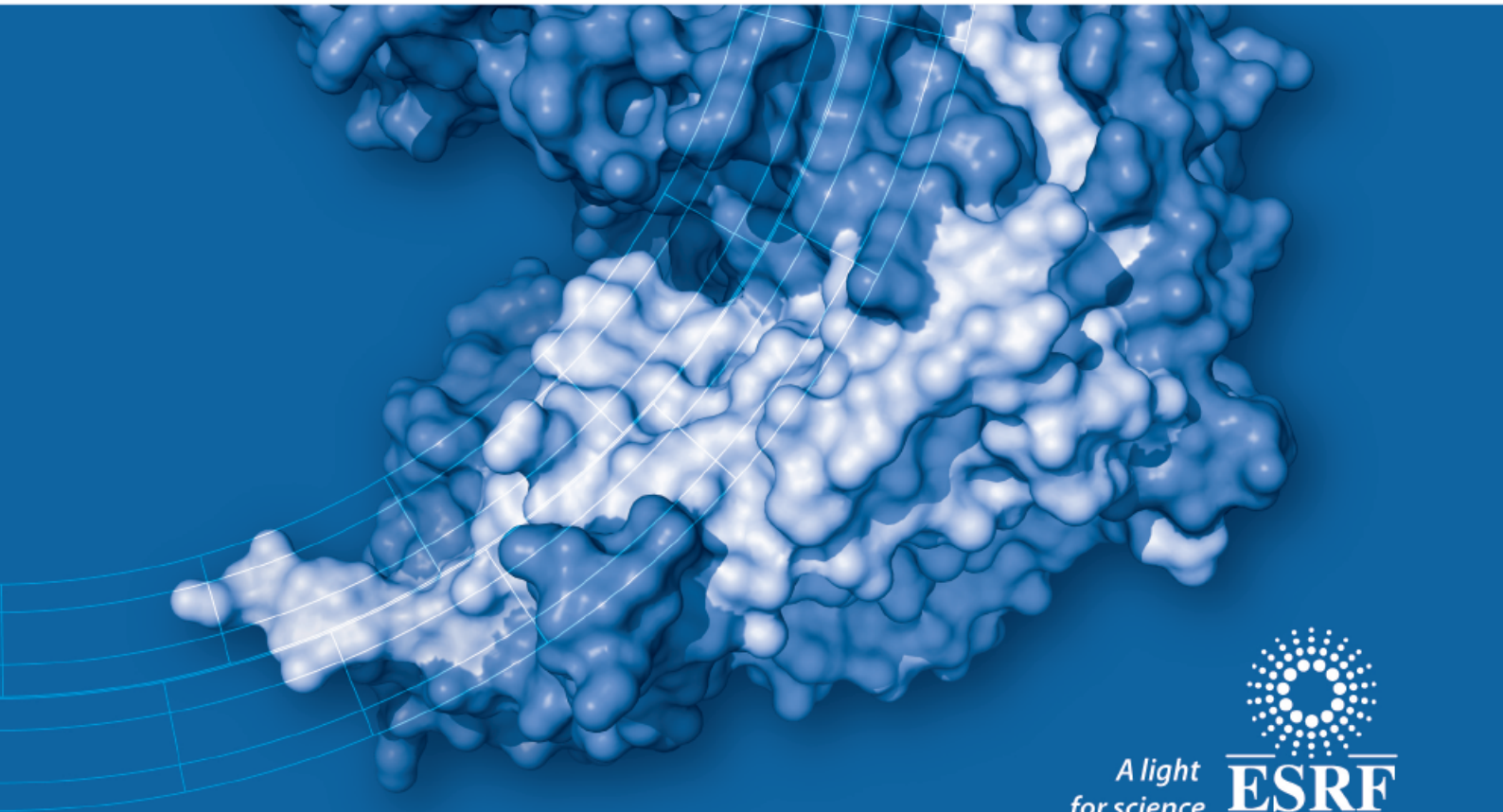

A light for science

ESRF

HIGHLIGHTS 2010

ESRF
European Synchrotron Radiation Facility

Dear Reader

Credit: ESRF / Molyneux Associates.

The operation of the ESRF in 2010 has been as excellent as in previous years, characterised by outstanding scientific productivity and by record-breaking performance of the accelerator complex.

The number of proposals, experimental sessions, user visits and publications in peer-reviewed journals was again very high, comparable to the record figures of 2009. Details are outlined in the chapter on *Facts and Figures*.
The scientific highlights in the following chapters confirm the important trend of coupling increasingly smaller X-ray beams with X-ray techniques such as scattering, diffraction and spectroscopy. They also underscore an increasing use of coherence in many experiments and in different disciplines, both in the traditional fields of materials science, condensed matter physics, chemistry and life sciences, and in the emerging fields of palaeontology, environment and cultural heritage.

In parallel to the user operation, the Upgrade Programme is now in full swing with important progress in all areas:

1) Outstanding results have been achieved in the Source Upgrade: 6 m straight sections were installed for several beamlines; operation at 300 mA was successfully demonstrated; and good progress was made in the refurbishment of the RF system, notably for the new solid state amplifiers.
A special effort was devoted to the stability of the source which made it possible to reduce the vertical emittance to a world record value of less than 5 pm in User Service Mode. The increased brightness benefits notably the micro- and nano-beams.
The High Pressure Beamline ID27, for example, now serves its users with a world record brightness of almost $1x10^{21}$ photons/s/mm^2/mr^2/0.1bw in the 200 mA operation mode.

2) The evolution of the beamline portfolio has been progressing well, despite the new challenges due to the need to reduce the number of public beamlines. The eight Upgrade Beamlines (UPBLs) are being constructed as planned and the major beamline refurbishments linked to the UPBL construction should remain unaffected. UPBL10 (MASSIF) and UPBL11 (TEXAS) are already under construction, and UPBL4 (NINA), UPBL6 (Inelastic Scattering) and UPBL7 (Soft X-rays) have entered into the construction planning phase. Most other UPBLs have had their Technical Design Report (TDR) presented to and supported by the Science Advisory Committee (SAC), which in turn is kept constantly abreast on the evolution of the beamline portfolio.

3) The instrumentation development programme recorded important achievements: these include delivery in user mode of nano-beams down to ~60 nm using both K-B and compound-refractive-lenses; precision mechanics for nano-optics; commissioning of a Pilatus-6M 2D pixel detector on a Structural Biology beamline; commissioning of the liquid phase epitaxial deposition apparatus to prepare unique scintillation materials for hard X-ray detection in imaging experiments; and development of unique, powerful software packages for instrument control and on-line data analysis.

4) The Experimental Hall extension project (EX2) is ready for tendering with a reduced scope imposed by budget constraints. The new data centre in the Central Building to keep up with the increasing computing needs is nearing completion and will enter service in 2011.

2010 will be remembered as the year when important changes began, and new opportunities arose for the ESRF. The economic situation in Europe requires the ESRF to evolve: certain member countries, despite continued support to the ESRF, cannot finance our budget for some years to come at the levels originally foreseen. ESRF Management and Council have worked hand in hand on a scheme to alleviate these financial difficulties. On 30 November, Council unanimously adopted a resolution allowing two member countries to reduce their financial contributions for three years, and this without compromising the quality of the scientific programme. All twelve member countries and seven scientific associates have renewed their long-term commitment to the ESRF, and especially to the continuation of its intergovernmental convention.

The resolution leads to a 6% budget reduction during 2011-2013 which shall be absorbed without compromising the quality of service for the 4000 scientists who use the ESRF. However, a reduction of this size meant difficult decisions had to be taken in 2010, and more lie ahead in 2011: the number of beamlines, and the operation time of the accelerator complex, must be reduced and some deliverables of the Upgrade Programme revised. These reductions shall be implemented in a way to limit as much as possible the impact on the scientific community. This impact will, however, to a large extent address users from countries forced to reduce their financial contribution, and which in return accepted a limitation of their beamtime.

The years ahead will be challenging for synchrotron science in general. Spectacular efforts over the past ten years saw the construction of excellent new synchrotron sources in particular in Europe, which reinforced its long-standing leadership. Today, important investments are foreseen in the U.S. and in Japan. More importantly, a strong programme is developing in Russia – building on a long tradition in synchrotron science – and in emerging market economies such as Brazil, China and India where strong scientific communities already use synchrotrons all over the world.

In the face of reduced resources in Europe, maintaining the present frontline position will need careful coordination to emphasise the complementarity of the ESRF with the other synchrotron sources. This will address issues like cost containment, efficiency, excellence in user services, technical developments and governance. Without coordination across Europe, we cannot maintain our leadership nor will we succeed in opening our laboratories to innovation, industry and new communities.

I am convinced that the ESRF, working in concert with others, can maintain a world leading role. We will create new opportunities for more unique beamlines on free insertion device straight sections of the ESRF storage ring. I expect new partners to be interested in exploiting these new and unique possibilities. The Council Resolution invites Management to attract, over the next three years, new members and scientific associates and to investigate other possible ways of collaboration with third parties. In parallel, Council and Management will work on new schemes where the funding of ESRF's needs is more closely linked with the use by scientists from the different members countries.

The first phase of the Upgrade Programme, despite the reduced building construction programme and a slightly lowered investment capacity for the other projects, maintains all innovative features enabling the ESRF to stay attractive to its users in the long term. These include eight unique Upgrade Beamlines for delivery by 2015. In parallel, Management has started reflecting on the second phase of the Upgrade Programme. A revised plan, along with options taking into account the new financial context will be presented to Council in spring 2011 with the aim to start discussions on new UPBLs with SAC and the User Communities in 2012, possibly beginning with the Users Meeting in February of that year.

In 2011, the Upgrade Programme will have a very limited impact on user operation, despite the start of construction work for EX2 in September 2011. Beamtime delivery should not be reduced by more than two weeks. In 2012, however, a long shutdown is planned with significant reduction of user operation from December 2011 to April 2012, and in August and September 2012. The overall reduction of beam delivery in 2012 will be about four months, with a return to normal user operation in 2013.

There have been some successful developments for new partnerships. In June 2010, the ESRF and the ILL launched the Partnership for Soft Condensed Matter (PSCM) which is now developing a programme to attract further partners from academia and industry. Partnerships and collaboration ideas are also developing in extreme conditions science, palaeontology, metallurgy, and technologies for synchrotron and neutron science. The two existing and future partnerships will greatly benefit from the new Science Building, located between the ESRF and the ILL with a direct connection to both facilities for the benefit of all users. This building, funded by French regional and local authorities, will be commissioned in 2012.

I would like to thank our Member and Associate Countries, and in particular their delegates to Council, AFC and SAC, for their continued support and trust. In particular, I wish to thank the Chairman and the Delegates of Council for having developed with Management a pragmatic solution to a difficult funding problem. Thanks to these efforts, the excellence of the ESRF will be maintained and new opportunities have been created. I am also very grateful to the members of the beamtime allocation panels and of the beamline review committees for their hard work assuring the scientific life of the facility. Special thanks go also to the European Commission which in 2008-2010 has provided crucial support through the ESRFUP contract for the preparation of the ESRF Upgrade. Today, through further opportunities given to the projects on the ESFRI roadmap, it continues supporting the ESRF in a very visible way. Special thanks go also to the French authorities, in particular the *Ville de Grenoble*, the *Grenoble-Alpes Métropole*, the *Conseil Général de l'Isère* and the *Région Rhône-Alpes* for granting the ESRF and the ILL funds for important infrastructure projects like the new Science Building and a new site entrance which enormously enhance our scientific visibility.

In this issue of the Highlights, a special thanks goes to all ESRF staff who have demonstrated a formidable motivation, hard work and perseverance in providing support to our users and in developing the Upgrade. Last but certainly not least, I wish to thank the thousands of excellent and dedicated users who make outstanding science possible, a few examples of which are outlined on the following pages. With their wonderful science carried out at the ESRF, they make all our efforts more than worthwhile.

Francesco Sette,
ESRF Director General.

Status of the Upgrade Programme

Progress during 2010

2010 saw the start of major works for the execution of Phase I of the Upgrade Programme with the first new beamlines now under construction in the existing experimental hall. Up to this point, works within the Upgrade had only minor impact on user operation, performance and productivity of the ESRF. A proposal for a new scheme to allocate public beamtime at the ESRF has been endorsed by SAC and Council and is now entering its implementation phase.

New Buildings

The project for the extension of the experimental hall is in the preparatory phase for the building works tenders. The preliminary design report was officially approved in May 2010 and the detailed design report in November 2010. These detailed studies have allowed the project to reach maturity. Adjustments to the initial Building Programme, including the extension of ID16 (Figure 1), have been made in order to meet both the scientific and budgetary requirements.

Credit: Sud Architectes.

Fig. 1: Architects view of the future ID16 building housing the two stations of the NanoImaging/NanoAnalysis (UPBL4 - NINA) project.

Progress in the studies allows technical solutions to be considered for the most challenging issues of the project. The construction schedule is already well defined and has been fixed in a way to minimise the impact on the user operation. The building works are planned to start in September 2011. The timescale includes two long shutdowns of the facility. The first shutdown (from December 2011 to April 2012) will be dedicated to the demolition of existing structures, modifications of existing networks and creation of the foundations for the extensions. The second one (a few weeks during the normal summer shutdown in 2012) will be dedicated to the completion of the 4 000 m^2 of high quality concrete slab on which many of the new beamlines will be constructed.

In parallel, and within the frame of the State/Region contract (CPER), studies are progressing for the construction of the Science Building (under the authority of the ILL), the extension of the restaurant and a new site entrance on the Avenue des Martyrs (under the authority of the ESRF). The CPER programme will enhance the scientific life and increase visibility of the EPN science campus.

Preparatory works have been started to free the space for the construction of the IBS2 building by moving the works committee to the centre of the ring and the subcontractor premises next to the technical buildings close to the river Drac. The IBS2 construction will start in May 2011 with a delivery planned for the beginning of 2013.

Upgrade of the Source

Upgrade of the accelerator system is progressing well. The much improved orbit measurement, resulting from the installation of the new electronics driving the electron beam position monitors, has enabled a higher precision in the horizontal to vertical coupling correction. The emittance of the electron beam has been reduced and stabilised below 5 pm for periods of up to a full week. An improved orbit stabilisation system is under development; it was made possible thanks to the new digital electronics.

The transformation of the straight sections of ID18 and ID30 for the accommodation of 6 m long undulators has been completed. New magnets, vacuum chambers, and undulators are under manufacture. An ambitious RF upgrade programme is being preparated that includes the replacement of some high power klystrons by solid state amplifiers and the development of new cavities with higher order modes damping. In 2010, the storage ring has been routinely operated with 300 mA of current during Machine Physics runs. The accelerator upgrade work was carried out during planned shutdowns and had no detrimental consequences on the User programme.

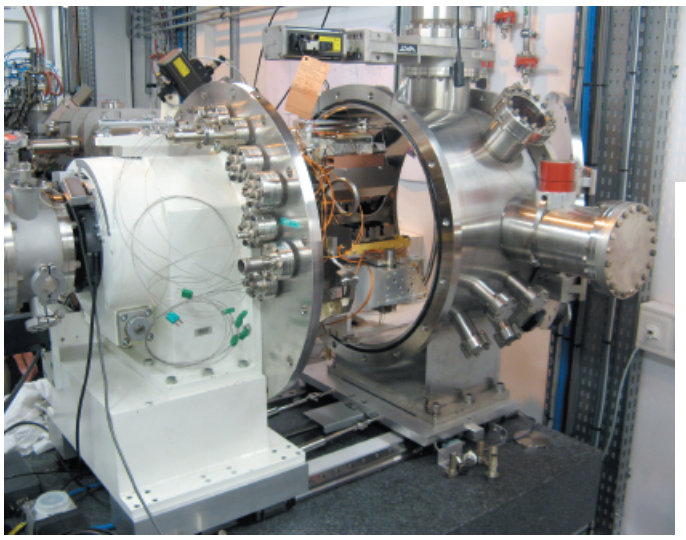

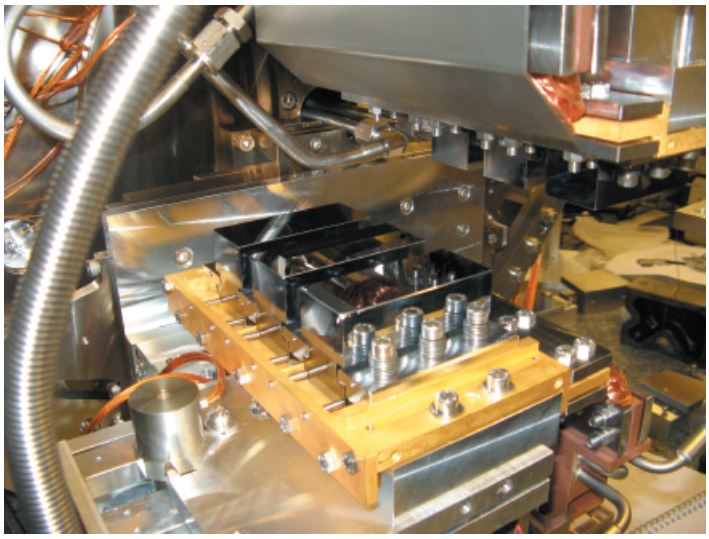

Fig. 2: The EXAFS beamline BM23 is the first new beamline to commence user operation following an upgrade with transfer from BM29. Left: Monochromator showing translation stage to change pairs of crystals; Below: Close-up of the 3 pairs of crystals (111, 311, 511), which enlarge the accessible energy range.

Renewal of Beamlines

Budgetary constraints have been absorbed mostly by further refining the number of beamlines to be moved in the floor plan for the public beamline portfolio of the ESRF while preserving the number of Upgrade Beamline (UPBL) projects at eight. The revised floor plan reduces the number of moving beamlines by three with the additional benefit of avoiding lengthy shutdown periods of the respective beamlines for users. The new floor plan has been endorsed in 2010 by SAC and Council for implementation.

Conceptual Design Reports (CDRs) and Technical Design Reports (TDRs) for five UPBL projects defining ten independent experimental stations have been produced, externally reviewed, and approved for execution in 2010. Work on CDRs and TDRs for the sixth UPBL and extensive refurbishment of the ID10 complex as well as ID19 has been started in parallel. The first new beamline, BM23, has finished its constructions phase and will commence full user service with the start of the 2011/I run, to be followed by UPBL11 finishing its construction phase in 2011 (Figure 2). Upgrade of instrumentation has already been started on all eight UPBL projects (Figure 3).

Fig. 3: T. Schulli and G. Carbone, scientists at beamline ID01 (UPBL1), with their new diffractometer for nanodiffraction analysis.

Enabling Technologies and Instrumentation

The Instrumentation Services and Development Division (ISDD) is deeply involved in the implementation of the Upgrade Programme for both the Experiments Division (ExpD) and Accelerator and Source Division (ASD).

Driven by the first UPBL projects, several key technological areas have been identified, *e.g.* X-ray mirror engineering, diamond technologies, nanofocussing optics, online data analysis, high-rate data collection. Expert working groups have been created to find innovative and reliable solutions. When possible these solutions are generic to allow cost-effective adaptation to multiple beamline projects. All ISDD scientists and engineers provide expertise in the preparation of TDRs ranging from ray-tracing simulation and heat load modelling to producing cost estimates for entire instruments.

Although the X-ray detector programme is still in a re-definition stage, several key elements of this programme have been started, including the implementation of a liquid phase epitaxy laboratory to secure the procurement of high quality scintillators. A collaboration contract with Science and Technology Facilities Council (STFC) for the production of a Ge microstrip detector for UPBL11 has been signed, as well as a three-year collaboration contract with PSI for the development of the EIGER detector. A new framework for imaging detectors, LiMA - Library for IMage Acquisition, has been developed. LiMA offers standardised interfaces with enhanced capabilities that are being developed in collaboration with other synchrotron facilities to ensure compatibility with a wide range of 2D detectors. Development of GPU accelerated data processing was successfully implemented for tomography reconstruction and will be adapted for other scientific applications. Concerning the beamline control electronics, more than 1000 motors are being controlled with standardised IcePAP electronics on beamlines. The UPBLs will also be equipped with these controllers.

Several critical X-ray optics projects such as high reflectivity X-ray multilayers, sub-60 nm KB mirrors, diamond monochromators and beam splitters and compound refractive lenses (CRLs) have been developed. The ESRF established a long-standing programme with several companies and academic institutes to ensure the production and tailoring of high-quality diamond single crystals for various applications. A new concept of transfocators combining linear and 2D CRLs was developed and installed at ID06. New beryllium linear refractive lenses were tested under white beam illumination at ID06. This heat-load test confirmed high stability of the lenses opening the opportunity to use new in-vacuum and white beam 1D transfocators for the ESRF upgrade beamline projects (*e.g.* UPBL4). Finally, in-line multi-lens interferometers were successfully applied to phase contrast imaging and the study of coherence preservations by crystals, multilayers and refractive lenses.

The Mechanical Engineering group has undergone internal reorganisation, including the creation of a procurement unit, a 150 m^2 lab dedicated to precision mechanical assembly and a room for clean assembly, located within the experimental hall. In collaboration with beamline staff, this group has also been working on specific UPBL projects including:

UPBL11: Transfer of beamline from BM29 to BM23; installation of a new experimental table in BM23; design and procurement of the ID24 polychromators and mirrors.

UPBL10: Geometric acceptance test of a robotic arm for sample screening and data acquisition; detailed design of beam splitters and canted beam shutter; BM29 mirror design and purchase.

UPBL4: Design of the *NA* branch's double mirror (high stability requirements); refurbishment of the Kohzu double crystal monochromator for *NA*; detailed specifications of slits and absorbers.

UPBL6: Pre-design of the two spectrometers (high resolution IXS spectrometer and large solid angle IXS spectrometer); preparation of the move of ID20 to ID06 with a modification of the beamline layout and design of a double multilayer mirror.

A new concept for the positioning systems of long X-ray mirrors for the UPBLs and ID06 has been developed, optimised for high stability, low thermal drifts, and fine position control.

Computing Infrastructure

Investments into the computing infrastructure have been kept on a low level for much of the year awaiting the construction of the new data centre in the ESRF central building. With completion now being imminent, contracts have been placed for the network cabling, the water cooled racks, a large StorageTek tape library, and a new blade computing cluster. The new hardware will be installed at the beginning of 2011. The new blade cluster is based on a mixed architecture of graphical processor units (GPUs) and multi-core Intel CPUs with a large amount of random access memory. It will be used as a data analysis platform for the massive data flow generated by the tomography experiments. Similar systems dedicated to life science data analysis and simulation are planned in the course of 2011.

P. Elleaume, R. Dimper, H. Reichert, S. Pérez and J. Susini

Dynamics and extreme conditions

This year's Highlights again reflect the broad spectrum of scientific applications within the Dynamics and Extreme Conditions Group, and in particular underline the importance of continuously improving the instrumentation and of developing new concepts and ideas.

The first part of the chapter is dedicated to fundamental phenomena. The detection of superradiance and the collective Lamb shift combine beautifully the unique properties of synchrotron radiation, the X-ray wave guide effect and the ^{57}Fe Mössbauer resonance as a two-level system. This intricate setup enabled the detection of the predicted minute energy shift of 24 neV at 14.4 keV, corresponding to a relative change of $\Delta E/E = 1.7 \times 10^{-12}$! The second contribution reveals that the previously thought "homogeneous" supercritical phase of fluids can be partitioned into a liquid- and a gas-like portion, with the disappearance of the positive sound dispersion at THz frequencies marking the boundary between these two regions. The third contribution provides an important new insight into glass physics. High-resolution inelastic X-ray scattering measurements on hot vitreous silica clearly reveal two distinctly different scattering regimes of phonon-like excitations which are intimately related to the peculiar behaviour of the thermal conductivity and specific heat of glasses at low temperature.

The second part of the chapter focusses on high pressure studies. The first two contributions witness the significant progress made in the study of materials in laser-heated diamond anvil cells (DACs). Very tightly focussed and stable X-ray and laser beams, in conjunction with carefully designed diagnostic tools, are the pre-requisites for reliable and trustworthy results. The work on tantalum puts an end to a long-lasting controversy between previous experimental results and theoretical predictions and sets the standard for future work on the melting of solids. The knowledge of melting curves as a function of pressure is of utmost importance to constrain geochemical models and explains seismological observations. This is nicely demonstrated by the X-ray diffraction work on peridotite. In addition to these "static" measurements, the direct determination of sound velocities by inelastic X-ray scattering provides valuable complementary information, as shown in the highlight on the composition of the Earth's inner core. The last contribution illustrates that the combination of three experimental techniques – X-ray diffraction, X-ray absorption and conventional Mössbauer spectroscopy – were required to unravel the subtle interplay between structural, electronic, and magnetic degrees of freedom in delafossite, a binary transition metal oxide.

The third part of the chapter is devoted to the study of electronic and magnetic properties. The discovery of strong magnetic circular dichroism in K-edge resonant inelastic X-ray scattering (RIXS) opens exciting new perspectives in the study of magnetic materials, taking full advantage of the bulk-, valence-, and site-sensitivity of hard X-ray RIXS. The study of the spin reorientation transition of epitaxially grown Fe on W(110) illustrates the strength of nuclear resonance scattering to detect magnetisation directions with atomic layer resolution and a precision of a few degrees. "Classical" correlated electron systems such as V_2O_3 still offer new insights thanks to advanced spectroscopies. A systematic study of the temperature, pressure, and doping dependence across the canonical Mott transition suggests that there might actually be two different mechanisms responsible for the metal-insulator transition. Finally, the X-ray Raman study on tetrahydrofuran clathrate hydrate formation gives a flavour of the kind of studies which will become routine once the IXS upgrade beamline UPBL06 becomes operational.

A significant amount of the experiments conducted on the beamlines rely on the excellent support services. The automatic diamond anvil cell gas loading system,

the laser drilling device, and the laser annealing setup were important developments of great benefit to the high-pressure community.

Other science-related activities kept the Dynamics and Extreme Conditions Group busy: ID26 and UPBL6 (inelastic X-ray scattering) were reviewed in Spring 2010, and received very positive feedback. In fact, the technical design report for this upgrade beamline (UPBL) was approved, and purchasing of the key components will start at the beginning of 2011. Finally, the group was involved in the organisation of the 7th International Conference on Inelastic X-ray Scattering which was jointly hosted by ESRF and Politecnico di Milano, and attracted more than 160 participants to Grenoble in October 2010.

M. Krisch

Fundamental phenomena

The collective Lamb shift in single photon superradiance

Principal publication and authors
R. Röhlsberger (a), K. Schlage (a), B. Sahoo (a), S. Couet (b) and R. Rüffer (c), *Science* **328**, 1248 (2010).
(a) Deutsches Elektronen Synchrotron DESY, Hamburg (Germany)
(b) Instituut voor Kern- en Stralingsfysica, Katholieke Universiteit Leuven (Belgium)
(c) ESRF

The interaction of many identical two-level atoms with a common radiation field leads to a profound modification of the temporal, directional and spectral characteristics of their collective emission compared to that of a single atom. A prominent example is the phenomenon of superradiance that manifests itself as a strong acceleration of the collective spontaneous emission [1]. It was predicted that the superradiant emission of light goes along with a radiative shift of the atomic transition energy, the collective Lamb shift [2]. In the optical regime this effect appeared to be extremely difficult to observe due to atom-atom interactions and multiple scattering effects.

Here we explore the manifestation of superradiance and the collective Lamb shift in the regime of hard X-rays by employing the Mössbauer isotope ^{57}Fe (resonance energy 14.4 keV, natural linewidth 4.7 neV) as a two-level system. Our approach does not only circumvent the intrinsic problems of previous approaches, but also provides a sufficiently high spectral resolution to detect small energy shifts.

To understand the collective Lamb shift we first look at the single-atom Lamb shift. The emission and reabsorption of virtual photons within the same atom leads to a small correction to its transition energy, also known as self-energy. The observation and explanation of this shift (for atomic hydrogen) paved the way for the development of quantum electrodynamics as the unified theory of light-matter interaction. Willis E. Lamb received the Nobel Prize in Physics in 1955 for his discovery.

If the atom is now surrounded by an ensemble of identical atoms, the emitted photon may be absorbed not only by the same atom but also by identical atoms within the ensemble. Considering such an ensemble of identical atoms as a 'giant' atom, the emission and reabsorption of photons within the ensemble itself again leads to a (complex-valued) self-energy correction of the transition energy.

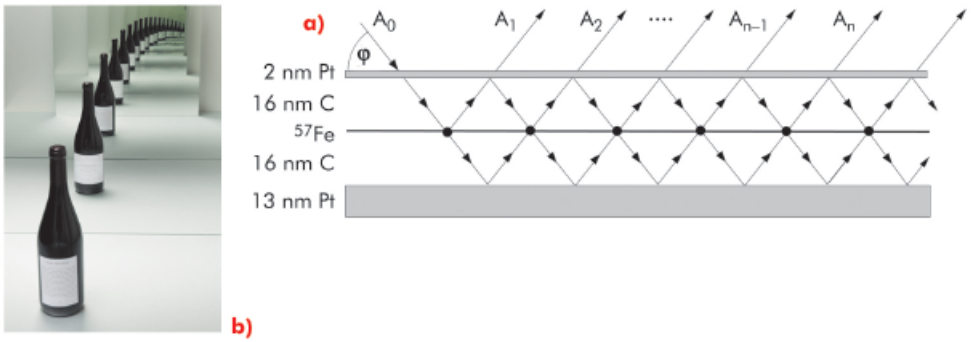

Fig. 4: a) Planar cavity used for observation of the collective Lamb shift in superradiant emission from ^{57}Fe. X-rays are coupled under the grazing angle φ into the first-order guided mode of the cavity. b) Formation of multiple images between two parallel mirrors. In the cavity this effect renders the ultrathin ^{57}Fe layer to appear optically thick, an important condition for superradiance.

The real part of this quantity is the collective Lamb shift, the imaginary part is the superradiant decay width.

In order to prepare a superradiant ensemble of atoms we have embedded ultrathin layers of ^{57}Fe in a planar cavity to resonantly excite them with synchrotron radiation pulses, coupled evanescently into the first-order guided mode (Figure 4a). The cavity geometry exhibits important features that facilitate the observation of the collective Lamb shift. First, the ensemble of atoms appears to be optically thin upon absorption. Second, multiple reflections of the radiation within the cavity render the ensemble of atoms to be optically thick, comparable to multiple images of an object between two parallel mirrors (Figure 4b). Thus, the optical thicknesses of the sample for absorption and emission are decoupled, which is an important condition for the observation of superradiance.

The measured signal in the experiment is the reflected radiation from the cavity, *i.e.* the superposition of all partial waves A_i in Figure 4a. In this geometry, the ensemble of ^{57}Fe atoms was excited into a purely superradiant state that decayed almost two orders of magnitude faster than a single atom. For the spectral analysis of the reflected radiation, a resonant single-line ^{57}Fe analyser foil was employed that was mounted on a Doppler drive typically used in Mössbauer spectroscopy. The transmission through the foil was recorded as function of the Doppler shift. The resulting energy spectra for two samples containing ^{57}Fe layers of 0.6 nm and 1.2 nm thickness are shown

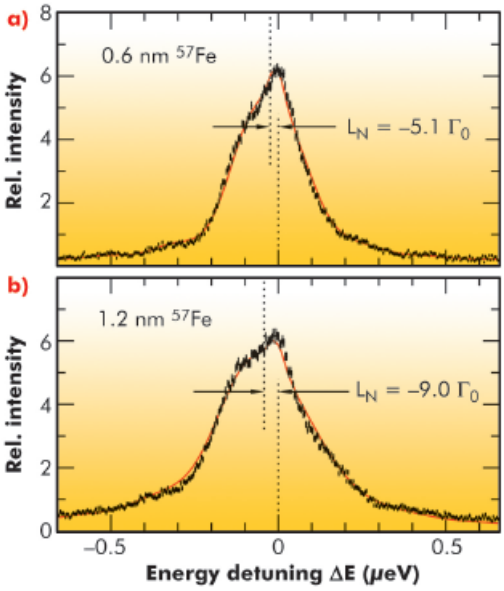

Fig. 5: Energy spectra of the two cavity samples containing ultrathin layers of a) 0.6 nm and b) 1.2 nm ^{57}Fe. The shift of the centre of mass of these curves is the collective Lamb shift.

in Figure 5a and b, respectively. Both curves are broadened far beyond the natural decay width of $\Gamma_0 = 4.7$ neV, reflecting the superradiant nature of the emission. One clearly observes a spectral shift of the centre of mass of the spectra towards lower energies. This is the collective Lamb shift. The measured data are in excellent agreement with calculations (solid red lines).

This experiment, carried out at beamline **ID22N**, has demonstrated a simple way to observe superradiance and the collective Lamb shift in the X-ray regime. This approach opens a new window to systematically explore cooperative effects in the interaction of light and matter with very high precision.

References
[1] R.H. Dicke, *Phys. Rev.* **93**, 99 (1954).
[2] R. Friedberg, S.R. Hartmann, and J.T. Manassah, *Phys. Rep. C* **7**, 101 (1973).

Principal publication and authors
G.G. Simeoni (a), T. Bryk (b,c), F.A. Gorelli (d,e), M. Krisch (f), G. Ruocco (e,g), M. Santoro (d,e) and T. Scopigno (e,g), *Nature Physics* **6**, 503 (2010).
(a) FRM II, Technische Universität München, Garching (Germany)
(b) Institute for Condensed Matter Physics, National Academy of Sciences of Ukraine, Lviv (Ukraine)
(c) National Polytechnic University of Lviv (Ukraine)
(d) LENS, European Laboratory for Non Linear Spectroscopy, Firenze (Italy)
(e) IPCF-CNR, UOS Roma (Italy)
(f) ESRF
(g) Università di Roma 'La Sapienza' (Italy)

Supercritical fluids: liquid-like to gas-like dynamical crossover at the Widom line

According to textbook definitions, each fluid substance is characterised by a peculiar critical pressure (P_c) and temperature (T_c), whose values define an upper thermodynamic limit. Above this limit, any classical distinction between liquid and gas phases loses its validity, and the system enters the supercritical fluid state. In the P-T phase diagram, (P_c,T_c) represents the so-called *critical point*. Despite intensive research efforts on fluids throughout the past century, knowledge about properties of fluids in the supercritical regime is limited, mainly due to technical difficulties encountered in dealing with the required complex sample environment.

Important new insights were recently gained through an inelastic X-ray scattering experiment on dense hot supercritical argon (at $T=4 \cdot T_c$ and $P>10^2 \cdot P_c$), conducted at beamline **ID28**, in conjunction with molecular dynamics simulations. We identified two distinct dynamical regimes (liquid-like and gas-like), contradicting the notion of a homogeneous supercritical phase. Specifically, our investigation revealed the sound propagation to be strongly dependent on the wavelength of the acoustic waves as well as on the thermodynamic conditions of the medium. As already observed in the subcritical region for most liquids, the measured hypersound velocity exceeds its adiabatic value (a dynamical feature known as *positive sound dispersion*). This implies the presence, even deep inside the supercritical regime, of at least one relaxation process such as the visco-elastic relaxation, reflecting the interaction of local structural changes (on *nm* length- and *picosecond* time scales) with acoustic sound waves, and considered to be a clear fingerprint of the liquid behaviour [1].

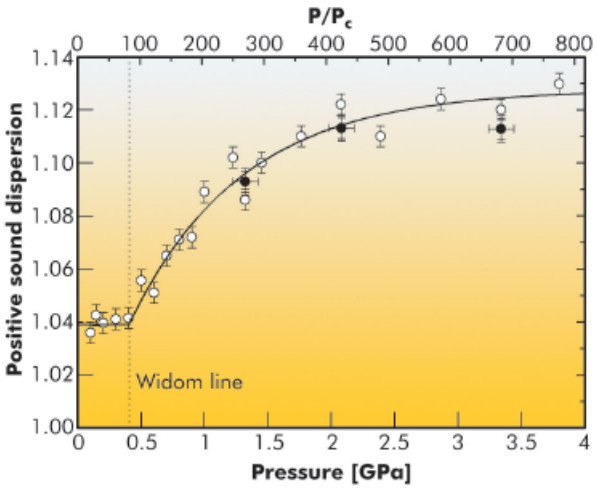

Fig. 6: Positive sound dispersion of argon as a function of pressure at 573 K. Full and open circles indicate the positive sound dispersion as obtained from IXS experimental data and from molecular dynamics simulations, respectively. The dotted line marks the point on the extrapolated Widom line at 573 K.

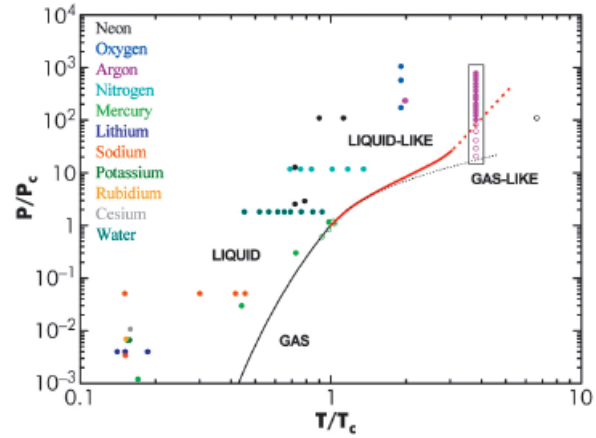

Fig. 7: Sketch of the (P/P_c, T/T_c) plane. Red line: Widom line of argon obtained from the NIST database (continuous) and its extrapolation (dotted). Black line: best fit of the liquid-vapour coexistence lines for argon, neon, nitrogen and oxygen using the Plank-Riedel equation. Dots with different colours correspond to different investigated systems (this study, and also ref. [2] and references therein). Isothermal, experimental and MD simulation data on argon are reported in pink inside the black rectangle. Open circles: weak positive sound dispersion, full circles: large positive dispersion.

Figure 6 reports the amount of positive sound dispersion, as a function of pressure, derived from experiment and molecular dynamics simulations. A sharp decrease from about 13% to 4% is observed on pressure decrease with a cross-over located at 0.4 GPa. This distinct decrease is due to the progressive disappearance of the structural relaxation process, and thus marks the transition from a collective liquid-like to a single particle gas-like behaviour. This clearly provides a connection between dynamics and thermodynamics, contradicting the widespread belief of a homogeneous supercritical phase. Furthermore, we speculate that the positive sound dispersion plays the role of an order parameter, sensitive to the local structure and able to amplify the degree of correlation between thermal heterogeneities and mechanical density fluctuations on a macroscopic scale.

Most remarkably, the crossover value of 0.4 GPa corresponds to the extrapolation of the so-called *Widom*

line (Figure 7) into the supercritical phase. This ascribes a much more general role to the Widom line, since the partition between liquid-like and gas-like regimes survives even above the theoretical definition of the Widom line itself. In analogy with the subcritical behaviour, the Widom line embodies the extrapolation of the liquid-vapour coexistence line into the supercritical region, thus supplying the first fundamental insight into the correspondence between subcritical and supercritical fluid behaviour.

This newly discovered relationship between thermodynamics and the viscoelastic behaviour of hot dense fluids is expected to allow major breakthroughs in areas such as the physics of planetary systems, solvation techniques for nanotechnologies, and in geophysics for the validation of seismological models based on the thermophysical properties of materials.

References
[1] T. Scopigno, G. Ruocco and F. Sette, *Rev. Mod. Phys.* **77**, 881 (2005).
[2] F.A. Gorelli *et al*, *Phys. Rev. Lett.* **97**, 245702 (2006).

Disorder induced sound attenuation in amorphous materials

Principal publication and authors
G. Baldi (a), V.M. Giordano (b), G. Monaco (b) and B. Ruta (b), *Phys. Rev. Lett.* **104**, 195501 (2010).
(a) IPCF-CNR, UOS ROMA, c/o Physics Department, University of Parma (Italy)
(b) ESRF

The thermal conductivity of amorphous materials is many orders of magnitude smaller than that of the corresponding crystalline structures and presents a peculiar plateau at temperatures of a few Kelvin [1]. The existence of this plateau requires the mean free path of propagating phonon-like excitations to decrease at least with the fourth power of frequency. This strong scattering regime is usually referred to as Rayleigh scattering, after the pioneering work of Lord Rayleigh [2]. In the same temperature range (T ~ 1-10 K) where the thermal conductivity shows the characteristic plateau, the specific heat of glasses, C(T), is marked by an excess over the normal T^3 behaviour, which appears as a maximum in $C(T)/T^3$. This maximum is associated with an excess of vibrational modes over the $\propto \nu^2$ Debye density of states at frequencies of a few terahertz; it is known as the boson peak. Substantially different theories of wave propagation in disordered media predict the presence of Rayleigh scattering in glasses in the frequency range below the boson peak position. Discriminating among the various theoretical models, however, is difficult since experimental access to the relevant frequency range is very challenging.

In addition to Rayleigh scattering, the sound waves in glasses can be attenuated by a variety of other attenuation mechanisms, all associated with some degree of anharmonicity. These mechanisms give rise to a complex frequency and temperature dependence of the sound attenuation and controversial results have been reported [3,4]. Exploiting the intense development of the inelastic X-ray scattering (IXS) technique during the last decade, we have obtained clear evidence that in vitreous silica this strong scattering regime is located in the few terahertz frequency range. We show as well that the Rayleigh scattering persists up to a crossover frequency which coincides with the position of the boson peak, confirming a clear connection between the damping of the acoustic-like excitations and the excess of vibrational modes.

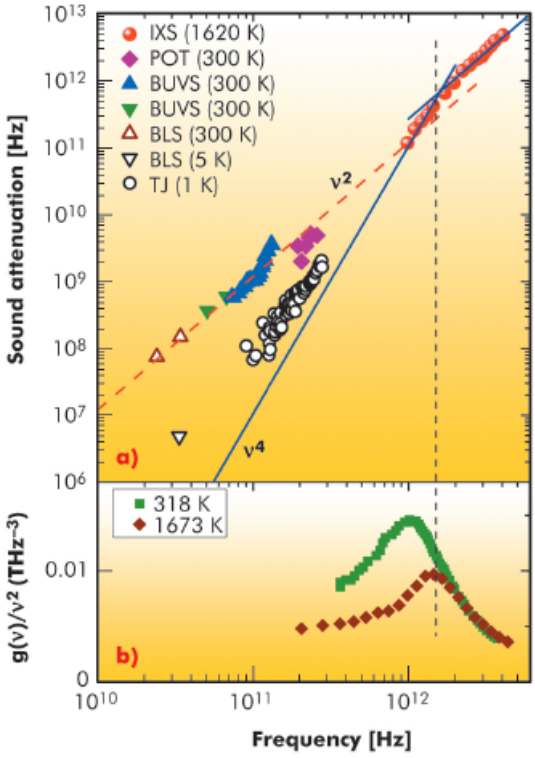

Fig. 8: a) Sound attenuation of vitreous SiO_2 as a function of frequency in log-log scale. The points at high frequency (red circles) are from the new IXS data at T=1620 K. Lower frequency data are from the literature: picosecond optical technique (POT), Brillouin ultraviolet scattering (BUVS), Brillouin light scattering (BLS) and a tunneling junction (TJ) technique. The dashed line (red) is a quadratic frequency slope. The blue lines are two power law fits, ~ν^2 and ~ν^4, to the IXS data. b) Reduced density of vibrational states from literature data, at the indicated temperatures. The vertical dashed line indicates the boson peak position at the temperature of the IXS experiment.

The experiment was performed at beamline **ID16**. IXS spectra were collected at several values of the scattering angle (different exchanged wavevectors). Each spectrum presents an elastic line and a Brillouin doublet corresponding to the longitudinal acoustic excitation. A suprasil fused-quartz sample was heated to a very high temperature, T=1620 K, to enhance the inelastic signal over the elastic one. At this temperature the boson peak position is 50% higher in frequency with respect to room temperature, allowing us to measure the longitudinal excitations with IXS at frequencies below the boson peak position in silica glass for the first time.

The sound attenuation coefficient obtained with IXS is plotted as a function of frequency in the upper panel of Figure 8, together with the values measured by lower frequency probes. The comparison between the data at room temperature and at a few Kelvin shows that the mean free path is temperature dependent up to 300 GHz and thus affected by anharmonic processes. In this frequency range the damping at room temperature follows an almost quadratic frequency dependence which extrapolates to the first point of the new IXS data. Here the disorder induced term, Rayleigh scattering, dominates the anharmonic/relaxational contributions. The sound attenuation is then proportional to the fourth power of frequency up to a crossover point, which coincides with the boson peak position at the investigated temperature (see the vertical dashed line in Figure 8).

In summary, the new IXS data give clear evidence of a Rayleigh scattering regime in glasses. This observation represents the first direct measurement of the Rayleigh law up to the boson peak frequency in vitreous silica, confirming the theoretical prediction of the existence in glasses of this peculiar attenuation mechanism.

References
[1] W.A. Phillips, *Amorphous Solids: Low Temperature Properties* (Springer, Berlin, 1981).
[2] J.W.S. Rayleigh, *The Theory of Sound* (The Macmillan Company, 1896) Vol. **II**.
[3] C. Masciovecchio *et al.*, *Phys. Rev. Lett.* **97**, 035501 (2006).
[4] A. Devos *et al.*, *Phys. Rev. B* **77**, 100201(R) (2008).

High pressure studies

Melting points under pressure: the end of a controversy

Principal publication and authors
A. Dewaele (a), M. Mezouar (b), N. Guignot (c), and P. Loubeyre (a), *Phys. Rev. Lett.* **104**, 255701-255704 (2010).
(a) CEA de Bruyères le Châtel (France)
(b) ESRF
(c) Synchrotron Soleil (France)

In recent years, great effort has been devoted to the investigation of the melting curve of elements at high pressure. However, melting remains a phase transition difficult to predict even with the most advanced theoretical methods. On the experimental side, attaining and measuring pressures of a few millions of atmospheres and temperatures of several thousands of K, and at the same time, reaching and identifying the equilibrium state of the material is also a challenge.

The melting curve of tantalum (Ta) exemplifies the efforts, problems and controversies in the determination of the melting curves of elements. The reported melting temperatures of tantalum were spread over several thousand degrees in the pressure range 100–300 GPa. Using shock compression, created by the impact of a projectile on the sample, a melting point of ~ 9700 K at 300 GPa has been determined. In laser-heated diamond anvil cells (LHDAC), where the sample is statically compressed between two diamonds and heated by a focussed infrared laser, melting points of ~ 3730 K at 100 GPa (obtained by visual detection) have been reported. This is only a few hundred K higher than the melting point at ambient pressure (3290 K), hence revealing a very flat melting curve as a function of pressure. Such a large discrepancy, outside the estimated error bars of the measurements, has stimulated many discussions. Various explanations have been proposed based on a possible difference in nature of the transformation seen by static and dynamic techniques [1].

We have used a new methodology, based on X-ray diffraction, to detect the melting of tantalum in an LHDAC, building on a previous study of lead [2].

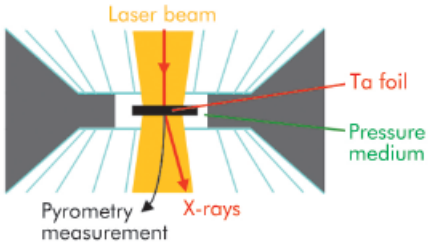

Fig. 9: Schematic drawing of the pressure chamber in the laser heated diamond anvil cell. Various pressure media (alkali halides, rare gas solids, oxides) have been used.

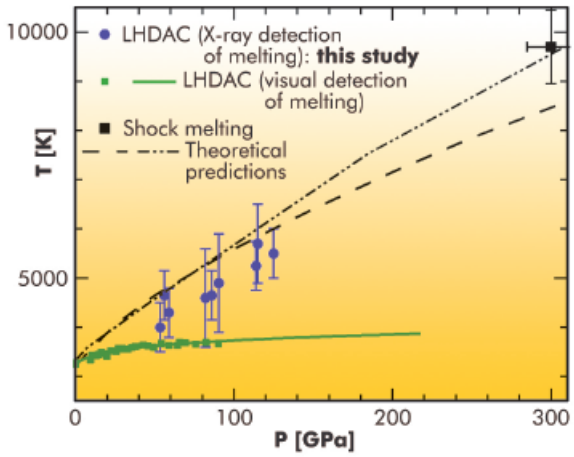

Fig. 10: Melting point determinations and predictions for tantalum.

At beamline ID27, X-ray and laser beams were focussed on a common point within the sample while its temperature was measured by pyrometry (Figure 9). By recording the sample's characteristic X-ray diffusion signal we were able to identify the state of the sample, including chemical reaction within it. The measurement of the solid sample specific volume further allowed the temperature path scenario provided by pyrometric measurements to be checked.

Our experiments showed that tantalum is chemically reactive in the LHDAC; in particular, it reacted with the diamond anvil to form a carbide. Such chemical reactions strongly perturb the observation of structural changes of the sample along a heating path. We also observed that the melting of the medium which surrounds the sample, called pressure medium, can affect pyrometry measurements because of a change of optical properties of the sample assembly and movements of the sample. This parasitic effect is a real problem for highly refractive materials such as Ta. A large fraction of our temperature measurements, biased by one of these effects, had to be discarded. The reliable data showed that the melting temperature of tantalum was much higher than previously measured in an LHDAC (for instance, 5500±500 K at 125 GPa). We furthermore observed that tantalum remained in the body-centred cubic phase up to the melting point.

Our new LHDAC melting point results reconcile both the shock melting point and theoretical predictions (see Figure 10). We believe that this study has set a new standard for LHDAC studies; a similar approach, based on *in situ* X-ray diffraction, should be used for the measurement of the iron melting curve.

References
[1] C.J. Wu, P. Söderlind, J.N. Glosli and J.E. Klepeis, *Nature Mater.* **8**, 223-228 (2009).
[2] A. Dewaele, M. Mezouar, N. Guignot and P. Loubeyre, *Phys. Rev. B* **76**, 144106-144113 (2007).

Melting of peridotite to 140 GPa

The solid mantle lies at 2900 km under our feet, and is made up essentially of oxides of magnesium, iron and silicon. It lies above the Earth's core, which mainly consists of liquid iron. With a pressure of around 1.4 million times the atmospheric pressure and a temperature of more than 4000 Kelvin, the solid mantle is the home for chemical reactions and changes in states of matter that are not completely understood. Seismologists have acknowledged an abrupt reduction of the speed of the seismic waves, which sometimes reaches 30% when getting close to the liquid core boundary. They called these regions ultra-low velocity zones or ULVZs. For the last 15 years, these observations have led scientists to formulate the hypothesis of partial melting of the Earth's mantle at the core-mantle boundary [1], but, until today, experimental validation at the appropriate temperatures and pressures has remained a challenge.

To check the hypothesis of the presence of a partial melt at the base of the mantle, we performed melting experiments on a natural peridotite composition (peridotite is the dominant rock of the Earth's mantle

Principal publication and authors
G. Fiquet (a), A.L. Auzende (a), J. Siebert (a), A. Corgne (b), H. Bureau (a), H. Ozawa (a,c) and G. Garbarino (d), *Science* **329**, 1516-1518 (2010).
(a) Institut de Minéralogie et de Physique des Milieux Condensés (IMPMC), Université Pierre et Marie Curie, CNRS, Université Paris Diderot, Institut de Physique du Globe de Paris (France)
(b) Institut de Physique du Globe de Paris (France) and Observatoire Midi-Pyrénées, Toulouse (France)
(c) Department of Earth and Planetary Sciences, Tokyo Institute of Technology (Japan)
(d) ESRF

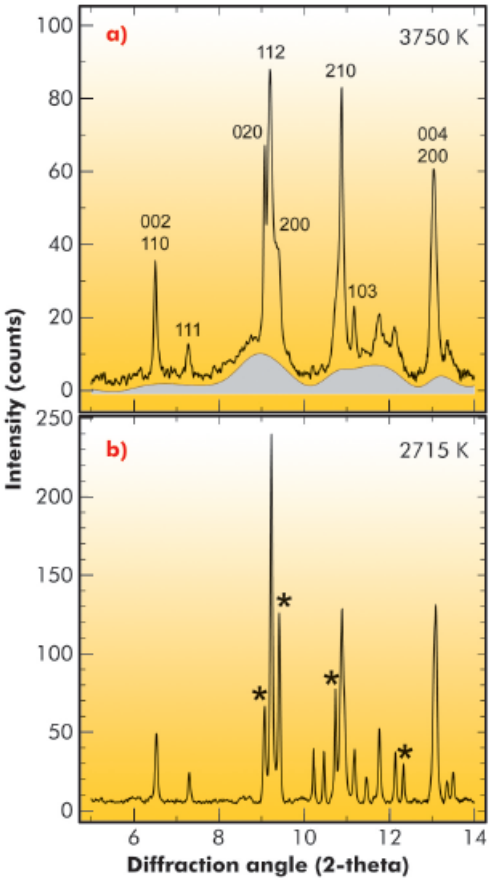

Fig. 11: Diffraction patterns collected at 61 GPa after normalised reference background subtraction: a) above solidus at 3750 K. The diffuse scattering liquid contribution is shown by the shaded area; it does not correspond to a physical structural model of the liquid. HKL indexes are given for remaining diffraction peaks that can be assigned to magnesium silicate perovskite, observed above the solidus temperature at this pressure. b) Subsolidus at 2715 K. Stars denote diffraction peaks of Ca-perovskite and ferropericlase affected by partial melting at these conditions.

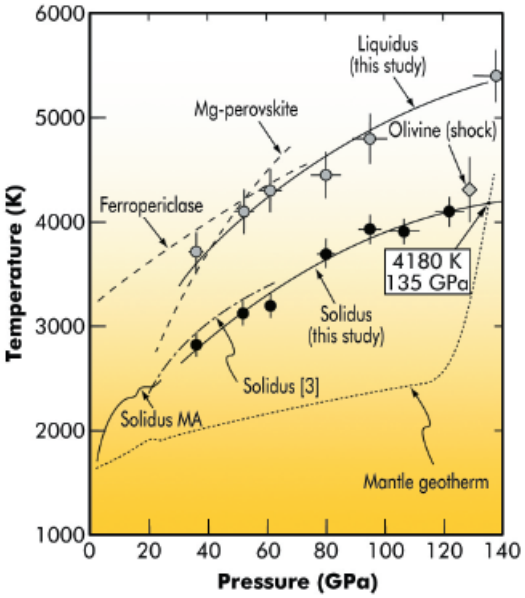

Fig. 12: Solidus (black solid circles) and liquidus (grey solid circles) of peridotite, along with melting curve data from the literature. Shown are the average estimate of the solidus for KLB-1 peridotite from previous multi-anvil work and melting data for a pyrolitic composition ([3], dot-dashed line). The solid grey diamond indicates the shock melting point of olivine. Melting temperatures of the major lower mantle phases Mg-perovskite and ferropericlase are indicated by long-dashed lines. Our solidus line, extrapolated to the core mantle boundary (solid line), intersects the Earth's mantle temperature profile (or geotherm) at 135 GPa and 4180 K.

above a depth of about 400 km; below that depth, olivine is converted to denser higher-pressure mineral phases). These experiments were carried out over a range of lower mantle pressures between 36 and 140 GPa, using a laser-heated diamond-anvil cell (DAC) coupled with *in situ* synchrotron measurements at the high-pressure beamline **ID27**. To ensure chemical homogeneity at the smallest scale and Fe as mostly Fe^{2+}, a glass was prepared from the peridotite starting material using an aerodynamic levitation device coupled with CO_2 laser heating, before being pressurised and heated in a laser-heated diamond-anvil cell. We then used *in situ* X-ray diffraction as the primary criterion for melting and to determine the order in which crystalline phases melt (Figure 11). From this we could establish, without any extrapolation, fusion curves of the deep Earth's mantle. We show that partial melting at the base of the mantle is possible when the temperature approaches 4200 K (Figure 12).

This observation reinforces the hypothesis of the presence of a deep magma ocean on the top of Earth's core, which could be as thick as 50 km and explain the presence of ULVZs shown by seismology. It is also attractive to link these observations with an episode of extensive melting that probably affected the primitive Earth, leading to the formation of a deep magma ocean. If the evolution of a terrestrial magma ocean resulted in the formation of a layer of melt at the base of the mantle early in the Earth's history, our experiments show that some relics of this early magma ocean may have survived at the core mantle boundary. We could also prove that the liquid produced during this partial melting is dense and that it can hold multiple chemical elements, among which are important markers of the dynamics of the Earth's mantle. Such a layer would thus be an ideal candidate for an unsampled geochemical reservoir hosting a variety of incompatible species, notably the planet's missing quota of heat-producing elements [2].

References
[1] Q. Williams and E.J. Garnero, *Science* **273**, 1528 (1996).
[2] M. Boyet and R.W. Carlson, *Science* **309**, 576 (2005).
[3] A. Zerr, A. Diegeler and R. Boehler, *Science* **281**, 243 (1998).

Composition of the Earth's inner core from high-pressure sound velocity measurements in Fe-Ni-Si alloy

Principal publication and authors
D. Antonangeli (a,b), J. Siebert (a,b), J. Badro (a,b), D.L. Farber (b), G. Fiquet (a), G. Morard (a) and F.J. Ryerson (b), *Earth Planet. Sci. Lett.* **295**, 292-296 (2010).
(a) IMPMC, IPGP, Univ. Pierre et Marie Curie, Univ. Paris Diderot (France)
(b) LLNL, Livermore-CA (USA)

The study of seismic wave propagation and normal mode oscillation are direct probes of the Earth's interior, sensing sound velocities and density. However, to derive accurate compositional models, these seismological observations need to be combined with experiments constraining the density and elasticity of highly compressed minerals. Looking at velocity vs. density, Birch proposed in the 1950's that the Earth's core is composed of iron alloyed with nickel and some "light element(s)". More recently, high-pressure measurements on several iron compounds (FeO, FeSi, FeS, FeS_2 and Fe_3C) suggested an Earth's inner core model of iron alloyed with silicon (2.3 wt.%) and traces of oxygen (0.1 wt.%). However, these results are based on assumptions that can only be confirmed by direct measurements on samples of realistic chemical compositions. Furthermore, a clear limitation of the proposed model is that it is derived only considering the aggregate compressional sound velocity (V_P), whereas the largest discrepancy between the seismological observations and mineral-physics results is reported for the shear wave velocity (V_S).

We carried out inelastic X-ray scattering measurements at beamline **ID28** on a Fe-Ni-Si alloy with 4.3 wt.% of Ni and 3.7 wt.% of Si ($Fe_{0.89}Ni_{0.04}Si_{0.07}$). We collected data from the hexagonal close-packed (hcp) phase, at 27, 37 and 47 GPa on quasi-hydrostatically compressed samples, and at 32, 68 and 108 GPa on non-hydrostatically compressed samples. We then derived V_P from the aggregate longitudinal acoustic phonon dispersion, and we obtained V_S combining our measurements with values of the bulk modulus. The densities (ρ) were directly determined by X-ray diffraction.

In Figure 13, the measured V_P is plotted as a function of ρ, together with values for pure Fe and $Fe_{0.78}Ni_{0.22}$ alloy. While no systematic offsets can be observed between data for pure Fe and Fe–Ni alloy, velocities for $Fe_{0.89}Ni_{0.04}Si_{0.07}$ are about 9% higher at the same density. We also note that our experimental results compare favourably with calculations on $Fe_{0.9375}Si_{0.0625}$ (Figure 13), further stressing that the increase in V_P is solely due to the Si incorporation.

Figure 14 shows the extrapolation of our results to core conditions, reported along with the density evolution of hcp-Fe as compared with the seismic velocity profile from the preliminary reference earth model (PREM). V_P for pure Fe is lower than the PREM, whereas adding 3.7 wt.% Si yields a velocity that is too high. If we consider simple linear mixing of Fe and $Fe_{0.89}Ni_{0.04}Si_{0.07}$ (*i.e.* an ideal solution mixing model), we match the PREM values of V_P and ρ for an alloy with 1.2 wt.% of Si (blue dashes in Figure 14). However, both Fe and $Fe_{0.89}Ni_{0.04}Si_{0.07}$

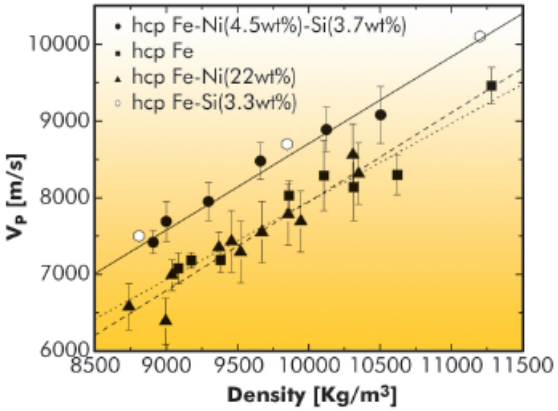

Fig. 13: Aggregate compressional sound velocity vs. density. Circles: $Fe_{0.89}Ni_{0.04}Si_{0.07}$; squares: Fe; triangles: $Fe_{0.78}Ni_{0.22}$; open hexagons (calculations): $Fe_{0.9375}Si_{0.0625}$. Lines are linear regressions to the experimental data (solid – $Fe_{0.89}Ni_{0.04}Si_{0.07}$; dotted – Fe; dashed – $Fe_{0.78}Ni_{0.22}$).

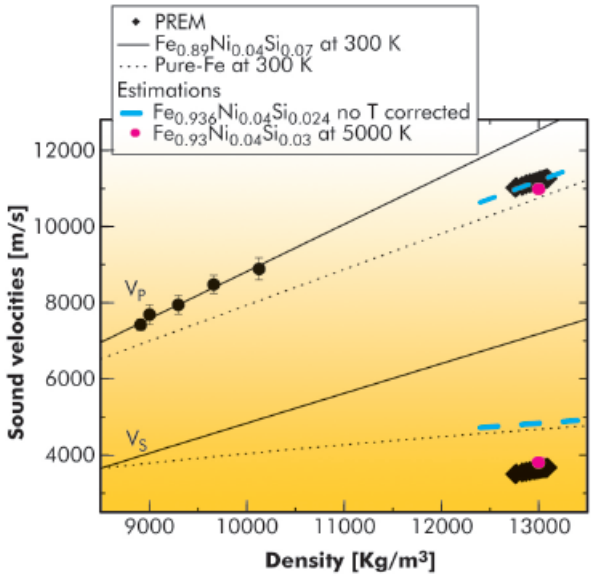

Fig. 14: Aggregate compressional (V_P) and shear (V_S) sound velocities and density extrapolations. Circles: IXS data on $Fe_{0.89}Ni_{0.04}Si_{0.07}$; diamonds: PREM. Solid lines – $Fe_{0.89}Ni_{0.04}Si_{0.07}$; dotted lines – pure Fe. Blue dashes are estimated values for $Fe_{0.936}Ni_{0.040}Si_{0.024}$ (≈1.2 wt.% Si), neglecting temperature corrections. Red dots are estimated values for $Fe_{0.93}Ni_{0.04}Si_{0.03}$ (≈1.5 wt.% Si) at 13000 Kg/m³ and 5000 K.

exhibit values of V_S significantly higher than PREM. From the above, it is clear that a simultaneous solution for V_P, V_S and ρ cannot be obtained by simply varying the amounts of Ni and Si.

At core temperatures (4000–6000 K) anharmonic effects are, however, expected, and we therefore applied temperature corrections (at constant density) to our ambient-temperature results. Starting from computational estimations for pure Fe, we assumed 4% softening of V_P and 30% softening of V_S at 5000 K and 13000 Kg/m^3. The thermal softening of V_P requires an increase in the Si content to ≈1.5 wt.% to match the seismic observations. Most importantly, this composition appears to provide a simultaneous solution for both V_P and V_S, consistent with PREM values (red dots in Figure 14).

Our results suggest an inner core composition containing 4–5 wt.% of Ni and 1–2 wt.% of Si. The exact amount of Si might vary depending upon the temperature corrections or if other elements are also present in the inner core. Our conclusions pertain strictly to solid Fe-alloys and hence the inner core. Elements such as oxygen that are expected to reside mainly in the outer core cannot be adequately constrained here. However, our proposed core composition matches all three primary geophysical observables (V_P, V_S and ρ) simultaneously for the first time. Taking literature values for the partition coefficient for silicon between the liquid and solid phase of iron, we estimate an entire core composition with Si ranging from 1.2 to 4 wt.%.

Principal publication and authors
W.M. Xu (a), G.Kh. Rozenberg (a), M.P. Pasternak (a), M. Kertzer (a), A. Kurnosov (b), L.S. Dubrovinsky (b), S. Pascarelli (c), M. Munoz (c), M. Vaccari (c), M. Hanfland (c), and R. Jeanloz (d). *Phys. Rev.* **B 81**, 104110 (2010).
(a) School of Physics and Astronomy, Tel Aviv University (Israel)
(b) Bayerisches Geoinstitut, University Bayreuth (Germany)
(c) ESRF
(d) Department of Earth and Planetary Science, University of California, Berkeley, CA (USA)

Pressure induced Fe ↔ Cu valence exchange and its structural consequences

Diamond anvil cells (DAC) can be used to reach pressures beyond 100 GPa. They have allowed the elucidation of electronic phenomena such as intra *d-d* or inter *p-d* bands overlap leading to correlation breakdown (the Mott transition), *spin-crossover* due to crystal field enhancement, and variation of the magnetic ordering temperature. The interest in these pressure-induced electronic transitions became more momentous after recognising their occurrence with simultaneous structural phase transitions, caused by an electronic transition.

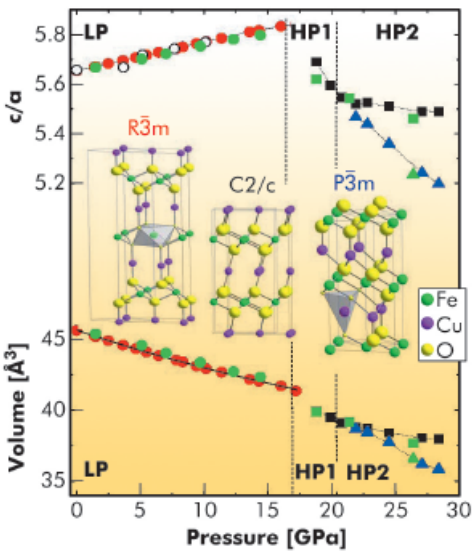

Fig. 15: Pressure dependence of the unit-cell volume and crystal anisotropy reflected by the c/a ratio at room temperature. Circles correspond to the *R*$\bar{3}$*m* phase, squares to the *C2/c*, and triangles to the *P*$\bar{3}$*m* structures. The open points correspond to data recorded at decompression. The discontinuous decrease in c/a and V occurs at the onset of the HP1 phase.

Here we report on the high pressure (HP) studies of a *binary* transition metal oxide, delafossite, which is composed of layers of Cu^{1+}, Fe^{3+} and O^{2-} ions ($CuFeO_2$) forming a hexagonal structure with *R*$\bar{3}$*m* symmetry (left inset in Figure 15). The triangular sub-lattices of antiferromagnetic Fe^{3+} moments are separated by layers of nonmagnetic Cu^{1+} and O^{2-} along the *c*-axis. The weak Fe-O-Cu-O-Fe superexchange creates a 2D magnetic structure resulting in a spin-frustrated system. Our earlier studies revealed that only above ~18 GPa a 3D structure is established with long range magnetic ordering at T_N = 40 K. This finding [1] motivated the present work for which the initial purpose was to search for the new structure that undergoes the 2D>3D transition.

The methods used for this study were ^{57}Fe Mössbauer spectroscopy, X-ray diffraction, and X-ray absorption spectroscopy (XAS), the latter two carried out at beamlines **ID09A** and **ID24**. XAS studies were performed both at the Fe and Cu *K*-edge using perforated anvils.

The sturdy O-Cu-O dumbbell backbones with orientation parallel to

the *c*-axis, are responsible for the unusual robustness of the anisotropic low pressure region (0-18 GPa). With increasing pressure *c/a* increases until the $R\bar{3}m$ structure becomes unstable and a first-order transition takes place, accompanied by reversal of the *c/a* slope and a discontinuous decrease in V(P) (HP1 range in Figure 15). In the new *C2/c* structure the O-Cu-O axis are tilted by 28° with respect to the *c*-axis. This signals the *offset* of the 2D nature of delafossite and allows the onset of magnetic ordering at 40 K; a typical example of a structurally induced electronic/magnetic transition.

With further pressure increase, we made an astounding observation. Mössbauer spectroscopy studies at P > 20 GPa uncovered a new phenomenon not observed hitherto, a pressure-induced *reduction* of Fe^{3+}, *e.g.* Fe^{3+} ($S = 5/2$) $\overset{P}{\underset{P}{\rightleftharpoons}}$ Fe^{2+} ($S = 2$). This dramatic occurrence can be seen in Figure 16. Up to ~ 23 GPa, within the *C2/c* stability field, Mössbauer spectra at T <<< T_N (40 K) revealed a single hyperfine field characteristic of a six-folded ferric oxide. At P > 23 GPa a new spectral component (red curve) appeared. Its hyperfine interaction parameters, hyperfine field and isomer shift are typical of an Fe^{2+}-O species. This new genus carried with it robust magnetic features: a threefold jump in T_N (see inset in Figure 16) that can be attributed only to new, enhanced, superexchange interactions.

The most reasonable mechanism for the $Fe^{3+} \rightarrow Fe^{2+}$ process is the simultaneous onset of a $Cu^{1+} \rightarrow Cu^{2+}$ valence change resulting from direct or indirect Fe-Cu *d*-band overlap.

The K-edge Cu and Fe XAS studies clearly confirmed this conjecture: the Cu-K-edge absorption edge shifts by about 1 eV in the 20-27 GPa range, while the iron edge shows a similar, however, negative shift. Given that within the family of pure iron (copper) oxides the absorption edge is observed to increase with increasing valence, our XAS results are consistent with the discussed valence transformations.

The creation of a Cu^{2+} - O bonding leads not only to the onset of a new *S*=1/2 magnetic sublattice but also to an increase in the copper coordination number, from 2 to 4. The 4-coordinated Cu^{2+} species cannot be accommodated within the *C2/c* framework, and as a result, domains of the $P\bar{3}m$ structure appear, characterised by the formation of tetrahedral CuO_4 distorted along the *c*-direction (HP2 range Figure 15). The XANES Cu simulation is in full accordance with the two Cu species valences and coordination numbers.

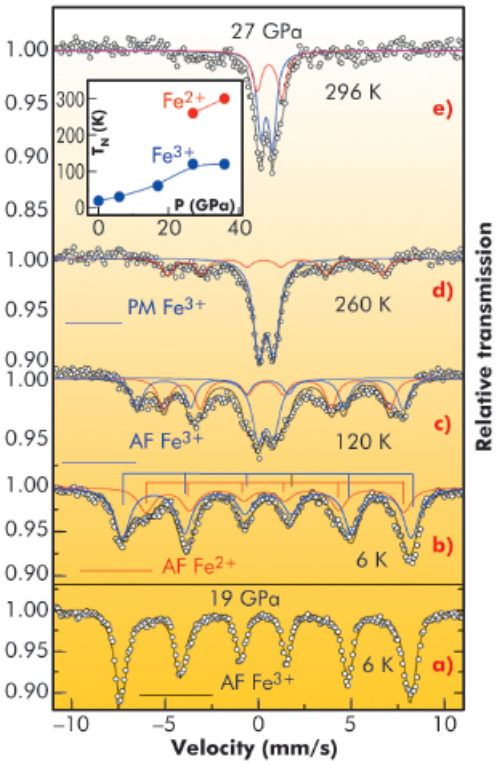

Fig. 16: Mössbauer spectra of $CuFeO_2$ recorded at 19 and 27 GPa. The inset summarises the T_N(P) of the two Fe species, Fe^{3+} and Fe^{2+} (PM - paramagnetic; AF - antiferromagnetic).

Epilogue: The HP studies of $CuFeO_2$ concludes with the formation of a new super-structure at P > 23 GPa composed of a sub-structure $Cu^{1+}Fe^{3+}O_2$ with space group *C2/c* and $Cu^{2+}Fe^{2+}O_2$ with space group $P\bar{3}m$. Their relative abundance at 29 GPa is 2:1 and their T_N's are 100 K and 300 K, respectively. The whole pressure process is reversible with no noticeable hysteresis.

References
[1] W.M. Xu, M.P. Pasternak, and R.D. Taylor, *Phys. Rev.* **B 69**, 052401 (2004).

Principal publication and authors
M. Sikora (a), A. Juhin (b,c), T.-C. Weng (c,d), P. Sainctavit (e), C. Detlefs (c), F. de Groot (b) and P. Glatzel (c), *Phys. Rev. Lett.* **105**, 037202 (2010).
(a) AGH University of Science and Technology, Krakow (Poland)
(b) Utrecht University (The Netherlands)
(c) ESRF
(d) currently at: SSRL, Stanford (USA)
(e) IMPMC, Université Pierre et Marie Curie, Paris (France)

Electronic and magnetic structures

Strong K-edge magnetic circular dichroism in 1s2p RIXS

X-ray magnetic circular dichroism (XMCD) is a powerful tool for the element-specific study of the magnetic structure of complex systems [1]. The spin and orbital polarisation of 3*d* valence orbitals is conveniently studied by dipole-allowed 2p → 3d transitions, *i.e.* *L*-edge absorption spectroscopy in the soft X-ray range. Most soft X-ray XMCD measurements are performed using total electron yield because significant self-absorption effects are observed when using total fluorescence yield detection. Thus, *L*-edge XMCD is mainly sensitive to the sample surface and, in addition, it is not compatible with demanding sample environments such as high-pressure cells. Hard X-rays are used at the *K*-edge but the very weak XMCD signal and the absence of spin-orbit split edges do not allow a detailed quantitative interpretation. Hence there is a need for a magnetic spectroscopy in the hard X-ray range that can provide information on the ordering and the value of 3d magnetic moments.

This goal can be achieved by coupling XMCD with 1*s*2*p* resonant inelastic X-ray scattering (RIXS) at the *K* pre-edge.

RIXS is a second-order optical process where first a core hole in a deep electron shell is created (intermediate state) that is then replaced by a shallower hole (final state). This results in sharper spectral features and often a rich multiplet structure that reveals electron-electron and spin-orbit interactions [2]. The 1*s*2*p* RIXS probes the evolution of the *Kα* emission (2*p* → 1*s*) following resonant excitation of a 1*s* electron. The *K*-edge absorption spectra of most 3*d* transition metal (TM) compounds show weak pre-edge features that are sensitive to the valence orbitals and are predominantly composed of the 3*d* density of unoccupied states. The $2p^5 3d^{n+1}$ final state electron configuration in 1*s*2*p* RIXS is identical to the 2*p* spin-orbit split $L_{2,3}$ absorption edges. The idea of our work was to combine a bulk sensitive hard X-ray probe with the

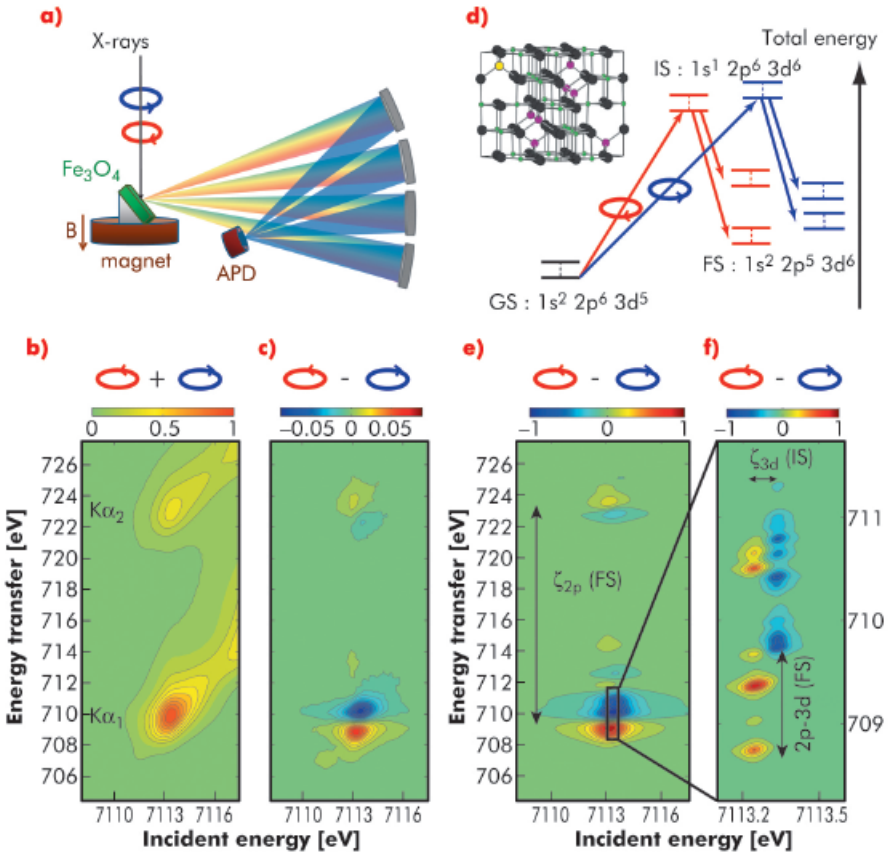

Fig. 17: The 1*s*2*p* RIXS-MCD in magnetite. a) The experimental setup including external magnetic field, circularly polarised incident X-rays (left and right, pictured as red and blue), a set of spherically bent crystal analysers and an avalanche photodiode (APD). b) Experimental 1*s*2*p* RIXS plane averaged over the two circular polarisations. c) Experimental RIXS-MCD plane, plotted as the difference between the RIXS planes measured for opposite helicities of circularly polarised light. d) Theoretical model used in the crystal field multiplet calculations, involving only a tetrahedral Fe^{III} ion of magnetite (yellow atom). e) The theoretical RIXS-MCD plane. f) The theoretical RIXS-MCD plotted for the $2p_{3/2}{}^5 3d^6$ final state with a reduced broadening reveals the origin of the energy shifts that yield the dichroism. The arrows indicate to which spin-orbit and multiplet interactions the splittings are proportional.

MCD sensitivity of a 2*p* (*L*-edge) core hole, *i.e.* to perform 1*s*2*p* RIXS at the K absorption pre-edge in 3*d* TM using circularly polarised X-rays.

1*s*2*p* RIXS-MCD experiments were performed at beamline **ID26** at room temperature on magnetite $[Fe^{III}]_{tetra}[Fe^{II}Fe^{III}]_{octa}O_4$ (**Figure 17a**). The experimental RIXS-MCD plane, plotted as the difference between left and right circularly polarised light, reveals a strong dichroic signal (**Figure 17c**). The comparison with the RIXS plane averaged over the two photon helicities (**Figure 17b**) shows that only the resonant features give rise to the XMCD. The experimental data are compared with the theoretical RIXS-MCD calculated within the crystal field multiplet approach (**Figure 17d**), assuming a dominant contribution of tetrahedral Fe^{III}. Good agreement between theory and experiment is achieved. The RIXS-MCD amplitude is as large as 16% and comparable to *L*-edge absorption MCD. Calculations show that the enhancement of the XMCD signal in RIXS is a result of increased splitting of the XMCD spectral features in the $2p^53d^{n+1}$ final state and the smaller lifetime broadening of the 2*p* as compared to the 1*s* core hole.

An interesting aspect of RIXS-MCD is the possibility of site-selective measurements in mixed valence and multisite compounds. As incident and emission energies depend on the oxidation state of the absorber, it is possible to increase the selectivity by tuning either of these, for example, at 7012 eV incident and 707 eV transfer energy (**Figure 17c**), to study the magnetic behaviour of octahedrally coordinated Fe^{II} in magnetite. This opens new opportunities for earth sciences and condensed matter physics, allowing for truly bulk sensitive, element- and site-selective measurements of 3*d* TM magnetic moments and their ordering under demanding sample environments.

References
[1] E. Beaurepaire *et al.*, *Magnetism: A Synchrotron Radiation Approach* (Springer, Berlin Heidelberg 2006).
[2] F. de Groot and A. Kotani, *Core Level Spectroscopy of Solids* (CRC Press, Boca Raton 2008); P. Glatzel and U. Bergmann, *Coord. Chem. Rev.* **249**, 65 (2005).

Non-collinear magnetisation structure of an epitaxial Fe/W(110) film in the vicinity of the thickness-driven spin reorientation transition

Bcc iron is known as an archetypal collinear ferromagnet. Deviations from this fundamental magnetic structure are expected for ultrathin Fe films as a consequence of symmetry breaking at surfaces or interfaces as well as of magnetoelastic effects originating from the misfit between the Fe film and the substrate. Recently, we have shown that, under certain conditions, collinear ferromagnetism becomes less favourable than a spin-spiral-like, vertically-inhomogeneous magnetisation state. This happens at the spin reorientation transition (SRT) in Fe films grown on W(110).

The SRT in the case of Fe/W(110) consists in the switching of spontaneous magnetisation during the film growth from the [1$\bar{1}$0] to the [001] in-plane direction as the iron film approaches the critical thickness, d_c. Our thickness-induced SRT was monitored *in situ* using grazing incidence nuclear resonant scattering (NRS) of synchrotron radiation [1]. The numerical analysis of the NRS data indicated that a non-collinear magnetisation structure is formed in the vicinity of the critical thickness, with a strong surface magnetisation pinning along the [1$\bar{1}$0] direction. With increasing thickness, the transition is initiated at the bottom atomic layers, neighbouring with the tungsten substrate, and finally is completed at the surface layer.

The measurements were done at the Nuclear Resonance beamline **ID18** [2]. ^{57}Fe was deposited on a freshly cleaned W(110) surface. Directly during the preparation, the NRS time spectra were collected in thickness steps corresponding to a fraction of a Fe monolayer. The deposition of Fe was not interrupted from the beginning up to the completion of the SRT process, and the spectra were accumulated *in situ* during the film growth. The fitted time spectra are shown in **Figure 18** for

Principal publication and authors
T. Ślęzak (a), M. Ślęzak (a), M. Zając (a.b), K. Freindl (a,c), A. Kozioł-Rachwał (a), K. Matlak (a), N. Spiridis (c), D. Wilgocka-Ślęzak (c), E. Partyka-Jankowska (d), M. Rennhofer (d,e), A.I. Chumakov (b), S. Stankov (b), R. Rüffer (b) and J. Korecki (a,c), *Phys. Rev. Lett.* **105**, 027206 (2010).
(a) AGH University of Science and Technology, Kraków (Poland)
(b) ESRF
(c) Polish Academy of Sciences (Poland)
(d) University of Vienna (Austria)
(e) AIT - Austrian Institute of Technology (Austria)

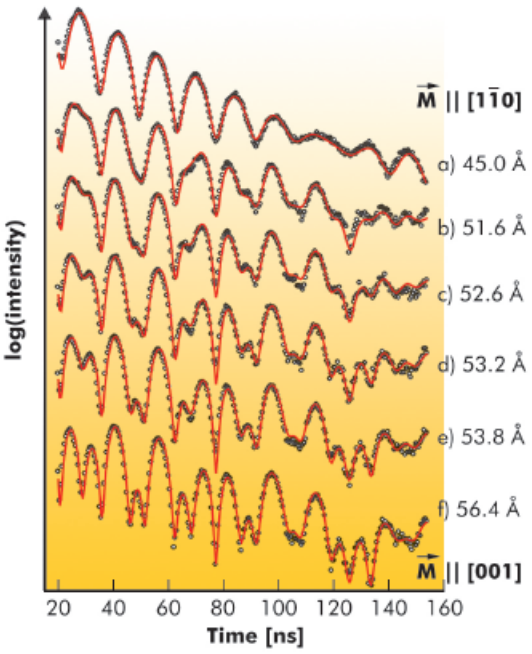

Fig. 18: Time spectra of nuclear resonant scattering in the vicinity of the SRT accumulated during continuous Fe evaporation. The corresponding Fe thicknesses *d* are labelled on the right.

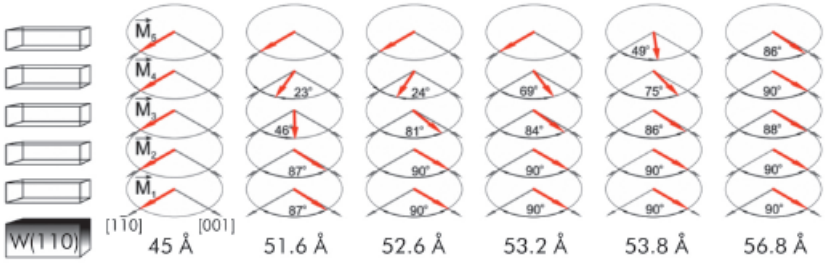

Fig. 19: Magnetisation structure of the epitaxial Fe/W(110) film during the thickness-induced SRT as derived from NRS measurements using a five sublayer model. The sublayer magnetisation vectors are labelled as $\vec{M}_{1-5}$.

selected Fe film thicknesses. A regular beat structure that is exemplified in Figure 18a reflects, according to the theoretical fits, the uniform magnetisation state along the [1$\bar{1}$0] direction, with the hyperfine magnetic field close to bulk Fe (B_{HF} = 32.9 T). Such a state persists up to a thickness of about d = 51 Å. The spectra for coverages larger than 56 Å (see Figure 18f) can be easily fitted assuming a homogeneous magnetisation, but now parallel to the [001] direction. It is clear that the SRT process is not abrupt but extends over a relatively large thickness range of δ ~ 6 Å, corresponding to three monolayers. The most unique and also challenging time spectra to fit were those accumulated during the progress of the SRT (Figure 18,b-e). The two most commonly considered ways of the magnetisation transition from [1$\bar{1}$0] to [001]: (i) coherent rotation and (ii) coexistence of [001] and [1$\bar{1}$0] magnetised domains, assuming a homogeneous magnetisation depth profile across the Fe(110) films, produced distinctly different spectra, however, neither of them could satisfactorily fit the experimental data in the transition.

The successful fits (Figure 18) could be obtained when the distribution of the magnetisation directions was modelled by dividing the film with thickness d into five sub-layers of equal thicknesses. For each sub-layer, an in-plane orientation of the hyperfine magnetic field (sub-layer magnetisation $\vec{M}_N$) was defined by the angle φ_N with respect to the [1$\bar{1}$0] in-plane direction. The orientation of the sub-layer magnetisations $\vec{M}_{1-5}$, as derived from the analysis of the NRS data, is shown schematically in Figure 19 for various thicknesses d of the Fe film. The onset of the transition was noticed for a thickness of 51.6 Å. The SRT from [1$\bar{1}$0] to [001] is initiated at the deepest layers, which switch first, while the magnetisation of the remaining sub-layers forms a fan-like structure. With increasing thickness, the magnetisation of the subsequent sub-layers rotates, and finally the transition is completed by the top-most surface layers.

Our studies clearly show that a non-collinear, exotic magnetic phase of epitaxial Fe films is stabilised at the vicinity of a critical SRT thickness.

References
[1] E. Gerdau and H. DeWaard, *Hyperfine Interact.* **123-124** (1999).
[2] R. Rüffer and A.I. Chumakov, *Hyperfine Interact.* **97-98**, 589 (1996).

Inequivalent routes across the Mott transition in V_2O_3 explored by X-ray absorption

Some materials exhibit metal-insulator transitions (MIT) without changes in crystal structure or long-range magnetic order. These phenomena, known as Mott-Hubbard transitions, are a fundamental signature of strong electronic correlations resulting from the interplay of the on-site Coulomb interaction U and bandwidth W. A particularly mind-boggling situation

happens at intermediate U/W strength, though progress has been made recently thanks to dynamical mean field theory (DMFT) approaches [1]. Cr-doped vanadium sesquioxide V_2O_3 appears as a textbook case for investigating such MIT. At ambient conditions, it is a paramagnetic insulator (PI) that is driven to a paramagnetic metal (PM) or an antiferromagnetic insulator (AFI) according to doping level (x), temperature (T) or pressure (P). The correlated nature of the transition in V_2O_3 has been confirmed by the observation of a quasiparticle at the Fermi level with bulk-sensitive photoemission spectroscopy [2], while soft X-ray absorption has revealed the multi-orbital, S=1, nature of the ground state [3] in contrast to earlier, single electron models. The underlying mechanism of the MIT, however, is still poorly understood and calls for further investigations throughout the entire phase diagram.

In a recent series of experiments carried out at beamlines **ID26** and **BM32**, we have probed the electronic properties of V_2O_3 by X-ray absorption spectroscopy at the V-edge. The spectra were acquired in the so-called "high-resolution" partial fluorescence yield (PFY) mode by monitoring the V Kα line intensity while varying the incident energy through the K-edge. We used a Ge crystal analyser as energy filter operated in Rowland circle geometry. The gain in resolution is especially appreciable in the pre-edge region that bears the critical information. Figure 20 illustrates our main results. The left panel shows the V-K edge measured at the T-induced MIT. The spectral changes mostly occur in the pre-edge region (features A to C) that directly relates to the *d* electronic properties. Discarding feature C of *p-d* hybridised character, the MIT mainly entails a change of the A/B intensity ratio. Aided by DMFT calculations, we understand these changes by the increase of the occupation, in the ground state, of the a_{1g} crystal-field split orbital, *i.e.* of the incoherent upper Hubbard band, at the transition. Interestingly, an entirely different behaviour is observed in the P-driven Mott transition. Figure 21 shows the pre-edges obtained by following different "pathways" in the phase diagram through the MIT as illustrated in the inset. Instead of a change of intensity, P yields an energy shift of the pre-edge features. The results, best visualised in the difference spectra, provide evidence for the equivalent roles of T and doping – also confirmed by photoemission – while P clearly

Principal publication and authors
F. Rodolakis (a,b), P. Hansmann (c,d), J.-P. Rueff (b,e), A. Toschi (c), M.W. Haverkort (d), G. Sangiovanni (c), A. Tanaka (f), T. Saha-Dasgupta (g), O.K. Andersen (d), K. Held (c), M. Sikora (h), I. Alliot (h,i), J.-P. Itié (b), F. Baudelet (b), P. Wzietek (a), P. Metcalf (j) and M. Marsi (a), *PRL* **104**, 047401 (2010).
(a) LPS, Orsay (France)
(b) Synchrotron SOLEIL (France)
(c) ISSP, Vienna (Austria)
(d) MPI, Stuttgart (Germany)
(e) LCPMR, Paris (France)
(f) Hiroshima University (Japan)
(g) Bose Center for Basic Sciences, Kolkata (India)
(h) ESRF
(i) CEA (Grenoble)
(j) Purdue University (USA)

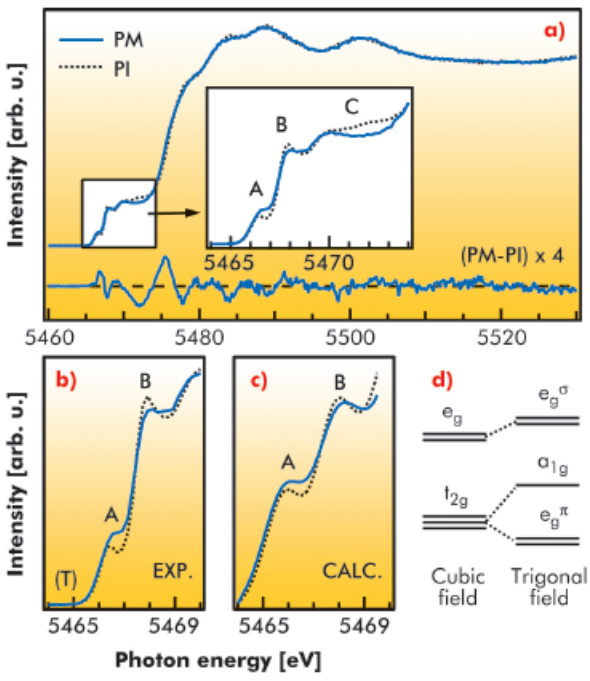

Fig. 20: V-K edge in V_2O_3 at the metal-insulator transition: Experiment and calculations.

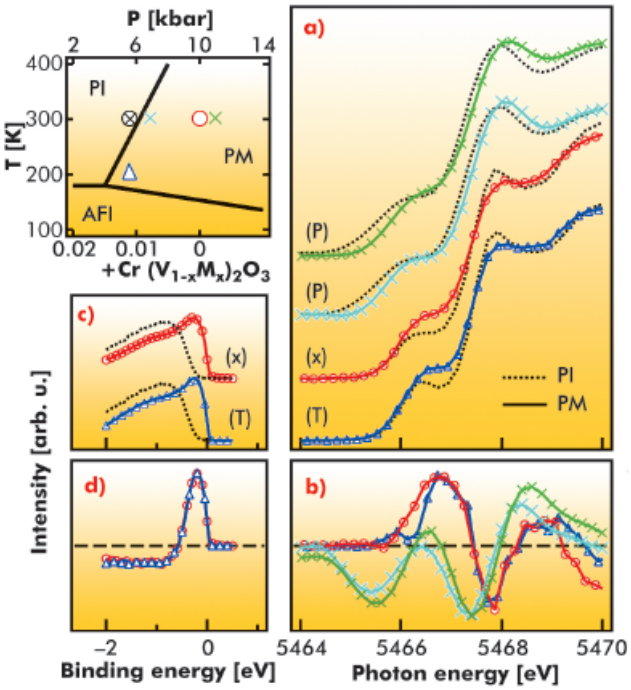

Fig. 21: Role of external parameters: The spectra provide evidence of the non-equivalence between P, T and doping (x) driven transitions. a) V K-edge absorption spectra, b) differences of absorption spectra, c) photoemission spectra, d) difference of photoemission spectra.

References
[1] A.I. Poterayev *et al.*, *Phys. Rev. B* **76**, 085127 (2007).
[2] F. Rodolakis *et al.*, *Phys. Rev. Lett* **102**, 066805 (2009) and references therein.
[3] J. Park *et al.*, *Phys. Rev. B* **61**, 11506 (2000).

steps out as a unique thermodynamics parameter. Thus, two different mechanisms for the MIT can be proposed: T and doping could act on the crystal field splitting through electron correlations while P more directly affects the electronic bandwidth by the compression of the lattice. There is evidence as well that both T and doping induce a metallic phase intermixed with insulating patches while pressure yields almost pure metallic character. We believe our finding may apply to other strongly correlated systems, with pressure opening inequivalent pathways through their phase diagrams.

Tetrahydrofuran clathrate hydrate formation

Principal publication and authors
H. Conrad (a,b), F. Lehmkühler (a,b), C. Sternemann (a), A. Sakko (c), D. Paschek (d), L. Simonelli (e), S. Huotari (c,e), O. Feroughi (a), M. Tolan (a) and K. Hämäläinen (c), *Phys. Rev. Lett.*, **103**, 218301 (2009).
(a) Fakultät Physik/DELTA, TU Dortmund (Germany)
(b) HASYLAB at DESY, Hamburg (Germany)
(c) Department of Physics, University of Helsinki (Finland)
(d) Rensselaer Polytechnic Institute, Troy (USA)
(e) ESRF

Since the oil disaster in the Gulf of Mexico, clathrate hydrates have gained media attention. These ice-like compounds consist of water nano-cages in which guest molecules, mainly gases, can be trapped. Hydrates, containing various alkane molecules from the oil, formed at the steel caps that were intended to collect the oil leaking from the drill hole. These hydrates blocked the caps and made controlled pumping impossible. A similar problem is known from gas and oil pipelines, where hydrate formation has to be inhibited to suppress blockages. Further interest in hydrates is for those existing in the ocean floor which could be used as an energy source and others may be used for safe gas storage, *e.g.* hydrogen for fuel cells [1]. Tetrahydrofuran (THF)-hydrogen double hydrates are interesting because the presence of THF decreases the hydrate stability pressure by approximately two orders of magnitude [1]. A schematic diagram of THF hydrate is shown in Figure 22. Hydrate formation from the liquid phase at molecular length scales was mainly studied by theoretical work, research that is important for inhibition of hydrate formation in the oil industry. Furthering this knowledge is essential for other applications such as gas storage. Various hydrate formation models based on molecular dynamics (MD) simulations have been published in the literature [1], however, experimental data are still rare. In a previous study we found that the hydrate formation at water-CO_2 interfaces follows a stochastical model instead of forming hydrate precursors in a supercooled liquid phase [2].

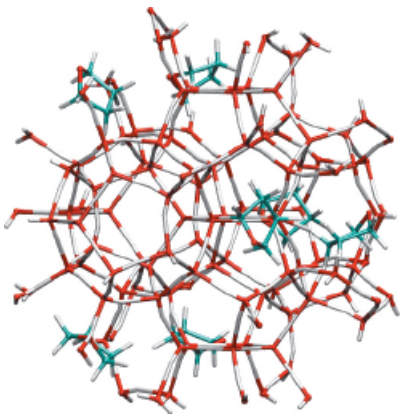

Fig. 22: Schematic picture of the THF hydrate structure. The cage structure formed by the water molecules is represented as red-white sticks. Because the THF molecules only occupy the large cages of the sII hydrate structure [1], a second guest can be placed in the small cages.

In contrast to the majority of hydrates that usually form at the water surface, THF hydrate forms from a liquid mixture of water and THF. Thus, bulk sensitive methods have to be used to study the THF hydrate formation process. We used X-ray Raman scattering at **ID16** to measure the oxygen K-edge of a liquid mixture at room and supercooled (T<277 K) temperatures. X-ray Raman scattering is very sensitive to changes in the sample's local structure [3]. In particular, the formation of hydrate precursors will influence the fine structure of the O K-edge. Furthermore, we measured spectra of THF hydrate at various temperatures to study a potential structural rearrangement, *e.g.* due to a strong guest-host interaction as suggested by MD simulations [4].

The experimental spectra are presented in Figure 23 together with difference spectra referenced to the spectra of the

liquid at room temperature. Apparently, the difference of the liquid phases is weak and in agreement with water spectra representing the temperature effect on the water's hydrogen bond network [5]. Thus, the formation of hydrate precursors is highly unlikely. Moreover, the difference between the two hydrate spectra suggests a structural change in the hydrate with an increase of order at lower temperatures. This is supported by DFT calculations that yield a good agreement with the experimental data for the hydrate at 254 K. Hence, a rearrangement of the hydrate structure to a less ordered sample is suggested for elevated temperatures. Altogether, we were able to favour a stochastic hydrate formation model without occurrence of hydrate precursor clusters for THF hydrate as were also observed at the water-CO_2 interface [3] and we found the first experimental evidence for a distorted THF hydrate structure at high temperatures.

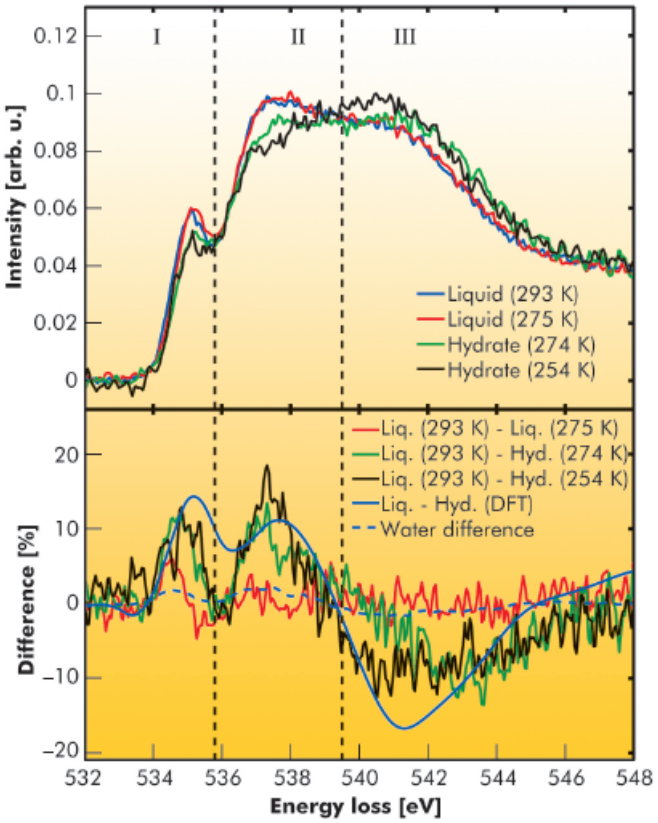

Fig. 23: X-ray Raman scattering spectra (top) and differences (bottom) of the liquid mixture and the hydrate. The data for water represents a difference between 295 K and 275 K [5].

References

[1] E.D. Sloan and C.A. Koh, *Clathrate Hydrates of Natural Gases*, CRC Press Inc. (2008).

[2] F. Lehmkühler, M. Paulus, C. Sternemann, D. Lietz, F. Venturini, C. Gutt and M. Tolan, *J. Am. Chem. Soc.* **131**, 585 (2009).

[3] J. Tse, D.M. Shaw, D.D. Klug, S.Patchkovskii, G. Vankó and M. Krisch, *Phys. Rev. Lett.*, **100**, 095502 (2008), T. Pylkkänen, V.M. Girodano, J.C. Chervin, A. Sakko, M. Hakala, J.A. Soininen, K. Hämäläinen, G. Monaco and S. Huotari, *J. Phys. Chem.* **B 114**, 3804 (2010).

[4] S. Alavi, R. Susilo and J.A. Ripmeester, *J. Chem. Phys.*, **130**, 174501 (2009).

[5] U. Bergmann, D. Nordlund, Ph. Wernet, M. Odelius, L.G.M. Petterson and A. Nilsson, *Phys. Rev. B.*, **76**, 024202 (2007).

Structure of materials

The development of advanced materials, used in modern manufacturing and technology, represent a "key enabling technology" underpinning industrial competitiveness and supporting contemporary lifestyles. Moreover, advances in materials science are intimately linked to advanced materials characterisation; the insight that such studies bring to understanding the behaviour and properties of a system leads ultimately to the development of improved materials. Thus materials research goes hand in hand with investigation via synchrotron radiation, particularly exploiting the X-ray energies available at a high-energy synchrotron like the ESRF. Studies by diffraction and spectroscopy reveal the composition, atomic structure, and crystalline state of materials, and imaging allows defects and aggregates to be observed. *In situ* studies can be particularly effective to follow materials under realistic operating conditions to watch their evolution in a working environment.

The highlights presented in this chapter are chosen from ESRF and CRG beamlines engaged in the broad field of research into materials systems, principally at the level of fundamental science, though it should be emphasised that ESRF beamlines can be equally exploited for analyses in the domain of applied research. The articles illustrate studies of bulk materials and the characterisation of surfaces and interfaces, and cover a number of themes.

One theme is the use of highly focussed X-rays and/or complementary microscopic probes to investigate nanostructures such as nanorods and nanocrystals (themselves often produced via an advanced procedure), to extract detailed information about structure, shape, orientation, defects, stress and strain. These are characteristics that have a profound influence on physical behaviour. A second theme is the interactions between molecules and surfaces as surfaces control the growth and structure of layers with potentially unique optical or electronic properties, for example for the development of molecular electronic devices. The techniques used include surface diffraction, reflectivity and X-ray standing wave analysis, coupled where appropriate with theoretical modelling of the interactions. Chemical interactions and the behaviour of molecules at surfaces are keys to discovering the mechanisms of heterogeneous catalysis, for example for the conversion of car exhaust gasses into less harmful emissions. *In situ* investigation of such systems, under realistic conditions of temperature and pressure, by surface diffraction, hard-X-ray diffraction and absorption spectroscopy can give new insights into the sometimes complex series of steps in such reactions. In another example, an investigation was carried out in a molten salt environment at 900°C, allowing elucidation of the pathway for the electrochemical extraction of titanium via the recently devised FFC Cambridge process that has potential for the production of Ti (and other metals and alloys) with more efficiency than current processes. Finally, materials scientists and chemists are continually devising new materials, and improving or discovering new properties for old ones. The technique of X-ray diffraction is used to examine the structural properties often under changing external conditions, *e.g.* under an electric field for potential piezoelectric materials, as a function of temperature for substances with electronic or magnetic ordering or superconductivity, or with varying chemical environment for porous materials allowing a detailed investigation of the adsorption of volatile materials. Such studies produce a wealth of new information, unavailable by other means.

Within the Experiments Division Structure of Materials Group, planning for the upgrade continued with the arrival of Tobias Schulli to take over as scientist responsible for ID01/UPBL1. A recent workshop was held to discuss how ESRF could better serve the needs of the metallurgy community, particularly via the capabilities of the high energy beamline ID15A. In the upgrade, part of ID15's programme will be transferred and optimised at the nanofocus high-energy UPBL2. This year, a refractive lens transfocator was installed at ID15 (similar to that installed last year on ID11) allowing great flexibility for focussing or condensing the beam. Both ID11 and ID01 continue their development and will be installing new, high-precision diffractometers early in 2011.

A. Fitch

X-ray nanobeam imaging of InSb/InP nanowire interface

Principal publication and authors
V. Favre-Nicolin (a,b), F. Mastropietro (a,c), J. Eymery (a), D. Camacho (a), Y.M. Niquet (a), B.M. Borg (d), M.E. Messing (d), L.-E. Wernersson (d), R.E. Algra (e,f,g), E.P.A.M. Bakkers (f), T.H. Metzger (c), R. Harder (h) and I.K. Robinson (i,j), *New J. Phys.* **12**, 035013 (2010).
(a) CEA-UJF, INAC, SP2M, Grenoble (France)
(b) Université Joseph Fourier, Grenoble (France)
(c) ESRF
(d) Department of Solid State Physics, Lund University (Sweden)
(e) Materials innovation institute (M2i), Delft (The Netherlands)
(f) Philips Research Lab., Eindhoven (The Netherlands)
(g) IMM, Solid State Chemistry, Radboud University Nijmegen (The Netherlands)
(h) Argonne National Lab., Argonne, Illinois (USA)
(i) London Centre for Nanotechnology, University College (UK)
(j) Diamond Light Source, Harwell Campus (UK)

Nanostructures have been developed during the past 15 years with the goal of achieving smaller sizes, as well as exploiting confinement effects for electronic and photonic applications. These objects have called for the development of new X-ray techniques using focussing optics: Fresnel zone plates (FZP), Kirkpatrick-Baez mirrors and compound refractive lenses, yielding an intense X-ray beam with a flux between 10^2 and 10^4 photons nm^{-2} s^{-1}. Such intense nanobeams allow Bragg diffraction on single objects smaller than 100 nm [1], from which the deformation and strain of the structure can be recovered [2].

In this study we report on the structure of heterogeneous InSb/InP nanowires (Figure 24) grown from Au seed particles with 30 nm diameter on $InP(111)_B$ substrates using metal-organic vapour phase epitaxy. To study the InSb/InP interface, we used beamline **ID01** with a coherent 8 keV FZP-focussed X-ray beam, of dimensions 300 (vertical) x 500 (horizontal) nm^2 (FWHM), which allowed different sections of the nanowire to be selected for diffraction (the total length of the InSb part is ~0.68 µm).

Figure 25 shows the diffraction patterns around the (333) reflection, recorded a) near the top of the InSb section, and b) close to the InSb/InP interface. In the latter image, asymmetric fringes appear in the vertical direction. To reproduce these fringes, we simulated the bottom of the InSb nanowire strain as a simple exponential decrease $\varepsilon_{zz} = \varepsilon_{zz}^0 e^{-z/\Delta}$ (Figure 25c). Since the precise relaxation law could not be predicted (the relaxation due to the 10.3% lattice mismatch occurs mainly through dislocations and radial relaxation), we tried several values for Δ, with Δ = 10 nm and ε_{zz}^0 = -2% giving the best agreement with the experimental pattern.

The simulated scattering (Figure 25d) reproduces well the fringes, which are due to the combination of the height of the wire selected by the beam (the fringes period) and the deformation (the asymmetric intensity). The shorter d_{111}-spacing at the bottom of InSb (relative to bulk InSb) is the signature of the interdiffusion during the deposition, with an $InSb_xP_{1-x}$ chemical composition varying in the first 10–20 nm of InSb.

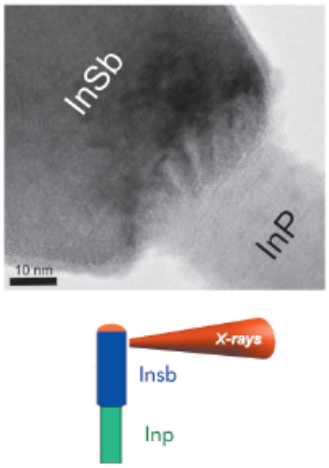

Fig. 24: Nanowire heterostructure, with InSb at the top (ø 60 nm) and InP at the bottom (ø 30 nm), grown along the [111] direction. The X-ray beam focussed by a Fresnel zone plate has a 300 nm vertical size, and is able to probe different parts of the nanowire.

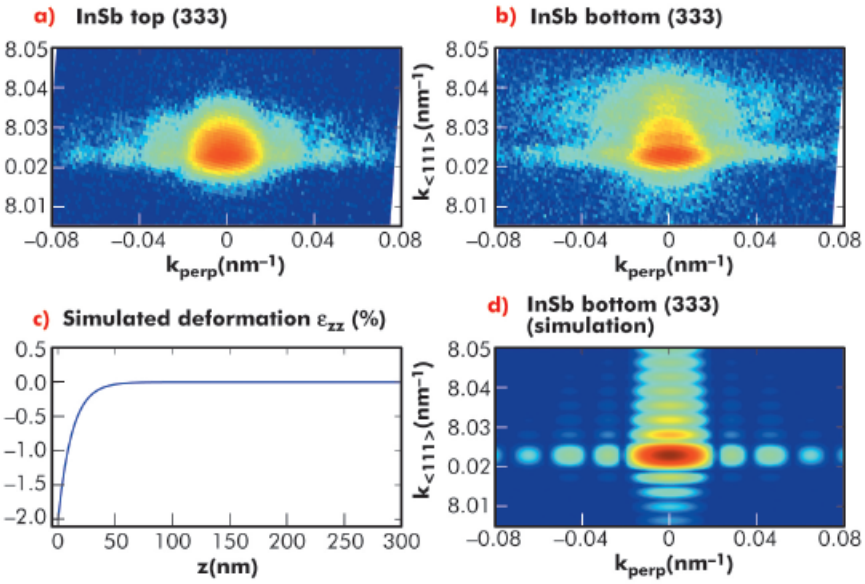

Fig. 25: Coherent diffraction scattering on the (333) reflection, measured (a) at the top of the InSb section and (b) near the interface with InP. The asymmetric fringes in (b) are due to an inhomogeneous strain (c) at the interface, as simulated in (d).

References
[1] V. Favre-Nicolin, J. Eymery, R.K. Koster and P. Gentile, *Phys. Rev. B* **79**, 195401 (2009).
[2] I. Robinson and R. Harder, *Nat. Mater.* **8**, 291–8 (2009).

In summary, coherent X-ray nanobeams can now be used to study single, nanometre-sized objects, and to record diffraction at different positions inside these objects. This is an important milestone for the study of semiconductor nano-structures: in these heterogeneous objects, inhomogeneous strain fields have an essential influence on the physical properties, and they can now be measured on synchrotron beamlines thanks to nanofocussing optics.

Principal publication and authors
V. Chamard (a) J. Stangl (b), G. Carbone (c), A. Diaz (c), G. Chen (b), C. Alfonso (d), C. Mocuta (c) and T.H.Metzger (c), *Phys. Rev. Lett.* **104**, 165501 (2010).
(a) Institut Fresnel, CNRS, Aix-Marseille University, Marseille (France)
(b) Institute of Semiconductor and Solid State Physics, Johannes Kepler Universität, Linz (Austria)
(c) ESRF
(d) IM2NP, CNRS, Aix-Marseille University, Marseille (France)

A 3D look inside nanocrystals

Classically, images are produced by lenses, which allow magnification of the sample within the resolution limit given by the Rayleigh criterion. However, precise knowledge of the complex-valued scattered field would provide a detailed and correct image. Therefore, the application of lensless imaging techniques has earned much attention recently, especially in the X-ray domain. Indeed, X-rays – with a wavelength in the 0.1 nm range – are particularly useful for nanoscience, where a detailed knowledge of the internal structure on the nanoscale is of fundamental importance to understand the properties of nanostructures.

Fourier transform holography [1] is a lensless microscopy method based on measurements of the coherently diffracted intensity: its utility arises from its capacity to yield not only the amplitude of the scattered field but also to encode the phase in the diffraction pattern, thereby allowing solution of the "phase problem". The phase information is contained in the interference of the coherently scattered waves from the sample and a reference. A single inverse Fourier transform of the intensity pattern allows direct reconstruction of the sample's electron density distribution. Several X-ray holography examples have been reported in the literature [2], performed in the forward direction geometry (*i.e.* near the origin of reciprocal space) practically restricting the imaging to two dimensions.

A novel approach to determine the 3D crystal structure of nanoscale materials by the use of X-ray Fourier transform holography in *Bragg geometry* is demonstrated in this work. The possibility to investigate reciprocal space near one of the Bragg points offers several key advantages: (*i*) access to the 3D diffraction intensity pattern for a generalisation of the X-ray holography method to the 3D case and (*ii*) sensitivity to the displacement field in the crystal, with nanoscale resolution. These are of great interest as non-destructive measurements of the 3D displacement field are challenging at the nanoscale.

Similar to Fourier transform holography, this method's Bragg approach makes use of the interference produced between the field scattered by the sample and a reference. However, in order to produce measurable interference in the vicinity of the sample Bragg peaks, a small *crystalline* reference, referred to as the reference crystal, with a lattice parameter close to that of the object crystal has to be located close to the object crystal. When these conditions are fulfilled, the sample's electron density is obtained by a single inverse Fourier transform of the far-field intensity pattern. The displacement field information appears

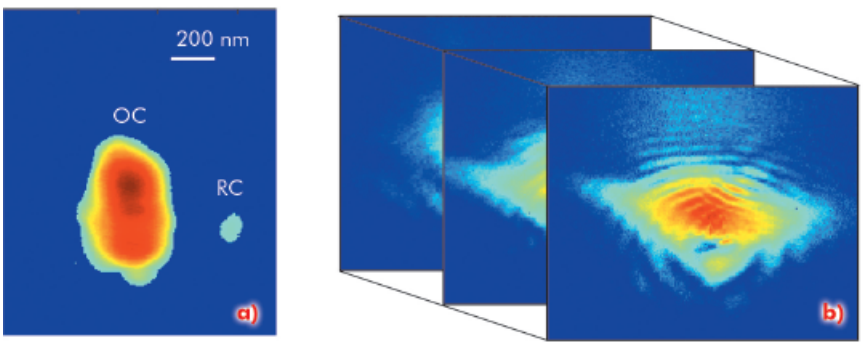

Fig. 26: a) The holographic sample: object (OC) and reference crystal (RC). b) 2D slices through the 3D coherent Bragg diffraction intensity distribution.

as a phase in the complex-valued electron density.

The sample used for this work consists of an object crystal and a small reference crystal (Figure 26a) produced by electron-beam lithography from a SiGe continuous layer (200 nm thick) on a Si (001) substrate. The experiment was carried out at beamline **ID01**. To increase the flux on the sample, a coherently illuminated Fresnel zone plate was used to produce a focussed coherent beam. The 3D coherently scattered intensity around the SiGe (004) Bragg peak was measured by a 2D Maxipix detector for different values of the rocking angle (Figure 26b). The observed low and high frequency fringes result from the interference of the waves scattered from the two crystals and are induced by their small and finite sizes. These slices are stacked in a 3D matrix for the inversion process: after a single inverse Fourier transform, retrieval of the 3D sample image is straightforward (Figure 27a). In addition to the shape, the internal view of the nanocrystal is obtained (Figure 27b), demonstrating the capability of the method to give access to the 3D description of the sample electron density and the displacement field.

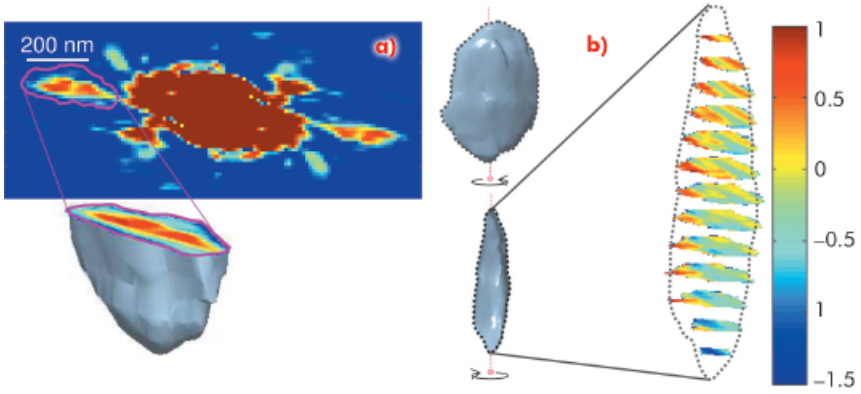

Fig. 27: a) The inverse Fourier transform of the 3D intensity distribution. b) Two views of the external shape and the internal phase distribution (colour scale in radians).

The simplicity and robustness of the inversion using Bragg Fourier transform holography paves the way to *in situ* investigations of inhomogeneous strain fields in nanocrystals and thus will be beneficial to the understanding of current strain related problems in nanomaterials research.

References
[1] D. Gabor, W.E. Kock, and G.W. Stroke, *Science* **173**, 11 (1971).
[2] S. Eisebitt *et al.*, *Nature* (London) 432, 885 (2004); L.-M. Stadler *et al.*, *Phys. Rev. Lett.* **100**, 245503 (2008).

Determining grain-resolved stresses in polycrystalline materials using three-dimensional X-ray diffraction

Principal publication and authors
J. Oddershede (a), S. Schmidt (a), H.F. Poulsen (a), H.O. Sørensen (a), J. Wright (b) and W. Reimers (c), *J. Appl. Cryst.*, **43**, 539–549 (2010).
(a) Center for Fundamental Research: Metal Structures in Four Dimensions, Risø DTU, Roskilde (Denmark)
(b) ESRF
(c) Technische Universität of Berlin, Berlin (Germany)

A new technique permitting characterisation of the position, orientation, size, and also the average stress state of each grain embedded in the bulk of a polycrystalline material during *in situ* processes would be a powerful tool for the materials scientist.

Here we present the first results obtained by extending the three-dimensional X-ray diffraction (3DXRD) microscopy technique implemented at beamline **ID11** to include the characterisation of grain-resolved stresses in around 100 grains. The material under investigation was a tensile sample of interstitial-free steel with a grain size of 0.1 mm and a cross section of 1 x 1 mm^2 mounted in a stress rig. The beam was defined with slits to illuminate a layer of thickness 0.15 mm covering the entire cross section of the sample perpendicular to the tensile axis. For each illuminated grain in the ensemble, a robust 12-parameter-per-grain fit of the centre-of-mass position, orientation and stress tensor, including error estimation and outlier rejection was performed using a newly developed algorithm. The precision obtained for each grain was approximately 10 µm in position, 0.05° in orientation, and 30, 50 and 15 MPa in the axial, normal and shear components of the stress, though some grains may have larger errors. The relative volumes of the grains were calculated from the peak intensities. A total of 96 grains were monitored during elastic loading and unloading. The centre-of-mass positions, relative volumes and axial stresses of the grains

at 5 MPa and 60 MPa are given in Figure 28. From the results, a three-dimensional orientation and stress/strain map of the polycrystal can be obtained by *e.g.* Laguerre tessellation [1] as shown in Figure 29. This can be used to determine the neighbour relations of the individual grains.

It should be emphasised that the data acquisition is fast enough to enable mapping of a representative volume within the sample, and that studies of up to 1000 grains have been performed [2]. Furthermore 3DXRD is easily combined with simultaneous tomography, relevant for applications such as visualising the location of reinforcements in composite materials or following the evolution of cracks.

In conclusion, a method has been developed that enables the study of metals and alloys which are typically polycrystalline and processed by plastic deformation and annealing. It is the stress evolution in processes like these, as well as in phase transformations, that can now be determined *in situ* at the single-grain level. The results can be correlated with grain sizes, orientations and neighbour relations and exploited in disciplines such as materials design and polycrystal deformation theory. In the latter, the ability to pinpoint active slip systems and study the effects of grain interactions is crucial for validating and extending the present polycrystal deformation models. This can be done with greater confidence from the present data. Finally the technique can be used to study local phenomena such as the stress field around a crack tip. If the material is too coarse grained for traditional strain scanning methods to apply, each grain may be used as an independent probe and a much improved map in terms of spatial resolution can be obtained.

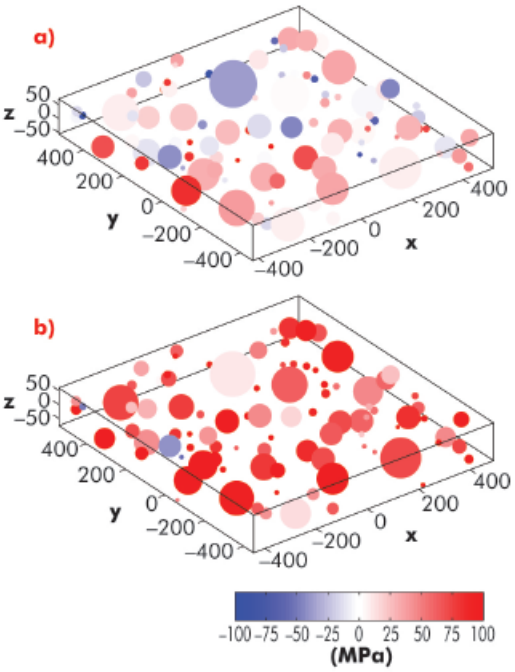

Fig. 28: Centre-of-mass grain positions within the mapped layer at a) 5 MPa and b) 60 MPa. The unit on the axes is micrometres and the tensile axis is along z. The relative grain volumes are indicated by the size of the spheres. The grains are colour coded according to the axial stress tensor component (see colour bar).

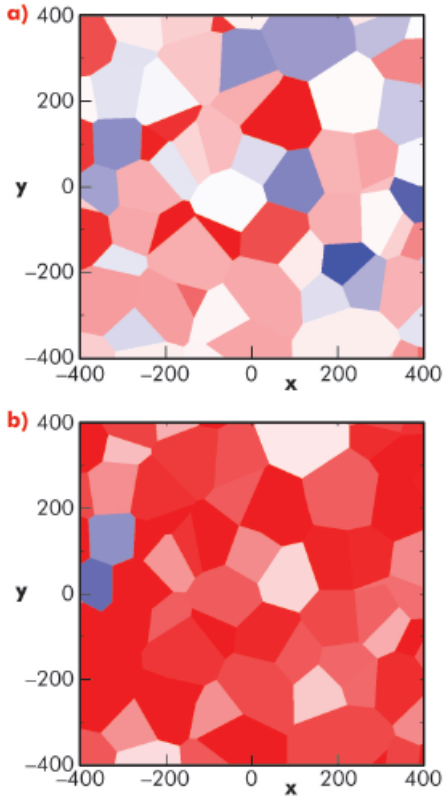

Fig. 29: Laguerre tessellations corresponding to the data shown in Figure 28 showing the neighbour relations of the grains.

References
[1] A. Lyckegaard, E.M. Lauridsen, W. Ludwig, R.W. Fonda and H.F. Poulsen, *Adv. Eng. Mater., in press*, 2010; DOI: 10.1002/adem.201000258.
[2] J. Oddershede, S. Schmidt, H.F. Poulsen and W. Reimers, *Mater. Sci. Forum* **652**, 63-69 (2010).

Evidence of double-walled Al-Ge imogolite-like nanotubes. A cryo-TEM, AFM and SAXS investigation

Principal publication and authors
P. Maillet (a), C. Levard (b,e), E. Larquet (c), C. Mariet, O. Spalla (a,e), N. Menguy (c), A. Masion (b,e), E. Doelsch (d,e), J. Rose (b,e) and A. Thill (a,e), *J. Am. Chem. Soc.* **132**, 1208–1209 (2010).
(a) CEA, IRAMIS, Laboratoire Interdisciplinaire sur l'Organisation Nanométrique et Supramoléculaire, Gif-sur-Yvette (France)
(b) UMR 6635 CNRS/Aix Marseille Université, Aix en Provence (France)
(c) Institut de Minéralogie et Physique des Milieux Condensés UMR 7590, CNRS, Université Pierre et Marie Curie, Université Paris Diderot, Institut de Physique du Globe de Paris (France)
(d) CIRAD, UPR Recyclage et risque, Montpellier (France)
(e) iCEINT international Center for the Environmental Implications of Nanotechnology, www.i-ceint.org.

Imogolites $(OH)_3Al_2O_3Si(OH)$ are natural minerals discovered in 1962 in Japanese volcanic soils. They are made of a curved gibbsite sheet $Al(OH)_3$ forming a nanotube of 2 nm in diameter. Tetrahedral silicon atoms inside the nanotube are linked to three Al-O-Si bonds. The mismatch between the size of the silicon tetrahedra and the vacant site of the gibbsite sheet leads to the curvature of the tube. The first synthetic imogolite was obtained as early as 1977. Imogolite nanotubes are extremely monodisperse in diameter with lengths up to the micrometre scale. However, early synthesis routes were only effective in very dilute conditions. The difficulty of synthesising large quantities of this mineral has probably hindered the development of industrial applications. Nevertheless, imogolites have been used as an anti-static agent in the formulation of photographic films.

Recently, a new synthetic process with increased synthesis yield was made possible by replacing silicon with germanium. Indeed, we were able to synthesise large quantities of an Al-Ge imogolite analogue. The structure of these analogues has been analysed in detail by small angle X-ray scattering at beamline **BM02**, by AFM and cryo-TEM microscopy.

The SAXS analysis unravelled the controversial nature of the so-called proto-imogolite (imogolite precursor) that was poorly known. We demonstrated that the proto-imogolite consists of roof tile shaped 5 nm imogolite nanotube pieces. The curvature of these pieces is less than that of the final tubes [1]. We have also shown that these imogolite analogues have the local structure of imogolite nanotubes, but with two different shapes depending on the synthesis conditions. It is possible to produce single-walled tubes of 3.5 nm in diameter, similar to their natural counterpart, and also double-walled tubes of 4 nm in diameter. Indeed, the SAXS results give distinctly different signals in the large-q range (**Figure 30**). In the case of single-wall nanotubes, regular oscillations are measured whereas the double-walled structure gives irregular oscillations due to the contribution of the inter wall scattering term. The differences between single and double-wall structures are confirmed by cryo-TEM observations of the samples (**Figure 31**). Such double-walled imogolite-like nanotubes are reported for the first time and open a new research field. Finally, using time resolved SAXS measurements, we have studied in detail the growth kinetics of the Al-Ge imogolite analogues.

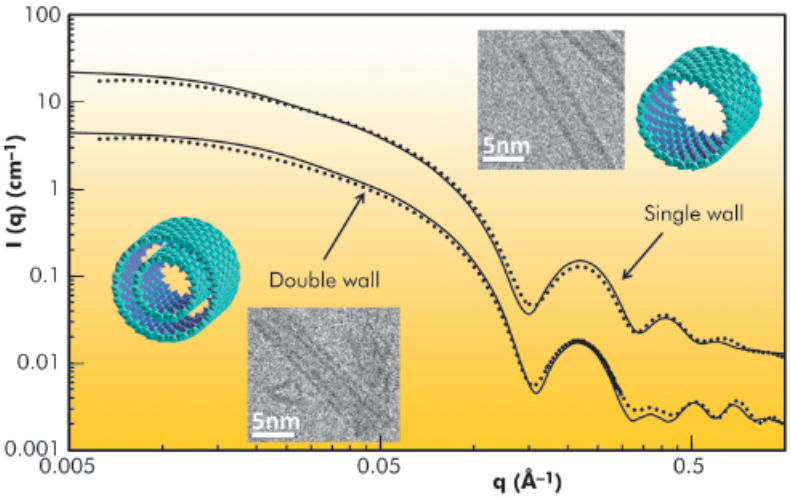

Fig. 30: SAXS curves of 0.5 and 0.25 M Al-Ge imogolite-like nanotubes. Experimental data are plotted using dots, and theoretical scattering curves of the represented structures are plotted using lines.

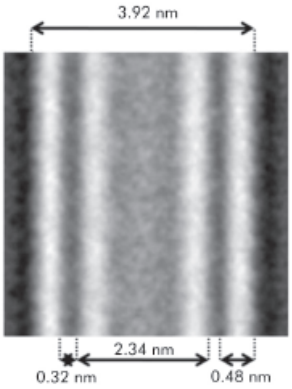

Fig. 31: Computer-assisted Cryo-TEM composite image obtained through the alignment and superposition of many nanotubes. The double-wall structure of the 0.25 M Al-Ge imogolite-like nanotubes is clearly observed.

References
[1] C. Levard, J. Rose, A. Thill, A. Masion, E. Doelsch, P. Maillet, O. Spalla, L. Olivi, A. Cognigni, F. Ziarelli and J.Y. Bottero, *Chemistry of Materials* **22**, 2466-2473 (2010).
[2] P. Maillet, C. Levard, O. Spalla, A. Masion, J. Rose and A. Thill, *Physical Chemistry Chemical Physics, in press.*

We show that the growth is mainly controlled by a reaction limited edge-edge assembly of the nanotubes. The complete simulation of the growth kinetics shows that it could be possible to accelerate considerably the growth kinetics of the imogolite nanotubes [2].

The precise SAXS measurements made at **BM02** allowed us to unravel and quantify a new structure of the Al-Ge imogolite analogues. The current research aims primarily at understanding the mechanisms of formation of these new double-walled nanotubes and also at controlling their organisation. In parallel, a toxicity study is being carried out in our laboratory.

Principal publication and authors
F.J. van den Bruele, J.A.A.W. Elemans, A.E. Rowan, W.J.P. van Enckevort and E. Vlieg, *Langmuir* **26**, 498-503 (2010).
Radboud University Nijmegen, Institute for Molecules and Materials (IMM) (The Netherlands)

Self-assembly of porphyrins on a single crystalline organic substrate

The crystallinity of a material is of great importance for electronic applications. This holds true especially for poorly conducting materials, which are used in, for example, organic electronics. For practical use, these materials need to be deposited on a surface, preferably in crystalline form. Better crystal quality with large domains can increase properties like conductivity by more than one order of magnitude. Control over the crystal growth direction is highly desirable, because, if only one growth direction is present, different domains will coalesce to form one single crystalline layer. Growth on single crystalline substrates can be used to control the direction of growth. A low-symmetry crystal substrate will induce fewer growth directions for the grown material and thus leads to better crystal quality. Inorganic substrates are the most commonly used substrates, but they are generally of high symmetry.

In our study we used potassium acid phthalate (KAP) as an organic substrate with low symmetry. It has an ionic structure, but the cleaved surface consists of apolar benzene rings. Because of π-π interactions, this surface provides an interesting template for the layer growth of many kinds of aromatic molecules. A purely organic porphyrin with C_{11} tails was grown from heptane on these KAP substrates by drop deposition and evaporation; an n-heptane layer was also studied for the purpose of comparison.

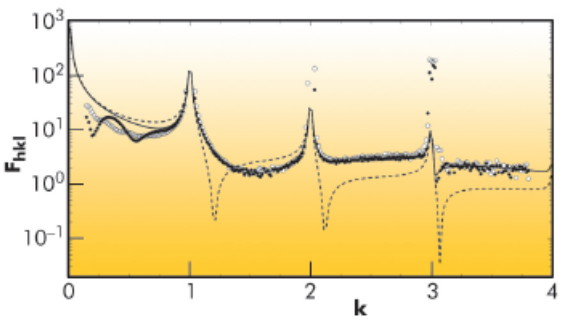

Fig. 32: Specular reflectivity curves of KAP with pure *n*-heptane film (filled circles) and with a porphyrin solution film (open circles), where F_{hkl} is the structure factor and k is the diffraction index perpendicular to the surface. The only noticeable difference is in the first fringes, which are caused by the film thickness. The solid curve is a fit of (010) KAP covered by a disordered monolayer of C atoms, representing the n-heptane solution. The dashed line is a fit of the (010) KAP substrate surface without this layer.

To grow ordered layers we used a wide range of solute concentrations going from undersaturated to supersaturated, which results in a large variety of different layer structures. These structures were studied with the complementary techniques of atomic force microscopy (AFM) and surface X-ray diffraction (SXRD) at **ID03** and **BM26/DUBBLE**. The surface of the underlying substrate was first characterised and shown to be bulk terminated using SXRD. *In situ* measurements of the growth solutions on the surface show the thickness of the solution film and the presence of out-of-plane ordering ('layering'), see Figure 32. However, the in-plane ordering could not be seen, probably, because of radiation damage. *Ex situ* these structures were studied by AFM and we found that round islands are formed at

the KAP surface at the lowest concentration of porphyrin solution. At somewhat higher concentrations, but still undersaturated, we enter the self-assembly regime. Here the islands show one preferred growth direction (Figure 33a) and grow together to form mono and multilayer structures. The step height of these structures is 2.5 nm, which corresponds to the planar porphyrin molecules lying perpendicular to the substrate surface. At higher concentrations, corresponding to a supersaturated solution, another stacked formation was found when more than 5 multilayers are formed. At these higher concentrations, the growth was no longer layer-wise, but nano-needles were formed, shown in Figure 33b. These nano-needles are oriented in the same direction, forming a single crystalline needle layer on the KAP surface. The molecular ordering in the nano-needles differs from that in the mono and multilayers. From the lattice spacing of 0.9 nm, as determined from X-ray diffraction, it follows that here the molecules are stacked in a tilted fashion, inclined by approximately 45 degrees. Both structures, the (multi)layers and the nano-needles, are oriented in one crystallographic direction over the whole substrate, which can reach an area of up to 1 cm^2. By using alternative organic crystals as substrates, the assembly can in principle be tuned to give organic crystal layers with unique electronic or photophysical properties.

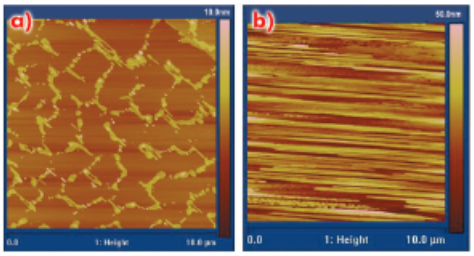

Fig. 33: AFM images of a) a honeycomb structure composed of oriented islands, b) nano-needle structure. The orientation of the porphyrin molecules in the nano-needles is determined via X-ray diffraction.

Structure and energetics of azobenzene on Ag(111): Benchmarking semiempirical dispersion correction approaches

Functional organic molecules at metal surfaces are studied because of their potential as a future molecular nanotechnology. A simulation platform is required that would allow the precise prediction of all relevant modes of the molecule-substrate interactions (chemical bonds of specific groups, Pauli repulsion, steric hindrance, and dispersion interaction). For this, the adsorption of organic molecules with highly polarisable conjugated ring systems on metals poses particular difficulties because the prevalence of dispersive van der Waals (vdW) interactions restricts the applicability of semilocal exchange and correlation (xc) functionals within density-functional theory (DFT). Since high-level theories that include nonlocal vdW interactions by construction are still barely tractable for large surface-adsorbed molecules, computationally inexpensive semi-empirical dispersion correction schemes to semi-local DFT (DFT-D) represent an appealing alternative. In these approaches, vdW interactions are considered approximately by adding a pairwise interatomic C_6R^{-6} term to the DFT energy. At distances below a cutoff, specified via the vdW radii of the atom pair, this long-range dispersion contribution is heuristically reduced to zero by multiplication with a short-range damping function.

The applicability of this DFT-D approach to organic molecules adsorbed at metal surfaces is uncertain. It is not clear how the results are affected by neglecting the screening of dispersive interaction between the adsorbate and more distant substrate atoms by the intervening metal layers. Moreover, adsorbate molecules, which also interact covalently with the substrate, exhibit bond distances that are so short that the uncertainties in the heuristic damping function of the dispersion term might mingle in an

Principal publication and authors
G. Mercurio (a), E.R. McNellis (b), I. Martin (c), S. Hagen (b,c), F. Leyssner (b), S. Soubatch (a), J. Meyer (b), M. Wolf (b,c), P. Tegeder (c), F.S. Tautz (a) and K. Reuter (b,d), *Phys. Rev. Lett.* **104**, 036102 (2010).
(a) Forschungszentrum Jülich (Germany)
(b) Fritz-Haber-Institut, Berlin (Germany)
(c) Freie Universität Berlin (Germany)
(d) Technische Universität München (Germany)

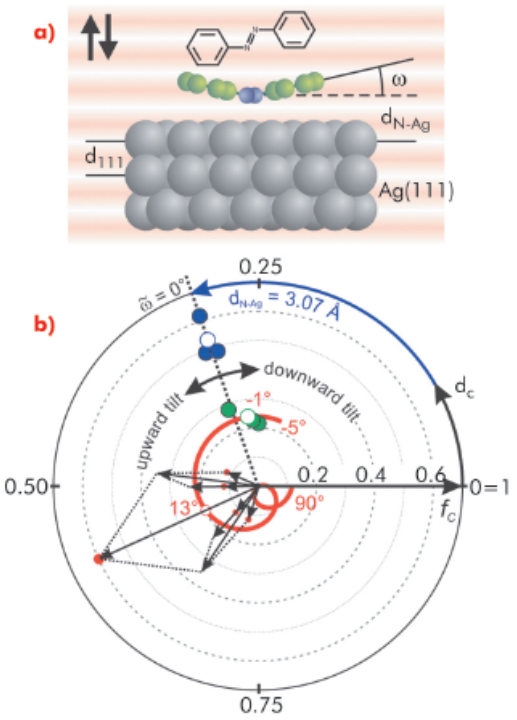

Fig. 34: a) Schematic adsorption model of azobenzene on Ag(111) in the X-ray standing wave field; b) Argand diagram of experimental coherent position d_c and fraction f_c for N1s (blue circles) and C1s (green circles). The red spiral represents the calculated d_c and f_c for C1s as ω sweeps from -5° to 90°; its intersection with experimental C1s data points defines the tilt angle of the phenyl rings.

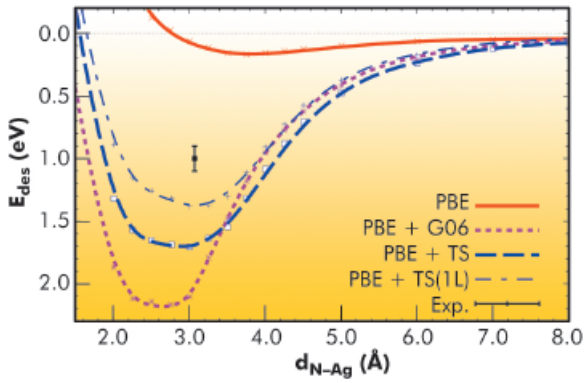

Fig. 35: Computed desorption energy curves and experimental point.

uncontrolled way with deficiencies of the employed semilocal DFT functional. Therefore, accurate experimental reference data are required to determine whether the improvements brought by including vdW interactions semi-empirically outweigh the aforementioned shortcomings.

We respond to this need by providing reference data for the molecular switch azobenzene on Ag(111) (Figure 34). The normal-incidence X-ray standing wave technique (NIXSW) at beamline ID32 was used to determine key structural parameters of adsorbed azobenzene. Additionally, the desorption energy was measured by temperature programmed desorption (TPD). Employing a novel analysis scheme for NIXSW (Figure 34b), we extracted not only the height of azobenzene diazo-bridge d_{N-Ag} that is straightforwardly accessible in NIXSW, but also the tilt of the phenyl rings ω. The derived structural data (d_{N-Ag} = 3.07±0.02 Å and ω = -1±1.5°) demonstrate an essentially undistorted planar molecular geometry and agree well with the results obtained with DFT-D scheme due to Tkachenko and Scheffler (TS) [1]. Indeed, while the DFT-PBE strongly overestimates the diazo-bridge adsorption distance (3.64 Å) demonstrating the well-known incapability of semilocal xc functionals to account for long-range dispersive interactions, the tested DFT-D schemes by Grimme (G06) [2] and TS reveal a sizable reduction of d_{N-Ag} to 2.75 and 2.98 Å (Figure 35). All three schemes predict almost flat molecular geometry in similar agreement with experiment.

Unfortunately, the improved structure in DFT-D goes together with a notable overbinding. Most probably the reason is the screening of dispersive attractions between the adsorbate atoms and more distant substrate atoms that is neglected in the strictly pairwise evaluation of the dispersion interaction as inspired by Hamaker theory. Mimicking this screening by reducing the number of substrate layers considered in the pairwise interaction C_6R^{-6} term to one and by even diminishing the C_6 coefficients of the Ag atoms in the topmost surface layer indeed shifts the computed binding energy curves closer to experimental values, but essentially without affecting the d_{N-Ag} (Figure 35).

In summary, we demonstrate that the existing DFT-D schemes are not suitable to describe comprehensively the role of vdW interactions for adsorption at metal surfaces because screening effects are not (yet) considered. However, the insight that the adsorption geometries are less sensitive to the neglect of screening is intriguing. It suggests that these schemes may provide significantly improved structural data at zero additional computational cost. Such structures are then a useful starting point for higher-level theory, aimed at refined binding energies or a more comprehensive understanding of the adsorption system.

References
[1] A. Tkatchenko and M. Scheffler, *PRL* **102**, 073005 (2009).
[2] S. Grimme, *J. Comput. Chem.* **27**, 1787 (2006).

Graphene on Ir(111): A weakly bonded system

Principal publication and authors
C. Busse (a), P. Lazić (b), R. Djemour (a), J. Coraux (c), T. Gerber (a), N. Atodiresei (b), V. Caciuc (b), R. Brako (d), A.T. N'Diaye (a), S. Blügel (b), J. Zegenhagen (e) and T. Michely (a), *submitted to PRL.*
(a) II. Physikalisches Institut, Universität zu Köln (Germany)
(b) Institut für Festkörperforschung (IFF) and Institute for Advanced Simulation (IAS), Forschungszentrum Jülich and JARA, Jülich (Germany)
(c) Institut Néel, CNRS-UJF, Grenoble (France)
(d) Ruđer Bošković Institute, Zagreb (Croatia)
(e) ESRF

Since its successful isolation from graphite in 2004 (Nobel prize in physics 2010 for A. Geim and K. Novoselov), graphene has attracted a huge amount of interest for its extraordinary structural and electronic properties. Epitaxial growth is the most suitable method for the preparation of large-area, well-ordered films [1]. On specific surfaces [Pt(111), Ir(111)] the interaction between graphene and the substrate is so weak that graphene behaves as quasi-freestanding [2].

The exact structural parameters for model systems such as graphene on Ir(111) or graphene on Ru(0001) are debated in the literature. This is mainly due to the large unit cell of the structures caused by the lattice mismatch as well as to the difficulties inherent in standard density functional theory (DFT) calculations to include correctly the significant non-local van der Waals (vdW) interaction. To make a precise measurement of the height distribution of the carbon atoms in graphene on Ir(111), we performed an X-ray standing wave (XSW) analysis at beamline **ID32**. An X-ray standing wave is created in the interface region of a crystal using Bragg reflection (see Figure 36a). The maxima of the XSW, which are periodic with the Ir lattice planes, are shifted by half the lattice plane distance when scanning through the Bragg reflection by changing the beam energy. The carbon atoms in the maximum of the standing wave field display the maximum photoelectron yield. Therefore, scanning the XSW field through the different heights and monitoring the photoemission signal allows a determination of the average carbon atom height. For graphene/Ir(111), we derived a mean height of $h = 3.38 \pm 0.04$ Å from the change in the area of the C1s peak in the photoelectron spectra (Figure 36b) at different photon energies (Figure 36c). This is similar to the interlayer distance in graphite (3.36 Å), which indicates that only weak bonding is present in this system.

To complement these experimental results, we performed *ab initio* DFT calculations including the vdW interaction. The results are visualised in Figure 37, where a variation of the carbon heights within the unit cell is clearly visible, with the highest values found in regions where the centre of the C hexagon is located on top of an Ir atom (top region) and the lowest values found for C are at the hcp- and fcc-regions. The mean value is $h = 3.41$ Å, in good agreement with the experimental results.

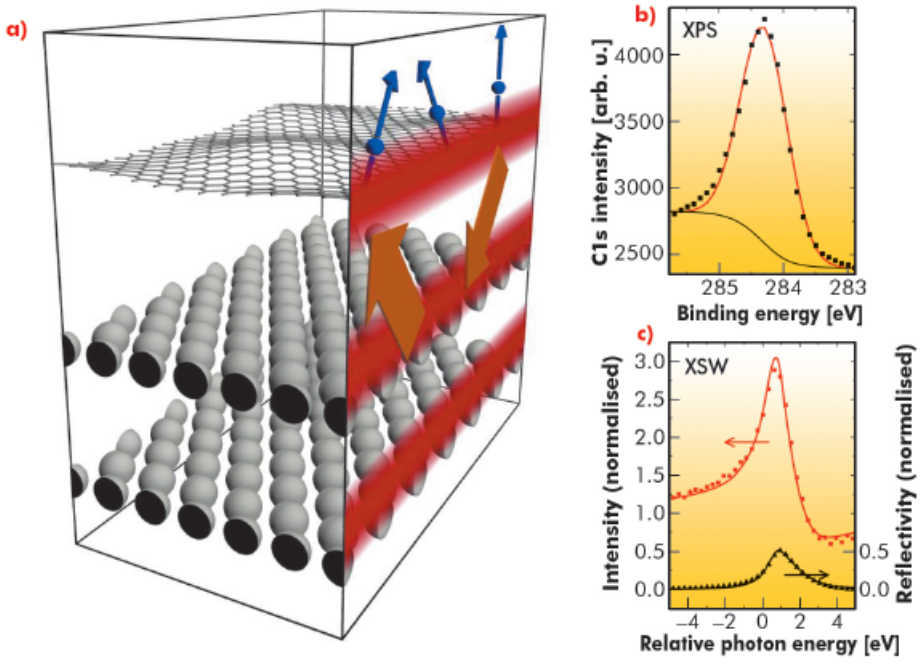

Fig. 36: a) Schematic representation of the X-ray standing wave experiments. The corrugated honeycomb mesh represents graphene, on top of two Ir(111) lattice planes. Orange arrows: Interfering incoming and outgoing X-ray beam. Red stripes: Standing wave pattern. Blue spheres and arrows: Emitted photoelectrons. b) Squares: X-ray photoemission intensity of the C1s-peak. Thin line: Shirley-type background, Thick line: Gaussian fit. c) X-ray reflectivity (triangles) and C1s photoemission yield during an XSW energy scan.

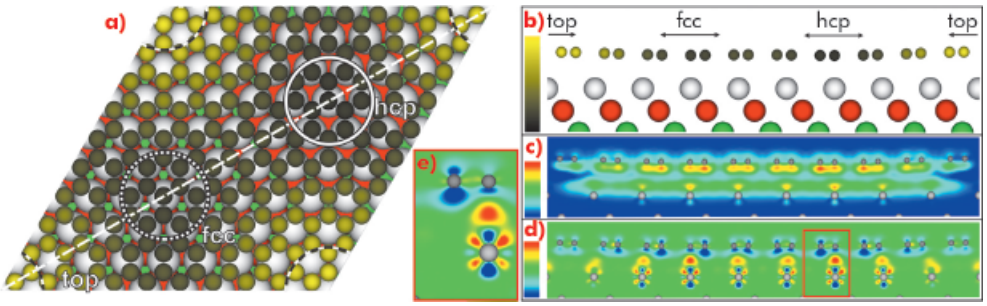

Fig. 37: a) Top view and b) side view (cut along the dashed line in (a)) of the relaxed geometrical structure of graphene/Ir(111) obtained by DFT including vdW interaction. The different regions (fcc, hcp, top) are marked by circles (a) or arrows (b-d). The colour scale indicated in (b) ranges from h = 3.20 Å (dark) to h = 3.65 Å (yellow). c) Real space visualisation of the nonlocal (*i.e.* vdW) binding-energy density caused by adsorption (blue: zero density, red: maximum density). d) The charge transfer upon adsorption. Blue: charge depletion, red: charge accumulation). e) Magnified view in the hcp region (see red box in (d)).

References

[1] J. Coraux, A.T. N'Diaye, C. Busse and T. Michely, *Nano Lett.* **8**, 565 (2008).

[2] I. Pletikosić, M. Kralj, P. Pervan, R. Brako, J. Coraux, A.T. N'Diaye, C. Busse and T. Michely, *Phys. Rev. Lett.* **102**, 056808 (2009).

The total binding energy found in our calculations is E_b = -50 meV/C, again similar to the corresponding value for graphite. Our advanced DFT approach makes it possible to divide the overall binding energy into nonlocal (*i.e.* vdW) contributions (-70 meV/C) and local (*i.e.* chemical) contributions (+20 meV/C, repulsion!). This shows that actually the vdW contribution (spatial distribution visualised in Figure 37c) dominates this system. Contrary to the impression given by the averaged values of the binding energies, the binding mechanism is not purely physisorption, although it is dominated by vdW. This becomes obvious when one studies the charge transfer caused by adsorption, visualised in Figure 37 (d and e). In the hcp- and fcc-regions, a small charge transfer from graphene to substrate takes place that leads to a charge accumulation at the graphene/Ir(111) interface. This indicates the formation of local bonding with a covalent character. Overall, the charge rearrangement leads to a shifting of the Dirac point to 0.2 eV above E_{Fermi}, which is consistent with experiment [2].

On the origin of the hydrophobic water gap

Principal publication and authors

M. Mezger (a,b), F. Sedlmeier (c), D. Horinek (c), H. Reichert (a,d), D. Pontoni (d) and H. Dosch (a), *J. Am. Chem. Soc.* **132**, 6735–6741 (2010).

(a) Max-Planck-Institut für Metallforschung, Stuttgart (Germany)

(b) Department of Chemical Engineering, University of California, Berkeley (USA)

(c) Physik Department, Technische Universität München (Germany)

(d) ESRF

The density deficit of water at hydrophobic interfaces, frequently called the hydrophobic gap, has been the subject of numerous experimental and theoretical studies in the last decade. Recent experiments give values for the interfacial depletion that consistently correspond to less than a monolayer of water. The main question that remained unanswered is its origin and how it is affected by the chemistry and molecular geometry of a particular hydrophobic coating [1].

Figure 38 shows several structural features, currently under discussion as possible contributions. Universal packing effects (a) adjacent to a hard wall can affect the liquid structure causing an oscillatory profile with a reduced average density near hydrophobic interfaces. For alkanes, the hydrogen atoms in terminal methyl groups are essentially invisible to X-rays but occupy some space (b). X-ray scattering techniques cannot distinguish this generic volume effect from depletion layers caused by interfacial water. Experiments and simulations indicated that the water molecules next to a hydrophobic

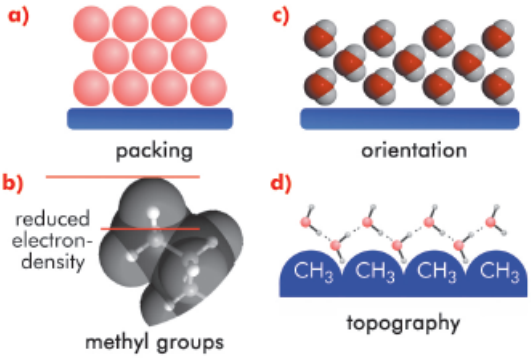

Fig. 38: Sketch illustrating various structural features that could contribute to the observed density depletion at hydrophobic interfaces.

interface are partially oriented (c). The hydrogens preferentially point towards the interface, resulting in a geometrically induced local electron depletion. Hydrogen bonds in water arrange more readily around interfacial protrusions than at flat surfaces (d). Thus, the nanoscopic topography can influence the magnitude of the density depletion. In addition to these structural effects, density fluctuations of the liquid result in a reduced contact density, which is most pronounced for very weak water-surface attractions.

So far, the majority of experimental and numerical studies used aliphatic hydrocarbons as generic hydrophobic model surfaces. To elucidate how the underlying mechanisms affect the extent of the interfacial depletion we carried out a combined high-energy X-ray reflectivity (XRR) and molecular dynamics simulation study of water adjacent to a perfluorinated hydrophobic surface with a spatial resolution on the molecular scale. Comparison of the computational results with the analysis of the XRR data (**Figure 39**) measured at the high-energy micro-diffraction setup at **ID15A** revealed the influence of the different contributions to the observed interfacial depletion.

Atomistic simulations of realistic molecularly packed surfaces and XRR on hydrocarbon [2] and perfluorinated self-assembled monolayers consistently confirmed the presence of interfacial depletion with layer thicknesses of at most 2.1 Å. Since the water depletion on perfluorinated substrates is comparable in size, but for which no effects from terminal methyl groups are present, then the methyl groups cannot solely explain the observed gap. Molecular dynamics (MD) simulations showed a broad orientation distribution of interfacial water molecules that is not influenced by the different polarity of the CH_3 and CF_3 head groups. This suggests that the share from orientational effects of the strongly fluctuating fluid adjacent to a hydrophobic solid is only a minor contribution. In contrast, the surface morphology strongly affects the interfacial depletion and can even be related in a counterintuitive way to the contact angle, commonly used as a macroscopic measure to quantify hydrophobicity. This is of particular importance for more complex soft and biological surfaces that tend generally to show strong corrugations on the length scale of a few angstroms. In addition, there are contributions from molecular packing and capillary wave-like fluctuations that are generic to all fluid interfaces with comparable solid–liquid and liquid–liquid interactions.

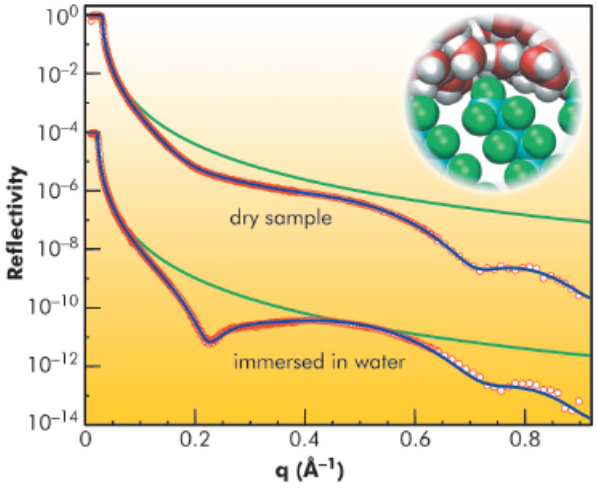

Fig. 39: X-ray reflectivity from a perfluorinated self-assembled monolayer in air and with the sample immersed in degassed water. Green lines give the Fresnel reflectivity R_F of an ideal silicon substrate. Blue lines are best fits to the experimental data. The inset shows a snapshot of an MD simulation of the self-assembled monolayer in contact with water.

The complex interplay between surface chemistry and topography precludes the existence of a universal relation between the macroscopic contact angle and the nanoscopic water depletion. Thus, there is no clear-cut distinction between hydrophobic and nonhydrophobic contributions to the magnitude and extent of the water gap. However, the combined MD simulation and X-ray reflectivity study for two hydrophobic model interfaces provide typical values that can serve as estimates for many complex interfaces.

References
[1] D. Chandler, *Nature* **445**, 831– 832 (2007).
[2] M. Mezger, H. Reichert, S. Schöder, J. Okasinski, H. Schröder, H. Dosch, D. Palms, J. Ralston and V. Honkimäki, *Proc. Natl. Acad. Sci. USA* **103**, 18401-18404 (2006).

Principal publication and authors
B.L.M. Hendriksen (a), M.D. Ackermann (a,b), R. van Rijn (a,b), D. Stoltz (a), I. Popa (b), O. Balmes (b), A. Resta (b), D. Wermeille (b), R. Felici (b), S. Ferrer (b,c) and J.W.M. Frenken (a), *Nature Chemistry* **2**, 730–734 (2010).
(a) Kamerlingh Onnes Laboratory, Leiden University (The Netherlands)
(b) ESRF
(c) Present address: CELLS - ALBA, Universita Autònoma de Barcelona (Spain)

Roughness as a motor for reaction oscillations

Oscillatory chemical reactions are often called 'chemical clocks' owing to their periodic nature. A well-known system that shows periodic oscillation of reaction rate is the catalytic oxidation of carbon monoxide over platinum and palladium surfaces. We have identified a new mechanism that makes this chemical clock 'tick'.

A catalyst is a substance that speeds up a chemical reaction without being consumed by the reaction. A notable example is the catalyst in the exhaust of a car, which facilitates the oxidation of poisonous carbon monoxide gas with oxygen to produce the less-harmful carbon dioxide. The rate of conversion of CO to CO_2 can spontaneously oscillate in time. A complex interplay of the reactants, CO and O_2, modifies the surface structure of the catalyst and thereby its catalytic activity. This causes the rate to oscillate for reactions at low pressures in ultrahigh vacuum systems, as has been beautifully demonstrated by Nobel laureate G. Ertl and co-workers [1]. However, at atmospheric pressures the structure of a catalyst surface is much harder to study because most analytical tools require low-pressure vacuum conditions.

We have developed a novel setup at beamline **ID03** that allows the surface structure of a single crystal Pd catalyst inside a flow reactor to be studied during the catalytic reaction by means of surface X-ray diffraction (SXRD) at atmospheric pressure [2]. With these experiments, we show that, during the rate oscillations, the Pd catalyst spontaneously switches between a metallic surface, with a low CO_2 production rate, and an oxidised Pd surface, which exhibits a much higher rate, as shown in Figure 40. These observations are in full agreement with earlier studies of the catalytic activity of ultrathin surface oxides.

Further experiments show that a smooth metal surface oxidises more easily, *i.e.* under the less-oxidising conditions of a higher CO partial pressure, than a rough metal surface. The authors suggest that this is due to the favourable adsorption of CO at the steps of a rough metallic Pd surface, which thermodynamically stabilises the metal surface. Only when the level of roughness is sufficiently low does the surface becomes oxidised.

The newly discovered mechanism responsible for the oscillatory behaviour, depicted schematically in Figure 41, was found by studying the evolution of the roughness of the metallic and oxidised surface during the oscillations. In the oxide phase of an oscillation cycle, the thin oxide layer becomes gradually roughened by reaction of CO with the oxygen atoms from the oxide layer. This is shown by the broadening of the diffraction peaks. At a certain level of roughness, the oxide layer becomes thermodynamically

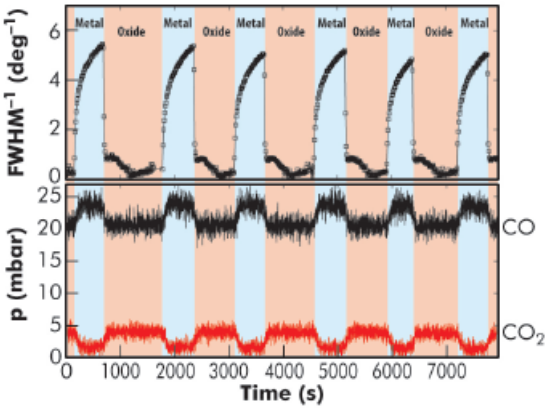

Fig. 40: Top panel: Inverse full width at half maximum (FWHM) of the diffracted intensity at a surface sensitive (anti-Bragg) position as a function of time. The inverse FWHM is proportional to the smoothness of the truncation of the Pd(100) crystal. Bottom panel: partial pressures of CO and CO_2 in the reactor. The partial O_2 pressure was 500 mbar. The sample temperature was kept constant at 447 K. The colours indicate whether the SXRD intensities identify the Pd(100) surface as a metallic structure (light blue) or as being covered by a thin oxide film (light red).

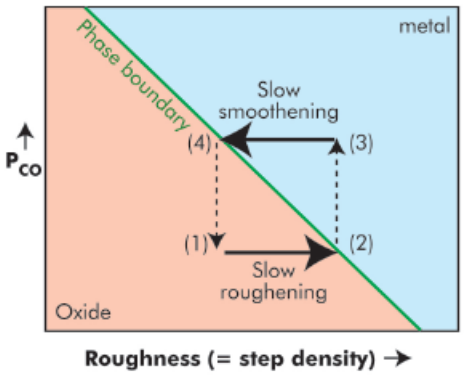

Fig. 41: Metal-oxide stability diagram. Each cycle takes the surface through stages (1) smooth oxide, (2) rough oxide, (3) rough metal, and (4) smooth metal, after which the next cycle starts again at (1). The phase boundary is determined by the roughness and the CO partial pressure.

unstable and disappears, leaving a less reactive metallic surface. This metallic surface becomes smooth again by metal atom diffusion, as shown by the narrowing of the diffraction peak, see Figure 40. The smoothening continues until the roughness is low enough to make the oxide surface thermodynamically stable again, at which point the surface immediately forms a highly-reactive oxide film. This completes the cycle and the process starts all over again from the beginning. Based on these observations, the authors conclude that the evolution of the roughness is responsible for the periodic switching between the metallic and oxidised surface and is at the heart of the mechanism that makes this chemical clock tick.

References
[1] R. Imbihl and G. Ertl, *Chem. Rev.* **95**, 697-733 (1995).
[2] R. van Rijn, M.D. Ackermann, O. Balmes, T. Dufrane, A. Geluk, H. Gonzalez, H. Isern, E. de Kuyper, L. Petit, V.A. Sole, D. Wermeille, R. Felici and J.W.M. Frenken, *Rev. Sci. Instrum.* **81**, 014101 (2010).

CO dissociation and transient carbon storage by supported Pd nanoparticles during CO/NO cycling

Heterogeneous catalysts provide the central technology for abating environmental pollution from industrial processes. The preeminent example of this is car exhaust catalysis where the catalyst (Pt/Rh or Pd- nanoparticles dispersed on an oxidic support) has to balance three chemical conversions: the reduction of toxic NO_x to benign N_2 and the oxidation of hydrocarbons and toxic CO to CO_2. A central issue is maintaining high activity levels during the cycling (so-called lambda oscillations) conditions typical of real operation. A basic understanding of how supported noble metal nanoparticles might achieve this is, therefore, of considerable importance.

Beamlines **ID24** (dispersive EXAFS) and **ID15** (hard X-ray diffraction, HXRD) have collaborated to derive a new way of seeing into the dynamic behaviour of such systems. This approach is an extension of an experiment developed on ID24 to couple time-resolved EXAFS (element specific local structure) to infrared spectroscopy (IR, for surface speciation and molecular functionality) and mass spectrometry (MS) [1]. By using the very hard (89 keV), high flux, X-rays available at ID15B, we can now combine HXRD with IR within the same sample environment developed for time resolved EXAFS/IR. As a result, we have observed previously hidden aspects of how Pd nanoparticles (ca. 3 nm diameter) participate in the oxidation of CO to CO_2, how this changes their structure and, subsequently, the disposition of CO molecules adsorbed upon them.

Figure 42 collates the HXRD (for a complete, 10 cycles, CO/NO cycling experiment), IR and MS (for single

Principal publications and authors
M.A. Newton (a), M. Di Michiel (a), A. Kubacka (b) and M. Fernàndez-Garcià (b), *J. Am. Chem. Soc.* **132**, 4540 (2010);
A. Kubacka (b), A. Martínez-Arias (b), M. Fernández-García (b), M. Di Michiel (a) and M.A. Newton (a), *J. Catal.* **270**, 275 (2010).
(a) ESRF
(b) Instituto de Catàlisis y Petroleoquímica, CSIC, C/Marie-

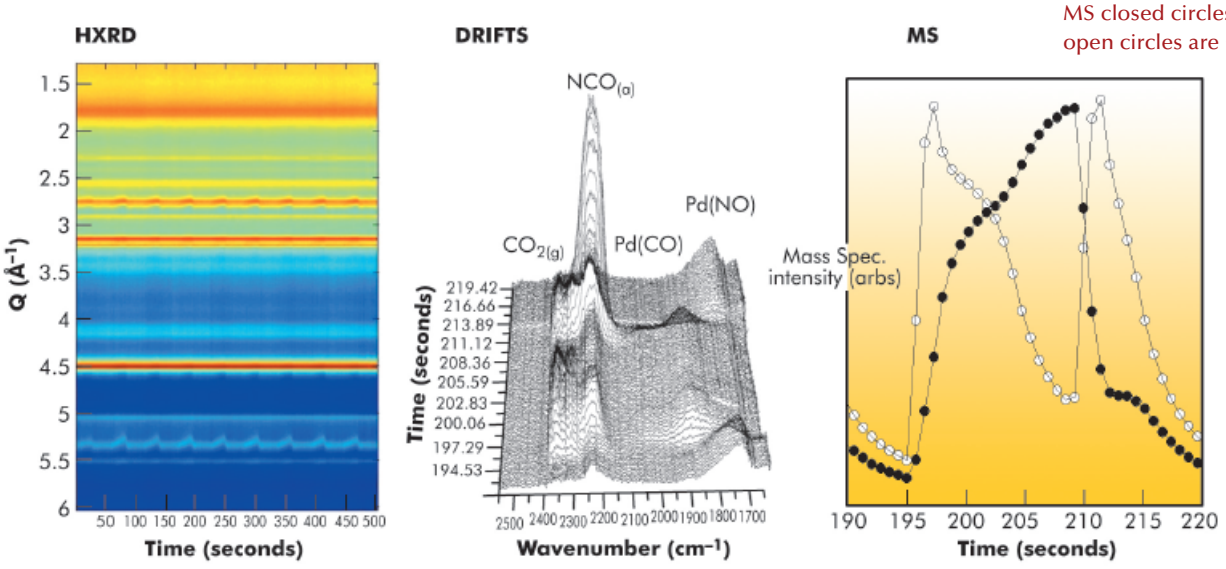

Fig. 42: DRIFTS, MS, and HXRD from a 2wt % Pd/Al_2O_3 sample during CO/NO cycling at 673 K. MS closed circles are CO and open circles are CO_2.

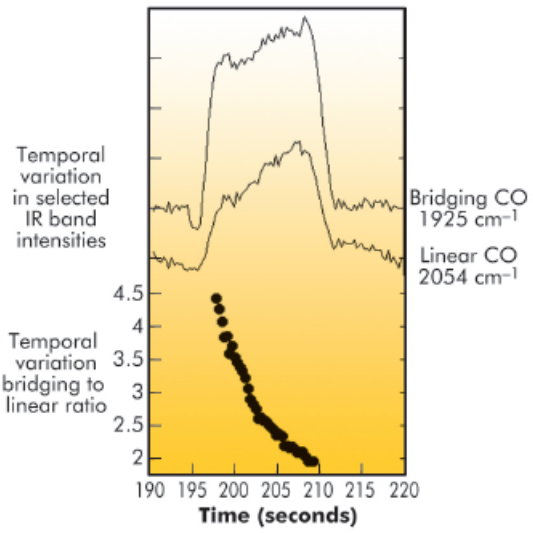

Fig. 43: Temporal variation in IR band intensities due to bridging and linear CO species adsorbed on Pd and their ratio during a single NO:CO:NO cycle at 673 K.

NO-CO-NO switches) obtained with this experiment. The HXRD shows that reflections due to Pd move as a function of the applied feedstock composition whereas those due to the Al_2O_3 support do not; that is to say, during the CO cycle the lattice constant of the Pd nanoparticles increases linearly with time. This is rapidly reversed upon switching back to a NO flow.

If we correlate the temporal character of this "breathing" with the MS data we can show that this correlates with a phase of CO_2 production from *within* the CO cycle. The structural change of the nanoparticles revealed by HXRD is directly linked to reactive events that lead to the target conversion of CO to CO_2.

These observations yield the following conclusions: during CO exposure an adlayer of molecular CO forms quickly on the Pd nanoparticles. From within that layer a proportion of the CO then dissociates. The atomic oxygen thus released reacts with some of the remaining molecular CO to yield the observed CO_2 (MS). The atomic carbon left behind then dissolves into the Pd nanoparticles whose lattice constant increases in proportion to the amount of carbon absorbed. Upon the return to an NO feedstock this stored carbon is then rapidly sequestered to yield CO_2 and the lattice constant of the Pd nanoparticles returns to its initial value. This behaviour is not expected on the basis of the chemistry of extended Pd surfaces which do not dissociate CO [2].

A further important observation arises from correlating the results of the IR spectroscopy with the HXRD. In Figure 43 we show the (IR derived) variation of bridging (Pd_2CO) and linear (PdCO) species, as well as their ratio (absorption band intensity: bridged/linear). This shows that the formation of the bulk PdC_x as a result of CO dissociation has a secondary effect, changing the partitioning of the remaining molecular CO between sites on the surface of the particles. As carbon is stored within the Pd particle, the occupation of CO in a linearly adsorbed site is significantly promoted.

To summarise we have developed a new experiment for studying working catalysts in a manner that combines IR with HXRD (ID15) or IR/EXAFS (ID24) within the same environment. We have directly observed previously hidden surface and bulk chemistry within a prototypical CO oxidation/NO reduction sequence.

References
[1] M.A. Newton, *Topics in Catalysis* **52**, 1410 (2009).
[2] For instance, R.P.H. Gasser, "An introduction to chemisorption and catalysis by metals" 3rd Ed. OUP (1987).

In situ diffraction of the electrochemical reduction pathway of TiO_2

Principal publication and authors
R. Bhagat (a), D. Dye (b), S.L. Raghunathan (b), R.J. Talling (b), D. Inman (b), B.K. Jackson (b), K.K. Rao (c) and R.J. Dashwood (a), *Acta Materialia* **58**, 5057–5062 (2010).
(a) University of Warwick, Coventry (UK)
(b) Imperial College, London (UK)
(c) Metalysis, Rotherham (UK)

It is widely thought that an electrochemical method will succeed the costly Kroll process, which is used to make the majority of titanium in the world. In 2000, Professors Fray, Farthing and Chen discovered a method of electrochemically deoxidising metal oxide in a $CaCl_2$ melt, in a process now known as the FFC Cambridge Process [1]. Since 2000, there has been significant research into understanding the reduction process for elements such as Ti, Ta, Zr, Cr, etc.
The FFC Cambridge process also has the potential to form alloys, such as Ti-6Al-4V, by co-reducing metal oxides, such as TiO_2, Al_2O_3 and V_2O_5.

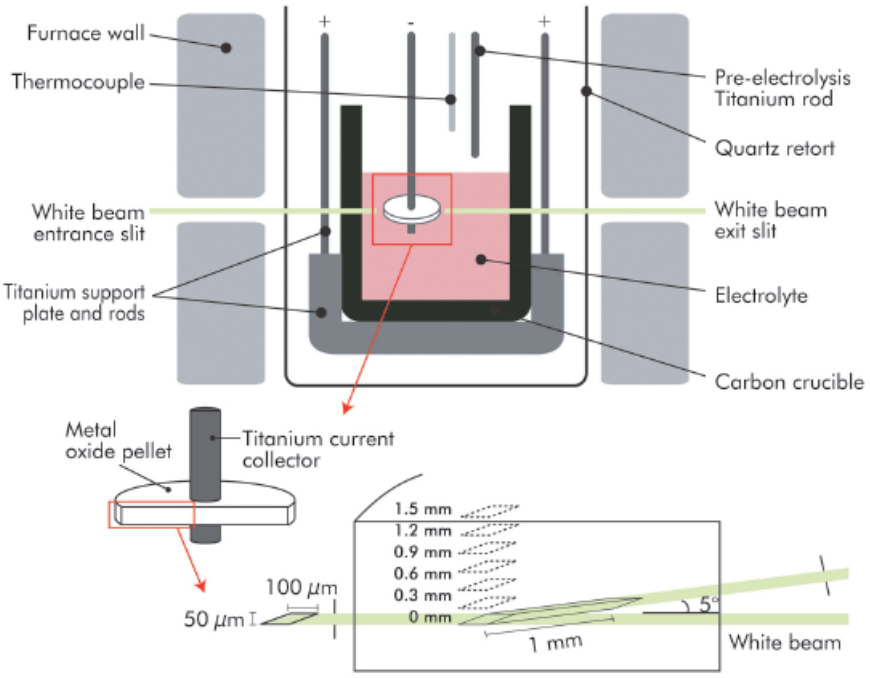

Fig. 44: Electrochemical reduction cell showing the sampling volumes employed.

This discovery has encouraged a broader exploration of electrochemical reduction as a competitive extraction route, which has the potential to replace current commercial extraction routes for elements like Ti, Ta, Zr, etc. Whilst reducing these metal oxides to metal is relatively simple, doing it consistently to form a product with low concentrations of impurities in an efficient way has proven to be more challenging. To achieve these goals, it is important to understand fundamentally the reactions taking place, so that it becomes possible to control the process. Unfortunately high temperature electrochemical studies (as shown in Figure 44), do not lend themselves to conventional analysis techniques.

Titanium is one of more difficult metals to produce from the FFC Cambridge process owing to the various phases that form during reduction; however, it remains one of the most lucrative. As such, titanium oxide reduction to titanium has been the most studied system with regards to the FFC Cambridge process. However, to date, studies were based on a combination of *ex situ* phase studies and voltammetric techniques, which have resulted in an ambiguous understanding of the reduction behaviour and role of intermediary phases. For instance, the formation mechanism for the intermediate phases $CaTiO_3$ and $CaTi_2O_4$ and TiC was much debated, with no clear evidence to show whether it was chemically or electrochemically formed.

In 2008, the authors proposed an experiment at **ID15A** where the phase evolution during the FFC Cambridge reduction of titanium dioxide to titanium metal could be logged *in situ*. The experiment would require a redesign of the classic FFC cell to make it X-ray transparent whilst being capable of completing an eighteen hour FFC Cambridge reduction. The diffraction patterns were analysed using Rietveld refinement and volume fraction and phase information was extracted, resulting in the phase map shown in Figure 45.

The most significant results are as follows. A reduction pathway from TiO_2 to Ti was presented and the formation of the phases $CaTiO_3$, $CaTi_2O_4$ and TiC

Fig. 45: Rietveld-refined phase evolution throughout the pellet. Centre -0 mm to near-surface, 1.2 mm.

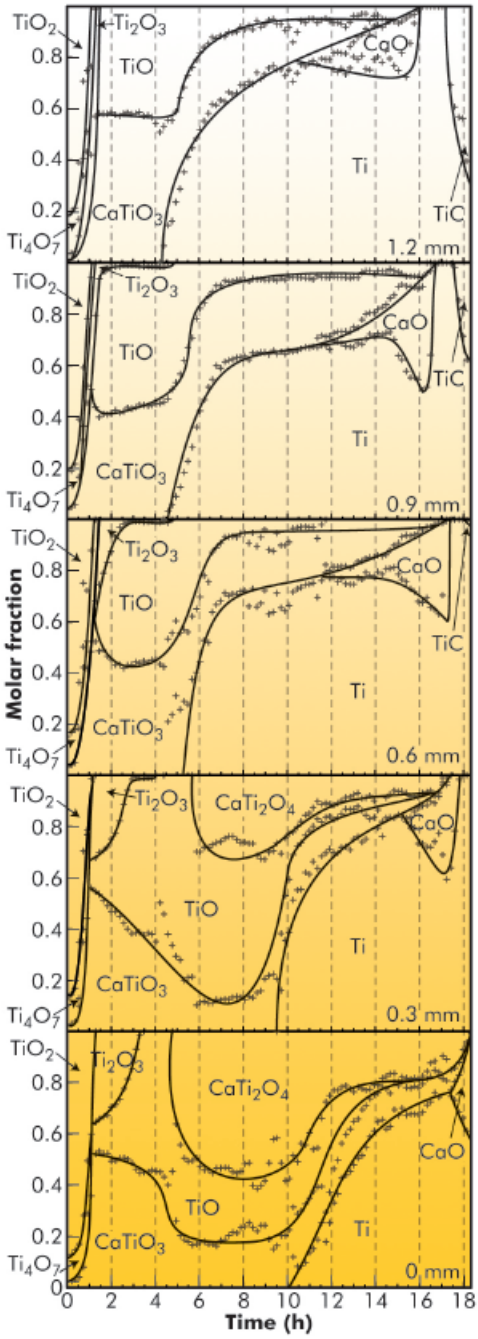

were discussed. $CaTiO_3$ was found to result from incorporation of CaO from the molten salt medium into titanium Magneli phases. $CaTi_2O_4$ was found to form as a comproportionation reaction between TiO and $CaTiO_3$, though this was found to occur only in the presence of Ti. It was found that TiC was formed via an electrochemically assisted route, *i.e.* carbon was electrochemically deposited onto the Ti which chemically reacted to form TiC.

The deoxidation of Ti could be interpreted by combining thermal coefficient of expansion values with data from the literature on the effect of interstitial O on the lattice parameter of Ti. Subsequently it was possible to correlate the formation of TiC to a critical value of interstitial O in Ti (14 at. % O). This discovery has the potential to enable commercial production of ASTM grade Ti powders.

This study demonstrates that high-energy synchrotron radiation can be used as a powerful tool to analyse electrochemical processes such as the FFC Cambridge process. Owing to the high temperature of operation (900°C) and the experimental conditions (argon atmosphere and corrosive molten salt) of the FFC process, analysis of the process thus far has been conducted through a combination of *ex situ* phase studies and voltammetric studies. Unfortunately this had competing interpretations of results and a number of competing hypotheses for the evolution of phases and their role during reduction. This study presents an unequivocal understanding of the FFC Cambridge process by analysing the *in situ* phase evolution. This study has furthered the understanding of the process and has accelerated the prospect of commercially available FFC produced Ti powders.

References
[1] G. Chen, D. Fray and T. Farthing, *Nature* **407**, 361-4 (2000).

Electric-field-induced phase-change behaviour in $(Bi_{0.5}Na_{0.5})TiO_3$–$BaTiO_3$–$(K_{0.5}Na_{0.5})NbO_3$: A combinatorial investigation

Principal publication and authors
J.E. Daniels (a,b), W. Jo (c), V. Honkimäki (a), J. Rödel (c) and J.L. Jones (d), *Acta Materialia* **58**, 2103-2111 (2010).
(a) ESRF
(b) School of Materials Science and Engineering, University of New South Wales, Sydney (Australia)
(c) Institute of Materials Science, Technische Universität Darmstadt (Germany)
(d) Department of Materials Science and Engineering, University of Florida, Gainesville (USA)

Electro-mechanical coupling in materials is a property that is widely exploited in many technological applications such as ultrasonic imaging, nanopositioning, and fuel injection systems. There has been much progress in recent years towards the development of lead-free piezoelectric ceramics in the hope of replacing widely used lead zirconate titanate (PZT) materials. From extensive work on PZT, it is known that good piezoelectric properties are obtained in samples with compositions near phase boundaries. A detailed investigation of possible candidate materials for useful piezoelectric ceramics shows that only a small number of elements are feasible as building blocks for new, competitive ceramics based on the perovskite structure. Preparation through traditional synthesis routes of the many concentrations in which these elements can be combined would be a difficult and painstaking process. Here we show that it is possible to create a compositional gradient by allowing diffusion between independent end member compositions during the ceramic sintering process. Independent compositions can then be probed within this gradient using a high energy X-ray micro-beam.

High-energy X-ray scattering experiments were carried out at beamlines **ID15A** and **ID15B**. A schematic of the experimental setup for ID15A is shown in Figure 46, where a beam energy of 75.3 keV was selected by a double bent Laue monochromator. Refractive lenses were used to focus the beam to approximately 45 x 45 μm^2 at the sample. The sample was placed inside an electric field chamber that was translatable in the direction parallel to the compositional gradient. X-ray diffraction images were collected in transmission using a large area detector. With this setup it was possible

to measure the sample composition using quantitative X-ray fluorescence and simultaneously obtain the structure of the materials as a function of the applied electric-field strength.

It was shown that samples in the range from $0.93(Bi_{0.5}Na_{0.5})TiO_3$–$0.07BaTiO_3$ to $0.86(Bi_{0.5}Na_{0.5})TiO_3$–$0.14(K_{0.5}Na_{0.5})NbO_3$ underwent quite different mechanisms of electric-field-induced strains (Figure 47). Macroscopic property measurements are unable to distinguish between competing mechanisms at the atomic and microstructural scales. Here, however, we demonstrated that within this compositional range a variety of electrostrictive, phase transformation, domain switching, and piezoelectric strain mechanisms were active. Depending on the final application, such mechanisms either have a positive or negative effect on the quality of the product, thus rapid characterisation such as this is an invaluable tool in the identification of useful materials.

Approximately ten independent compositions could be sampled within the combinatorial specimen. However, most of these compositions are close to the end-member concentrations owing to the limited diffusion of atomic species at the boundary during sintering. Further development of sample preparation methods to increase these diffusion lengths is needed. An ideal experiment would involve a graded boundary width of 2 mm and a beam size of 20 μm (readily available at synchrotron X-ray sources). If such an experiment could be realised then it may enable up to 100 compositions to be sampled, increasing the productivity of sample preparation significantly when exploring large phase diagrams. A set of binary combinatorial samples, as studied here, could be selected in order to map the entire BNT-BT-KNN ternary phase diagram with greatly increased speed over regular sample preparation and analysis techniques.

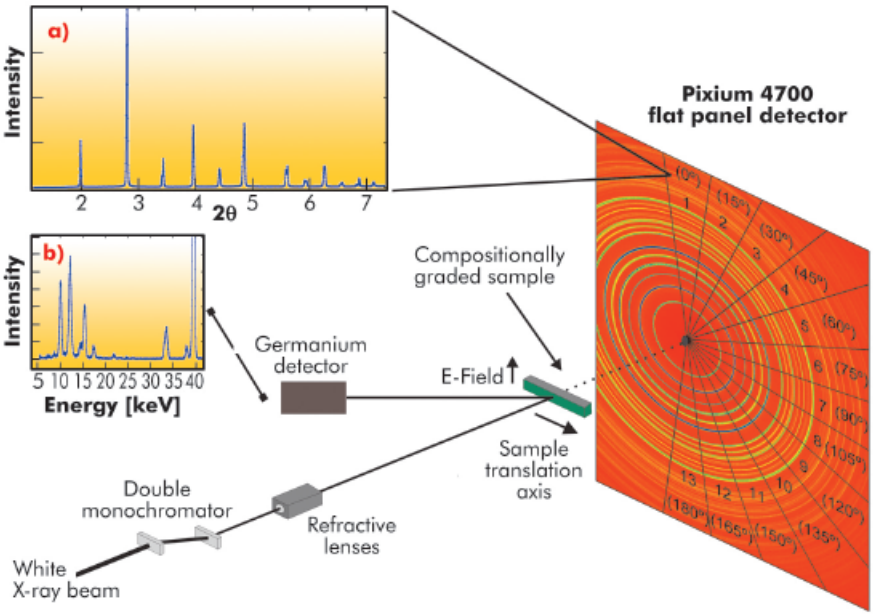

Fig. 46: Schematic diagram of the experimental setup at ID15A.

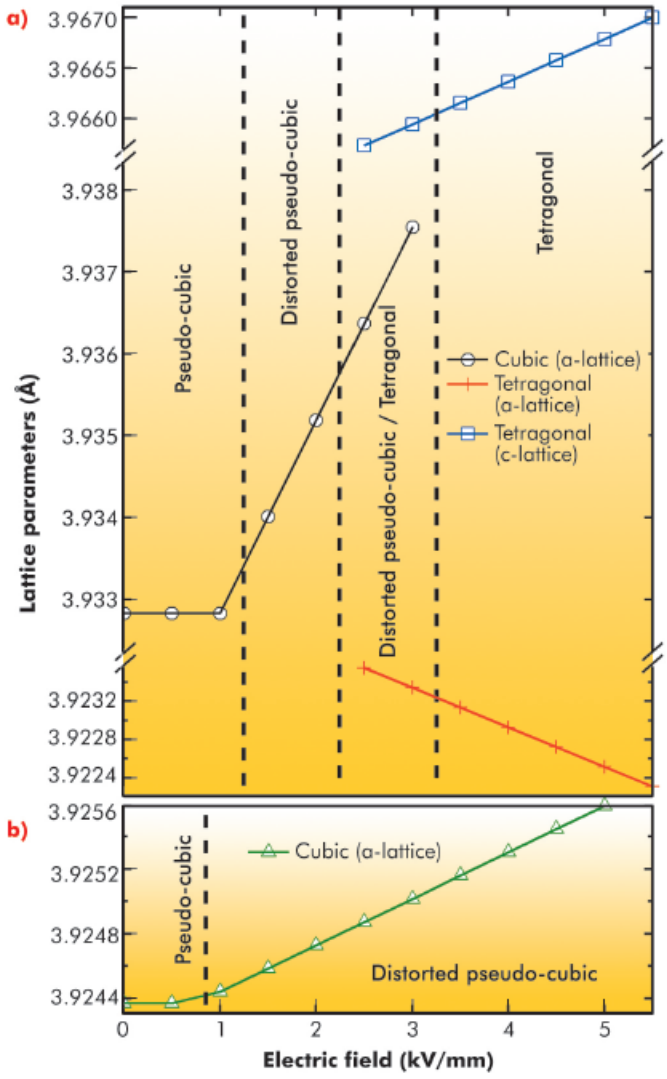

Fig. 47: Change in electric-field-induced lattice parameters of two compositions within the compositional gradient. a) BNT-7BT shows a two step process in which the structure first strains electrostrictively before undergoing a structural transformation; b) BNT-14KNN shows purely electrostrictive strains.

Principal publication and authors
M. Riccò (a), D. Pontiroli (a), M. Mazzani (a), F. Gianferrari (a), M. Pagliari (a), A. Goffredi (a), M. Brunelli (b), G. Zandomeneghi (c), B. H. Meier (c) and T. Shiroka (d), *J. Am. Chem. Soc.* **132**, 2064 (2010).
(a) Dipartimento di Fisica, Università di Parma (Italy)
(b) Institut Laue Langevin, Grenoble (France)
(c) Physical Chemistry Laboratory, ETH-Zurich (Switzerland)
(d) Laboratorium für Festkörperphysik, ETH-Zurich (Switzerland)

Fullerenium salts: a new family of C_{60} based materials

Fullerides are C_{60} charge transfer salts that have notable electronic transport and magnetic properties, like high-T_c superconductivity [1], molecular magnetism, and ionic conductivity [2]. These compounds, usually intercalated with alkali or alkaline-earth ions, always contain C_{60} in its reduced (negative, anionic) state. Analogous compounds where fullerene is oxidised -in the positive, cationic state- referred to as fullerenium salts, are difficult to synthesise owing to the high fullerene oxidation potentials and to the marked electrophilic propensity of C_{60}^{n+}. Nevertheless, theoretical calculations suggest that in such systems a huge increase of the superconducting critical temperature should be expected with respect to that observed in anionic fullerides.

Here we describe the first preparation and the structural characterisation of a member of this new class of C_{60} based materials, whose formula is $C_{60}(AsF_6)_2$. Its synthesis was achieved thanks to the oxidising power of the strong Lewis acid AsF_5 and also the weak nucleophilic character of its conjugate base that allowed the stabilisation of the highly reactive C_{60}^{2+} cations, which unexpectedly organise themselves to form a novel 1D polymer in the crystalline state.

High-resolution synchrotron and neutron powder diffraction were necessary to achieve a definitive structural identification of this material. At room temperature, both techniques showed the presence of a single phase, which was indexed with an orthorhombic cell (a = 10.450(3) Å, b = 9.993(6) Å, c = 32.07(1) Å), although the study of the molecular configuration has proven that the true symmetry is monoclinic, space group *I*2/m with β ≈ 90°. The density of the compound, determined by gas

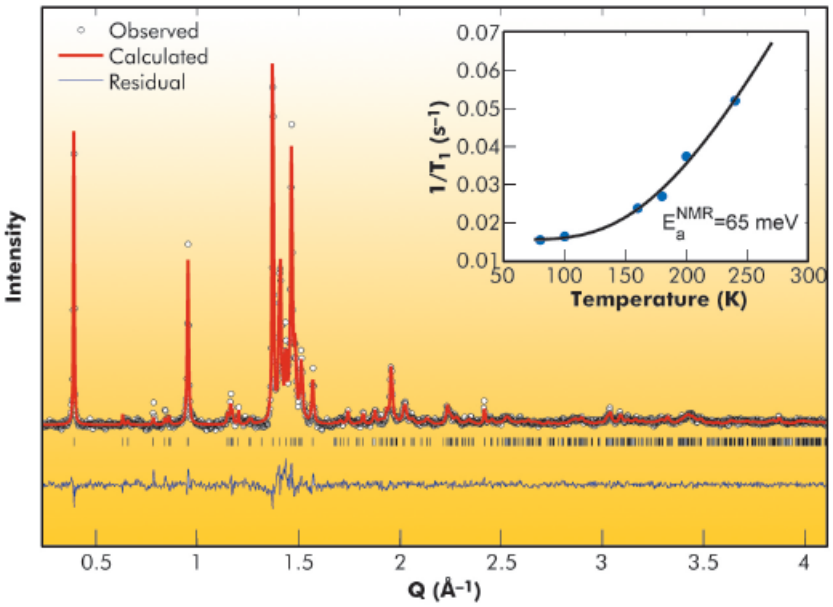

Fig. 48: Observed (o) and calculated (solid red line) powder diffraction pattern of $C_{60}(AsF_6)_2$ at 300 K, from synchrotron data (**ID31**). *Inset*: ^{13}C NMR spin-lattice relaxation rate of $C_{60}(AsF_6)_2$ vs. temperature. The curve represents the best fit to an activated Arrhenius law $1/T_1 = 1/T_{1par} + 1/T_{10}$ exp $(-E_a^{NMR}/k_BT)$ with activation energy E_a^{NMR} = 65 meV.

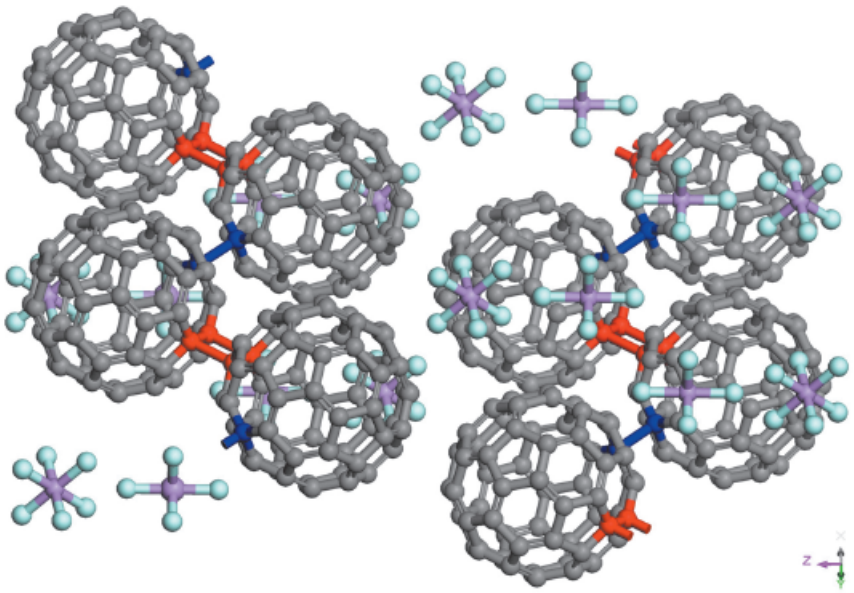

Fig. 49: The 1D polymeric structure of $C_{60}(AsF_6)_2$, consisting of polymeric chains connected alternatively by single C-C bonds and four-membered carbon rings (view along the [110] crystallographic direction).

picnometry, of 2.2(2) g cm^{-3} suggested that the correct stoichiometry is $C_{60}(AsF_6)_2$. Rietveld refinement was performed at the same time on both synchrotron (see Figure 48) and neutron data: while the former allowed localisation of the various components of the cell, the latter permitted the determination of the precise molecular orientation. After trials with different dispositions compatible with the symmetry group, the agreement factors invariably improve after ordering the C_{60} units in an unusual zigzag configuration, as shown in Figure 49. This arrangement is compatible with the presence of both alternated four-membered carbon rings ([2+2] cycloaddition) and single C-C bonds between the fullerene molecules along the zigzag chain.

Nuclear magnetic resonance (see inset of Figure 48), SQUID magnetometry and DC conductivity show that this polymer is a diamagnetic semiconductor while the lack of the theoretically predicted high T_c superconductivity could be ascribed to the strong reduction of crystal and molecular symmetry upon polymerisation. Nonetheless, the small value of the energy gap (approx. 65 meV) could suggest the proximity of a metallic phase.

The higher density of states (DOS) at the Fermi energy of the 5-fold-degenerate h_{1u} HOMO derived band, as compared to the 3-fold-degenerate LUMO involved in the anionic fullerides, leads to the prediction of a substantial increase of the critical temperature in a hypothetical cubic superconducting fullerenium compound. However, our evidence suggests that the high reactivity of C_{60}^{2+} ions triggers the formation of intermolecular bonds. One can hypothesise that these compounds would have been polymeric in their hole-doped state and consequently hardly superconducting.

In conclusion, the successful synthesis of the first fullerenium salt in the solid state highlights the marked propensity of C_{60} cations to polymerise. The polymerisation also suppresses the expected exotic properties of a hole-doped C_{60} compound. The preparation of a monomeric compound either by thermal depolymerisation of the present system or by co-intercalation of inert molecules is now under study.

References
[1] Y. Ihara, H. Alloul, P. Wzietek, D. Pontiroli, M. Mazzani and M. Riccò, *Physical Review Letters* **104**, 256402 (2010).
[2] M. Riccò, M. Belli, M. Mazzani, D. Pontiroli, D. Quintavalle, A. Janossy and G. Csanyi, *Physical Review Letters* **102**, 145901 (2009).

Suppression of antiferromagnetic order and emergence of superconductivity in Co- and Ni-doped NaFeAs

Principal publication and authors
D.R. Parker (a), M.J.P. Smith (a), T. Lancaster (b), A.J. Steele (b), I. Franke (b), P.J. Baker (c), F.L. Pratt (c), M.J. Pitcher (a), S.J. Blundell (b) and S.J. Clarke (a), *Phys. Rev. Lett.* **104**, 057007 (2010).
(a) Department of Chemistry, University of Oxford (UK)
(b) Department of Physics, University of Oxford (UK)
(c) ISIS Facility, STFC-Rutherford Appleton Laboratory (UK)

The emergence of iron-based high temperature superconductors [1] with maximum values of the superconducting transition temperature, T_c, exceeding 50 K, has resulted in the discovery of many new superconductors. These have the common feature of FeAs, FeP or FeSe anti-PbO-type layers separated by electropositive cations, or by thicker fluorite-type or perovskite-related oxide layers. A huge experimental and theoretical effort has been devoted to understanding the origin of superconductivity in these apparently-non-BCS superconductors.

NaFeAs with the anti-PbFCl structure type (Figure 50) was synthesised following the discovery of superconductivity in stoichiometric LiFeAs. NaFeAs may be made stoichiometric, and although there have been reports of isostructural materials which are slightly deficient in Na, these have not been well characterised. It is a general feature of many of the iron-based superconductors that, when the compounds are stoichiometric and iron has a formal oxidation state of +2 and the $FeAs_4$ tetrahedra are fairly close to regular (*e.g.* NaFeAs, $BaFe_2As_2$, LaFeAsO), the compounds are itinerant antiferromagnets in which magnetic ordering at T_N drives a structural distortion at T_S (where $T_S \geq T_N$). When these compounds are doped either on the iron site, or on the sites in the

intervening layers, or when a hydrostatic pressure is applied, the magnetic ground state is suppressed and superconductivity emerges. The exceptions are some of the phosphides and LiFeAs and FeSe which have superconducting ground states when stoichiometric [2].

The ordered moment in NaFeAs is extremely small (~0.1 – 0.3 μ_B per Fe) so the magnetically ordered state is more amenable to investigation using muon-spin rotation spectroscopy (μSR) than neutron powder diffraction. Furthermore the size of the structural distortion, which is driven by the magnetic ordering, scales with the size of the ordered moment per Fe atom, so quantitative analysis of the small tetragonal-to-orthorhombic distortion in NaFeAs requires high resolution such as that available on ID31.

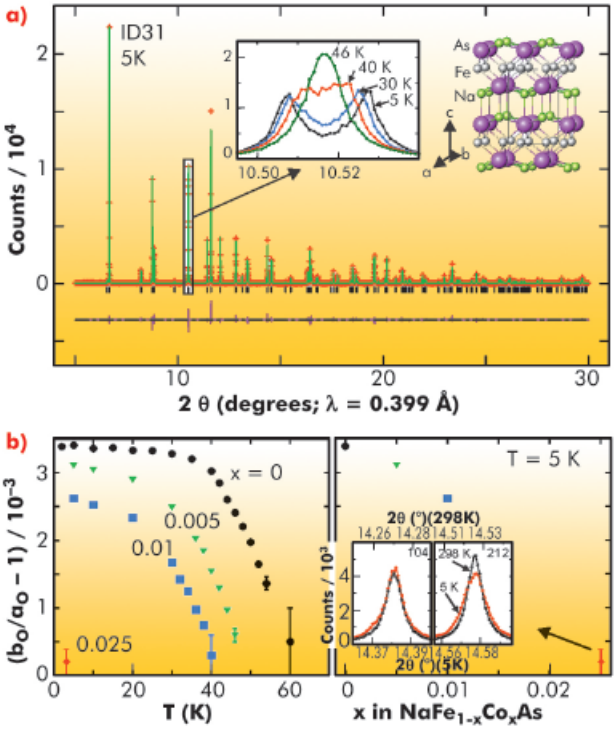

Fig. 50: a) Refinement of the structure of $NaFe_{0.995}Co_{0.005}As$ against ID31 data at 5 K. The thermal evolution of the splitting of the tetragonal 112 reflection into the orthorhombic 022/202 is shown. b) The evolution of the distortion is shown for several compositions. For $x = 0.025$, which lies well into the superconducting (SC) region, there is no resolvable orthorhombic distortion, although slight broadening of the tetragonal 212 reflection is evident on cooling from 298 K to 5 K. a_O and b_O are the orthorhombic lattice parameters.

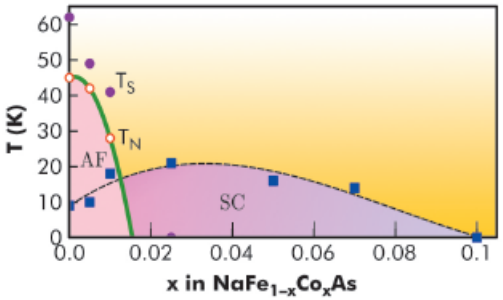

Fig. 51: Phase diagram for Co-doped NaFeAs. The magnetic ordering temperatures (T_N) in the antiferromagnetic (AF) region were determined from muon spin rotation experiments. The structural distortion temperatures were determined from the measurements on ID31.

Zero-field μSR measurements to probe magnetic order were made on the GPS beamline at the Swiss Muon Source. Stoichiometric NaFeAs shows clear oscillations in the muon decay asymmetry characteristic of magnetic ordering with a Neél temperature of 45.0(2) K. Doping with small amounts of Co on the Fe site in NaFeAs has a dramatic effect on the magnetic ordering – the oscillations are heavily damped even at a doping level of 0.5% Co and the Neél temperature decreases rapidly with increasing doping. The antiferromagnetic ordering in these iron compounds results in an orthorhombic distortion of the structure on cooling and we probed this in NaFeAs using the high-resolution neutron powder diffractometer HRPD at the ISIS facility and used **ID31** to probe the distortion and its temperature evolution in the cobalt-doped materials. **Figure 50** shows the Rietveld refinement against ID31 data of the sample $NaFe_{0.995}Co_{0.005}As$ and the inset shows the evolution of the splitting of the tetragonal 112 reflection as the system distorts from tetragonal *P4/nmm* to orthorhombic *Cmma* with a $\sqrt{2}a_T$ x $\sqrt{2}a_T$ x c_T expansion of the tetragonal cell. The suppression of the antiferromagnetic ordering is accompanied by a decrease in the size of the structural distortion and in the temperature at which the distortion becomes evident in the powder diffraction data. By the time sufficient doping has been carried out (~2.5% Co) to drive the system well into the superconducting regime (**Figure 51**) the distortion is no longer evident even at the high resolution available on ID31.

Further experiments will probe the mixed region between about 1% and 2% Co doping where magnetic order and superconductivity coexist in order to help determine the interplay between magnetism and superconductivity in these compounds.

References

[1] Y. Kamihara, T. Watanabe, M. Hirano and H. Hosono, *J. Am. Chem. Soc.* **130**, 3296 (2008).

[2] M.J. Pitcher, T. Lancaster, J.D. Wright, I. Franke, A.J. Steele, P.J. Baker, F.L. Pratt, W. Trevelyan Thomas, D.R. Parker, S.J. Blundell and S.J. Clarke, *J. Am. Chem. Soc.* **132**, 10467 (2010).

Flexible porous coordination polymers for selective adsorption

Among crystalline porous solids, metal organic frameworks (MOFs) deserve special interest. These hybrid solids, built up from inorganic subunits connected through polytopic ligands (such as poly-carboxylate and poly-pyrazolate) have the faculty to change their pore size reversibly upon external (temperature, pressure, light) or internal (entrapped guests) stimuli while remaining crystalline. This dynamic porosity leads to unusual sorption properties, which are attractive for applications in the area of fluid storage, capture or separation. One of the most archetypical examples of such a solid is MIL-53(M) (MIL stands for Materials Institute Lavoisier), a metal (M = Al, Cr, Fe) terephthalate built up from inorganic chains and linear ligands presenting one dimensional diamond-shaped micropores. In the last few years, a multi-technique approach has been developed to study the adsorption of important gases (H_2, CH_4, CO_2, alkanes, etc.) in these solids [1]. It could be of interest in industrial applications to obtain alcohol of very high purity. Therefore, the sorption of polar vapours (water, methanol and ethanol) in MIL-53(Cr) has been explored. Upon adsorption, the solid evolves from a large-pore form to a narrow-pore form (Figure 52), for which the pore volume depends on the nature of the guest. At higher alcohol pressure, the structure evolves once again to a large-pore form, whereas the narrow pore form is retained in the presence of water. The specific host-guest interactions associated with these adsorption processes were probed by microcalorimetry, X-ray structure investigation, IR and Raman spectroscopy, thermal analysis and molecular modelling. The *in situ* powder X-ray diffraction experiments were carried out at beamline **BM01A**. These studies revealed that the strength of the interaction depends on the nature of the adsorbed species (water < alcohols), and finally concludes that this solid is potentially interesting for the selective adsorption of alcohol from

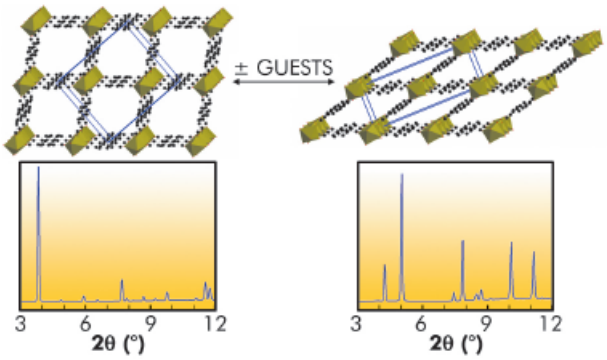

Fig. 52: The "breathing" behaviour of MIL-53 upon adsorption/desorption of guests, and the corresponding powder X-ray diffraction patterns which allow a direct evaluation of the pore size. Left: large-pore form; right: narrow-pore form.

Principal publications and authors

S. Bourrelly (a), B. Moulin (b), A. Rivera (c), G. Maurin (c), S. Devautour-Vinot (c), C. Serre (d), T. Devic (d), P. Horcajada (d), A. Vimont (b), G. Clet (b), M. Daturi (b), J.-C. Lavalley (b), S. Loera-Serna (a), R. Denoyel (a), P.L. Llewellyn (a) and G. Férey (d), *J. Am. Chem. Soc.* **132**, 9488-9498 (2010);

T. Devic (d), P. Horcajada (d), C. Serre (d), F. Salles (c), G. Maurin (c), B. Moulin (b), D. Heurtaux (d), G. Clet (b), A. Vimont (b), J.-M. Grenèche (e), B. LeOuay (d), F. Moreau (d), E. Magnier (d), Y. Filinchuk (f), J. Marrot (d), J.-C. Lavalley (b), M. Daturi (b) and G. Férey (d), *J. Am. Chem. Soc.* **132**, 1127-1136 (2010).

(a) Laboratoire Chimie Provence, CNRS, Université Aix-Marseille (France)
(b) Laboratoire Catalyse et Spectrochimie, CNRS, ENSICAEN, Université de Caen (France)
(c) Institut Gerhardt, CNRS, ENSCM, Université de Montpellier (France)
(d) Institut Lavoisier de Versailles, CNRS, Université de Versailles St-Quentin en Yvelines (France)
(e) Laboratoire de Physique de l'Etat Condensée, CNRS, Université du Maine (France)
(f) Swiss Norwegian Beamline,

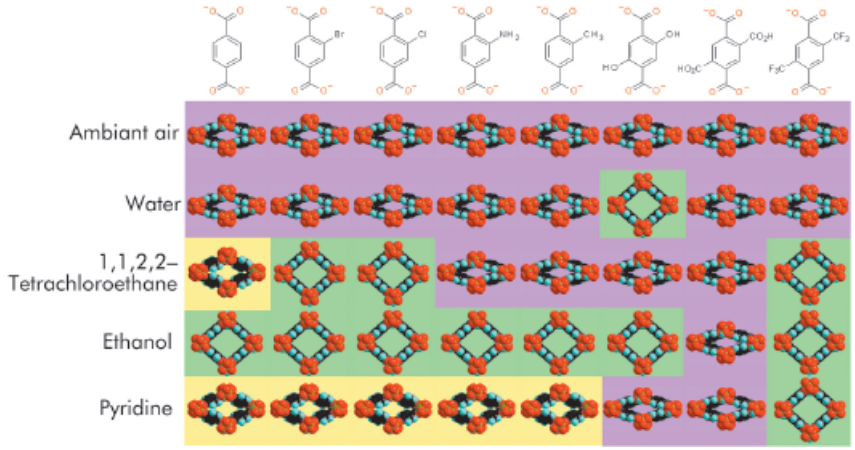

Fig. 53: Effect of the nature of the grafted organic group on the pore opening of functionalised MIL-53(Fe)s upon adsorption of various liquids. Pink: narrow-pore form; green: large-pore form; yellow: intermediate-pore form.

Reference
[1] C. Serre, S. Bourrelly, A. Vimont, N.A. Ramsahye, G. Maurin, P.L. Llewellyn, M. Daturi, Y. Filinchuk, O. Leynaud, P. Barnes and G. Férey, *Adv. Mater.* **19**, 2246-2251 (2007).

water/ethanol mixtures. Alternatively, the introduction of functional groups on the organic linker is an easy way to modify the pore surfaces, and thus to tune the sorption properties, affecting both the strength of the host-guest interactions and the pore opening. With this aim, various functionalised MIL-53(Fe) solids were prepared. While the hydrated form (under ambient air) of all these solids is associated with a narrow-pore form (see Figure 53), they present contrasting behaviours when immersed in liquids. Powder X-ray diffraction indeed reveals that the pore opening (and thus the number of adsorbed molecules), strongly depends on the nature of both the liquid and the grafted group (Figure 53). Besides the appearance of a large-pore form requires that the host-guest interactions (hydrogen bonding) overcome the intraframework interactions. Providing that this requirement is fulfilled, the adequacy of the chemical nature of both components (liquids-grafted groups) could lead to selective adsorption.

Soft condensed matter

As in the previous years, this section comprises a selection of highlights that is a sub-set of many interesting scientific results published over the year. Contributions are included from both the public beamlines in the Structure of Soft Matter group and the CRG beamlines. One of the striking features of this year's articles is the strong emphasis on the complementary techniques and implications of modelling and simulations. Many of these contributions are not standalone examples and scattering results are interpreted with the aid of complementary techniques. A positive aspect is the use of advanced computer simulations to extract quantitative details. Evidently, there is strong overlap with other disciplines such as materials and biological sciences.

The arrested states in soft matter systems continue to attract renewed interest. In the first article, Ruzicka *et al.* present evidence for the Wigner glass state in Laponite clay suspensions by a combination of SAXS experiments, theory and computer simulation. The second article, by László *et al.*, identifies the jammed dynamics in PNIPA gel using XPCS and relates the microscopic relaxation rate to the macroscopic deswelling ratio. The third article, by Poulos *et al.*, reports the scale-dependent dynamics of the nematic phase of goethite suspensions by means of XPCS and poses the difficult question on the crossover from the microscopic particulate dynamics to the macroscopic continuum hydrodynamics.

Proteins and other biomolecules at interfaces continue to be the focus of research using surface and interface sensitive techniques. The article by Singh *et al.* reveals the different steps in lysozyme adsorption at the air-water interface. Schneck *et al.* explain the crucial role played by charged saccharides in the survival of bacteria against antimicrobial peptides.

Accardo *et al.* present an interesting technical development suitable for near contact-free manipulation of protein (lysozyme) droplets using ultra-hydrophobic surfaces. Knaapila *et al.* report on the microstructure of an aligned polymer blend (polyfluorene in polyethylene) and the relationship with the photoluminescence property of the blend. Past Highlights issues have seen articles on the dynamics of the self-assembly process of surfactants, block copolymers, peptides, etc. Here, Besenius *et al.* demonstrate the directional self-assembly of chiral supramolecular polymers in water to form elongated rod-like assemblies.

Time-resolved pump-probe solution X-ray scattering continues to shed new light on the chemical reaction pathways. Kong *et al.* demonstrate two different pathways in the photolysis of $Ru_3(CO)_{12}$ in cyclohexane depending on the photexcitation energy or its proximity to the electronic absorption bands. Finally, the article by Okemefuna *et al.* illustrates the usefulness of solution SAXS in the structural elucidation of highly flexible proteins such as complement factor H which are not amenable to crystallographic studies.

The past year also saw some apprehensions within the Soft Matter user community regarding the status of the newly established Partnership for Soft Condensed Matter and the ID10 A and B beamlines. This situation was a consequence of the difficult budgetary situation imposed on the ESRF. Finally, it has been decided by the ESRF management to combine the XPCS and liquid surface and interface scattering activities at ID10 A and B, respectively into one beamline with two stations operating alternately. To facilitate this change, a major refurbishment of the ID10 beamline complex is foreseen. This will allow us to enhance the performance of both XPCS and surface and interface scattering techniques significantly, though the total available beam time will be halved.

Among the other major technical developments, the ID13 nano-endstation has become fully operational. ID09B has successfully commissioned a state-of-the-art picosecond laser system and multilayer X-ray optics. The technical design for UPBL9a, the extension of ID02 to an ultra high resolution small-angle scattering beamline, is underway.

T. Narayanan

Principal publication and authors
B. Ruzicka (a), L. Zulian (b), E. Zaccarelli (c), R. Angelini (a), M. Sztucki (d), A. Moussaïd (d) and G. Ruocco (e), *Phys. Rev. Lett.* **104**, 085701 (2010).
(a) IPCF-CNR, Dipartimento di Fisica, Roma (Italy)
(b) ISMAC, CNR, Milano (Italy)
(c) ISC-CNR, Dipartimento di Fisica, Roma (Italy)
(d) ESRF
(e) Dipartimento di Fisica, Roma (Italy)

Multiple arrested states in colloidal clays

Dynamical arrest in soft colloidal systems has recently become the subject of intense research activity. Gels and glasses have been identified respectively at low and high concentrations. Interesting scenarios arise when, in addition to a short-ranged attraction, particles have a residual electrostatic charge that builds up a long-range repulsion in the effective potential. To investigate the formation of multiple arrested states, colloidal clays have emerged as suitable candidates. Laponite is a prototype system showing a very complex phase diagram because of the anisotropy of the particles, combined with the presence of attractive and repulsive terms in the interactions [1].
A subtle aging dynamics give rise to (at least) two final arrested states obtained by a simple increase of Laponite volume fraction from low ($C_w < 2.0\%$) to high ($C_w \geq 2.0\%$) values in the absence of added salt [2]. More recently, the static properties of these two states have been investigated in detail [3], showing that while the low C_w state has an inhomogeneous character, the high C_w state is homogenous, allowing for the identification of these two arrested states, respectively, as gel and glass.

Here we report the structure factor S(Q) measured with small angle X-ray scattering at beamline **ID02** together with theoretical and numerical calculations in the high concentration window, for $2.0 \leq C_w \leq 3.0\%$ (Figure 54). The experimental data can be fully described, in terms of peak position, peak height and compressibility, by theoretical $S^{th}(Q)$ by using a Yukawa potential, which accounts in an average way for the screened electrostatic repulsion between Laponite platelets or clusters. Numerical $S^{num}(Q)$ obtained by Monte Carlo simulations of 200 discs at the same density as that extracted from the fits are also in good agreement with experimental and theoretical values, as shown by the inset of Figure 54.

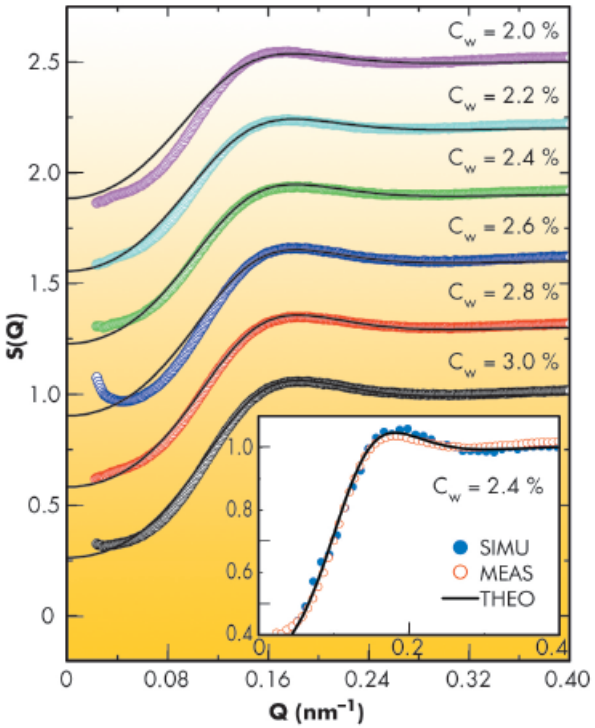

Fig. 54: Comparison between measured SM(Q) (symbols) and theoretical $S^{th}(Q)$ (lines) for several high concentration samples at tw~50 h. For clarity, curves have been shifted along the vertical axis progressively by 0.3. Inset: measured SM(Q) (open circles), theoretical $S^{th}(Q)$ (lines) and simulated Sn(Q) (closed circles) for $C_w = 3.0\%$.

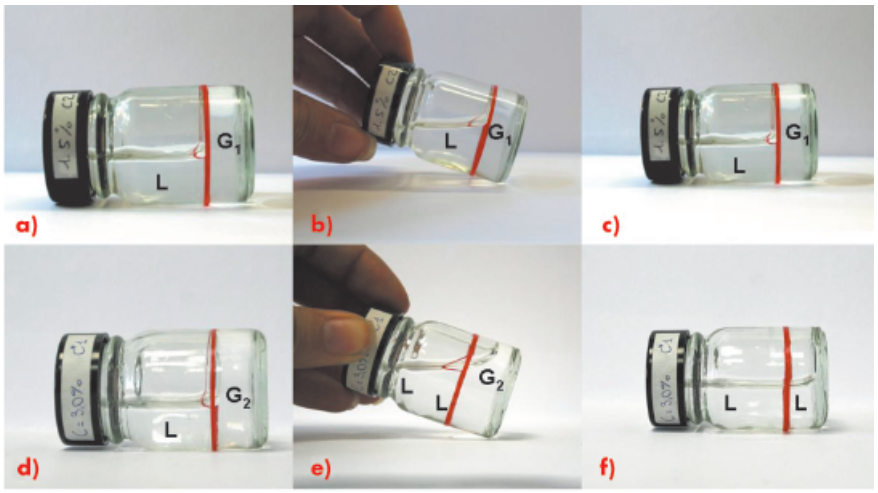

Fig. 55: Starting (a)(d), intermediate (b)(e), and final (c)(f) states of arrested samples at low $C_w = 1.5\%$ and high $C_w = 3.0\%$ concentrations. While the initial gel state G1 is not macroscopically affected by the addition of water (c), the glassy state G2 fluidises (f).

Hence, the combination of experiment, theory and simulation allows us to identify the observed arrested state at high concentrations as a Wigner glass stabilised by the residual electrostatic repulsion.

The same conclusion can be reached by performing the dilution experiment illustrated in Figure 55 for a low (C_w = 1.5% - upper panels) and a high (C_w = 3.0% - lower panels) concentration sample. Here the samples are left to age up to the final arrested states, respectively, of gel (G1) and glass (G2) nature for low and high concentrations [2]. After arrest takes place, water (L) is added and panels (a) and (d) show the identical situation for the two cases. However, the evolution of the two samples soon becomes dramatically different. The arrested state of the high-concentration sample (G2) starts to fluidify [panel (e)] to a final liquid state [panel (f)], while the low concentration sample does not show any macroscopic changes of its solid like state [panels (b) and (c)]. This experiment permits identification of the dominant interactions ruling arrest. When the arrest is generated by attraction, the presence of additional water does not affect it because the Laponite bonds (of strong electrostatic nature) cannot be broken. On the other hand, when the state is stabilised by repulsion, the increase of free volume allows a rearrangement of Laponite platelets on average to a larger distance. If the distance is larger than the characteristic repulsive length (namely the electrostatic Debye length), the glass is destabilised to melting to a liquid state. The different behaviour between the two samples upon dilution confirms the different nature of the two arrested states: a Wigner glass (G2) and a gel (G1), dominated, respectively, by repulsive and attractive interactions at high and low concentrations.

In conclusion, through the combination of SAXS and dilution experiments, theory and simulation, we have shown the presence of a disconnected Wigner glass state in a charged colloidal clay. This arises at a larger concentration with respect to the one where a gel network is found, thanks to the different time scales controlling the repulsive (short-time) and attractive (long-time) interactions.

References
[1] B. Ruzicka, E. Zaccarelli, L. Zulian, R. Angelini, M. Sztucki, A. Moussaid, T. Narayanan and F. Sciortino, *Nature Materials* **10**, 56 (2011).
[2] B. Ruzicka, L. Zulian and G. Ruocco, *Phys. Rev. Lett.* **93**, 258301 (2004); *Langmuir* **22**, 1106 (2006).
[3] B. Ruzicka *et al.*, *Phys. Rev. E* **77**, 020402(R) (2008).

Jamming kinetics: PNIPA gels

Anomalous relaxation behaviour continues to be detected in an increasing number of materials, including glasses, sand piles, and more broadly, *jammed* systems [1,2]. A striking feature of dense colloidal suspensions and other such disordered crowded systems is their difference from dilute suspensions, where motion is diffusive and fluctuations decay at a rate $\Gamma = Dq^2$ (q being the momentum transfer and D the diffusion coefficient). In jammed systems, the intensity correlation functions are instead compressed exponentials of the form $\exp[-(\Gamma t)^n]$, ($n > 1$), with hyper-diffusive dispersion relationships $\Gamma \sim q^p$, ($p \approx 1$). Although microscopic explanations have been advanced for this type of dynamics, the origin of the behaviour is poorly understood.

Jamming was recently identified in the out-of-equilibrium state of poly(N-isopropyl acrylamide) (PNIPA) hydrogels undergoing deswelling. PNIPA hydrogels belong to a class of environmentally sensitive systems that display a volume phase transition (VPT) at a critical temperature $T_{VPT} \approx 34$°C, above which they shrink by expelling solvent. Depending on the sample preparation, the rate of shrinkage can be very slow indeed. This stimulus-responsiveness is the basis of numerous medical and industrial applications, for which the contraction time is often of crucial importance. At the VPT, microphase separation occurs promptly, with formation of microscopic polymer surfaces that scatter visible light so strongly that observations of the bulk material by standard dynamic light scattering are excluded. X-ray photon correlation spectroscopy (XPCS), however, offers a unique window for investigating their internal dynamics.

Principal publication and authors
K. László (a), A. Fluerasu (b,c), A. Moussaïd (b,d) and E. Geissler (d), *Soft Matter* **6**, 4335-4338 (2010).
(a) Department of Physical Chemistry and Materials Science, Budapest University of Technology and Economics (Hungary)
(b) ESRF
(c) present address: NSLS-II, Brookhaven National Laboratory, Upton, NY (USA).
(d) Laboratoire Interdisciplinaire de Physique, Université J. Fourier de Grenoble (France)

Three different PNIPA gel samples were synthesised with increasing degrees of inhomogeneity. Macroscopic measurements of deswelling were made on the disks by immersing them in water at 50°C and measuring their diameter d with a video camera as a function of time t. The responses exhibit essentially two types of behaviour (Figure 56). Gels containing small amounts of cross-linker deswell extremely slowly, but above a given cross-link content an abrupt increase of some 3 orders of magnitude in their deswelling rate occurs. The disk diameter decreases linearly with time until the equilibrium volume is reached (in the logarithmic scale of the figure, these linear decays appear curved). A linear decay implies that the gel deswells by uniform expulsion of the solvent. All points in the gel thus approach each other with velocity $\mathbf{v} = \alpha\mathbf{r}$, where $\mathbf{r}$ is the separation between any two points and α, the divergence of the velocity, defines the rate of deswelling. The speckle pattern scattered by the shrinking gel correspondingly moves uniformly outwards to increasingly large values of q. The time required for a speckle to migrate over one pixel of the detector determines the intensity correlation function, $g_2(t)$-1, which decays to zero linearly with time at a rate Γ that is proportional to q.

Qualitatively, the linear time dependence predicted for the intensity correlation functions $g_2(t)$-1 (Figure 57) fits well with the XPCS measurements obtained at **ID10A** on a PNIPA gel (sample 1 in Figure 56) at 50°C. The linear dependence of Γ on q is also recovered.

Quantitatively, the XPCS measurement yields for the deswelling rate at this temperature $\alpha = 2.3\ 10^{-3}\ s^{-1}$. Owing to the sensitivity of this system to inhomogeneities, the deswelling rate may be accelerated in the X-ray beam, becoming comparable with that of sample 3 in Figure 56, for which the macroscopic deswelling rate is $2.6\ 10^{-3}\ s^{-1}$.

These results show that in PNIPA hydrogels the linear dependence both on t and on q of the intensity correlation function stems from the divergence of the velocity. The same mechanism is also likely to operate in other jammed systems undergoing densification (or expansion), notably colloid suspensions. The associated linear form of the intensity correlation function offers an alternative to the compressed exponential form usually assumed.

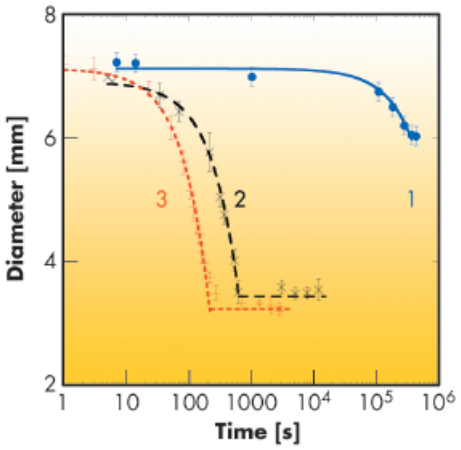

Fig. 56: Variation of diameter of PNIPA hydrogel disks at 50°C, for samples of increasing cross-link density 1, 2 and 3. Lines are fits to $d = d_0 - vt$, where v is the velocity of the disk at its rim.

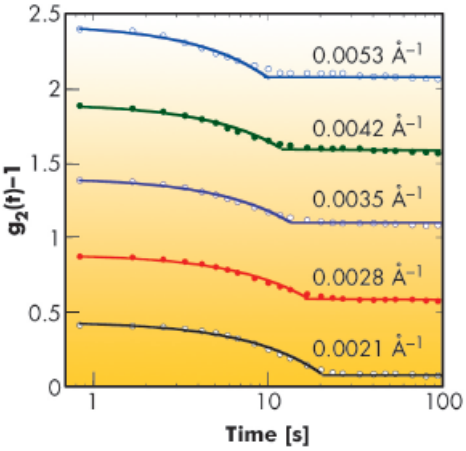

Fig. 57: XPCS intensity correlation functions of deswelling for a PNIPA gel at 50°C at different q. Lines are fits to the linear decay $(1-\Gamma t)$ with $\alpha = 2.3\ 10^{-3}\ s^{-1}$. Successive curves vertically offset by 0.5.

References

[1] A.J. Liu and S.D. Nagel, *Soft Matter* **6**, 2869-2870 (2010).

[2] A.O.N. Siemens and M. van Hecke, *Physica A* **389**, 4255-4264 (2010).

Scale-dependent slowdown in a colloidal nematic phase

Principal publication and authors
A.S. Poulos (a), D. Constantin (a), P. Davidson (a), B. Pansu (a), É. Freyssingeas (b), A. Madsen (c) and C. Chanéac (d), *Journal of Chemical Physics* **132**, 091101 (2010).
(a) Laboratoire de Physique des Solides, Orsay (France)
(b) Laboratoire de Physique ENS-Lyon, Lyon (France)
(c) ESRF
(d) Laboratoire de Chimie de la Matière Condensée, Paris (France)

Nematics are the simplest example of a phase with no positional order, but still exhibiting orientational order (and hence anisotropy). This combination endows them with remarkable qualities: although fluid, they have elastic properties and, consequently, long-lived fluctuations. A great deal is known about the large-scale dynamics of nematic systems, which is well described by a generalised hydrodynamic model. However, there is much less data on their short-range behaviour (over length scales comparable to the inter-particle distance) due to a lack of suitable techniques. Understanding the dynamics at this scale, where interaction between particles defines the structure of the system, is essential for building a complete picture of the phase.

X-ray scattering methods are suitable for exploring these distance and time scales. X-ray photon correlation spectroscopy (XPCS) gives access both to the static structure factor S(q) and the collective diffusion coefficient D(q). Based on very general thermodynamic arguments, these parameters are related by $D(q) \sim 1/S(q)$ ("de Gennes narrowing"). In colloidal suspensions, a more refined treatment must take into account the hydrodynamic interactions, which further modulate this dependence through a hydrodynamic function $H(q) = S(q) \times D(q)/D_0$ (where D_0 is the diffusion coefficient at infinite dilution).

We measured the hydrodynamic function for a fluid nematic phase of goethite (α-FeOOH) nanorods (with an aspect ratio of about ten). The experiments were performed at **ID10A** using an X-ray energy of 8 keV, in the uniform filling mode of the storage ring. The scattered signal was detected by a two-dimensional Maxipix detector consisting of 256×256 pixels, and the intensity autocorrelation functions were calculated by ensemble averaging over equivalent pixels. A typical SAXS pattern of an aligned nematic sample is displayed in Figure 58a. We show in Figure 58b the corresponding structure factor $S(q_\perp)$, along the direction perpendicular to the director **n** (which indicates the average orientation of the particles).

We recorded the time correlation function g(t) of the scattered signal and analysed it to obtain the relaxation rate Ω. The diffusion coefficient is obtained as $D(q) = \Omega(q)/q^2$. The static and dynamic data, as well as the hydrodynamic function H(q) defined above, are presented in Figure 59. Unexpectedly, we found that, below the position of the structure maximum, D decreases sharply by more than a factor of three with respect to its high-q (*i.e.* short distance) value (Figure 59b); the fit with a sigmoidal function is also shown. Combined with the decrease of S(q) in the same range (Figure 59a), this yields a hydrodynamic slowing down (decrease of H(q) in Figure 59c) by a factor of ten, much stronger than that seen in hard sphere suspensions, a result that emphasises the strength of hydrodynamic interactions in reduced dimensions.

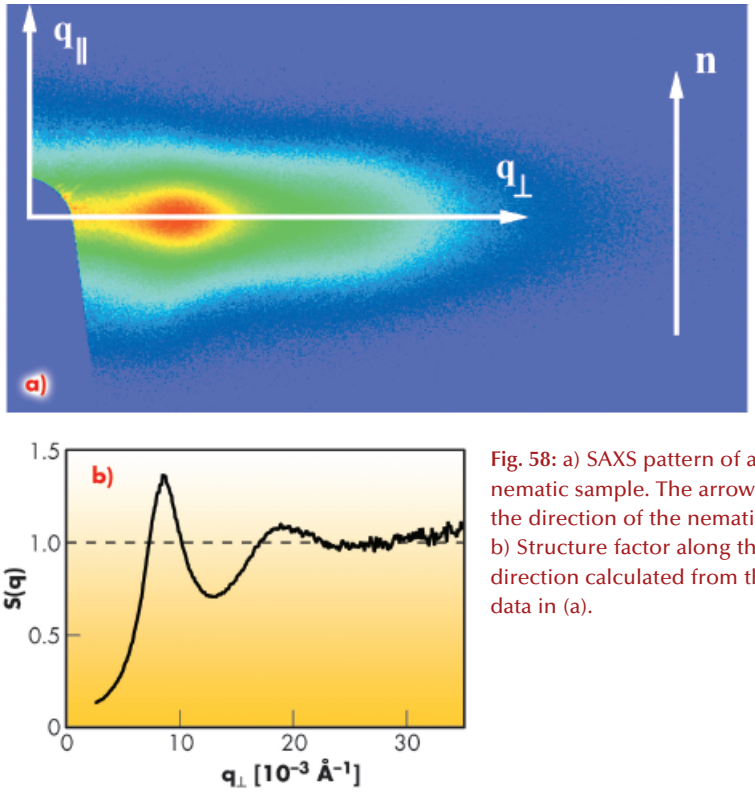

Fig. 58: a) SAXS pattern of an aligned nematic sample. The arrow indicates the direction of the nematic director **n**. b) Structure factor along the $q_\perp$ direction calculated from the SAXS data in (a).

In summary, we measured for the first time the dynamics of a colloidal nematic phase down to the inter-particle distance, revealing non-trivial and scale-dependent hydrodynamic effects, namely a reduced collective diffusion coefficient at long distances. The onset of the slowing down corresponds rather well to the position of the peak in the structure factor. Therefore, our experiments suggest a crossover between two different kinds of behaviour at scales smaller and larger than the inter-particle distance, raising the fundamental (and very difficult) question of the transition between the microscopic level of the individual particles to the macroscopic one described by continuum theories.

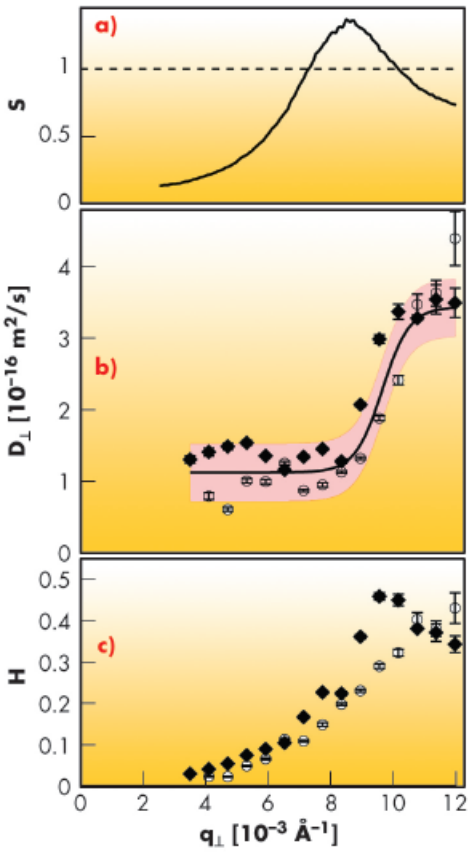

Fig. 59: a) Static structure factor $S(q_\perp)$. b) Diffusion coefficient $D(q_\perp)$. The symbols correspond to two different measurements performed on the same sample. The solid line and the greyed area are the fit by a sigmoidal function and the ±σ prediction bands. c) Hydrodynamic function $H(q_\perp)$ obtained from the data in (a) and (b).

Principal publication and authors
A. Singh (a,b), O. Konovalov (a), J. Novak (a,c) and A. Vorobiev (a), *Soft Matter* **6**, 3826 (2010).
(a) ESRF
(b) Current address: Banasthali University, Rajasthan (India)
(c) Current address: Institute of Solid State Physics, Graz (Austria)

Watching protein layers grow

Proteins in an aqueous solution spontaneously form a two-dimensional (2D) layer at the air-water interface. A complex mechanism guides the assembly of proteins through interactions among proteins, interface and the bulk medium. The air-water interface is a convenient medium which provides us with a straightforward way for manipulating these interactions. For instance, decorating a bare water surface with different kinds of surfactant molecules, changing their surface concentration, controlling the temperature and the ionic concentration of the aqueous medium are achieved by simple means. The air-water interface is thus an ideal template for guiding 2D self-assemblies of proteins. Recent years have witnessed the increased use of the air-water interface for growing 2D protein crystals. Inevitably, this has led to a considrable interest in the exploration of mechanism behind self-assembly of proteins at surfaces. However, the hierarchical structures at various length-scales and the associated large range of time-scales pose a big challenge to both experiments and computer simulation.

Here we report our experimental study at beamline **ID10B** on the mechanism of lysozyme monolayer growth at the air-water interface decorated with amphiphilic molecules (ETH^T4001). The protein was inserted into the aqueous subphase and the interface was monitored with the grazing incidence X-ray off-specular scattering (GIXOS) technique [1] in a time-resolved experiment keeping the incident angle fixed and measuring the scattering signal on a position sensitive detector as shown in Figure 60a. When the grazing angle is below the critical angle, the scattering signal carries the structural information from an interfacial layer of only ~7 nm thick. Figure 60b demonstrates the evolution of signal on the detector after protein injection into the subphase. The constantly changing signal clearly suggests the dynamic nature of the interface, which systematically evolves

towards equilibrium. The integrated signal intensity, Figure 60c, is marked with segmental evolution separated by kinks at various points during the growth.

The growth of a protein layer at the interface involves a multitude of processes such as protein adsorption, conformational changes, relaxation via the diffusion of proteins and therefore clustered domains within the interface are expected to occur at different time-scales. The sudden change in growth rate of integrated intensity thus can be understood in terms of a sequence of different dynamical processes. However, the main problem is to make a clear distinction between the intermediate steps. In this study, for the first time, we suggest a scheme to distinguish between adsorption and relaxation processes by simultaneously measuring surface pressure and diffuse X-ray scattering. The obtained protein coverage is shown in Figure 61a. In support of this study we performed another experiment using the grazing incidence X-ray fluorescence (GIXF) technique. In this geometry the fluorescence signal is only sensitive to protein adsorption to the interface and not to the structural relaxation at the interface. The sulphur signal in Figure 61 (b,c) is representative of lysozyme as its polypeptide chain contains 10 sulphur atoms. The counter-ion profiles (Figure 61d) evolve during the entire period of measurement, whereas the sulphur signal attains saturation. The changing counter-ion profile suggests that the protein layer constantly evolves even after protein coverage is saturated. The evolution at this stage is due to the relaxation of the layer through the diffusion of proteins or cluster of proteins along the interface.

Our study brings new insight into the mechanism of protein monolayer growth at the air-water interface. The time-resolved measurements provide ample evidence to suggest that the growth mechanism involves a sequence of processes characterised with different time-scales. In the hierarchy of evolution, protein adsorption is followed by relaxation via reorganisation of protein at the interface. It was demonstrated here that time-resolved GIXOS and GIXF together brings out crucial information to distinguish between adsorption and relaxation.

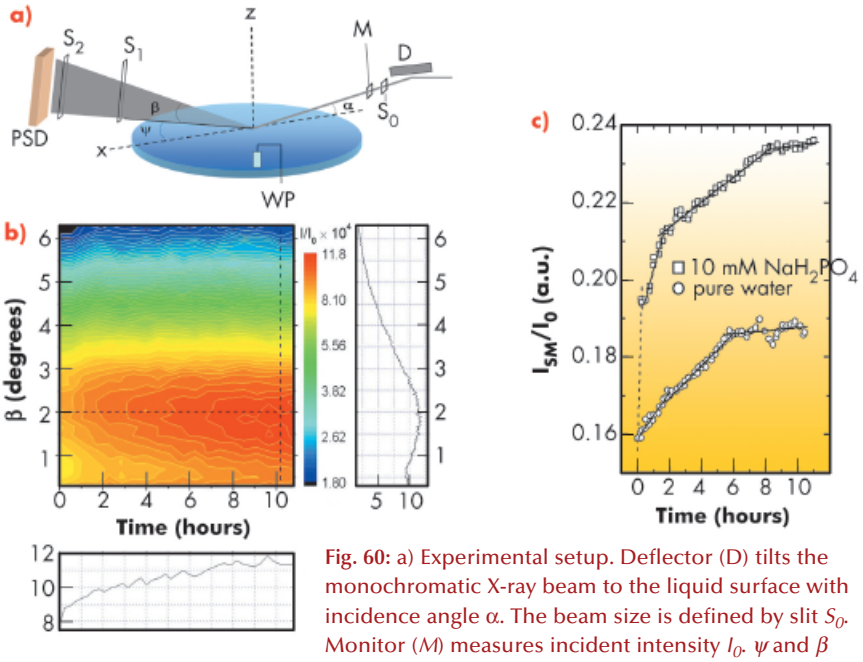

Fig. 60: a) Experimental setup. Deflector (D) tilts the monochromatic X-ray beam to the liquid surface with incidence angle α. The beam size is defined by slit S_0. Monitor (M) measures incident intensity I_0. ψ and β are in-plane and out-of-plane scattering angles. Long slits S_1 and S_2 define the horizontal resolution. PSD - position sensitive detector; WP - Wilhelmy plate. b) The 2D colour map represents the intensity evolution at PSD normalised on monitor. Vertical and horizontal slices of the 2D map corresponding to the dashed lines are on the right and bottom of the map. c) Evolution of intensity integrated on PSD.

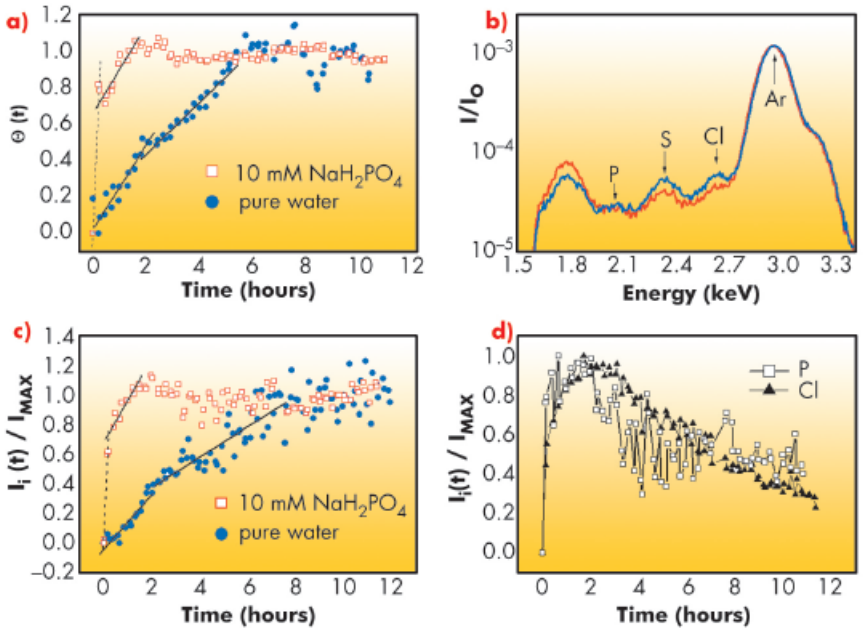

Fig. 61: a) protein coverage obtained from diffuse X-ray scattering, b) GIXF signal from the interface, c) the evolution of sulphur signal, d) the evolution of counter ions (Cl, P).

References
[1] S. Mora, J. Daillant, D. Luzet and B. Struth, *Europhys. Lett.*, 66, 694 (2004).

Authors
E. Schneck (a), R. Oliveira (b), D. Pink (c), O. Konovalov (d) and M. Tanaka (a).
(a) University of Heidelberg (Germany)
(b) University of Cordoba (Argentina)
(c) St. Francis Xavier University (Canada)
(d) ESRF

Crucial roles of charged saccharides in the survival of Gram-negative bacteria

The outer surface of Gram-negative bacteria displays a dense layer of saccharide chains connected to lipids, called lipopolysaccharides (LPSs). Since the removal or mutation of LPSs is known to result in the death of Gram-negative bacteria, LPSs are supposed to play crucial roles in the survival of bacteria against antimicrobial peptides. This finding inspires the design of various antibacterial compounds that primarily target LPSs. For example, cationic antimicrobial peptides (CAPs) have drawn increasing attention as alternatives to chemical food preservatives and commonly used antibiotics. To date, many *in vivo* studies demonstrated that divalent cations (Ca^{2+}, Mg^{2+}) significantly increase the survival rate of bacteria. However, the structural evidence from experimental approaches at the molecular level is still missing.

Here we reveal the influence of molecular structure (genetic mutation) and divalent cations on the survival of Gram-negative bacteria against cationic peptides like protamine. As the minimal experimental model of outer membranes of Gram-negative bacteria, we prepared the monolayers of LPSs purified from various bacterial strains at the air/water interface. The impact of mono- and di-valent ions and protamines on the fine structures of model membranes were probed by grazing-incidence X-ray diffraction (GIXD) and grazing-incidence X-ray scattering out of the specular plane (GIXOS) experiments at beamline **ID10B** (Figure 62a). GIXD enables one to gain the lateral ordering of hydrocarbon chains in the membrane plane, while GIXOS allows the determination of vertical electron density profiles perpendicular to the membrane plane.

Figure 62b shows the intensity integrated along q_z plotted as a function of q_{xy} for a deep rough mutant lipopolysaccharide (LPS Re) monolayer on a Ca^{2+}-loaded subphase. The measured GIXD signal exhibits a single peak with its maxima located at $q_z = 0$, indicating that the hydrocarbon chains of LPS Re molecules take an upright conformation and form a hexagonal lattice. In contrast, the GIXD signal measured at the same area per molecule showed no detectable peak in the absence of Ca^{2+}, suggesting that Ca^{2+} also increases the lateral ordering of hydrocarbon chains. This finding was supported by coarse-grained Monte Carlo (MC) simulations, suggesting that the LPS headgroups become more compact in the presence of Ca^{2+}.

GIXOS measured at an azimuthal angle near the incidence plane can be translated to the corresponding reflectivity curve within a significantly reduced radiation time (by a factor of 100). Figure 63a shows the reconstructed electron density profiles of the LPS Re monolayers on Ca^{2+}-free (blue) and Ca^{2+}-loaded (red) subphases, indicating that Ca^{2+} induces

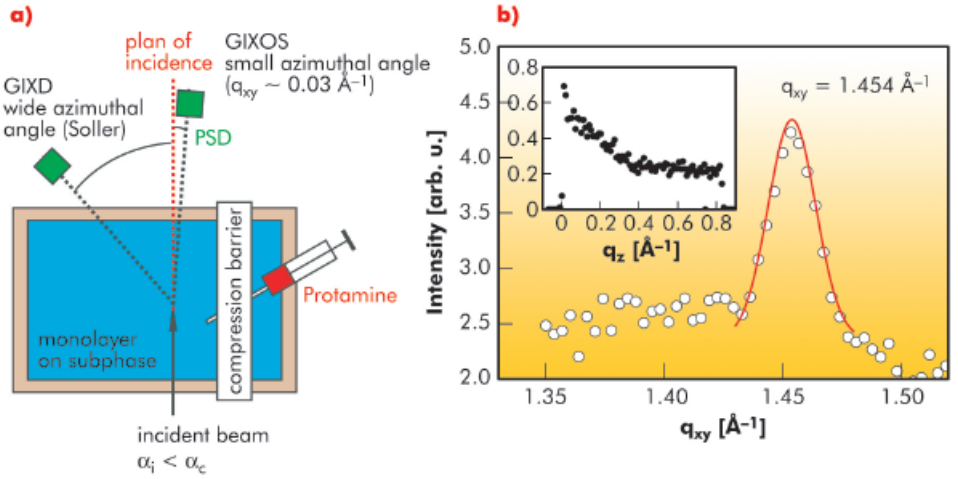

Fig. 62: a) Schematic illustration of the grazing incidence X-ray scattering setup at the air/water interface. b) The measured intensity integrated along q_z plotted vs. q_{xy}, and the intensity integrated along q_{xy} vs. q_z (inset).

an increase in headgroup electron density and/or a reduction in the roughness of the headgroup/water interface. MC simulations supported the experimental finding, suggesting that Na^+ ions in the charged saccharide region (called the Kdo core) are displaced in the presence of Ca^{2+} ions (Figure 63b). When protamine is injected beyond the survival level of bacteria, we observed the complete destruction of the LPS Re monolayers in the absence of Ca^{2+}. In contrast, the film remained completely intact in the presence of Ca^{2+}, suggesting that Ca^{2+} accumulated near the Kdo core generate an electrostatic barrier.

To highlight the crucial role of charged saccharides, we carried out the same series of experiments with the acid hydrolysis product without the Kdo core (Lipid A). The Lipid A monolayer is different from the LPS Re monolayer in that it does not stay fully intact against protamine even in the presence of Ca^{2+}, suggesting the crucial role of the Kdo core in bacterial survival. This finding agrees well with the fact that Lipid A is not sufficient for the growth of most of Gram-negative bacteria.

References
R. Oliveira *et al.*, *Phys. Rev. E* **81**, 041901 (2010).
E. Schneck *et al.*, *Proc. Natl. Acad. Sci.* **107**, 9147 (2010).
R. Oliveira *et al.*, *C. R. Chimie* **12**, 209 (2009).
E. Schneck *et al.*, *J. R. Soc. Interf.* **6**, S671 (2009).

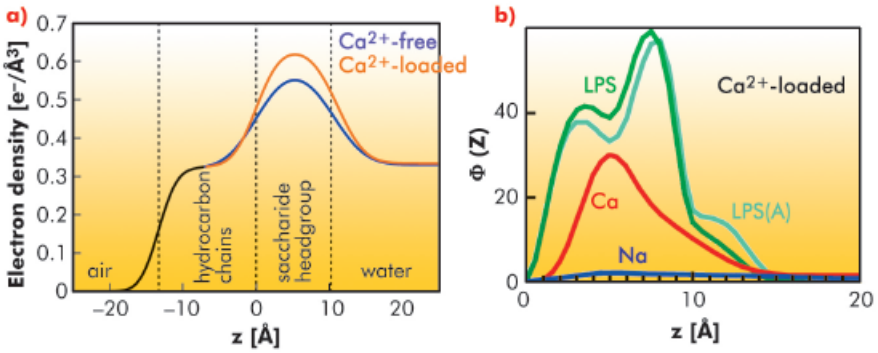

Fig. 63: a) Electron density profiles of LPS Re monolayers on Ca^{2+}-free (blue) and Ca^{2+}-loaded (red) subphase reconstructed from GIXOS. b) The number densities $\Phi(z)$ of saccharides (LPS), Na^+ ions (Na), and Ca^{2+} ions (Ca) on Ca^{2+}-loaded subphase calculated by MC simulations.

Biomimetic ultrahydrophobic surfaces for X-ray diffraction studies on biological solution droplets

Principal publication and authors
A. Accardo (a,b,c), F. Gentile (c,a), F. Mecarini (c,a), F. De Angelis (c,a), M. Burghammer (b), E. Di Fabrizio (c,a) and C. Riekel (b), *Langmuir*, **26**, 15057–15064 (2010).
(a) Center of Bio-Nanotechnology and Engineering for Medicine, University Magna Græcia, Catanzaro (Italy)
(b) ESRF
(c) Italian Institute of Technology, Genova (Italy)

The discovery of super-hydrophobic properties in plant leaves (Lotus effect) [1] has resulted in an intense effort for developing techniques that allow the generation of super-hydrophobic features. Applications of ultra-hydrophobic surfaces (UHS) range from self-cleaning, anti-fouling and anti-wetting textiles, flow-enhancement in microfluidic devices, and recently, even to the biomedical field [2]. Two smart and efficient micro-fabrication techniques have been developed within a collaboration project between the ESRF and two Italian nanofabrication facilities (BIONEM and IIT) to obtain ultrahydrophobic surfaces from commercial flat PMMA sheets with a high X-ray transmission (Figure 64a). The developed surfaces have been fabricated through either a two-step process comprising an optical lithography phase and a plasma etching phase or a single reactive ion etch attack. The similarity between these artificial surfaces and those existing in nature is striking (Figure 64 b,c). With such processing it is possible to make a ready-to-use device in just 12 minutes. Furthermore, the plasma etch technique makes it possible to process several surfaces at the same time.

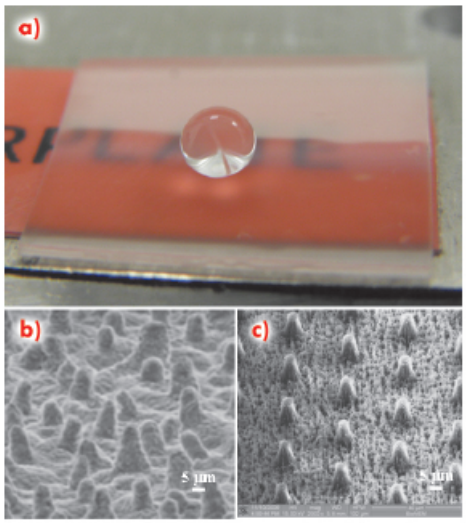

Fig. 64: a) PMMA ultra-hydrophobic surface; b) Features of a *Nelumbo Nucifera* lotus leaf; c) PMMA micro-structured surface.

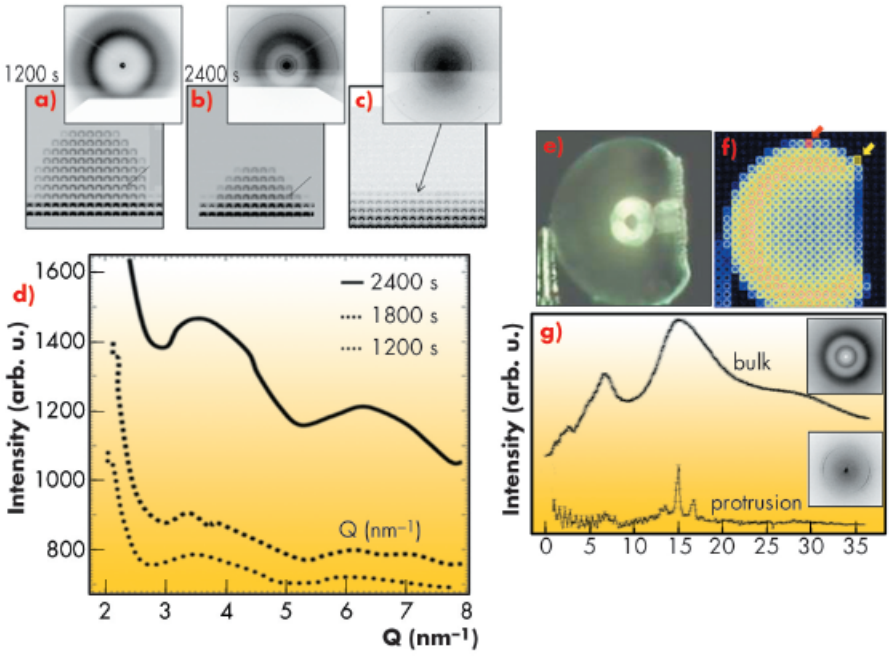

Fig. 65: a-c) Composite raster SAXS/WAXS images of drying lysozyme droplet; d) Azimuthally averaged pattern at selected times after the onset of the drying process; e) Optical image of solidified lysozyme solution droplet residual; f) composite image from 2D raster-scan; g) Upper curve: diffraction pattern from bulk of sphere (red rectangle/arrow in part (f)) and azimuthally averaged pattern. Lower curve: diffraction pattern from protrusion of sphere (yellow rectangle/ arrow in part (f)) and azimuthally averaged pattern.

There is currently significant interest in the study of self-assembly processes with the aim of creating novel templates for biofilm deposition, microassay chip manufacturing and other next-generation materials. Materials are usually deposited on surfaces through the drying of solution droplets but microscopic details on deposition processes are often lacking. We have now been able to show that the evaporation of lysozyme (and other biological molecules such as cytochrome C or synthesised peptides [3,4]) solution droplets on ultrahydrophobic PMMA surfaces results in the formation of easily detachable hollow residuals. This is due to the low interaction between the ultrahydrophobic substrate and the aqueous droplets. The process of evaporation of droplets of about 4 µl has been studied *in situ* by X-ray small- and wide-angle scattering techniques using a beam of about 1 µm (Figure 65 a-d). The SAXS patterns observed at different stages of the evaporation process agree well with simulated lysozyme solution scattering patterns, which is remarkable given the ultra-small volumes probed in a single exposure of < 0.8 pL. An analysis of the diffraction patterns of the solid residuals suggests that the bulk of these hollow residuals is composed of a mixture of about 1/3 < 20 nm nanocrystalline domains and 2/3 short-range order material (Figure 65 e-g). The particle size at the attachment points is about 5 times larger, which is probably due to a shearing process during evaporation.

The current experiments are a first step towards the integration of an electrode platform to move droplets by means of electrical fields. Indeed such ultrahydrophobic PMMA surfaces represent a potential near contact-free sample support for the study of homogeneous nucleation, chemical reactions and phase transformations in aqueous inorganic and organic solution droplets in combination with SAXS & WAXS µbeam techniques.

References

[1] C. Neinhuis and W. Barthlott, *Ann. Bot.* **79**, 667–677 (1997).

[2] F. Gentile, G. Das, M.L. Coluccio, F. Mecarini, A. Accardo, L. Tirinato, R. Tallerico, G. Cojoc, C. Liberale, F. De Angelis and E. Di Fabrizio, *Microelec. Eng.* **87**, 798-801 (2010).

[3] A. Accardo, F. Gentile, F. Mecarini, F. De Angelis, M. Burghammer, E. Di Fabrizio, C. Riekel, Microelec. Eng., DOI:10.1016/j.mee.2010.12.044 (2011).

[4] C.A.E. Hauser, R. Deng, A. Mishra, Y. Loo, U. Khoe, F. Zhuang, D.W. Cheong, A. Accardo, M.B. Sullivan, C. Riekel, J.Y. Ying, U.A. Hauser, PNAS, DOI:10.1073/pnas.1014796108 (2011).

Aligned polyfluorene blends

Phase behaviour and structure are essential factors in defining the physics and material properties of luminescent polymers such as polyfluorenes where attention is increasingly being devoted to larger scale structures incorporating intermolecular assemblies and the resulting microstructures. Bottom-up methods such as block copolymer synthesis have conventionally been used to study structures beyond the molecular level. While phase separation in such systems is constrained by the chemical bonds, blending two or more polymers into a single material expands the available parameter space and allows material properties to be tailored. Polymer blends can result in

materials that have complete miscibility or are macrophase separated.

Macroscopic alignment of polyfluorene blends controls the macroscopic anisotropy within the blend and is reflected in the anisotropic optical characteristics. An interesting example is provided by King *et al.* [1] who demonstrated how an oriented blend of polyfluorene PF2/6 and polyethylene can be used as a tool to track the orientation of singlet and triplet transition dipole moments.

Heeger *et al.* [2] combined blending with alignment and studied the structural formation of another luminescent polymer poly(phenylene vinylene) incorporated in polyethylene. These authors raised the fraction of the luminescent polymer up to 30 wt% and aligned the samples, and studied them using X-ray diffraction. They found that the 30 wt% blend forms a uniform mixture of crystallites in non-aligned samples but a uniform mixture of chains in aligned samples. This structure was denoted as an interstitial microfibre. It is not known whether these kinds of microfibre phenomena play a role in polyfluorene blends.

We carried out fibre X-ray diffraction (XRD) and grazing-incidence X-ray diffraction (GIXRD) of aligned PF2/6 on beamline **BM28** (XMaS) and reported the microstructure of an aligned blend. Our experiment aimed to provide a structural counterpart to the optical work of King *et al.* [1] who used a low polyfluorene fraction (< 0.7 wt%). Also, we aimed to provide the materials counterpart to the work of Heeger *et al.* [2] who used a different polymer and a high guest fraction. To cover the concentration regimes of both studies, the polyfluorene fraction was varied between 0.25 wt% and 15 wt%.

Figure 66 shows an optical fluorescence image and AFM topography of the aligned material. Figure 67 shows typical XRD patterns of the corresponding film giving information of aligned polyfluorene crystallites (reflections at lower *q*) within aligned polyethylene crystallites (reflections at higher *q*). The information of the degree of their mutual alignment (mosaic) is also obtained by considering the integrated intensities of the different diffraction peaks.

We distinguished two cases: if the polyfluorene fraction is high (7-15 wt%) the blend was found to be a macroscopically uniform mixture of aligned polyethylene and polyfluorene crystallites (with a coherence length ~30 nm); if the polyfluorene fraction was low (0.25 wt%), the blend behaves similarly but the coherence length was significantly decreased (~8 nm). The photoluminescence data indicate chains are located in the vicinity of each other. Therefore, the reduction in coherence length is understood to involve a decrease in crystallite size. Unlike the case of poly(phenylene

Principal publication and authors
M. Knaapila (a), H.L. Vaughan (b), T.P.A. Hase (c), R.C. Evans (d), R. Stepanyan (e), M. Torkkeli (f), H.D. Burrows (d), U. Scherf (g) and A.P. Monkman (b), *Macromolecules* **43**, 299-305 (2010).
(a) Institute for Energy Technology (Norway)
(b) Durham University (UK)
(c) Warwick University (UK)
(d) University of Coimbra (Portugal)
(e) DSM Research (The Netherlands)
(f) University of Helsinki (Finland)
(g) University of Wuppertal (Germany)

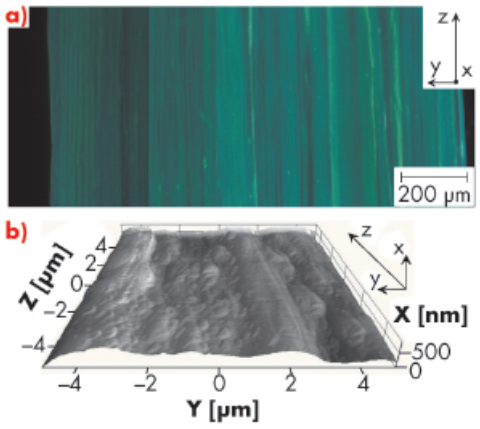

Fig. 66: An aligned polyfluorene blend: a) Optical fluorescence micrograph, photoluminescence of polyfluorene appears as bluish lines; b) AFM topography, aligned along the z axis.

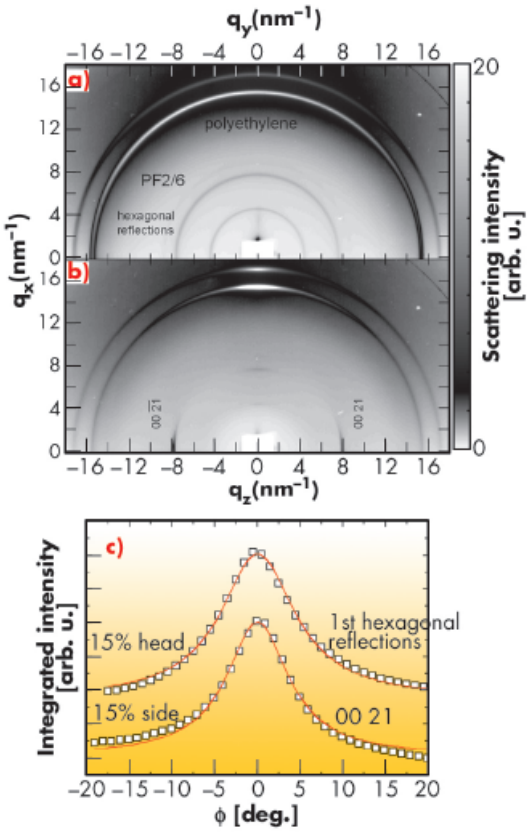

Fig. 67: XRD patterns of the aligned film measured with incoming beam a) parallel and b) perpendicular to the alignment direction, showing main reflections of both polymers. c) Integrated intensities of the main polyfluorene reflections. Φ is the angle between incident beam and y or z axes.

References
[1] S.M. King, H.L. Vaughan and A.P. Monkman, *Chem. Phys. Lett.* **440**, 268-272 (2007).
[2] C.Y. Yang, A.J. Heeger and Y. Cao, *Polymer* **41**, 4113-4118 (2000).

vinylene) [2], the crystallites are present in a very well aligned sample. This difference between the poly(phenylene vinylene) type polymer and polyfluorene can be explained in terms of compatibility, entanglement, and backbone stiffness. This kind of work provides an insight into the crystallite segregation in aligned polyfluorene blends. Similar blending and alignment procedures have been used for a diverse set of luminescent polymers but they have not, however, been studied by XRD.

This work required a high brilliance beam and advanced instrumentation that allowed us to work with small and thin films and very small polymer fractions. The importance of good control of the background scattering was also critical.

Principal publication and authors
P. Besenius (a), G. Portale (b), P.H.H. Bomans (c), H.M. Janssen (d), A.R.A. Palmans (a) and E.W. Meijer (a), *Proc. Natl. Acad. Sci. U.S.A.* **107**, 17888-17893 (2010).
(a) ICMS and MST, Eindhoven University of Technology (The Netherlands)
(b) DUBBLE, ESRF
(c) SMG, Eindhoven University of Technology (The Netherlands)
(d) SyMO-Chem (The Netherlands)

Controlling the growth and shape of chiral supramolecular polymers in water

Until recently, self-assembly in dilute aqueous environments has predominantly dealt with linear amphiphiles that form closed structures, such as spherical or cylindrical micelles, and vesicles. Morphological control in objects of defined size or shape is increasingly well understood. Surprisingly, however, the generality of these concepts has not been translocated into another area of increasing interest, namely, the self-assembly of one-dimensional arrays. The development of discotic monomers has proven to be a valuable route to allow the synthesis of rod-like supramolecular polymers that have potential applications in functional soft matter including electronics, sensing and regenerative medicine. Considering the enormous interest in such systems, it is surprising that efforts to control the size and shape of nano- and micrometre size one-dimensional objects are rare [1]. To manipulate the growth of aqueous one-dimensional supramolecular polymers, we have utilised electrostatic repulsive contributions in analogy to surfactant type self-assembly. However, rather than simply relying on solvophobic effects based on the lipophilic segments of the amphiphile, we have used noncovalent polymerisable moieties to craft building blocks that are designed to code for ordered supramolecular architectures.

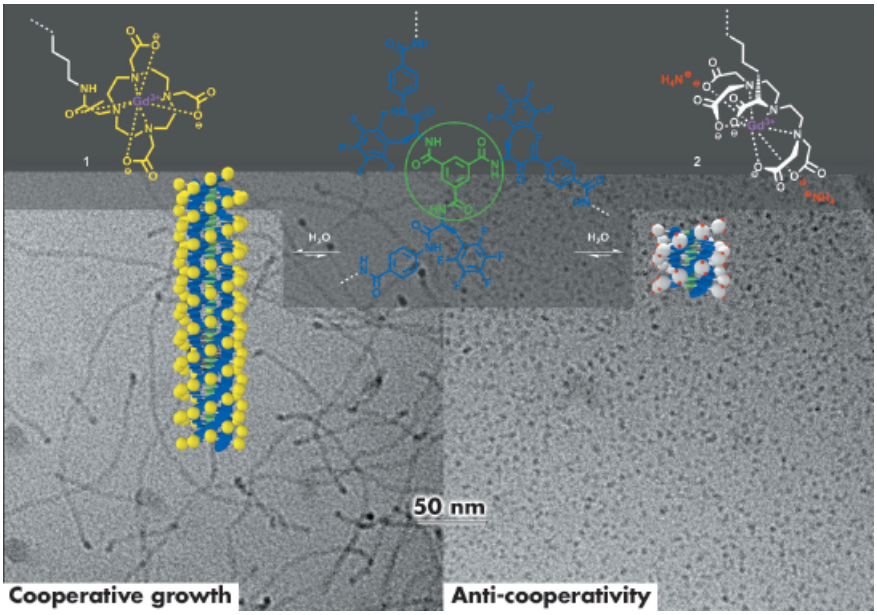

Fig. 68: Schematic representation of the self-assembly of the discotic amphiphiles **1** and **2**.

The molecular design of our self-assembling unit is based on the well-studied C_3-symmetrical benzene-1,3,5-tricarboxamide (BTA) core (Figure 68, depicted in green) that directs the self-assembly into triple hydrogen bonded helices. This moiety was extended with a fluorinated *L*-phenylalanine and an aminobenzoate spacer (Figure 68, depicted in blue), creating a hydrophobic pocket in the core of the discotic to shield the triple hydrogen-bonding motif. By increasing the ionic character of the peripheral Gd(III) complexes in the charge neutral discotic **1** to the negatively charged discotic **2**, we aimed at introducing frustration in the one-dimensional growth of the stacks. Cryo-TEM imaging at the Eindhoven University of Technology and small angle X-ray

scattering (SAXS) experiments on beamline **BM26B** revealed that it is possible to switch from elongated, rod-like assemblies to small and discrete objects (**Figures 68 and 69**), by balancing attractive non-covalent forces within the hydrophobic core of the polymerising building blocks with electrostatic repulsive interactions on the hydrophilic rim.

Furthermore, the concentration dependent aggregation process of rod-like stacks could be studied as suggested by SAXS profiles: at 0.25 mM of discotic **1**, rods of 23 nm in length and 6.2 nm in diameter are formed. At 0.5 mM the rod length is 27 nm and at 1 mM the length increases well above 75 nm. The order in the self-assembled objects and their growth mechanism were also characterised using circular dichroism, UV/Vis and ^{1}H-NMR spectroscopy. In line with our continuous efforts in elucidating the mechanisms of supramolecular polymerisations [2], we have focussed on correlating the morphological properties of the materials with the appropriate mechanistic details of the self-assembly pathways: cooperative growth of monomer **1** leads to very high molecular weight supramolecular polymers, whereas frustrated growth of discotic **2** and the resulting anticooperativity, results in the formation of small and discrete objects, without compromising their thermodynamic stability. The latter are very promising building blocks for the development of supramolecular magnetic resonance imaging (MRI) contrast agents.

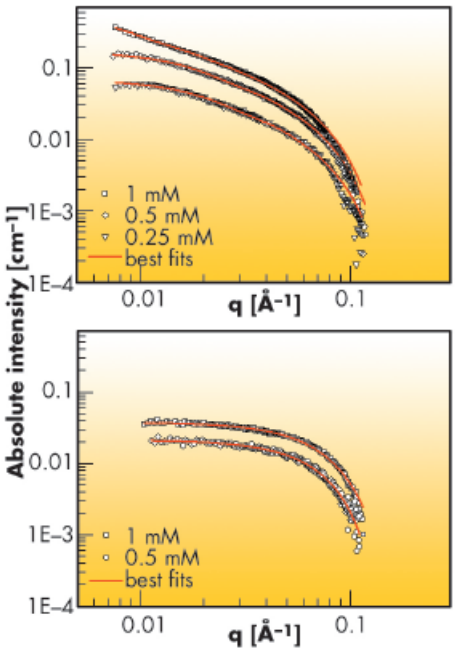

Fig. 69 SAXS profiles of the self-assembled discotics **1** (upper graph) and **2** (lower graph) at different concentrations.

This is a unique example for directional self-assembly in water whereby the supramolecular polymer shape and size can be dictated by Coulombic interactions. In analogy to many systems found in nature, mechanistic details of the self-assembly process emphasise the importance of cooperativity as a key feature that dictates the physical properties of the supramolecular polymers.

References
[1] L.C. Palmer, Y.S. Velichko, M. Olvera de la Cruz and S.I. Stupp, *Phil. Trans. R. Soc. A* **365**, 1417-1433 (2007).
[2] T.F.A. de Greef, M.M.J. Smulders, M. Wolffs, A.P.H.J. Schenning, R.P. Sijbesma and E.W. Meijer, *Chem. Rev.* **109** 5687-5754 (2009).

Ultrafast X-ray solution scattering reveals different reaction pathways in the photolysis of $Ru_3(CO)_{12}$ after ultraviolet and visible excitation

The triangular metal carbonyl cluster, $Ru_3(CO)_{12}$, plays an important role in photocatalysis and photoenergy conversion and has served as the paradigm for the photochemistry of transition metal carbonyls. However, detailed mechanisms for the photochemical reactions are rarely available, mainly due to the lack of efficient methods to study them. Ultrafast X-ray solution scattering has been shown to give information that is generally difficult to extract from ultrafast optical spectroscopy such as the time course of changes in bond lengths and angles, including those of short-lived intermediates, on a timescale of picoseconds to milliseconds [1]. Following this approach, our recent time-resolved X-ray solution scattering study on $Ru_3(CO)_{12}$ in cyclohexane excited at 390 nm revealed a new intermediate, $Ru_3(CO)_{10}$, that escaped detection in a previous spectroscopic study [2].

Principal publication and authors
Q.Y. Kong (a), J.H. Lee (b), K.H. Kim (b), J.H. Kim (b), M. Wulff (c), H. Ihee (b) and M.H.J. Koch (d), *J. Am. Chem. Soc.* **132**, 2600-2607 (2010).
(a) Synchrotron SOLEIL, GIF-sur-Yvette (France)
(b) Center for Time-Resolved Diffraction, Department of Chemistry, Graduate School of Nanoscience and Technology (WCU), KAIST, Daejeon (Republic of Korea)
(c) ESRF
(d) EMBL, Hamburg Outstation,EMBL c/o DESY, Hamburg (Germany)

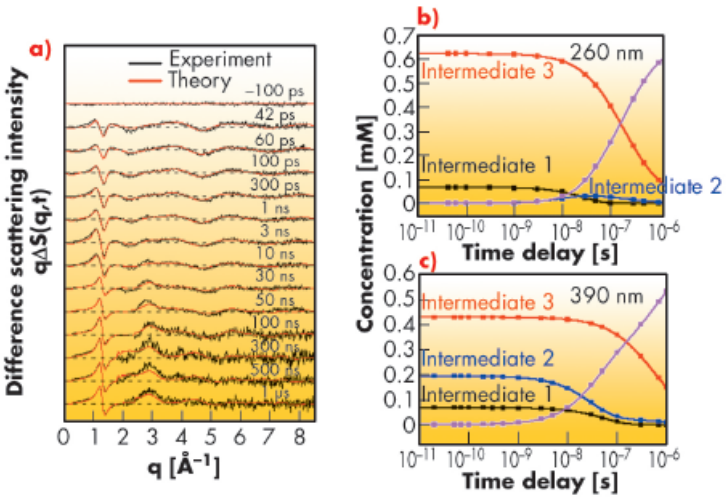

Fig. 70: a) Time-resolved difference scattering intensities $q\Delta S(q,t)$ as a function of time delay after photolysis of $Ru_3(CO)_{12}$ in cyclohexane at 260 nm. The black curves correspond to the experimental data and the red curves to the least-squares fits. Comparison of the time course of the concentration changes of intermediates 1 (black), 2 (blue) and 3 (red) during the photoreaction of $Ru_3(CO)_{12}$, after excitation b) with 260 nm and c) with 390 nm.

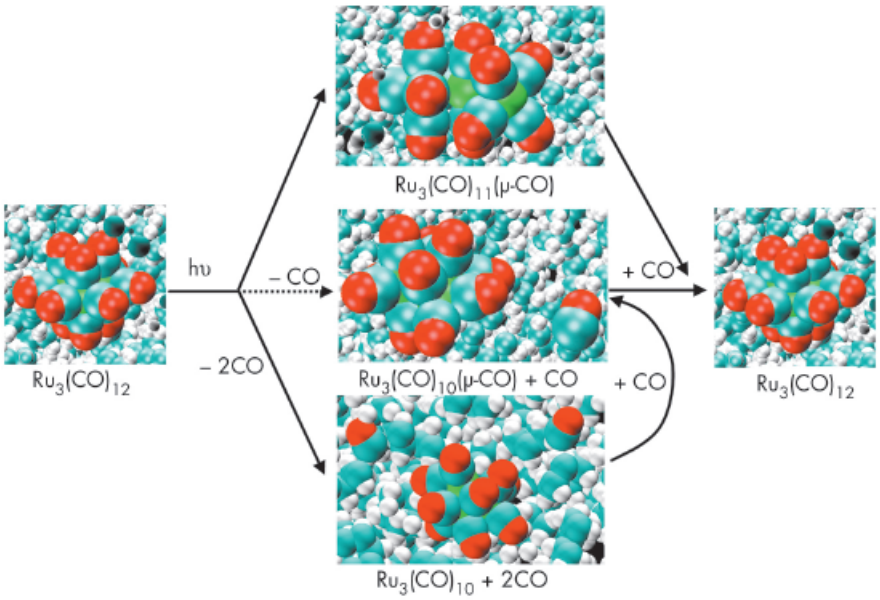

Fig. 71: Ultrafast X-ray solution scattering reveals different reaction pathways in the photolysis of $Ru_3(CO)_{12}$ at 260 nm and 390 nm. The major difference in the photolysis at 260 nm and 390 nm is due to $Ru_3(CO)_{10}(\mu\text{-CO})$. After excitation at 260 nm, it is formed from $Ru_3(CO)_{10}$ by recombination with a free CO, whereas, after excitation at 390 nm, it is formed from the starting molecule $Ru_3(CO)_{12}$ at the onset of the reaction. The commonality of the reaction between 260 nm and 390 nm excitation is the formation of $Ru_3(CO)_{10}$ as the major photoproduct. In the figure, the solid arrows show the reaction pathways at 260 nm, while solid plus dash arrows show the reaction pathways at 390 nm.

References

[1] T.K. Kim, J.H. Lee, M. Wulff, Q.Y. Kong and H. Ihee, *ChemPhysChem* **10**, 1958-1980 (2009).

[2] Q.Y. Kong, J.H. Lee, A. Plech, M. Wulff, H. Ihee and M.H.J. Koch, *Angew. Chem., Int. Ed.* **47**, 5550-5553 (2008).

The UV-vis spectrum of $Ru_3(CO)_{12}$ in cyclohexane has two prominent absorption bands: the first centered at 390 nm and the second with a peak at 238 nm and an absorption shoulder at 260 nm. Electronic absorption studies indicate that the lower energy band at 390 nm originates from the electronic transition $\sigma\rightarrow\sigma^*$ in metal d-orbitals, resulting in heterolytic cleavage of one of the Ru-Ru bonds. The short-wavelength absorption band in the UV range has been attributed to metal to ligand charge transfer (MLCT) which ultimately results in loss of one carbonyl group in solution. Ultrafast X-ray solution scattering illustrated that these different absorption processes lead to distinct photofragmentation pathways when $Ru_3(CO)_{12}$ is excited by different wavelengths. The photodissociation of $Ru_3(CO)_{12}$ dissolved in cyclohexane was studied on beamline **ID09B** employing a pump-probe experimental setup. Ultraviolet (260 nm) and visible (390 nm) laser pulses (2 ps) were used for excitation and 100 picosecond X-ray pulses for probing the transient intermediates. In these experiments, the sample flows through a nozzle that produces a layer of liquid of 300 µm thickness. The pump-probe sequence is repeated with different time delays between pump and probe at a frequency of 986.3 Hz and the scattered signal is accumulated on a MarCCD detector. The difference X-ray scattering intensities ($q\Delta S(q,t)$) illustrating the structural changes due to the laser excitation are shown in Figure 70a as a function of different time delays.

Time-resolved X-ray solution scattering on photolysis of $Ru_3(CO)_{12}$ in cyclohexane at 260 nm and 390 nm reveals different photodissociation pathways. Upon UV excitation at 260 nm, at the onset of the reaction, the species formed are only $Ru_3(CO)_{11}(\mu\text{-CO})$ for the metal-metal cleavage channel and the intermediate $Ru_3(CO)_{10}$ with 2 CO loss. In the course of the reaction, the major photoproduct $Ru_3(CO)_{10}$ then recombines with a free CO to $Ru_3(CO)_{10}(\mu\text{-CO})$, which eventually decays into the starting molecule $Ru_3(CO)_{12}$ by recombination with another CO (Figure 70b). After excitation at 390 nm, three intermediates are formed from the initial molecule $Ru_3(CO)_{12}$ at the onset of the reaction: $Ru_3(CO)_{11}(\mu\text{-CO})$, $Ru_3(CO)_{10}(\mu\text{-CO})$ with bridged CO and $Ru_3(CO)_{10}$ with terminal CO only (Figure 70c). The different photofragmentation pathways of $Ru_3(CO)_{12}$ in cyclohexane upon UV excitation presumably originate from the higher photon energy which favours the simultaneous loss of two CO leading to $Ru_3(CO)_{10}$ only for the CO loss reaction channel at the onset of reaction (Figure 71).

New results may help stop age-related macular degeneration at the molecular level

Principal publications and authors
A.I. Okemefuna, L. Stach, S. Rana, A.J. Ziai Buetas, J. Gor, R. Nan, A. Miller and S.J. Perkins, *The Journal of Biological Chemistry* **285**, 1041-1052 (2010); *The Journal of Biological Chemistry* **285**, 1053-1065 (2010).
Research Department of Structural and Molecular Biology, University

Age-related macular degeneration, or AMD, is painless but affects the macula, the part of the retina that allows one to see fine detail. The earliest hallmark of AMD is the appearance of protein, lipid and zinc deposits under the retinal pigment epithelial cells. These yellowish deposits are usually discovered by an ophthalmologist during routine eye tests and are commonly known as "drusen". AMD is the number one cause of vision loss in the elderly, causing 57% of blindness in the UK alone.

A key insight into the molecular beginnings of AMD was obtained by determining how two key proteins interact normally to prevent the onset of the condition. By the use of a multidisciplinary strategy that included X-ray scattering at beamline **ID02**, researchers at UCL clarified for the first time how an abundant blood protein called complement Factor H (of innate immunity) binds with another protein called C-reactive protein, to reduce the potentially damaging effects of an overactive immune system. In the eye, during ageing processes, cells will die naturally for all sorts of reasons. In conditions of high inflammation, at the same time as the levels of C-reactive protein in the retina increase dramatically, uncontrolled complement activity may cause damage to the retina. It is mostly the debris of broken up retinal cells that is deposited as drusen. The role of C-reactive protein is to coat these damaged cells, while the importance of factor H is to slow down high inflammation.

The interaction between factor H and C-reactive protein was previously hindered by a lack of understanding of their solution properties. For unbound C-reactive protein, X-ray scattering, analytical ultracentrifugation and surface plasmon resonance showed that pentamers and decamers were formed in solution with the same dissociation constant at 16-23 μM (Figure 72). The study emphasised the importance of working with 2 mM calcium and 140 mM NaCl in order to avoid protein denaturation, especially after the immobilisation procedure used in surface plasmon resonance. For Factor H, scattering and ultracentrifugation has already shown that Factor H formed dimers, trimers and higher oligomers in addition to the major monomer form.

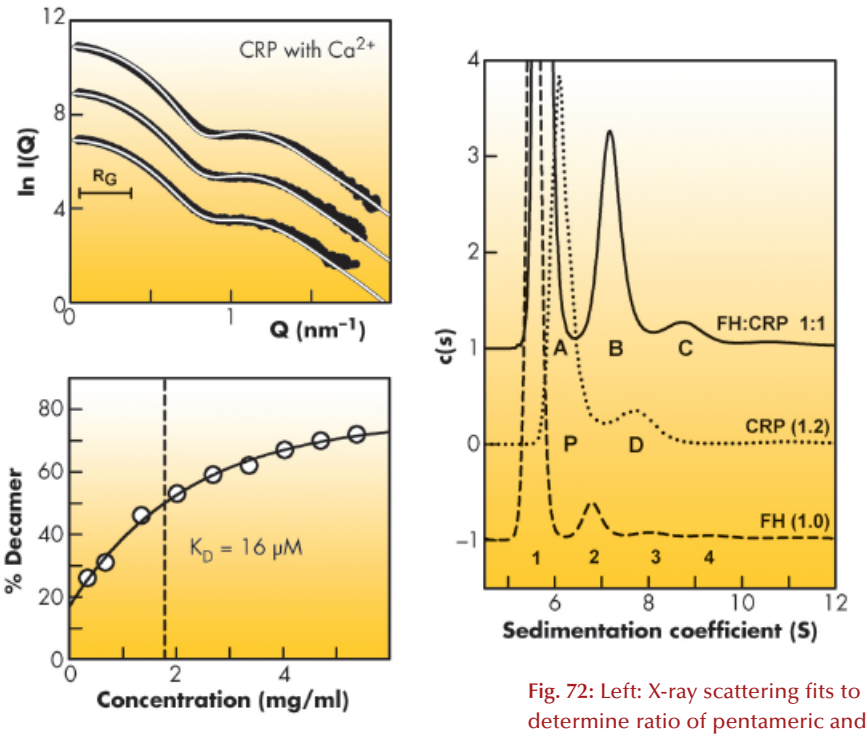

Fig. 72: Left: X-ray scattering fits to determine ratio of pentameric and decameric C-reactive protein starting from the two crystal structures. The resulting dissociation constant K_D is shown underneath the curve fit. Right: Analytical ultracentrifugation of the complex of factor H and C-reactive protein. The size distribution analyses c(s) are shown, in which the peaks 1, 2, 3 and 4 in factor H and peaks P and D for C-reactive protein are replaced by new peaks A, B and C when the two proteins were mixed.

On mixing the two proteins together, ultracentrifugation showed that decamer and dimer/trimer formation in the two proteins was suppressed (Figure 72), proving that the proteins interact, but only in the right buffer with undenatured proteins. Surface plasmon resonance confirmed the interaction with a dissociation constant of 4 μM. Scattering showed conformational changes that occurred when the proteins were mixed. Two molecules of C-reactive protein bind to Factor H at two different sites. It was then found that a common genetically modified form of Factor H (with His402) does not bind to C-reactive protein as

well as the normal form (with Tyr402) (Figure 73). People with modified Factor H are more vulnerable to an immune system attack in the eye and, thus, drusen may build up.

While there is no known cure for AMD, existing therapies aim to treat the symptoms and delay progression. The new biophysical results revealed from this work clarified one of the major molecular interactions that had proven hard to unravel by other immune techniques.

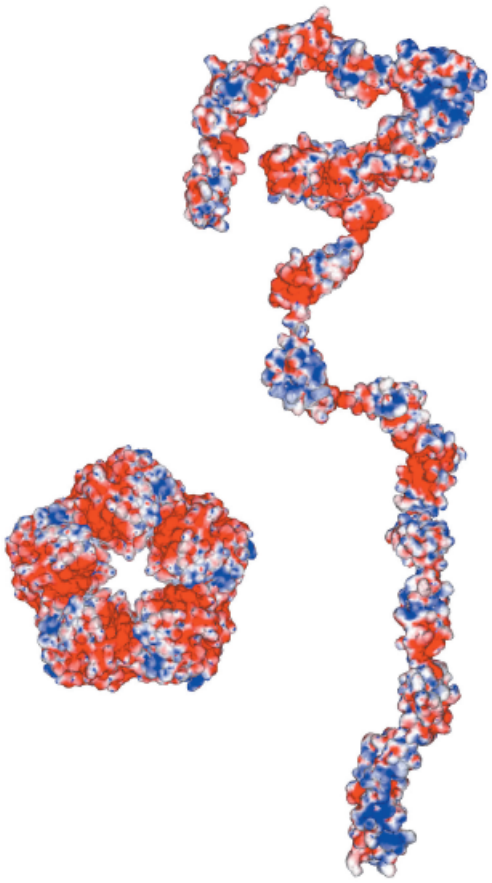

Fig. 73: Electrostatic surfaces of complement factor H with 20 SCR domains, a regulator of the innate immune system, and the C-reactive protein pentamer, the classic acute phase protein. Red denotes acidic regions while blue denotes basic regions. Both proteins are drawn to the same scale. The factor H solution structure was determined by constrained X-ray scattering modelling, while the C-reactive protein structure was determined from protein crystallography.

Electronic structure and magnetism

Looking back at the year 2010 gives us an opportunity to present a selection of exciting results arising from work at the Electronic Structure and Magnetism group beamlines. We can reflect on how these results offer promise for the future. Similarly, it is timely to look forward to improvements to the experimental facilities, their upgrade began in 2010, and will undoubtedly provide many more research Highlights.

The pursuit of basic research and understanding its place in creating technologies of the future are essential ingredients in the articles selected for this year's Highlights. The article by Mannini *et al.* (page 64) on molecular magnets presents as a goal of these studies the creation of devices at the molecular level for magnetic, electronic, photonics and sensor applications. This is also reflected in the article by Arrio *et al.* (page 65), which presents results on a photomagnetic molecular magnet. The switching of such materials using light, temperature, electrical or magnetic stimuli represents one of the most interesting current directions in the search for scaled down devices.

The quest for room temperature dilute magnetic semiconductors, Edmonds *et al.* (page 67), is another example of basic research contributing to the materials of the future. This could, in particular, have an impact on the future magnetic recording and storage devices.

The interest in interfacial studies has its roots also in the possibility of tailoring new functionality. Many new phenomena, of potential applied use, are also being observed at interfaces. Conducting layers produced at the interface between insulators is one dramatic example [1]. In the article by Garcia-Barriocanal *et al.* (page 68), the authors show how X-ray spectroscopy can highlight the subtle electronic structure changes that occur at interfaces and help to understand and control the properties at such interfaces.

Other materials of resurgent interest are the multiferroics. The article by Fabrizi *et al.* (page 70) shows how X-ray magnetic scattering can help in understanding their domain structure, which is important for their use in real devices of the future.

Much of the research also addresses current problems and there are many examples in this year's Highlights. Understanding the chemistry of actinides in our environment is of great importance to the nuclear industry (Galbis *et al.*, page 71) and appreciating how materials remove heavy metals during the gasification of coal (page 73) is of clear environmental interest.

Turning to the evolution of our research facilities, the past year has seen the closure of BM29 and ID24 for a major refurbishment as part of the ESRF Upgrade Programme. The standard EXAFS part of the new ID24/BM23 complex has been rebuilt and now enters the commissioning phase, with user operation recommencing in the first half of 2011.

BM23 is optimised for standard EXAFS in transmission geometry in a large energy range (4-75 keV) and in addition acts as a user/in-house EXAFS/XRD rapid access facility for sample characterisation. It complements the solid platform of highly specialised XAS/XES beamlines, allowing the ESRF to offer a complete spectrum of X-ray absorption spectroscopy techniques, an offer unequalled in Europe. Examples of Highlights from BM29 can be seen in the articles by D'Angelo *et al.* (page 74) and Poulston *et al.* (page 73).

Commissioning the new ID24 dispersive EXAFS stations will start in mid-2011. The facility will provide optimised branches for small and large spot activities. The new complex will focus on investigating solid and molten matter at extreme conditions of pressure, temperature and magnetic fields using *in situ* static and dynamic XAS. We will provide the users community with the first "*in situ*" laser heating facility optimised for X-ray absorption spectroscopy. This facility will address fundamental questions such as understanding the local structure of molten metals at high pressure, and the kinetics of chemical reactions at extreme conditions. Applications will cover hot topics in geophysics such as the partitioning

of Fe in the upper/lower mantle (see Highlight article Andrault *et al.*, page 75), to the synthesis and characterisation of new materials for extreme environments, such as those envisaged for fusion reactors.

From the perspective of the chemical sciences, the new beamlines offer much. In particular, the small spot branch of ID24 will offer new opportunities for tackling the time-resolved study of homogeneous chemical reactions and aspects of solid-state chemistry. The large spot branch will be equipped with an infrared spectrometer equipped with a novel optical system providing a unique hub for the continuing exploitation of dispersive EXAFS/infrared measurements in the fields of catalysis and related disciplines. Most notably a combination of step scan infrared and ultrafast dispersive EXAFS measurements together with photo-excitation or laser heating will offer a unique possibility for studying fundamental aspects of thermally or photon driven catalysis and solid state chemistry on the milliseconds to nanoseconds timescales. An example of highlight work in this area can be found in the article by Newton *et al.* (page 37) in the chapter on Structure of materials.

N.B. Brookes

References

[1] See for example: H. Chen, A.M. Kolpak and S. Ismail-Beigi, *Advanced Materials* **22**, 2881 (2010) and references therein.

Authors

M. Mannini (a), G. Poneti (a), L. Margheriti (a), Ph. Sainctavit (b), A. Dei (a) and R. Sessoli (a).

(a) Department of Chemistry "Ugo Schiff" & INSTM research unit, University of Florence (Italy)

(b) Institut de Minéralogie et de Physique des Milieux Condensés, CNRS, Université Pierre et Marie Curie, Paris (France)

Investigation of electronic structure and magnetism of bistable molecules with X-ray absorption

Molecular material science, developed in the last century for electronics, photonics and sensors applications, is currently moving towards the scaling down of devices to the single molecule level. For this, a single molecule, or a series of them, has to be integrated into the hybrid nanostructure of the device. Moving from the bulk to the single molecule requires analytical tools with appropriate sensitivity. Synchrotron light has great potential for this through the use of X-ray absorption-based spectroscopy (XAS) techniques. Here we summarise the results of the experiments carried out at beamline **ID08** on two classes of molecular systems, a molecular nanomagnet [1] and a valence tautomeric system [2], characterised respectively by a molecular magnetic memory effect and light and temperature induced switching of the magnetic and electronic properties.

One of the simplest and most frequently studied molecular nanomagnets is obtained by assembling a single terbium (III) ion with two phthalocyanine molecules ($TbPc_2$) in the double decker neutral structure shown in Figure 74. This molecule, at cryogenic temperatures, features a magnetic hysteresis - hence the name single molecule magnet - and the origin of this behaviour is related to the magnetic anisotropy of the single molecule. $TbPc_2$ can be evaporated and assembled in a quasi-crystalline structure depending on the thickness of the film, as we have recently demonstrated [3]. The measurement of the amplitude of the dichroic contribution at the Tb $M_{4,5}$ edge (shown in Figure 74) as a function of the applied magnetic field yields the magnetisation curve of this molecular system, clearly evidencing the presence of slow dynamics in the magnetisation that depends on the orientation of the film with respect to the external field.

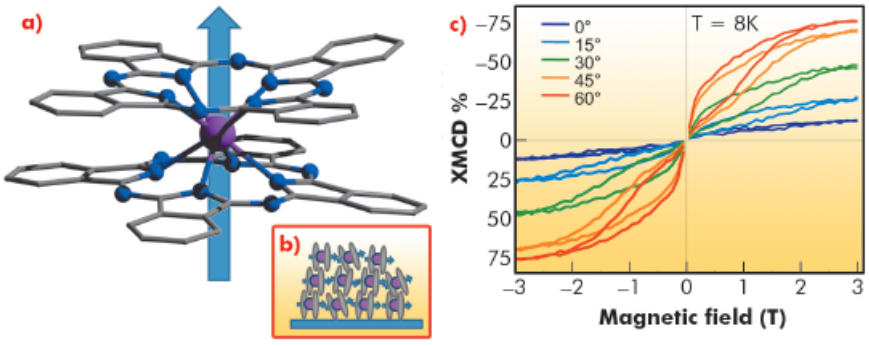

Fig. 74: a) Structure of the $TbPc_2$ system; b) its assembly in a thick film deposited on Al_2O_3. c) Angular dependence of the X-ray magnetic circular dichroism (XMCD)-detected hysteresis loops measured at 8K for the thick film.

This effect originates from the molecular arrangement: $TbPc_2$ assembles in a standing configuration with the easy-axis of the magnetisation parallel to the surface, as confirmed using linear polarised light in an X-ray natural linear dichroism (XNLD) experiment [3]. Different behaviour is observed for a monolayer deposited on gold, where the molecules assemble in the lying-down configuration, with the easy-axis of the magnetisation perpendicular to the surface.
In this case the magnetisation dynamics are faster.

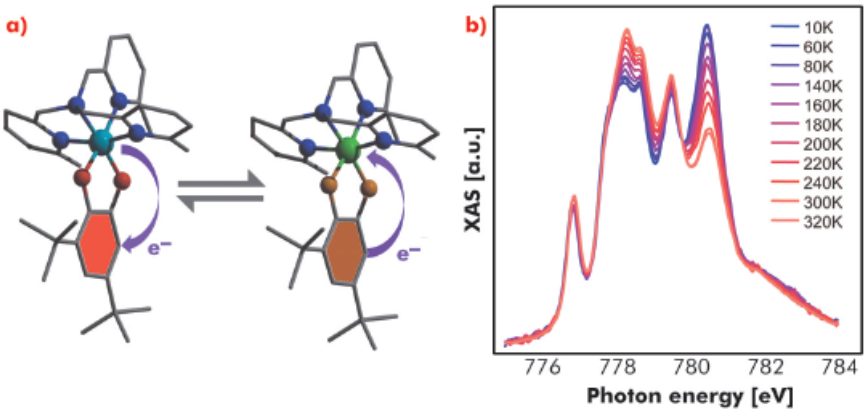

Fig. 75: a) Structure of the Co-Diox system and representation of the valence tautormerism. b) Co L_3 XAS spectra of the Co-Diox system as a function of temperature.

Another intriguing class of molecules studied at ID08 belongs to the Co-dioxolene (Co-Diox) family. These systems display temperature-, pressure- or light-driven intramolecular electron transfer between the metallic core and the surrounding dioxolene ligand, resulting in the possibility of switching their electronic configuration with an external stimulus. The states involved in this valence tautomerisation process – low spin-Co^{III}-catecholate, diamagnetic and dominant at low temperature, and high spin-Co^{II} – semiquinonate, paramagnetic and favoured at high temperatures – can be directly followed in an XAS experiment. It was possible to follow the tautomerisation of the Co-Diox system as a function of temperature by measuring the fine structure of the Co L_3 absorption edge (Figure 75). The light induced switching of the molecules to high spin-Co^{II} at low temperature could be triggered by IR laser light. An analogous process has been found to arise from X-ray irradiation, suggesting the existence of an additional mechanism for the photo-induction [4].

Both experiments represent key steps towards the use of X-rays as fundamental tools to study technologically important and innovative molecular based materials for use in future high-tech devices.

References
[1] D. Gatteschi, R. Sessoli and J. Villain *Molecular nanomagnets*, Oxford University Press, Oxford, UK (2006).
[2] A. Dei, D. Gatteschi, C. Sangregorio and L. Sorace, *Acc. Chem. Res.* **37**, 827-835 (2004).
[3] G. Poneti, M. Mannini, L. Sorace, P. Sainctavit, M.-A. Arrio, E. Otero, J.C. Cezar and A. Dei, *Angew. Chem. Int. Ed.* **49**, 1954-1957 (2010).
[4] D. L. Margheriti, D. Chiappe, M. Mannini, P.-E. Car, P. Sainctavit, M.-A. Arrio, F.B. de Mongeot, J.C. Cezar, F.M. Piras, A. Magnani, E. Otero, A. Caneschi and R. Sessoli, *Adv. Mater.* **22**, 5488-5493 (2010).

Photomagnetic molecular magnet

One of the current challenges in magnetism is the design of nanometric magnetic materials, such as thin films, nanoparticles and high spin molecules. The advantage of developing molecular magnets is their well-defined sizes and the flexibility of the constituent metal ions. During the last decade, the field of molecular magnetism has been driven by tailoring molecular magnets that could be activated by external parameters such as temperature, light irradiation or pressure [1]. The family of Prussian blue analogues is of particular interest with the recently synthesised copper octacyanomolybdate presenting interesting photomagnetic properties.

Indeed the molecular system goes from a non-magnetic (paramagnetic behaviour) to a magnetic state. The molecules undergo a reversible magnetic transition under light irradiation for which the origin remains puzzling.

We will focus on $[Mo(CN)_6(CN\text{-}CuL)_2]$, L being N,N',dimethyl ethylene diamine (labelled $MoCu_2$-Meen). Before irradiation, the molecules behave as uncoupled Cu^{II} paramagnetic ions (with central S=0 diamagnetic Mo^{IV} ion) whereas after irradiation (405 nm) they behave as superparamagnetic molecules with one Cu^{II} ions coupled

Principal publication and authors
M-A. Arrio (a), J. Long (b), C. Cartier dit Moulin (b), A. Bachschmidt (b), V. Marvaud (b), A. Rogalev (c), C. Mathonière (d), F. Wilhelm (c) and Ph. Sainctavit (a), *J. Chem. Phys C.* **114**, 593–600 (2010).
(a) Institut de Minéralogie et de Physique des Milieux Condensés, CNRS/UPMC/IPG/IRD, (France)
(b) Institut Parisien de Chimie Moléculaire, CNRS/UPMC (France)
(c) ESRF
(d) Institut de la Matière Condensée de Bordeaux, CNRS/Université Bordeaux 1 (France)

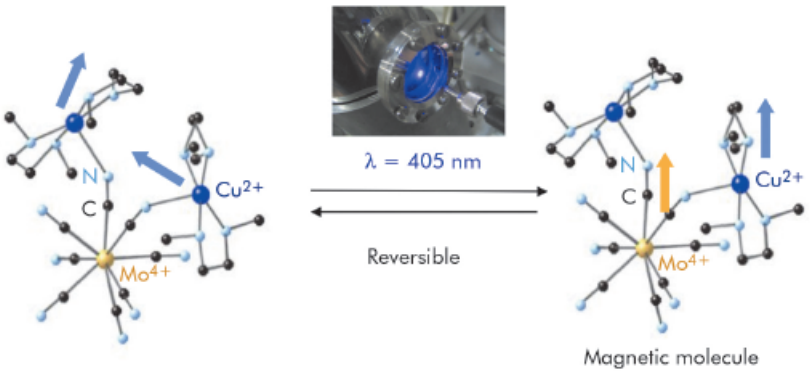

Fig. 76: Photomagnetic transition schema of the $MoCu_2$-Meen molecule. Photoconversion occurs with a laser (405 nm) installed in front of the viewport (see the image) or directly by the X-ray photons.

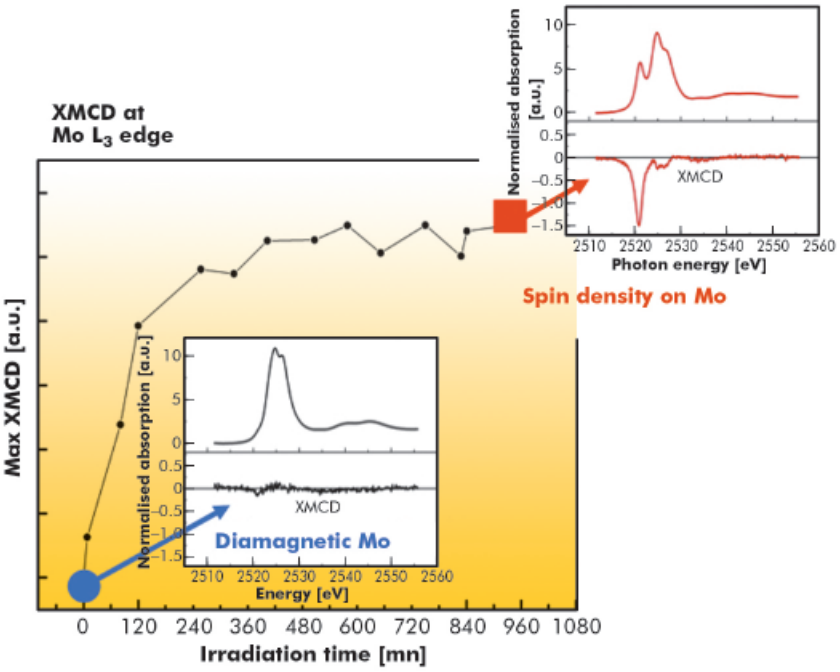

Fig. 77: Time dependant XMCD measurements at the Mo L_3 edge. The maximum intensity of the XMCD signal is drawn as a function of time. The blue dot is the XMCD measurement at time zero (no irradiation). The red square is the XMCD measurement for complete photoconversion of the molecule (after 15 hours).

to the molybdenum ion (see Figure 76). The commonly proposed mechanism based on classical SQUID measurements is a photoinduced charge transfer from Mo^{IV} (S = 0) to Cu^{II} (S = 1/2) leading to the formation of Mo^{V} (S = 1/2) and Cu^{I} (S = 0) with strong ferromagnetic coupling between the other Cu^{II} spin carriers.

X-ray magnetic circular dichroim (XMCD) spectroscopy provides a unique tool to identify the magnetic states of the different metallic ions. In this highlight we present Mo $L_{2,3}$ edge measurements that probe the 4d electronic occupation and magnetic state. XMCD gives the oxidation state and the spin state of the molybdenum ion. Beamline **ID12** is unique in that it can provide circular polarisation at Mo $L_{2,3}$ edges. We used its EMPHU undulator that emits flexible polarisation (circular left and circular right).

At this energy range (2500-2610 eV) the polarisation rate delivered by the Si(111) double crystal monochromator is very low: it drops down to about 12% at the Mo L_3 edge (2523 eV) and 4% at the Mo L_2 edge (2629 eV). The difficulty of the experiment resides also in the particular low X-ray flux configuration that we adopted to avoid radiation damage: ESRF 4-bunch mode and 25-µm thick aluminium foil inserted upstream.

X-ray and laser (405 nm) induced photomagnetic phases were both studied by XMCD and found to be essentially identical. We measured the XMCD spectrum in a magnetic field of ± 6 T and at 10 K before and after photoconversion.

Figure 77 shows the XMCD signal before and after irradiation. Before irradiation, no signal is found as expected for the spin zero Mo^{IV} ion. After irradiation, the measured XMCD signal shows the molybdenum magnetic transformation. The mainly negative XMCD signal shows that the Mo spin is in the direction of the magnetic field. After careful normalisation of the spectra, we extracted the oxidation state and magnetic spin moment of molybdenum. We found that the molybdenum photomagnetic state is S = 1 high spin Mo^{IV}: the two electrons of Mo^{IV} ($4d^2$) are in two different non degenerate 4d orbitals and gives an S = 1 spin. There is no change in the oxidation state of the Mo ions and the only way to explain the existence of spin density evidenced by the XMCD signal is to suppose the formation of high spin Mo^{IV} (S = 1) entities. Under such a hypothesis, the X-ray photo-induced species would be $Mo(HS)^{IV}Cu^{II}_2$–Meen (HS = high spin). This new experimental finding has been supported by a very recent theoretical model developed by Carvajal *et al.* [2].

Our XMCD measurements have established the presence of an unsuspected high spin Mo^{IV} species that has never been observed before. This might explain highly energetic photomagnetic properties and pave the way towards the understanding of molybdenum based photomagnetic compounds. Such a magnetic characterisation could only be done by XMCD measurements.

References
[1] O. Sato, *J. Photochem. Photobio. C: Photochem. Rev.* **5**, 203-223 (2004).
[2] M.-A. Carvajal, M. Reguero and C. de Graaf, *Chem Com.* **46**, 5737-57399 (2010).

Element-specific magnetism across the metal-insulator transition in (Ga,Mn)As

Principal publication and authors
P. Wadley (a), A.A. Freeman (a,b), K.W. Edmonds (a), G. van der Laan (b), J.S. Chauhan (a), R.P. Campion (a), A.W. Rushforth (a), B.L. Gallagher (a), C.T. Foxon (a), F. Wilhelm (c), A.G. Smekhova (c) and A. Rogalev (c), *Phys. Rev. B* **81**, 235208 (2010).
(a) School of Physics and Astronomy, University of Nottingham (UK)
(b) Diamond Light Source (UK)
(c) ESRF

Substitution of Mn into the semiconductor GaAs leads to some remarkable and closely correlated effects on its electrical and magnetic properties (Figure 78). At Mn concentrations above around 1%, ferromagnetic ordering takes place below a critical temperature T_C, while a transition from insulating to metallic conductivity occurs at around 2% Mn doping. The important role of charge carriers in coupling together the spins of distant Mn ions has been highlighted in experiments showing a control of T_C using electric fields [1]. This potentially offers new applications at the interface between microelectronics and spintronics. However, the occurrence of magnetic order on both sides of the metal-insulator transition is a long-standing puzzle and a subject of considerable recent debate. The detailed origins of the transition and accompanying stepwise changes in electronic and magnetic properties are poorly understood.

To address this issue, we performed an X-ray magnetic circular dichroism (XMCD) study at beamline ID12 on a series of (Ga,Mn)As and (In,Ga,Mn)As thin films with varying Mn concentration spanning the metal-insulator transition. By probing the XMCD at both the Mn and As *K* absorption edges, we were able to obtain element-specific information on the electronic and magnetic properties. Furthermore, features in the spectrum associated with states in the vicinity of the Fermi level were found to be strongly sensitive to the Mn concentration, offering a microscopic insight into the relationship between conductivity and magnetism in this material.

The key results are shown in Figure 79, where the As and Mn *K* edge absorption and XMCD spectra are plotted for samples on either side of the metal-insulator transition. The As XMCD manifests itself as a sharp peak that barely coincides with the onset of the absorption edge. The presence of an XMCD signal at lower energy than the absorption edge is an indicator of a density of unoccupied As 4*p* states near the valence band edge, with a net orbital magnetic moment.
The As XMCD increases with the Mn concentration, and a sum rule analysis reveals a linear relationship between the As 4*p* orbital magnetic moment and the magnetisation M_S measured by bulk magnetometry (Figure 79a, inset). However, at a value of M_S that coincides approximately with the onset of the metal-insulator transition, the As 4*p* moment falls to zero.

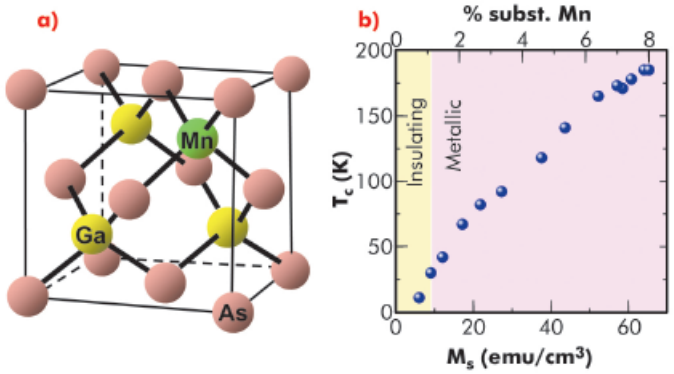

Fig. 78: a) Mn incorporated in the zincblende GaAs structure. b) Ferromagnetic transition temperature T_C versus concentration of magnetic moments.

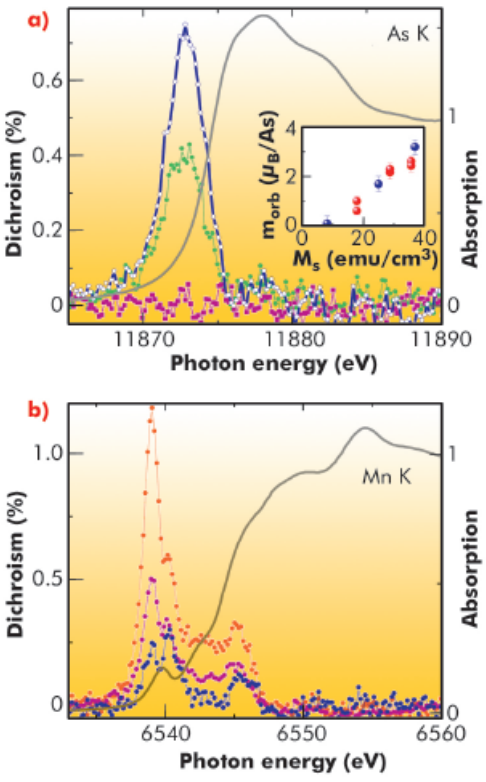

Fig. 79: a) As *K* edge absorption spectrum (grey curve) and XMCD spectra for films with effective Mn concentrations 4.5% (blue), 3.2% (green), 1.1% (pink). Inset: As 4*p* orbital magnetic moment versus magnetic moment concentration M_S. b) Mn *K* edge absorption spectrum (grey curve) and XMCD spectra for films with effective Mn concentrations 4.5% (blue), 1.1% (pink), 0.6% (orange).

Reference
[1] I. Stolichnov, S.W.E. Riester, H.J. Trodahl, N. Setter, A.W. Rushforth, K.W. Edmonds, R.P. Campion, B.L. Gallagher, C.T. Foxon and T. Jungwirth, *Nature Mater.* **7**, 464 (2008).

Different behaviour is observed at the Mn *K* edge (**Figure 79b**). The Mn XMCD spectrum consists of at least three distinct peaks, the largest of which are centred at a pre-edge peak in the absorption spectrum. The lowest energy peak in the XMCD spectrum shows a sharp decrease on crossing the metal-insulator transition. We ascribe this peak to transitions from the Mn 1*s* core level to *p-d* hybridised states lying just above the Fermi level. The reduced Mn XMCD in the metallic regime, combined with the emergence of an As 4*p* orbital polarisation, is a direct indication that the character of the states close to the Fermi level (*i.e.*, the states involved in conduction) changes from Mn-like to As-like.

To conclude, our results point to a qualitative change in the character of states near the Fermi level on going from the low-doped insulating state to the high-doped metallic state. Therefore, the *K* edge XMCD spectra provide a signature of the localisation of charge carriers in (Ga,Mn)As and related compounds, potentially offering a new insight into the nature of the metal-insulator transition in dilute magnetic systems.

Ti magnetism at $LaMnO_3/SrTiO_3$ interfaces

Principal publication and authors
J. Garcia-Barriocanal (a,b), J.C. Cezar (c), F.Y. Bruno (a), P. Thakur (c), N.B. Brookes (c), C. Utfeld (d), A. Rivera-Calzada (a), S.R. Giblin (e), J.W. Taylor (e), J.A. Duffy (f), S.B. Dugdale (d), T. Nakamura (g), K. Kodama (g), C. Leon (a), S. Okamoto (h) and J. Santamaria (a), *Nature Comm.* **1**:82 (2010); DOI:10.1038/ncomms1080
(a) GFMC. Dpto. Física Aplicada III, Universidad Complutense de Madrid (Spain)
(b) SpLine Spanish CRG Beamline at the ESRF, Grenoble (France)
(c) ESRF
(d) H.H. Wills Physics Laboratory, University of Bristol (UK)
(e) ISIS Facility, Rutherford Appleton Laboratory, Chilton (UK)
(f) Department of Physics, University of Warwick, Coventry (UK)
(g) Japan Synchrotron Radiation Research Institute, SPring-8, Sayo (Japan)
(h) Materials Science and Technology Division, Oak Ridge National Laboratory, Oak Ridge (USA)

Titanates and manganites share a common (perovskite) structure with similar lattice parameters, which allows the growth of high quality epitaxial interfaces. However, both systems are electronically very different. In manganites, the strong electron-lattice coupling lifts orbital degeneracy, which causes a null expectation value of the orbital moment. In titanates, orbital degeneracy due to the smaller Jahn-Teller distortions might allow non-zero values of the orbital magnetic moment. Novel forms of ferromagnetic superexchange interaction unique to t_{2g} electron systems have been

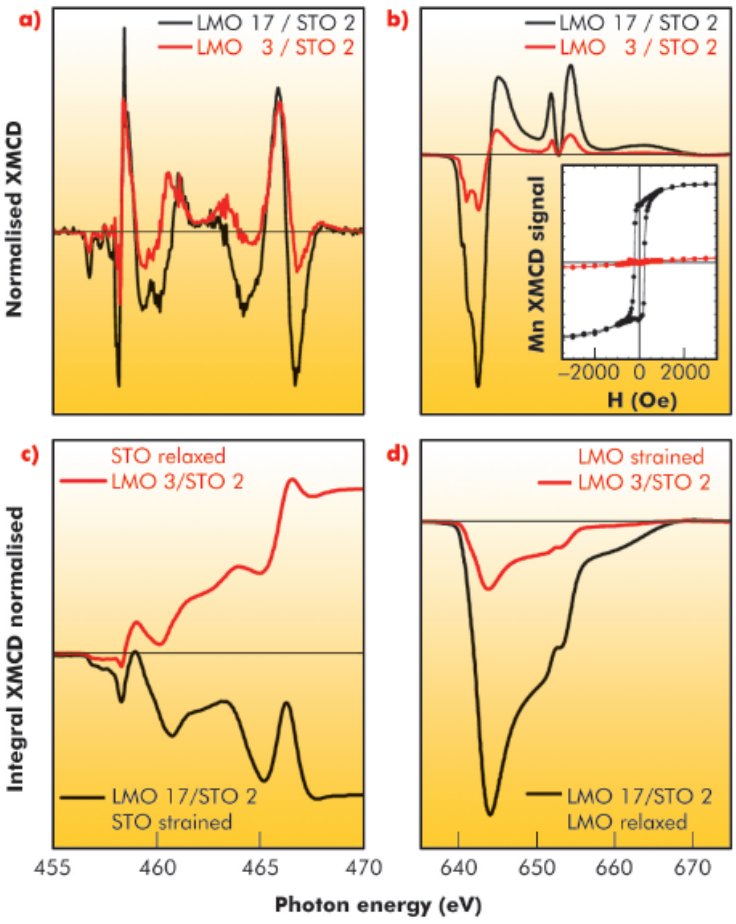

Fig. 80: a) Ti and b) Mn XMCD spectra of the [LMO 3/STO 2] (red) and [LMO 17/STO 2] (black) superlattices normalised to the L_3 t_{2g} (Ti) and L_3 (Mn) edge jump measured at 6 K. Inset: Mn hysteresis loops obtained from Mn XMCD signal. Integrated XMCD spectra for the same samples for c) Ti and d) Mn.

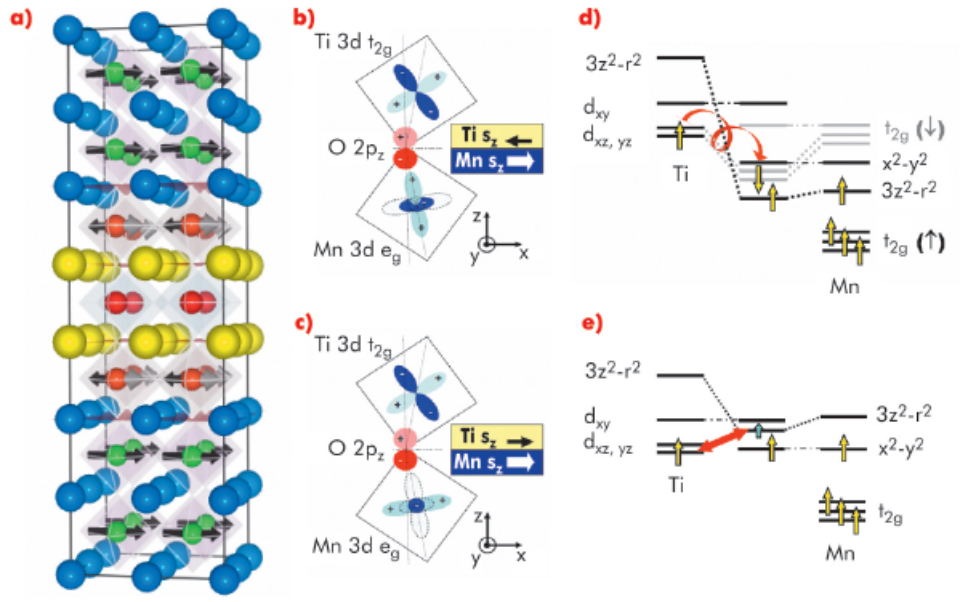

Fig. 81: a) Schematic illustration of the LMO/STO superlattice and of the interface magnetic structure. Colour code: Ti (red), Mn (green), La (blue) Sr (yellow). Black (grey) arrows symbolise the spin (orbital) moments. Sketches of the orbital occupation and Mn - Ti magnetic couplings for the superlattices b) [LMO 17/STO 2] and c) [LMO 17/STO 2]. Panels d) and e) illustrate a possible hybridisation scheme and the resulting magnetic coupling.

theoretically predicted [1], although their experimental observation has remained elusive. Experiments at beamline **ID08** using X-ray magnetic circular dichroism (XMCD) have found a new kind of Ti^{3+} ferromagnetism at $LaMnO_3/SrTiO_3$ (LMO/STO) epitaxial interfaces. This results from charge transfer to the empty conduction band of the titanate and has spin and orbital contributions, evidencing the role played by orbital degeneracy.

We have grown LMO/STO superlattices on (100) oriented STO single crystalline substrates with atomically sharp interfaces using a high oxygen pressure RF sputtering technique. Atomic column resolution electron energy loss spectroscopy (EELS) shows the presence of Ti^{3+} at the interface plane [2] indicating a charge transfer mechanism. Samples have a magnetic moment as evidenced by strong XMCD signals at Ti and Mn edges (see **Figure 80**). Data correspond to two superlattices, one with 17 unit cell thick LMO and 2 unit cell thick STO [LMO 17/STO 2] and the other has 3 unit cells thick LMO and 2 unit cells thick STO [LMO 3/STO 2]. **Figures 80c and d** display the integrated area under the XMCD spectra for Ti and Mn edges. While the integrated area under the Mn XMCD spectra show that the orbital moment is essentially quenched as expected, there is an important orbital component of the magnetic moment of the Ti aligned antiparallel to the spin, evidencing the effect of spin orbit interaction (Hund's third rule).

The shape of the XMCD signal of both the Mn and Ti depends strongly on the layer thickness ratio, and clearly indicate a change in the sign of the coupling mechanism of Ti and Mn spin moments at the interface from antiparallel for [LMO 17/STO 2] to parallel for [LMO 3/STO 2].

A simple (mean-field) molecular orbital picture provides a simple explanation for the magnetic coupling of Ti and Mn moments at the interface (see **Figure 81**). In the [LMO 17 / STO 2] superlattice there is strong hybridisation between the preferentially occupied Mn $d(3z^2\text{-}r^2)$ band at the interface and the empty $d(3z^2\text{-}r^2)$ band of Ti. The dominant superexchange process occurs between the Ti t_{2g} electrons and the half filled Mn t_{2g} bands, which is antiferromagnetic according to the Goodenough-Kanamori rules. In the [LMO 3/STO 2] superlattices there is no hybridisation between the occupied Mn $d(x^2\text{-}y^2)$ and Ti orbitals across the interface. Ferromagnetic coupling in [LMO 3/STO 2] results from the superexchange interaction on Ti d(xz,yz)-Mn $d(3z^2\text{-}r^2)$ bonds.

In conclusion, we have shown a novel form of Ti magnetism at a titanate/manganite interface. The magnetic alignment (ferromagnetic or antiferromagnetic) of Ti and Mn moments can be tuned by structural parameters. This result will provide important clues for the understanding of the effects of orbital degeneracy in superexchange coupling.

References
[1] T. Mizokawa, D.I. Khomskii and G. Sawatzky. *Phys. Rev. B* **60**, 7309 (1999).
[2] J. Garcia-Barriocanal, F.Y. Bruno, A. Rivera-Calzada, Z. Sefrioui, N.M. Nemes, M. Garcia-Hernández, J. Rubio-Zuazo, G.R. Castro, M. Varela, S.J. Pennycook, C. Leon and J. Santamaria, *Adv. Mat.* **22**, 627 (2010).

Principal publication and authors
F. Fabrizi (a,b), H.C. Walker (a,b), L. Paolasini (a), F. de Bergevin (a), T. Fennell (b,c), N. Rogado (d), R.J. Cava (d), Th. Wolf (e), M. Kenzelmann (f) and D.F. McMorrow (b), *Phys. Rev. B* **82**, 024434 (2010).
(a) ESRF
(b) University College London (UK)
(c) ILL
(d) Princeton University (USA)
(e) Karlsruher Institut für Technologie (Germany)
(f) PSI (Switzerland)

Imaging multiferroic domains using X-ray polarisation-enhanced topography

Imaging ferroelectric and magnetic domains have largely remained two separate fields. Recent developments at beamline **ID20** have led to a technique that provides topographic images of the spatial distribution of the magnetic domains in multiferroics, such as $Ni_3V_2O_8$, while the ferroelectric domains are cycled through a hysteresis loop by an applied electric field.

$Ni_3V_2O_8$ is an example of a magnetoelectric multiferroic in which magnetism and ferroelectricity not only coexist, but are coupled together. These materials present an interesting opportunity for technological applications, but this is reliant on overcoming an outstanding challenge, namely understanding the evolution of the domain states in external applied magnetic fields. The work we present here is a first step in this direction.

In $Ni_3V_2O_8$ there is a phase transition at T = 6.3 K to an incommensurate magnetic structure, that is accompanied by the onset of a finite spontaneous electric polarisation. Based on neutron diffraction, it was proposed that this phase corresponded to a cycloidal order of the spins on two different symmetry nickel sites – spine and cross-tie. Circularly polarised X-rays naturally couple to the handedness of spin cycloids, and through a complete Stokes polarimetry analysis of the scattered beam it is possible to identify information on magnetic structures that is typically inaccessible through neutron diffraction experiments. It was determined using just four reflections that, in fact, the moment on the cross-tie sites remains disordered, such that the onset of ferroelectricity is associated with the cycloidal ordering of the moments on the spine sites.

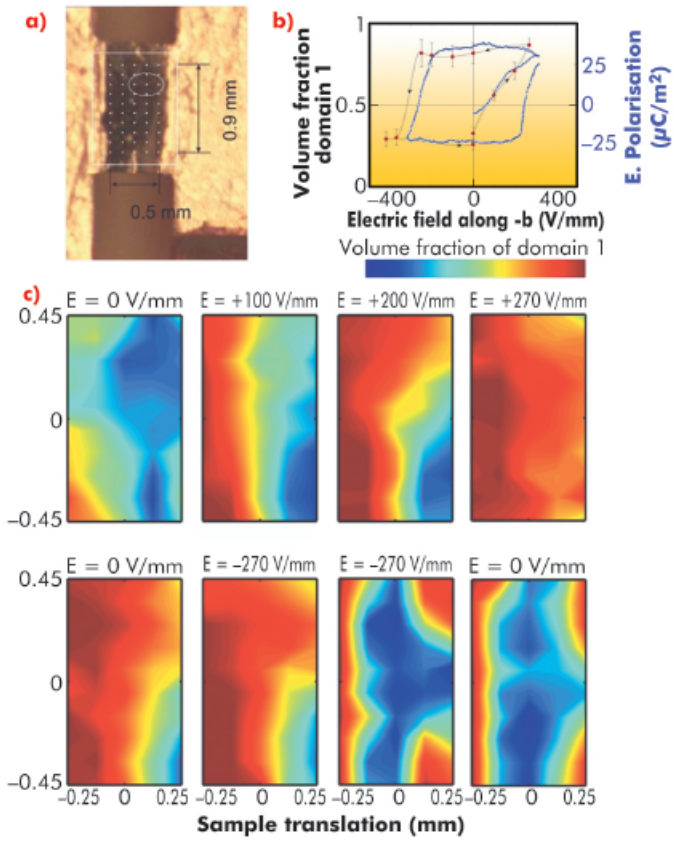

Fig. 82: a) Photograph of sample between the Cu electrodes forming a capacitor. b) Variation in the domain populations and the electric polarisation as a function of applied electric field. c) Topographic images of the domain population distributions as a function of the electric field.

For our experimental setup, our sample of $Ni_3V_2O_8$ was mounted such that the spin cycloid lay in the horizontal scattering plane, which resulted in the polarisation state of the scattered beam being strongly sensitive to the domain populations. The scattering process converts the incident circular polarisation state into a linear polarisation state inclined at 45 degrees to the scattering plane, described by the Stokes parameter P2. By determining the value of P2 at different points over the sample surface it is then possible to extract the domain populations.

To establish the evolution of the domains as a function of field, the sample was initially cooled to 5 K with no voltage across the sample. The incident beam spot was then reduced in size and the sample rastered through the beam measuring the value of P2 at each spot and hence finding the percentage of left- and right-handed magnetic cycloidal domains. Then a voltage was applied whilst remaining at 5 K, before repeating the measurements of P2. Figure 82c reveals that this method allows us to resolve inhomogeneities in the domain populations with good resolution. The evolution of the domain populations is gradual, with the boundary between the two shifting as a function of applied electric field, as opposed to the

nucleation of one domain within the other, which would lead to a more randomised distribution. It is also clear that the data reveals edge effects, where the domains become pinned close to the edges of the sample. By averaging the domain populations over the central unaffected area it is possible to extract a magnetic domain population hysteresis loop. On comparing this loop with electric polarisation measurements (Figure 82b), we find an excellent agreement, indicating that, by imaging the magnetic domains in multiferroic $Ni_3V_2O_8$, we are in effect also imaging the ferroelectric domains.

The demonstration of the possibility to image the multiferroic domains in $Ni_3V_2O_8$ opens up the prospect to use this technique to image domains in other related materials and even in operational devices. With the improvement in focussing offered by the ESRF Upgrade Programme, the spatial resolution of this technique will be reduced to 100 nm and below, at which point it will become possible to image not only the domains, but also the structure of the domain walls, the engineering of which ultimately determines the usefulness of any given material.

Hydration structure of the Cf(III) aqua ion

Principal publication and authors
E. Galbis (a), J. Hernández-Cobos (b), C. Den Auwer (c), C. Le Naour (d), D. Guillaumont (c), E. Simoni (d), R.R. Pappalardo (a) and E. Sánchez Marcos (a), *Angew. Chem. Int Ed.* **49**, 3811 (2010).
(a) Departamento de Química Física. Universidad Sevilla (Spain)
(b) Instituto de Ciencias Físicas, UNAM, Cuernavaca (México)
(c) Radiochemistry Process Department, CEA Marcoule (France)
(d) Institut de Physique Nucleaire Orsay, Université Paris-Sud (France)

Properties of actinide cations in aqueous solutions have been of fundamental interest since the beginning of the nuclear technologies. The primary feature of actinide ions in water is the aqua ion structure, $[An(H_2O)_n]^{m+}$, since it is intimately linked to complexation and transfer processes. The rareness and hazardousness nature of the heavier actinide elements has prevented a complete examination of the trend along the series [1]. Therefore, the expected actinide contraction of their aqua ions reflected in the shortening of the first water sphere and concomitant decreasing of the total first coordination number (CN) along the series is not fully confirmed. Due to the position of Cf(III), an accurate enough description of its aqua ion may certainly shed light on this fundamental question. This work presents an alternative way of study for this extreme case, by coupling new highly refined EXAFS data obtained at the **BM20/ROBL** beamline with the first Monte Carlo simulations of Cf(III) in water.

A 2 mM solution of ^{249}Cf in perchloric acid was prepared. Figure 83 shows the experimental and fitted k^2-weighted Cf L_{III}-edge EXAFS spectra, using two model structures for the aqua ion: the square antiprism configuration (SA), which represents an octahydrate and the trigonal tricapped prism (TTP), which implies an ennea-hydrate. Since no experimental estimation of the global amplitude factor S_o^2 could be

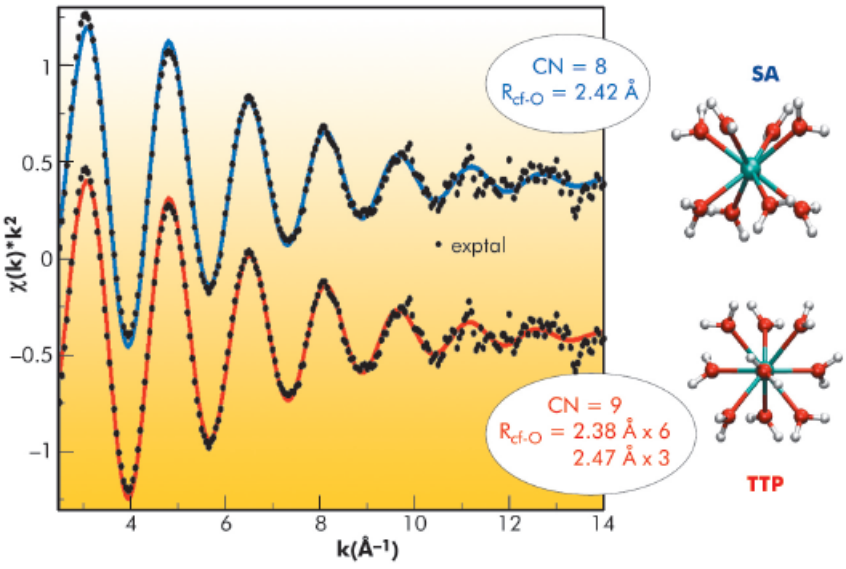

Fig. 83: Experimental (black points) and fitted (SA (CN = 8) blue and TTP(CN = 9) red lines), Cf EXAFS spectrum.

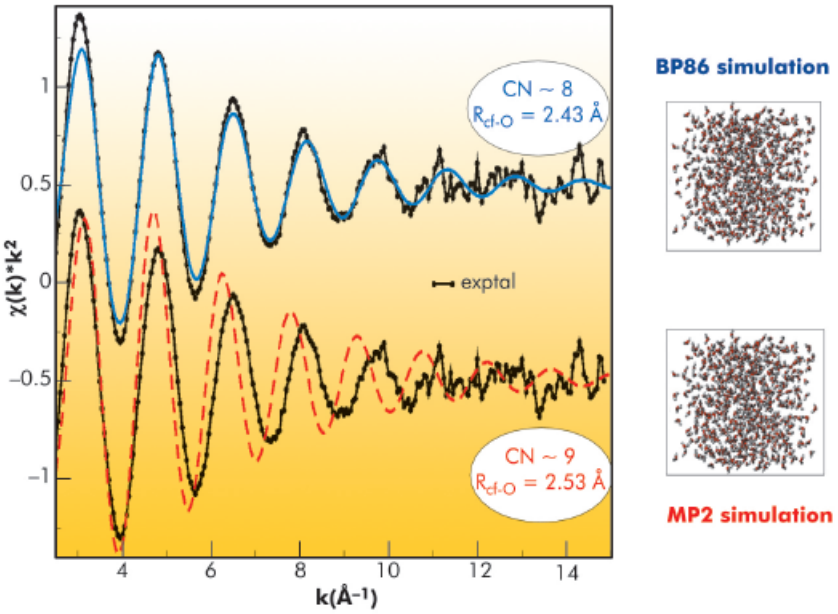

Fig. 84: Comparison of the experimental Cf EXAFS spectrum (black points) with the simulated spectra: BP86 (blue line) and MP2 (red line).

obtained for the Cf case, coordination numbers were fixed to the model values of 8 (SA) fitted at 2.41 Å (σ^2 = 0.0077 Å^2) and 9 (*i.e.* 6+3, TTP), fitted at 2.38 Å (σ^2 = 0.0068 Å^2) and at 2.47 Å (σ^2 = 0.0039 Å^2). The weighted averages of the Cf-O distances are comparable and there is no clear visible difference between the two fitted curves. Therefore, distinction between a TTP and an SA structure for the aqua ion cannot be unambiguously deduced from the fittings performed.

Computer simulations of Cf(III) in water represent a completely independent approach to this system. *Ab initio* based Cf-H_2O intermolecular potentials (IP) have been developed. Two different quantum-mechanical (QM) potential energy surfaces were employed, one based on the MP2 method and the other on the DFT method (BP86 functional) [2]. Monte Carlo (NVT) simulations of a system formed by 1 Cf(III) and 500 water molecules were carried out. 2Giga configurations were generated for analysis. The MC simulation using the BP86-based IP leads to an average CN for the first hydration shell close to 8, and the first maximum of the Cf-O RDF appears at 2.43 Å, whereas the MC simulation that uses the MP2-based IP gives a CN close to 9 with the maximum for the Cf-O RDF at 2.53 Å. The absence of experimental data other than the EXAFS spectrum precludes the adoption of a convincing criterium to clearly select an IP.

The experimental EXAFS spectrum was compared with those derived from the structural information provided by MC simulations, (Figure 84), applying a methodology already proposed for solving other delicate structural problems [3]. The agreement for the case of the BP86 simulation is remarkable, where the intensity of the signal and the in-phase behaviour is maintained up to high *k* values.
For the MP2 case, the spectrum shows an intensity less similar to the experimental one and a progressive out-phase behaviour. Bearing in mind that the first simulated spectrum is derived from the BP86 MC simulation, where CN ~8 and R_{Cf-O} = 2.43 Å, whereas the second simulated spectrum comes from the MP2 MC simulation where CN~9 and R_{Cf-O} = 2.53 Å, we must conclude that Cf(III) aquaion must be mainly octacoordinated. Then, as far as Cf(III) is the heaviest actinide aquaion for which there is experimental information, the actinide contraction is supported by the present study (R_{U-O} = 2.56Å and CN = 9±1; R_{Pu-O} = 2.51Å and CN = 9±1; R_{Cm-O} = 2.47Å and CN = 9±1) [1].

This work illustrates the benefits which can be obtained from the combination of experimental XAS spectroscopies and computer simulations. Likewise, it traces out a scarcely explored combined methodology that could be useful for other complex chemical problems.

References
[1] S. Skanthakumar, M.R. Antonio, R.E. Wilson and L. Soderholm, *Inorg. Chem.* **46**, 3485 (2007).
[2] A. Moritz, X.Y. Cao and M. Dolg, *Theor.Chem Acc.*, **117**, 473 (2007).
[3] P.J. Merkling, A. Muñoz-Páez and E. Sánchez Marcos, *J. Am. Chem. Soc.* **124**, 10911 (2002).

EXAFS and XRD characterisation of palladium sorbents for high temperature mercury capture from fuel gas

Principal publication and authors
S. Poulston (a), T.I. Hyde (a), H. Hamilton (a), O. Mathon (c), C. Prestipino (c), G. Sankar (a,b) and A.W.J. Smith (a), *Phys. Chem. Chem. Phys.* **12**, 484 (2010).
(a) Johnson Matthey Technology Centre, Sonning Common, Reading (UK)
(b) Department of Chemistry, University College London (UK)
(c) ESRF

Acknowledgements
GS thanks Royal Society for an Industrial Fellowship and Johnson Matthey plc for hosting the fellowship.

The gasification of coal is a potentially important way of utilising coal reserves, for example in integrated gasification combined cycle (IGCC) power plants or in the production of syn-gas for chemicals. The syn-gas or fuel gas (CO, CO_2, H_2) derived from this process contains low concentrations of heavy metals that were present in the coal and become volatile during gasification. Release of mercury vapour in its elemental form can lead to environmental and technical problems during fuel/syn gas utilisation.

Palladium can be used for mercury vapour removal from fuel gas at elevated temperatures [1]. The overall thermal efficiency of an IGCC system is improved with removal of mercury at higher temperatures using sorbents capable of operating at these temperatures. The sorbent samples Pd/Al_2O_3 and Pd/SiO_2 have significantly different Hg adsorption capacities at operating temperatures, with higher Hg capacities for the Pd/SiO_2 sorbent than Pd/Al_2O_3, although Pd dispersions are higher for the Pd/Al_2O_3 sorbent.
A detailed structural investigation using complimentary chemical and physical (XRD, EXAFS) methods was undertaken to understand whether the mercury is adsorbed on the support or interacts with palladium leading to the formation of an alloy-type material.

Long range order as determined by *ex situ* XRD shows significant differences in the nature of the alloys formed on the two sorbents following exposure to Hg in a syn gas feed at 204°C.
The Pd/Al_2O_3 sorbent produced a single homogeneous solid solution of Pd-Hg consistent with the limited literature reports on the Hg-Pd phase diagram, whilst the silica supported Pd produced an alloy of varying composition.

Pd K and Hg L3-edge EXAFS data were collected at 20 K on the **BM29** beamline. Consistent with *ex situ* XRD, the EXAFS analysis (both Pd and Hg edge) of the Pd/Al_2O_3 sorbent exposed to fuel gas containing mercury can be interpreted as a Pd–Hg alloy phase. The near neighbour distances obtained from both the Pd and Hg edge EXAFS were found to be very similar suggesting a uniform alloy was formed. However, the most striking difference between the Pd K-edge and Hg L3-edge results was that Pd is surrounded predominantly by Pd whilst the Hg is surrounded by Pd; no significant Hg–Hg contacts (from Hg L3-edge EXAFS) or Pd–Hg contacts (from Pd K-edge EXAFS) were observed. This is most likely due to the low concentrations of mercury in the system and, in addition, the mercury atoms being randomly distributed throughout the palladium lattice in such a way that palladium atoms are mainly in contact with palladium (Figure 85).

In contrast, Hg exposed Pd/SiO_2 sorbent showed markedly different results. The refined Hg–Pd distance from the Hg L3-edge, supported by *ex situ* XRD indicates that there is alloy formation similar to that in the Hg exposed Pd/Al_2O_3 sample. However, the Pd K-edge data suggest there are mainly Pd–Pd scatterers present. In particular the first neighbour distances obtained from Pd K-edge data differ by ca. 0.03 Å compared to Hg L3-edge results and the Pd–Pd distance was very close to that obtained for untreated Pd/SiO_2 material. On the other hand the Hg L3-edge results are similar to those obtained for the Hg exposed Pd/Al_2O_3 system indicating that there is a Hg–Pd alloy present in the system.
This suggests a more complex structure to the Pd–Hg particles than is present in the Hg exposed Pd/Al_2O_3 sample. One model consistent with the XRD and EXAFS data is a core in the metal particles that contains predominantly Pd–Pd neighbours with the periphery of the particle consisting of Pd–Hg

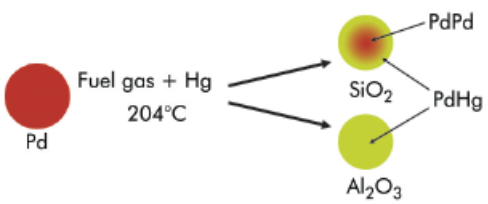

Fig. 85: Proposed Pd-Hg interactions as determined by XAS and XRD from silica and alumina sorbents.

References
[1] S. Poulston, E.J. Granite, H.W. Pennline, C.R. Myers, D.C. Stanko, H. Hamilton, L. Rowsell, A.W.J. Smith, T. Ilkenhans and W. Chu, *Fuel* **86**, 2201 (2007).

neighbours. It is likely, therefore, that there is a gradual change in composition with Pd–Hg alloy in the near surface part of the metal particles, the Hg concentration progressively decreasing through the particle leading to a Pd metal particle-like phase dominating the core.

In conclusion, detailed XRD and XAS studies reveal that, during the reaction with fuel gas containing Hg vapour at 204°C, a uniform alloy is formed in the Pd/Al_2O_3 sorbent, whereas particles containing predominantly a Pd core and Hg-Pd alloy at the periphery are formed in the Pd/SiO_2 sorbent. This information has proven beneficial in developing a better understanding of pollutant removal with sorbent material and in particular the effect of Pd particle size in determining the Pd-Hg interaction.

Hydration structure of the bromide ion in aqueous solution

Principal publication and authors
P. D'Angelo (a), V. Migliorati (a) and L. Guidoni (b), *Inorg. Chem.* **49**, 4224 (2010).
(a) Dipartimento di Chimica, Università di Roma "La Sapienza" (Italy)
(b) Dipartimento di Chimica, Ingegneria Chimica e Materiali, Università degli Studi dell'Aquila (Italy)

The solvation properties of ions and the role of the surrounding water molecules are important throughout biology and chemistry. While much experimental and theoretical work has been devoted to the characterisation of the structural and dynamical behaviour of cations in water, the hydration properties of halides are still the subject of intense debate. For the bromide ion, the hydration number as determined by X-ray and neutron diffraction and X-ray absorption is in the range 6-7.4 and the Br-O first shell average bond length determined by X-ray diffraction is between 3.19 and 3.40 Å. These scattered results underline the difficulty of defining the halide coordination shells also as a consequence of the fast water exchange between the first and second hydration shells.

Here we report on the first study of the hydration structure of the bromide aqua ion using a combination of state-of-the-art density functional theory (DFT)-based Car-Parrinello molecular dynamics (CPMD) simulations and extended X-ray absorption fine structure (EXAFS) spectroscopy. This experimental technique is particularly well suited for the investigation of the local solvent structure of ions dissolved in water due to its atomic selectivity and its sensitivity to dilute solutions. Beside the quantum mechanical CPMD simulation, we have also performed a classical molecular dynamics (MD) simulation of the bromide ion in aqueous solution and compared the results obtained from these two different theoretical approaches. Structural arrangements of water molecules around the bromide ion are characterised by the Br-O and Br-H radial distribution functions, and the results obtained from the classical MD and CPMD simulations are depicted in Figure 86. In both cases, the presence of a nonzero first minimum in the Br-O g(r)'s and of a second minimum in the Br-H g(r)'s indicates that the first solvation shell is not well-defined and that several exchange events may take place between the first and second hydration sphere. The first difference between the classical and the CPMD simulation is the Br-water first shell distance, which is shorter in the classical trajectory (R_{Br-O} is 3.33 and

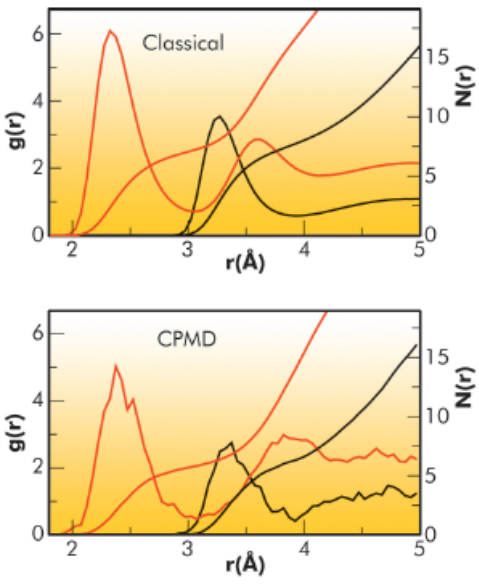

Fig. 86: Br-O (black line) and Br-H (red line) radial distribution functions obtained from the classical MD and CPMD simulations. Running integration numbers are also shown.

3.27 Å for the CPMD and classical MD simulation, respectively). The picture that emerges from our simulations is that the pair potentials used in the classical approach are too rigid giving rise to a first hydration shell which is too tightly bound to the bromide ion. Conversely, in the CPMD trajectory the first coordination shell is more flexible and unstructured, without a well-defined configuration of water molecules around the ion. Both in the MD and CPMD trajectories, the bromide ion transits among several coordination numbers, but while in the classical case the dominant species existing in solution are seven- and eight-fold hydration complexes, only six-fold complexes play a dominant role in the CPMD case. Moreover, in both simulations the first hydration shell is slightly asymmetric, but the asymmetry is more pronounced in the CPMD trajectory; this asymmetry is responsible for the presence of an induced net dipole moment on the bromide ion (μ = 0.85D), indicating that the bromide electron density is strongly influenced by the presence of the surrounding water molecules and that the inclusion of polarisation effects is essential to provide a correct description of the anion-water interactions.

Finally, the MD structural results were compared with EXAFS experimental data. χ(k) theoretical signals have been calculated starting from the classical and CPMD Br-H and Br-O g(r)'s and the structural parameters derived from the simulations were kept fixed during the EXAFS analysis. The importance of the hydrogen contribution to the EXAFS spectra of metal cations in aqueous solution has been previously pointed out and here for the first time it has been possible to also include the hydrogen scattering in the EXAFS analysis of anion aqueous solutions. In the case of the classical MD simulation, a rather poor agreement between the theoretical and experimental spectrum was found, while the spectrum calculated from the CPMD g(r)'s matched the experimental data very well, thus showing that the structural and dynamical information derived from the CPMD simulation was basically correct (Figure 87).

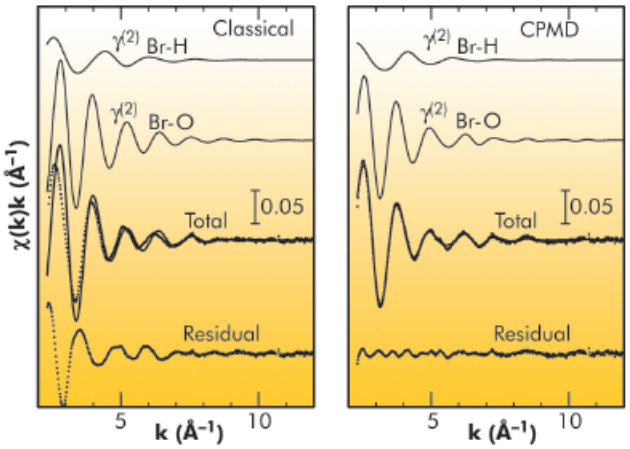

Fig. 87: Comparison between the EXAFS theoretical signals (solid line) calculated from the classical MD and CPMD Br-O and Br-H g(r)'s and experimental data (dotted line). The residual signals are also shown.

In conclusion, we have shown that advanced DFT based simulation techniques, which take into account both polarisation effects and many body interactions, are necessary to provide a proper description of the hydration properties of halide anions. Moreover, by taking advantage of the reliable information on the bromide ion local hydration structure obtained from the CPMD trajectory, it has been possible to include the hydrogen scattering in the EXAFS analysis of anion aqueous solutions.

The deepest phase transition in the Earth's mantle

The D"-layer is a 100-300 km thick layer lying just above the core-mantle boundary at 2900 km below the surface of the earth, under a pressure of ~100 to 135 GPa. In this region, seismic observations provide evidence of heterogeneities in wave propagation and sound velocities. Since the perovskite (Pv) to post-perovskite (PPv) phase transition was discovered for $MgSiO_3$ [1], various authors attempted to explain *all* peculiar seismic features on the basis of this transformation. Indeed, the local structure is quite different in these two phases; the PPv is layered (Figure 88), which enhances

Principal publication and authors
D. Andrault (a), M. Muñoz (b), N. Bolfan-Casanova (a), N. Guignot (c), J.P. Perrillat (d), G. Aquilanti (d) and S. Pascarelli (d), *Earth and Planetary Science Letters* **293**, 90-96 (2010).
(a) LMV, Université Blaise Pascal, Clermont-Ferrand (France)
(b) LGCA, Université Joseph Fourier, Grenoble (France)
(c) SOLEIL, Gif-sur-Yvette (France)
(d) ESRF

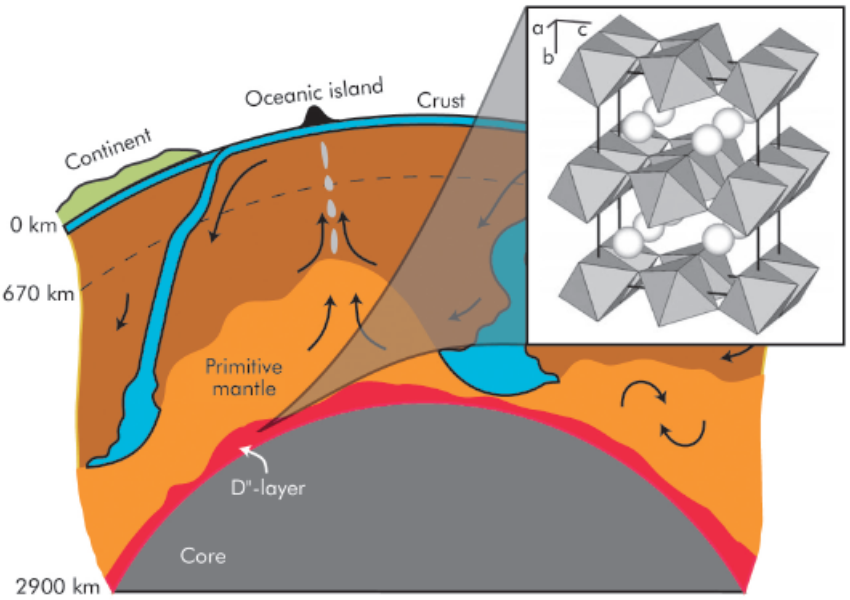

Fig. 88: Experiments at extreme conditions provide insight into the composition of the D''-layer just above the core-mantle boundary at 2900 km below the surface of the Earth [3]. The post-perovskite structure of $MgSiO_3$, which is analogous to $CaIrO_3$ [1,2], is also presented.

significantly its elastic anisotropy, and could help to explain the seismic heterogeneities [2]. However, most of the previous experimental investigations of the Pv to PPv transition mechanism suffer from the limitation that the $MgSiO_3$ composition is too simple. When more significant mantle compositions were investigated (*i.e.* the composition $(Mg,Fe)(Si,Al)O_3$), the chemical analyses were only performed *ex situ* on samples recovered at ambient conditions. In the present work, we investigated the mineralogical content and the Fe distribution in various geological samples *in situ* at high pressure and temperature using tandem analyses of X-ray absorption spectroscopy at the Fe K-edge (**ID24**) and X-ray diffraction (**ID27**). These techniques permit the phase relations between the minerals to be determined for bulk samples, in contrast to the thin films that were analysed in previous studies. Pressures up to 180 GPa were obtained using diamond-anvil cells, exceeding the pressure of 135 GPa found at the core-mantle boundary. YAG laser heating was used to reach temperatures of more than 3000 K.

Synthesis of the Pv and PPv grains was carefully monitored using X-ray diffraction, for variable heating duration and temperatures. The sharpness of the Bragg lines and occurrence of a multitude of small spots on the 2-dimensional X-ray pattern indicate efficient atomic diffusion at the scale of the grain size and quasi-equilibrium crystallisation of the silicate phases. The diffraction patterns reveal the presence of two crystalline phases, Pv and PPv, up to the maximum pressure investigated. Relative proportions of the different minerals were quantified based on Rietveld refinements. We then performed Fe K-edge XANES on the same samples in order to retrieve the Fe coordination site and thus the preferential Fe distribution between Pv or PPv phases (**Figure 89**). Combined with PPv fractions determined using X-ray diffraction, we calculated the Fe-partition coefficient between the two phases.

Our results show that the main PPv phase is depleted in Fe, compared to

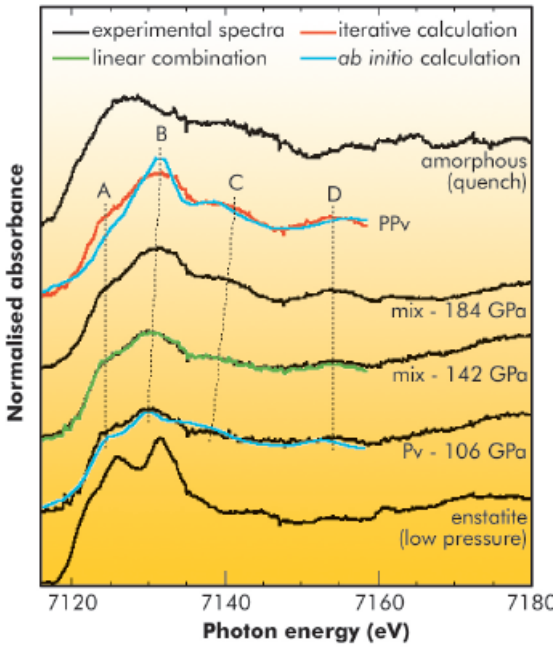

Fig. 89: X-ray absorption spectra recorded at the Fe K-edge as a function of the synthesis pressure (black lines). Experimental data are compared with calculations (coloured lines). XANES spectrum of the enstatite starting material (lowest) and quenched amorphous (highest) are shown for comparison. The features B and C shift significantly with increasing pressure while A and D remain unchanged. This is associated to changes in the Fe local structure when the Fe environment changes progressively from Pv to PPv with increasing pressure from 106 to 184 GPa.

the Pv phase. Also, we report the proportion and composition of each mineral in the P-T conditions of the D"-region. These results are significant for our interpretation of geophysical data. Fe and Al produce a progressive phase transition from Pv to PPv, in contrast with pure $MgSiO_3$. This progressive transition mechanism is incompatible with the sharp seismic features reported for this mantle region. Thus, more complex models are required that include additional sources of chemical heterogeneity. Furthermore, the occurrence of a PPv-phase with a minimum Fe-content has two major implications: (i) it should enhance the radiative thermal conductivity in the D"-layer, since Fe-free minerals are generally transparent to visible light. This can induce a much higher temperature in the lowermost mantle; (ii) the FeO activity in the mantle is enhanced at the core-mantle boundary, as evidenced by a FeO content up to ~0.30 mole percent in ferropericlase. Thus, FeO should diffuse to the outer core, with a concomitant loss of FeO in the lowermost mantle. This can affect the density of the material located in the D"-layer and can induce unstable dynamical behaviour in this region.

References

[1] M. Murakami, K. Hirose, K. Kawamura, N. Sata and Y. Ohishi, *Science* **304**, 855 (2004).

[2] N. Guignot, D. Andrault, G. Morard and M. Mezouar, *Earth and Planetary Science Letters* **256**, 162 (2007).

[3] Derived from L.H. Kellogg, B.H. Hager and R.D. van der Hilst, *Science* **283**, 1881-1884 (1999).

Structural Biology

The impact of stable beamline automation can be seen in both the quality and quantity of this selection of highlights representing the work of the ESRF's structural biology community. Most of these excellent results would not have been possible without the tools put in place over the past decade. Limited space for this compilation has meant the omission of much work that is of extremely high standard. Nevertheless, several scientific themes do emerge.

Whilst reaching the level of performance that we have been seeking – a task that has only been possible thanks to the combined efforts of all members of the Structural Biology Group, our colleagues at the EMBL in Grenoble and others elsewhere – 2010 marks the beginning of major changes in our beamline portfolio. Preparation of the new beamline complex on ID30 and BM29 is progressing fast, with the site prepared and construction underway. BM29 will become the new home for our Protein Solution Scattering beamline, benefiting from a wide wavelength range and a close interaction with both ID29 and ID30. We expect that the transfer from ID14-3 will be possible during 2011.

The upgrade of the ESRF's structural biology facilities is based upon the premise that the resolution of challenging problems will require extensive access to synchrotron beamlines. Thus, the upgrade of our resources will provide new tools allowing both for the selection of the best crystals on which to carry out experiments and for the execution of the best possible experiment on the crystals selected. This approach will inevitably result in a change in the way in which projects are pursued. Many more samples will be examined before proper data collection and, once a plan for the best possible experiment has been developed, the relevant samples will be transferred to the most appropriate beamline for data collection. The first paper in this chapter covers initial work in this area and describes the detailed characterisation of protein crystals using “diffraction cartography”.

The study of macromolecular machines produces crystals that are extremely difficult to work with, however the reward for persistence is the exquisite beauty of the structures finally revealed and a number of the contributions report on the fruits of very long term projects. On page 80 Efremov *et al.* report the latest high resolution structure of the respiratory complex I from prokaryotes. This work combines information derived from crystal structures of the hydrophilic and membrane bound domains with that of the entire complex I to provide insights into the mechanism of action of this fundamental molecular machine. Illumination as to the basic chemistry and functional evolution of the ribosome is reported by Belousoff *et al.* (page 85). The conversion of solar energy into chemical bonds is essential for the survival of all higher life forms. On page 88, Amunts *et al.* describe the latest results in their efforts to provide high resolution details of the plant photosystem I supercomplex. Extensive crystal screening and use of microbeams (with relatively large crystals) have enabled the group to extend the resolution of their structure to 3.3 Å. The crystal structure of the torque ring of the bacterial flagellar motor is reported by Lee *et al.* on page 98 and provides a molecular basis for the explanation of rotational switching by this motor.

The structures of membrane-associated proteins also figure prominently among the highlights. The elucidation of the structure of the hydantoin transporter in its 'inward open' form completes the set for this transporter and has provided molecular details of the alternating access model of transport used by secondary active membrane transport proteins to harness electrochemical gradients to help effect the movement of small molecules or ions across membranes (Shimamura *et al.* page 83). The localisation and movement of transmembrane proteins between different membranes in a cell is performed by the cell's vesicular transport system. The resolution of the structure of the AP2 clatherin adapter complex in an open, liganded form (Jackson *et al.*, page 93) follows on from the determination structure of the closed form of the complex (in 2002) and provides clear evidence for the complex's mechanism of action. Signal peptides play a role in directing proteins outside the cell. The crystal structure of a signal recognition particle 54 (SRP54) fused with a signal peptide (Yanda *et al.*, page 96) sheds light on the roles of Leu and Met side chains in the M domain of SRPs, in the binding of signal peptides with diverse sequences.

DNA binding is a feature of many proteins and is integral for the successful maintenance of cellular function. Three of the articles presented here examine various aspects of the roles of DNA binding proteins. These include the binding to mitochondrial DNA by the regulator mTERF (Jiménez-Menéndez *et al.*, page 89), a transcriptional regulation mechanism based on the ordering of intrinsically disordered domains upon DNA binding (Garcio-Pino *et al.*, page 92) and the repair of double stranded DNA breaks by the DNA dependent protein kinase (Sibanda *et al.*, page 99).

The discovery and development of new drugs is an important activity for both academic groups and pharmaceutical companies. Work toward the development of novel therapeutics for *Leishmaniasis* is reported (Frearson *et al.*, page 86), the structure

characterisation of the nuclease domain of a herpesvirus terminase - a potential target for the development of antiviral molecules against herpesviruses - is described (Nadal *et al.*, page 103), and the mechanism of action of a new class of antibiotics is discussed (Bax *et al.*, page 94). The disruption of quorum sensing as a potential tool in the development of antimicrobial compounds is also addressed (Bokhove *et al.*, page 104). None of these results would have been possible without access to automated high intensity beamlines.

The study of spider silk has provided numerous examples of research using micro-beams, in particular on ID13. On page 82, Askarieh *et al.* report the structure of a key protein responsible for forming the large assemblies involved in the formation of spider silk. Their model helps understand the pH regulation of the process. The diversity of life is demonstrated in the work of Hehemann *et al.* (page 90), where analysis of high resolution crystal structures combined with bioinformatic detective work reveal an unexpected link between a marine porphyranase and a human gut bacterium present only in Japanese individuals!

Other reports in this chapter reveal the complementary nature of the ESRF's resources, the excellent service provided by the CRG beamlines and the international context within which the ESRF works. In many cases, the experimental data supporting the work is provided by more than one ESRF beamline or generated by combining data obtained at the ESRF and at other synchrotron centres. The future will see this trend increase. The demand for synchrotron beamtime for structural biology continues to increase and the productivity and imagination of this part of the ESRF's user community shows no signs of diminishing.

S. McSweeney and G. Leonard

Diffraction cartography: enhanced sample evaluation and data collection in macromolecular crystallography

Principal publication and authors
M.W. Bowler (a), M. Guijarro (a), S. Petitdemange (a), I. Baker (a,b), O. Svensson (a), M. Burghammer (a), C. Mueller-Dieckmann (a), E.J. Gordon (a), D. Flot, (a) S.M. McSweeney (a) and G.A. Leonard (a), *Acta Cryst.* **D66**, 855-864 (2010).
(a) ESRF
(b) Department of Biology and Biochemistry, University of Bath (UK)

The large multi-component complexes and membrane proteins now routinely studied in Structural Biology tend to produce either very small crystals or crystals that can be extremely heterogeneous in their diffraction properties. The increasing availability of micro-focussed X-ray beams coupled with experimental environments optimised for MX has allowed the design of advanced sample evaluation (mesh scans) and data collection (helical oscillation) protocols. Here we present two examples of how mesh scans can be used in the most challenging projects: searching, within a sample-containing loop, for crystals of maximum dimension of 10 µm using an X-ray beam of 5 µm diameter and selecting the most ordered regions of relatively large crystals using an X-ray beam of 30 µm diameter.

For many projects, particularly those initially producing microcrystals, the rapid identification of crystallisation conditions yielding protein crystals is a considerable advantage. However, locating microcrystals within a large loop is problematic. Lens effects frequently make it difficult to locate small, thin crystals with visible light and the lack of explicit cryoprotection often means that the resulting glass in which microcrystals are contained is opaque. In such cases, the most convenient way to identify both the position and composition of crystals is to use X-ray diffraction coupled with a mesh scan capability. An interface has been implemented within the beamline control GUI MXCuBE [1] based on developments made on beamline ID13. In the sample display area of the GUI, the limits of a grid are drawn and a step size for sampling the grid chosen (Figure 90a). Each position in the grid is associated with a specific coordinate (expressed in the position of the motors *phiz* (vertical translation of the

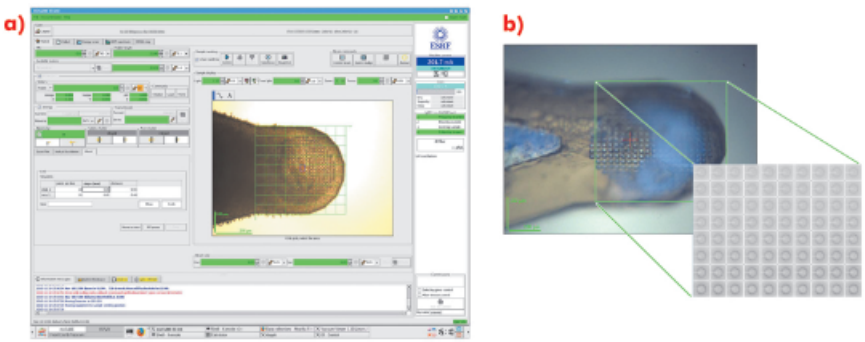

Fig. 90: Using a mesh scan to locate microcrystals. Crystals were swept into micromeshes and plunged into liquid nitrogen, producing an opaque glass containing several microcrystals. a) A mesh is drawn over the desired area within the MXCuBE GUI and a diffraction image collected at each point. b) Images correspond to specific locations within the loop so that a crystal can be centred in the X-ray beam.

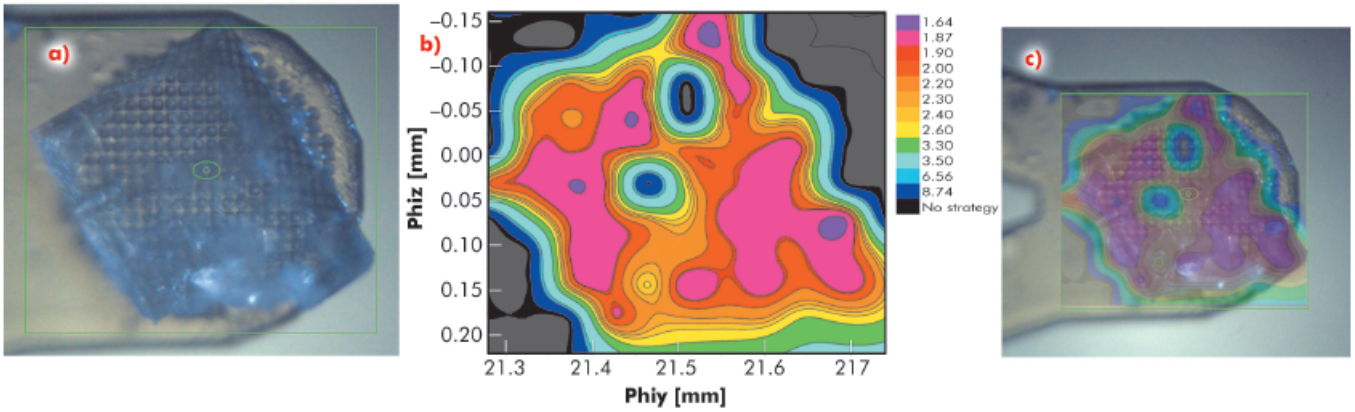

Fig. 91: Diffraction cartography of a single crystal of bovine mitochondrial F_1-ATPase. a) A mesh scan was carried out over the entire area of the crystal (green box) using 40 µm steps (X-ray beam size 30 µm). b) Diffraction images were processed with EDNA and the 'ranking resolution' in Å (blue lowest, mauve highest) plotted against the goniometer axis motor positions *phiy* and *phiz*. Contour lines mark areas of equal diffraction quality. c) Overlay of the diffraction quality map on the crystal.

References

[1] J. Gabadinho, A. Beteva, M. Guijarro, V. Rey-Bakaikoa, D. Spruce, M.W. Bowler, S. Brockhauser, D. Flot, E.J. Gordon, D.R. Hall, B. Lavault, A.A. McCarthy, J. McCarthy, E. Mitchell, S. Monaco, C. Mueller-Dieckmann, D. Nurizzo, R.B.G. Ravelli, X. Thibault, M.A. Walsh, G.A. Leonard and S.M. McSweeney. *J. Synch. Rad.* **17**, 700-707 (2010).

[2] T. Warne, M.J. Serrano-Vega, J.G. Baker, R. Moukhametzianov, P.C. Edwards, R. Henderson, A.G. Leslie, C.G. Tate and G.F. Schertler, *Nature* **454**, 486-491 (2008).

[3] M.F. Incardona, G.P. Bourenkov, K. Levik, R.A. Pieritz, A.N. Popov and O. Svensson, *J. Synch. Rad.* **16**, 872-879 (2009).

goniometer axis) and *phiy* (horizontal translation)) so that the position and diffraction qualities of a previously invisible crystal are recorded (**Figure 90b**).

In many of the most challenging projects it has proved essential to be able to collect partial diffraction data sets from multiple positions within a crystal and to combine these to produce a complete data set [2]. However, intra-crystal variation in diffraction quality means that it is not always obvious, *a priori*, from which regions of a crystal partial data sets should be collected. To identify which regions of a crystal will produce the best data, we have developed an automated process combining mesh scans and on-line data analysis with an intuitive presentation of data that systematically defines the most ordered parts of a crystal. We call this process diffraction cartography. The results both map diffraction quality (as determined by EDNA [3]) to different areas of the crystal being studied and define the shape and location of the crystal. **Figure 91** shows that diffraction cartography reveals a large variation in predicted data quality across the face of a crystal of bovine F_1-ATPase (a large complex, 20 nm in the largest dimension). The results can be projected onto the optical view of the crystal clearly defining crystal shape and position as well as the best volumes for subsequent data collection.

Principal publication and authors

R.G. Efremov, R. Baradaran and L.A. Sazanov, *Nature* **465**, 441-445 (2010).

Medical Research Council Mitochondrial Biology Unit, Wellcome Trust/MRC Building, Cambridge (U.K.)

Architecture of respiratory complex I: the "steam engine" of the cell?

Complex I is the first, and largest, enzyme of the respiratory chain in mitochondria and bacteria. It transfers two electrons from NADH to quinone and couples (by an unknown mechanism) this process to the translocation of four protons across the membrane. Complex I plays a central role in cellular energy production, providing about 40% of the proton-motive force required for ATP synthesis. Complex I dysfunction has been implicated in many human neurodegenerative diseases. Mitochondrial complex I consists of 45 subunits, whilst the prokaryotic enzyme is simpler, consisting of 14 "core" subunits with a total mass of about 550 kDa. It represents a useful 'minimal' model of human complex I.

The complete structure of complex I at atomic resolution is currently unknown. Our earlier crystal structures of the

hydrophilic domain of complex I from *Thermus thermophilus* established the electron transfer pathway from NADH through flavin mononucleotide (FMN) and seven iron-sulphur (Fe-S) clusters to the likely quinone binding site at the interface with the membrane domain. The three largest hydrophobic subunits of complex I, NuoL/Nqo12, NuoM/Nqo13 and NuoN/Nqo14 (*Escherichia coli*/*T. thermophilus* nomenclature), are homologous to each other and to the Mrp antiporter family, and so are likely to participate in proton translocation.

To determine the structure of the entire enzyme, we crystallised the membrane domain of complex I from *E. coli*. The crystals contain six subunits NuoL, M, N, A, J and K (total mass 216 kDa), and lack NuoH, which dissociates readily from the complex. After extensive optimisation, the crystals diffracted to 3.9 Å resolution, with data being collected at beamlines **ID29** and **ID23-2**, as well as at the SLS. Phasing using TaBr cluster derivatives allowed us to build an α-helical model (C_α trace), consisting of 55 TM helices (**Figure 92 a,b**). A pattern of 14 TM helices repeated three times allowed us to assign these to the homologous subunits NuoL, M and N. Each subunit also contains, in the same positions, two discontinuous TM helices (shown in red and orange in **Figure 92**). Such helices are thought to be important for the function of many transporters and channels by introducing charge and flexibility into the membrane.

Unexpectedly, the structure revealed a 110 Å-long amphipathic α-helix, spanning almost the entire length of the membrane domain. We assigned this lateral helix (HL, purple in **Figure 92**) to the C-terminal extension of subunit NuoL, which is present in all species and so is likely to be functionally essential.

We also crystallised the entire complex I from *T. thermophilus* and obtained diffraction data to 4.5 Å resolution. The structure was solved by molecular replacement using the structure of the hydrophilic domain from *T. thermophilus* and the α-helical model of the membrane domain from *E. coli* as search probes. Subunit NuoH/Nqo8 was present in these crystals and was added to the model. The complete membrane domain now contains 63 TM helices and is one of the largest membrane protein complexes yet described (**Figure 92c**).

As seen in previous electron microscopy studies, full-length complex I is L-shaped. However, the exact positioning of the hydrophilic domain relative to the membrane domain is unexpected, as it results in a significant distance between the Fe-S cluster N2 and the predicted bilayer surface. Therefore, it appears necessary for the hydrophobic quinone to move out of the membrane by about 10 Å in order to be reduced by cluster N2. This is unusual and may be part of the coupling mechanism, aiding conformational changes.

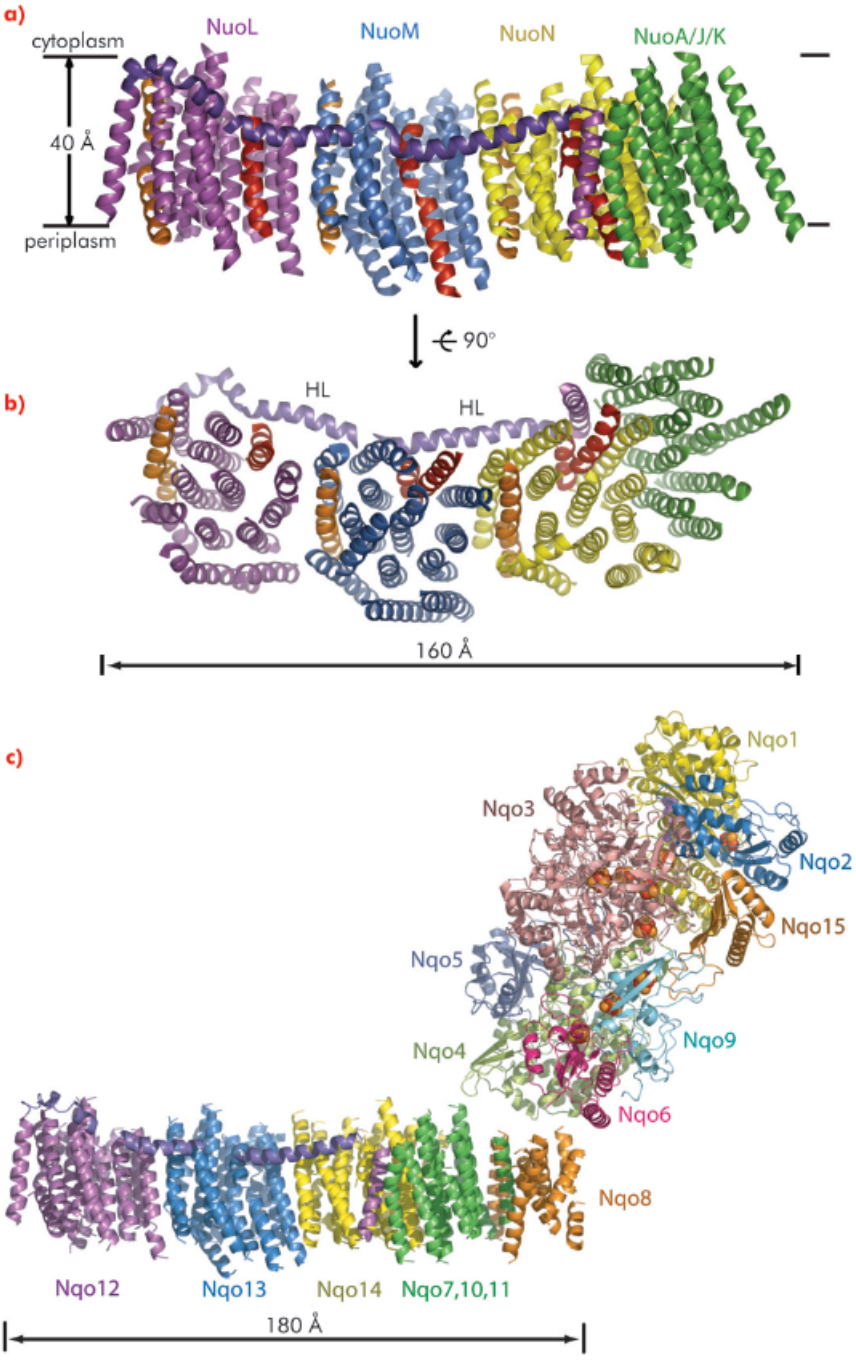

Fig. 92: The α-helical model of the membrane domain of *E. coli* complex I: a) Side view, in the membrane plane; b) View from the periplasm into the membrane. c) The structure of the entire complex I from *T. thermophilus*.

The overall architecture of the complex revealed here strongly supports the idea that proton translocation is driven by long-range conformational changes (Figure 93). It is likely that movements of several helices in the hydrophilic domain (indicated by arrows in Figure 93) produce a piston-like motion of helix HL along the membrane domain. This movement can synchronously tilt the three nearby discontinuous helices, changing the conformation of ionisable residues inside the respective proton channels and resulting in the translocation of three protons. The fourth proton per catalytic cycle may be translocated at the interface of the two domains. Thus, complex I appears to resemble a steam engine, where the energy of electron transfer is used to move a piston, which then drives, instead of wheels, a set of discontinuous helices.

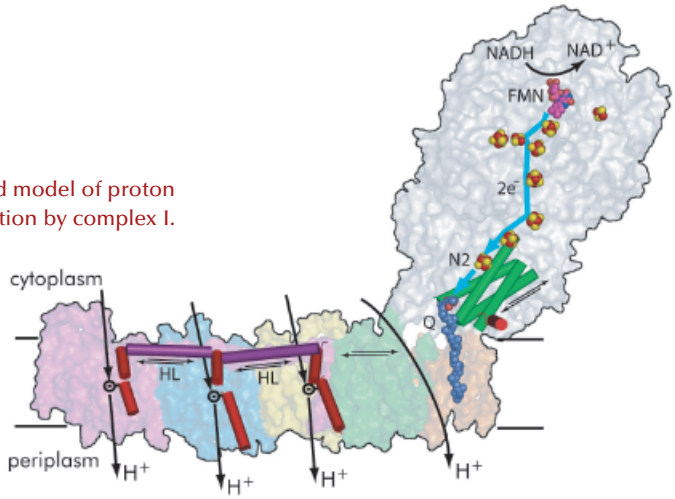

Fig. 93: Proposed model of proton translocation by complex I.

Insight into the mechanism of spider silk assembly

Principal publication and authors
G. Askarieh (a,b), M. Hedhammar (c), K. Nordling (c), A. Saenz (d), C. Casals (d), A. Rising (c), J. Johansson (c) and S.D. Knight (a), *Nature* **465**, 236-238 (2010).
(a) Department of Molecular Biology, SLU, the Biomedical Centre, Uppsala (Sweden)
(b) Department of Chemistry, Oslo University (Norway)
(c) Department of Anatomy, Physiology and Biochemistry, SLU, the Biomedical Centre, Uppsala (Sweden)
(d) Department of Biochemistry and Molecular Biology I & CIBER Enfermedades Respiratorias, Complutense University of Madrid (Spain)

Spider silk is known for its remarkable mechanical properties, combining strength, toughness, and extensibility. This high-performance biopolymer is constructed of specific proteins, spidroins, with a repetitive sequence flanked by two different conserved non-repetitive domains. Spiders have evolved an elegant silk production system in which various specialised glands are optimised to fulfil different needs. Some spiders can spin up to seven different types of silk that are used for different purposes, such as protection of the eggs in the egg-case or construction of a capture-spiral. Spidroins are stored as a highly concentrated liquid-crystalline solution ('dope') that, upon silk formation, converts into β-sheet rich structures in which inter- and intramolecular interactions between repeat regions convey strength (alanine-blocks) and elasticity (glycine-rich motifs). Understanding the mechanisms underlying spider silk production will facilitate development of silk-based biomaterials, with interesting possibilities for industrial and scientific applications.

We recently published work providing insight into how spider silk assembly is controlled and how premature spidroin aggregation prior to silk assembly is avoided. Conversion of spidroins from a highly concentrated protein dope to spider silk is believed to be triggered by gradually changing environmental conditions along the length of the spinning apparatus, including an alteration in ion composition, a lowering of the pH from neutral to below 6.3, retraction of water, and increased shear forces [1]. Recombinant miniature spidroins consisting of a few repetitive spidroin segments capped by the carboxy-terminal domain of major ampullate spidroin (MaSp) 1 from the nursery web spider *Euprosthenops australis* form metre-long fibres irrespective of pH. We discovered that the amino-terminal domain of MaSp1 (NT) serves as a relay within the physiologically relevant pH range; at neutral pH, NT can be stored at very high concentrations (> 210 mg/ml) without aggregation, but, below pH 6.4, NT forms larger protein assemblies with a hydrodynamic size of ~700 nm. NT assembly is reversible and can be blocked by a pH increase to above 6.4, and/or by introducing 300 mM NaCl. When NT is combined with other parts from the spidroin to generate minispidroins, immediate and irreversible self-assembly occurs at pH values around 6.3, whilst above pH 7

assembly is delayed (Figure 94). This inhibitory effect of NT is even more prominent at high (pH 8) and low (pH 3) pH levels where the minispidroins require days to assemble.

The 1.7 Å X-ray structure of NT, determined using data collected at **ID14-2, ID14-4, ID23-1** and **ID23-2**, revealed a symmetric homodimer of dipolar, antiparallel five-helix bundle subunits without any known structural homologues (Figure 95). The dimer interface is largely hydrophobic, and the interface residues are highly conserved throughout known spidroins. Homology modelling suggests that both the dimerisation and charge distribution observed in NT is conserved for spider silks with widely different mechanical properties and repeat unit sequences. We studied the effects of pH and salt concentration on the assembly process over the entire pH range from pH 3-11. Our results showed that specific local electrostatic interactions, that are available only around pH 6.3, are crucial for functional (wt-like) assembly of minispidroins. The crystal structure of NT revealed numerous conserved acidic residues at or near the dimer surface that could mediate electrostatic assembly interactions. We identified three conserved acidic residues that might play a role in pH-sensitive assembly and probed their role through site directed mutagenesis. We discovered that none of these residues alone are required for determining the pH of the transition from soluble to assembled material, but that two of the residues (D40 and E84) are required for wt-like assembly. Our results present a first insight into the mechanism of spider silk assembly at the atomic level. The pH sensitive relay-like behaviour of NT regulates this process by inhibiting precocious aggregation during storage, and accelerating self-assembly as the pH is lowered along the spider's silk extrusion duct.

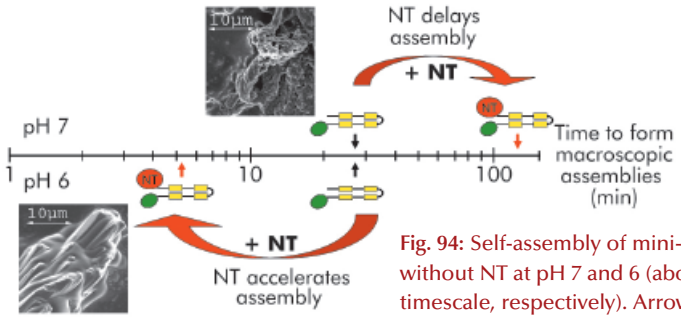

Fig. 94: Self-assembly of mini-spidroins with or without NT at pH 7 and 6 (above and below timescale, respectively). Arrows indicate when macroscopic structures were first detected. Scanning electron micrographs represent early structures of minature spidroins without NT at pH7 (above axis) and of minature spidroins with NT at pH 6 (below axis).

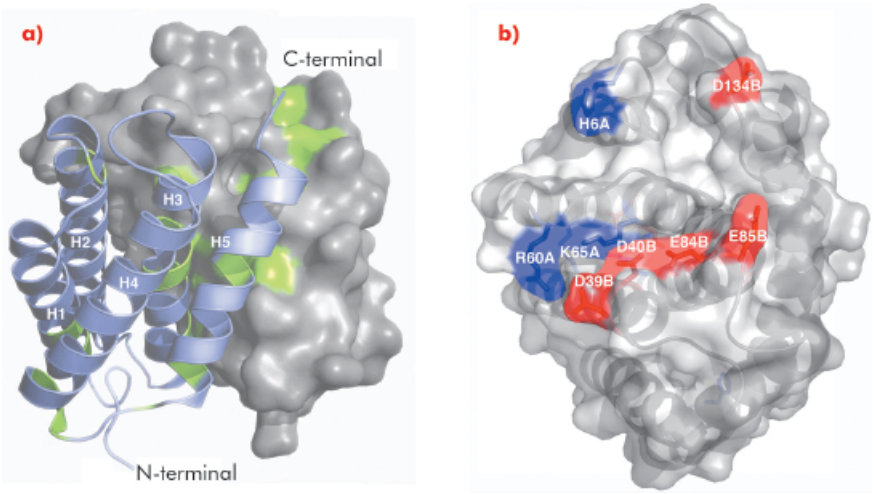

Fig. 95: a) Overall structure of NT dimer where one subunit is shown in surface representation, the other as ribbons. Strictly conserved residues are highlighted in green. b) Surface exposed charged residues shown in red (acidic) and blue (basic), viewed at 90° rotation compared to the figure to the left.

References
[1] A. Rising , M. Widhe, J. Johansson and M. Hedhammar, *Cell Mol Life Sci.* (2010); DOI:10.1007/s00018-010-0462-z.

Molecular basis of the alternating access model of membrane transport in a sodium-hydantoin transporter

Secondary active membrane transport proteins harness electrochemical gradients to facilitate the movement of small molecules or ions across membranes. They are proposed to use an alternating access model of transport [1], the principle of which is that the protein switches conformations to present the substrate binding site to alternate sides of the membrane without ever fully opening a channel from one side to the other. Due to the difficulty of elucidating the structures of these relatively unstable proteins in

Principal publication and authors
T. Shimamura (a,b,c), S. Weyand (a,b,d), O. Beckstein (e), N.G. Rutherford (f), J.M. Hadden (f), D. Sharples (f), M.S.P. Sansom (e), S. Iwata (a,b,c,d,g), P.J.F. Henderson (f) and A.D. Cameron (a,b,d), *Science* **328**, 470-473 (2010).
(a) Division of Molecular Biosciences, Membrane Protein Crystallography Group, Imperial College, London (UK)
(b) Human Receptor Crystallography Project, ERATO, Japan Science and Technology Agency, Kyoto (Japan)
(c) Department of Cell Biology, Graduate School of Medicine, Kyoto University (Japan)
(d) Membrane Protein Laboratory, Diamond Light Source (UK)
(e) Department of Biochemistry, University of Oxford (UK)
(f) Astbury Centre for Structural Molecular Biology, Institute for Membrane and Systems Biology, University of Leeds (UK)
(g) Systems and Structural Biology Center, RIKEN (Japan)

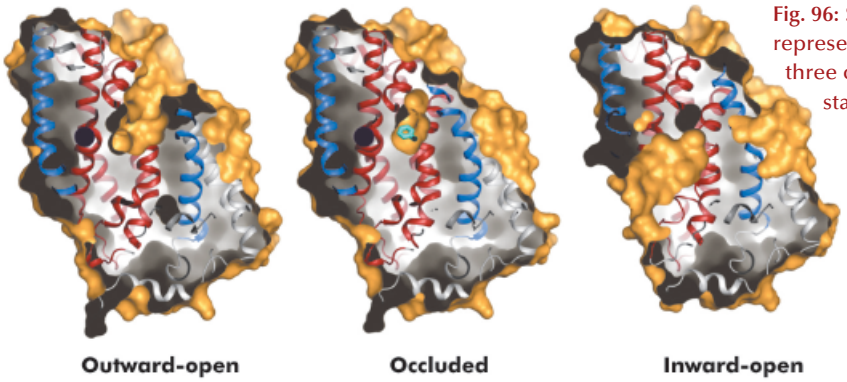

Fig. 96: Surface representations of the three conformational states of Mhp1.

multiple states there has been a paucity of molecular detail regarding the mechanism.

The hydantoin transporter from *Microbacterium liquefaciens*, Mhp1, belongs to the nucleobase cation symport-1 family responsible for transporting nucleobases into bacteria, fungi or plants. The uptake of hydantoins by Mhp1 is driven by the concentration gradient of sodium between the two sides of the membrane, probably with one sodium ion being transported for every hydantoin substrate. Sodium is present at a lower concentration inside the bacteria relative to the surrounding environment. Mhp1 is comprised of 12 transmembrane helices [2] with a fold that appears to be widespread amongst secondary active transporters [3]. Previously we reported the structures of Mhp1 in two different conformations, an outward-open form with sodium bound and an occluded form with both sodium and substrate present. We have now solved the crystal structure of an inward-open form (Figure 96). Data extending to a resolution of 3.8 Å were collected on **ID29**. The structure was solved by the selenium SAD method following location of the selenium atoms using initial phases from molecular replacement and density modification.

The refined structure clearly shows the substrate-binding site to be open on the inward-facing side and sealed completely on the outside (Figure 96).

Combining this crystal structure with those we have previously determined, we have been able to postulate how the protein can move from one state to the other. In this regard, it is convenient to consider Mhp1 as being composed of the following units: a four helix bundle, a "hash motif" so called because the four helices in this motif resemble the # sign, two "flexible helices" and the C-terminal region (Figure 97). The sodium and substrate binding sites are located at the interface of the bundle and hash motifs. Upon substrate binding in a large cavity that can be seen in the outward open structure, one of the flexible helices bends to block the substrate in its binding site thus occluding it from the outside. The protein can then undergo a more dramatic conformational change to the inward-facing state. The major difference between the outward and inward-facing structures is that the hash motif has rotated 30° relative to the bundle. This movement effectively opens the substrate binding site on the inward-facing side and further blocks it to the exterior. This movement is accompanied by some smaller changes as shown in Figure 97. The rotation of

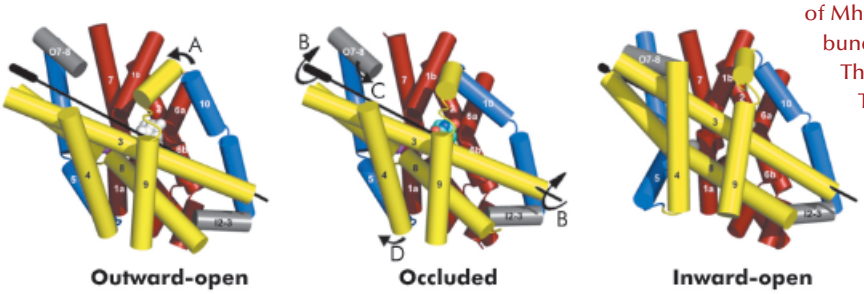

Fig. 97: Conformational changes between the three states of Mhp1. The hash motif is coloured yellow, the four helix bundle red and the flexible helices blue. The C-terminus and loops have been omitted for clarity. The arrows show the movements.
A) A flexible helix bends over the substrate.
B) The hash motif rotates around the axis shown.
C) A small extracellular helix (shown in grey) packs onto the outside of the membrane.
D) A second flexible helix bends to open the pocket on the inside.

the hash motif relative to the bundle effectively destroys both the sodium and substrate binding sites.
The binding of sodium therefore will pull the equilibrium between the inward and outward-facing states towards the latter. In this conformation the protein is primed to bind the substrate. Upon binding the substrate the outward-facing state will be destabilised allowing the protein to open up to the cytoplasm where the sodium and substrate can diffuse into the bacteria.

References
[1] O. Jardetzky, *Nature* **211**, 969-970 (1966).
[2] S. Weyand *et al.*, *Science* **322**, 709-713 (2008).
[3] J. Abramson and E. Wright, *Curr Opin Struct Biol* **19**, 425-32 (2009).

Remnant of a prebiotic machine functioning within the contemporary ribosome

Principal publication and authors
M.J. Belousoff (a), C. Davidovich (a), E. Zimmerman (a), Y. Caspi (a,b), I. Wekselman (a), L. Rozenszajn (a,c), T. Shapira (a), O. Sade-Falk (a,d), L. Taha (a,d), A. Bashan (a), M.S. Weiss (e) and A. Yonath (a), *Biochemical Society Transactions* **38**, 422–427 (2010).
(a) The Department of Structural Biology, Weizmann Institute, Rehovot (Israel)
(b) Present address: Harvard FAS Center for Systems Biology, Cambridge, MA (USA)
(c) Present address: University of Toronto, Ontario (Canada)
(d) Present address: Hebrew University of Jerusalem (Israel)
(e) EMBL Hamburg Outstation, c/o DESY, Hamburg (Germany)

Ribosomes are the universal cellular ribozymes (RNA enzymes) responsible for the translation of the genetic code into proteins. Their structures have become available during the last decade by X-ray crystallography using synchrotron radiation. Digging into these structures has revealed a remnant of a prebiotic machine for chemical bonding that is still functioning within all contemporary ribosomes.
These multi-component riboprotein assemblies are of molecular weights of 2.5 MDa and 4 MDa (for prokaryotic and eukaryotic sources, respectively). Even in bacteria they contain over 4500 RNA nucleotides and 52 different proteins. Structure analysis accompanied by biochemical assays indicated that, despite the size difference, the ribosome functional regions, namely the decoding centre and the active site (peptidyl transferase centre, PTC), are composed of ribosomal RNA (rRNA), and are highly conserved across all domains of life.

In the contemporary ribosome, the PTC is situated in the centre of a universal semi-symmetrical substructure composed of 180 nucleotides, an unusual feature of the otherwise asymmetric ribosome. The architecture of this structural element positions the ribosome's substrates in favourable stereochemistry for peptide bond formation and nascent protein elongation as well as for substrate-mediated catalysis. It thus provides all of the ribosome's catalytic contributions for peptide bond formation and confines the void required for the motions involved in substrate translocation within the PTC.

This internal symmetry substructure exists in all known ribosome high-resolution structures and its exceptionally high sequence conservation (over 95%) indicates its ancient origin. This entity has a pocket-shape structure that seems to be a relic of an ancient ribozyme, which was capable of catalysing various reactions, including peptide bond formation and non-coded amino acid polymerisation. This dimeric RNA assembly could be formed from two self-folded RNA chains of identical, similar or different sequences, spontaneously or by gene duplication or gene fusion. Based on the presumed capability of the prebiotic 'pocket-like' construct to accommodate substrates with stereochemistry enabling peptide bond formation, it is suggested that the semi-symmetrical region of the contemporary ribosome originated from a semi symmetrical entity, which we named 'proto-ribosome'.

The fold of each half of this semi-symmetrical region is similar to motifs that have been identified in various natural ribozymes (*e.g.* gene regulators, riboswitches, RNA polymerases, ribozymes catalysing phosphodiester cleavage, RNA processing and RNA modification). Some of these ribozymes are believed to be relics from the prebiotic world and hence are supposed to be sufficiently stable to survive environmental alterations and evolution stresses.

Dimerisation in a symmetrical manner could have occurred by utilising chemical complementarity obtained by tertiary interactions (*e.g.* the common GNRA system that includes the

abundant and ubiquitous 'A-minor' structural motif), or assisted by other molecules acting as small chaperones that offer stabilisation. Additional structural support could be obtained from short peptides that have high affinity to RNA, or from oligo peptides that could form structural arrangements similar to protein/RNA interactions within the contemporary ribosome. These short peptides could have been produced without carrying coded sequences. According to this suggestion, a proto-ribosome that produced peptides with amino acid composition that was sufficiently biased in order to fulfil simple tasks was provided with better fitness, thus had higher probability to be retained.

We are assessing the feasibility of a dimeric proto-ribosome capable of the formation of chemical bonds according to the following scheme. We are first testing the tendency of various RNA chains to dimerise. These are tested for their ability to bind small molecules, nucleotides and amino acids conjugated with short nucleotides, and then to form chemical bonds between them. Among the various RNA segments that have been constructed, several, albeit not all, chains with sequences resembling those observed in the current ribosome, are capable of forming dimers that may adopt a 'pocket-like' structure. Specifically, a marked preference was detected for the dimerisation of sequences resembling the P-region, including those that underwent mutational alterations by *in vitro* site-directed mutagenesis. This noticeable preference may indicate a higher stability of this portion of the symmetrical region, or its higher significance in nascent chain elongation. This is in accord with the contemporary accommodation of the initial tRNA at the P-site of the PTC, in which each half hosts a slightly different substrate.

The emergence of coded translation that includes the growing complexity of the ribosome into the size and shape allowing programmed translation occurred after those oligopeptides that were produced accidentally but found useful in the RNA world, survived and formed some kind of replication machinery. Co-evolution of the proto-ribosome into the modern complex molecular machine dictated the production of carriers that could decode this code while bound to the cognate amino acid, namely the tRNA molecules.

N-myristoyl transferase inhibitors as new leads to treat neglected diseases

In the developing world, over 350 million people are at risk from neglected diseases. Existing drugs to treat diseases such as African sleeping sickness, Chagas' disease, *Leishmaniasis,* and Malaria are often expensive, difficult to administer, unsafe and increasingly ineffective due to development of resistance. The parasites that give rise to these neglected diseases are well understood but this knowledge has not yet been translated into modern therapeutics for such diseases.

Protein *N*-myristoylation is a ubiquitous eukaryotic co- and post-translational modification and is required for membrane targeting and biological activity of many important proteins. The *N*-myristoylation reaction, *i.e.*, the transfer of myristic acid from myristoyl-coenzyme A (CoA) to the amino group of *N*-terminal glycine residues within specific sequence contexts, is catalysed by the enzyme myristoyl-CoA: protein *N*-myristoyltransferase (NMT) [1]. NMT has been shown by gene knockout and RNAi to be essential for viability of the parasites *Leishmania major* and *Trypanosoma brucei*, therefore it has been identified as a viable target for the development of novel therapeutics [2]. A diversity-based library of 62000 compounds was therefore screened against NMT from *T. brucei* (TbNMT) yielding lead-like, chemically tractable hits. One hit series, based upon a pyrazole sulphonamide core, was

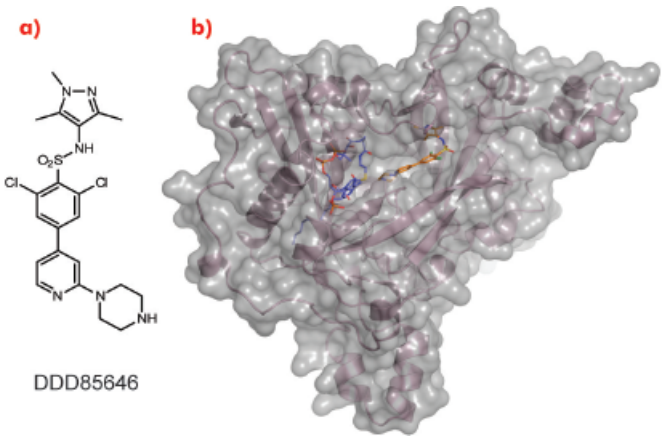

Fig. 98: a) Chemical structure of DDD85646. b) the crystal structure of LmNMT (pink ribbon, grey surface) in complex with myristoyl coA (blue C atoms) and DDD85646 (gold C atoms).

developed to generate a lead compound DDD85646 that showed on-target potencies of 2 nM.

As a crystal structure of TbNMT has not yet been elucidated, we used *Leishmania major* NMT (LmNMT) as a structural surrogate due to its high level of sequence similarity to TbNMT, especially within the active site region. Our lead series of inhibitors also showed similar levels of potency against LmNMT as against TbNMT. The crystal structure of the ternary complex of LmNMT with bound co-factor myristoyl CoA and our lead molecule DDD85646 was then solved using data measured at beamline **ID14-1**. This structure, refined to a resolution of 1.6 Å, showed the pyrazole sulphonamide ligand DDD85646 to occupy the peptide binding cleft of LmNMT (**Figure 98**).

Comparison of the crystal structure of the ternary complex to that previously reported for *Saccharyomyces cerevisiae* NMT (ScNMT) in complex with a non-hydrolysable myristoyl CoA analogue and a prototypical substrate peptide GLYASKLA (PDB 1IID) shows that DDD85646 mimics the key recognition interactions between enzyme and peptide (**Figure 99**). The basic centre of the piperazine moiety mimics the N-terminal amide of the substrate peptide, interacting with the C-terminal carboxylate via a tightly bound water molecule. The sulphonamide forms a water bridged interaction with the backbone amide of Gly 397 and the side chain of His 219, with the water molecule occupying a similar position to the serine side chain of the substrate peptide. The sulphonamide moiety induces a pronounced kink in the molecule, allowing the trimethyl pyrazole moiety to pack into a hydrophobic cleft, forming a hydrogen bond with the side chain of Ser 330.

Regular access to ESRF beamlines has allowed us to use structural information to confirm that our novel small molecule DDD85646 binds in the active site of the target protein (NMT). Ongoing studies to identify novel templates and privileged binding pockets using fragment-based strategies are also facilitated by access to the high quality MX beamlines at the ESRF. This allows us to guide the development of chemical series to further optimise our target efficacy and selectivity to generate molecules suitable for clinical development.

Principal publication and authors
J.A. Frearson (a), S. Brand (a), S.P. McElroy (a), L.A.T. Cleghorn (a), O. Smid (a), L. Stojanovski (a), H.P. Price (d), M.L.S.Guther (a), L.S. Torrie (a), D.A. Robinson (a), I. Hallyburton (a), C.P. Mpamhanga (a), J.A. Brannigan (c), A.J. Wilkinson (c), M. Hodgkinson (d), R.Hui (e), W Qiu (e), O.G. Raimi (b), D.M.F van Aalten (b), R. Brenk (a), I.H. Gilbert (a), K.D. Read (a), A.H. Fairlamb (a), M.A.J. Ferguson (a), D.F. Smith (d) and P.G. Wyatt (a), *Nature* **464**, 728-732 (2010).
(a) Division of Biological Chemistry and Drug Discovery, College of Life Science, University of Dundee (UK)
(b) Division of Molecular Microbiology, College of Life Science, University of Dundee (UK)
(c) Structural Biology Laboratory, Department of Chemistry, University of York (UK)
(d) Centre for Immunology and Infection, Department of Biology and Hull York Medical School, University of York (UK)
(e) Structural Genomics Consortium, University of Toronto (Canada)

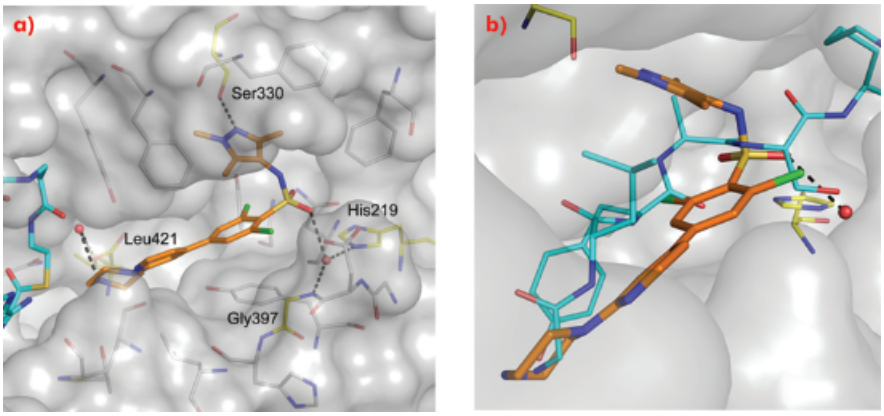

Fig. 99: a) The mode of binding of DDD85646 (gold C atoms) to LmNMT (grey surface). Key water molecules are shown as red spheres, H-bonds as black dashed lines. Protein residues that interact with the ligand are highlighted (yellow C atoms) and labelled for clarity. b) DDD85646 mimics the binding mode of the substrate peptide GLYSAKLA (cyan C atoms).

References
[1] T.A. Farazi, G. Waksman and J.I. Gordon, *J. Biol. Chem.* **276**, 39501-39504 (2001).
[2] H.P. Price, M.R. Menon, C. Panethymitaki, D. Goulding, P.G. McKean and D.F. Smith, *J. Biol. Chem.* **278**, 7206-7214 (2003).

Principal publication and authors
A. Amunts, H. Toporik, A. Borovikova and N. Nelson, *J Biol Chem.* **285**, 3478-3486 (2010).
Department of Biochemistry, George S. Wise Faculty of Life Sciences, Tel Aviv University (Israel)

Towards atomic resolution of the plant photosystem I supercomplex

The conversion of solar energy into chemical bonds by the photosynthetic machinery of plants, green algae and cyanobacteria is essential for the survival of all higher life forms.

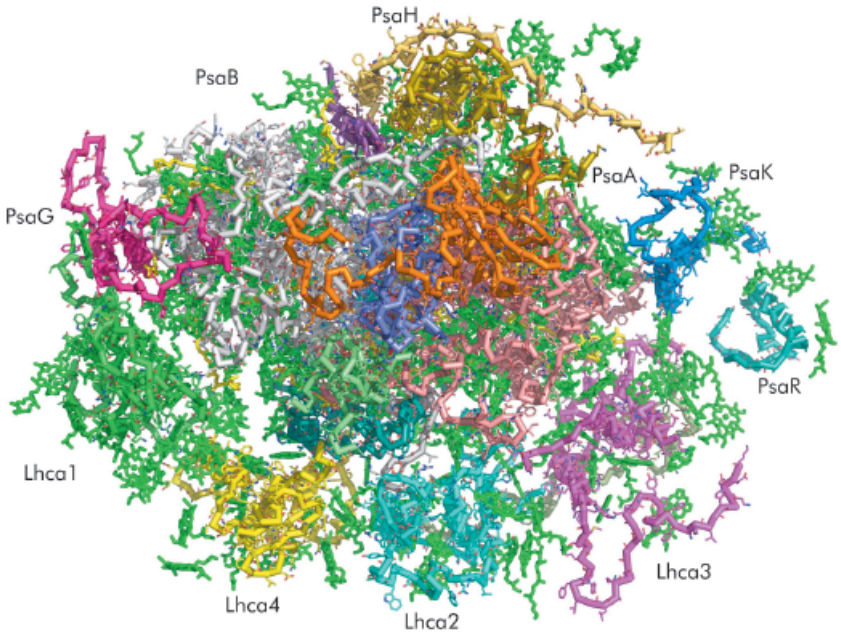

Fig. 100: A view from the stroma of the at 3.3 Å crystal structure of plant PSI. The 14 subunits of the reaction centre and the four light-harvesting proteins (Lhca1 - Lhca4) are depicted in different colours. The chlorophylls and other prosthetic groups are as described in Figure 101.

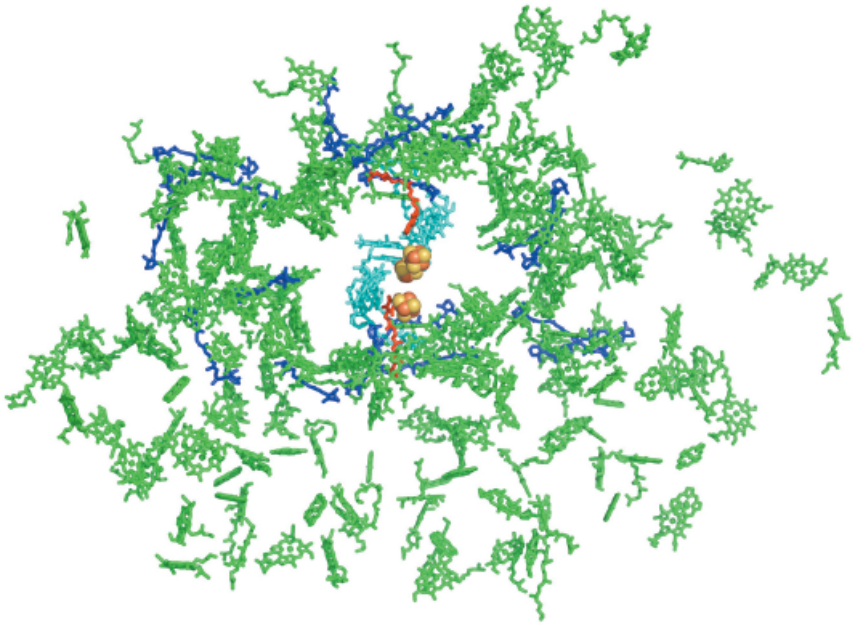

Fig. 101: A view from the stroma on the prosthetic groups currently modelled in the structure of the plant PSI supercomplex. Chlorophyll moieties are coloured in green or, in the case of those involved in electron transfer, cyan. The electron density of 109 of the chlorophyll molecules modelled exhibited complete or partial phytol chains thus allowing assignment of the orientation of their QX and QY transition dipole moments. The 2 phyloquinones modelled are shown in red and the 18 carotenoids moieties in blue. The 3 Fe_4S_4 clusters are depicted as yellow and brown spheres.

The primary event of this process - light induced charge translocation - is catalysed by photosystem I (PSI) and photosystem II (PSII), two multisubunit protein complexes embedded in the thylakoid membrane and acting in series. PSI harnesses light energy to transfer an electron from the soluble copper protein, plastocyanin, at one side of the membrane to ferredoxin and eventually NADPH on the opposite side. In the dark, NADPH (and ATP) provides the energy for assimilation of CO_2 into carbohydrates. In 2003, the structure of plant PSI was solved at 4.4 Å resolution [1]. The components visible in this crystal structure were a β-carbon model of 16 proteins, including 45 transmembrane helices, 2 phyloquinones, 3 Fe_4S_4 clusters and 167 chlorophyll molecules.

Continuous and progressive improvement of crystal quality and the ready access to ESRF resulting from the BAG programme have enabled recent determinations of the crystal structure of PSI first to 3.4 Å [2] then to 3.3 Å resolution. One of the most important factors that allowed higher resolution data to be obtained was the availability of the micro-focussing MX end station **ID23-2**. We were among the first to realise the advantage of using a highly-focussed beam with relatively large samples. For PSI, average crystal dimensions are 100×30×5 μm^3 and, because they are so thin, they have a tendency to bend. This tendency results in elongated and much less clear spots in diffraction patterns taken with larger X-ray beams. The high intensity micro-focussed beam used together with a recently developed helical-motion data collection capability resulted in much better data sets that revealed several components of PSI that had not been detected in previous crystal structures (**Figure 100**).

The current 3.3 Å resolution plant PSI crystal structure reveals 18 protein subunits containing 46 transmembrane helices, 173 chlorophylls, 18 β-carotenoids, 3 Fe_4S_4 clusters and 2 phyloquinones (**Figure 101**).

Ten of the 12 plant PSI reaction centre core complex subunits (PsaA, PsaB, PsaC, PsaD, PsaE, PsaF, PsaI, PsaJ, PsaK, and PsaL) are closely related to those of the PSI of cyanobacteria. Other subunits (PsaG and PsaH) have unique structural functions related to interactions of the reaction centre core with four light-harvesting complexes of LHCI (Lhca1 - Lhca4) and provide a potential site of interaction with LHCII. The four LHCI proteins assemble into two dimers arranged in series and form a half-moon shaped belt that docks to the subunit F side of the reaction centre. The association of the PSI core with the LHCI belt is both weak and asymmetric (Figure 100). Only one of the four Lhca proteins (Lhca1) is firmly attached to the reaction centre. It may serve as an "anchor" for the assembly of the other Lhca monomers. Formation of the LHCI dimers and the interactions between them does not involve transmembrane helices. However, the solvent exposed C and N termini of each Lhca monomer attach to solvent exposed loops on the neighbouring monomer.

The structural information on proteins, co-factors and the interactions between them described in this work provides a significant step towards our understanding of how the very large PSI supercomplex has evolved. Nevertheless, only atomic resolution structures of the two components of PSI - the reaction centre and the LHCI - will allow calculations designed to explain the unprecedented quantum yield of this PSI system. We hope that this daunting goal will be achieved before too long.

References
[1] A. Ben-Shem, F. Frolow and N. Nelson, *Nature* **426**, 630-635 (2003).
[2] A. Amunts, O. Drory and N. Nelson, *Nature* **447**, 58-63 (2007).

Structural basis of DNA binding by human mitochondrial mTERF

Principal publication and authors
N. Jiménez-Menéndez (a,b), P. Fernández-Millán (a), A. Rubio-Cosials (a), C. Arnan (a,b), J. Montoya (c), H.T. Jacobs (d), P. Bernadó (b), M. Coll (a,b), I. Usón (a,e) and M. Solà (a), *Nat. Struct. Mol. Biol.* **7**, 891 (2010).
(a) Institute Molecular Biology Barcelona-CSIC (Spain)
(b) Institute of Research in Biomedicine (Spain)
(c) Biochemistry and Molecular and Cellular Biology, University of Zaragoza (Spain)
(d) Institute of Medical Technology and Tampere University Hospital, University of Tampere (Finland)
(e) Institució Catalana de Recerca i Estudis Avançats (Spain)

Human mitochondrial DNA (mtDNA) is a circular double chain of 16.6 kDa. Its regulation is carried out by nuclear-encoded proteins, including the regulator mTERF, which binds to several strategic mtDNA sites where it controls processes such as transcription termination or replication pausing [1]. mTERF shows its highest affinity for 28 base pairs (bp) found in the $tRNA^{Leu(UUR)}$ gene. We set out to characterise the structural basis of this interaction and crystallised two protein constructs, full-length mTERF and mTERF-ΔN (43 residues shorter than the mature protein), in complex with oligonucleotides of 15 and 12 bp, respectively, harbouring the binding site.

The crystal structure of mTERF (solved using diffraction data collected on **ID14-4**, **ID23-1**, **ID29** and **ID23-2**) shows that the fold of the protein consists of a central region made up of nine structural repeats, TERF-I to IX, which correspond to tandem sequence motifs identified throughout the mTERF family, flanked by a N-terminal extension and a C-terminal α-helix, C (Figure 102a). Within each TERF repeat, roughly 35 amino acids fold into three α-helices arranged in a left-handed (*zurdo* in Spanish) triangular superhelix (Figure 102b, top). The nine repeats successively rotate, building up a solenoid-like structure - the zurdo domain - which further twists to the right, presenting a convex and a concave face. Previously characterised helical-repeat solenoids (Armadillo, HEAT or pumilio domains) show a right-handed helical connectivity (Figure 102b, bottom), while left-handed

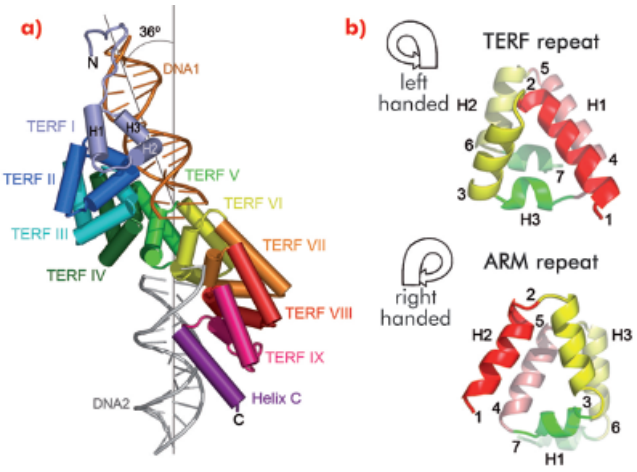

Fig. 102: a) Each of the repeats TERF-I to IX consist of three helices, H1, H2 and H3. In the crystal structure a single mTERF molecule binds two short dsDNA oligonucleotides, DNA1 (orange) and DNA2 (grey), related by ~36°.
b) Left- and right-handed superhelices. From point 1 on, the TERF superhelix curves to the left while the ARM repeat shows right-handed tracing.

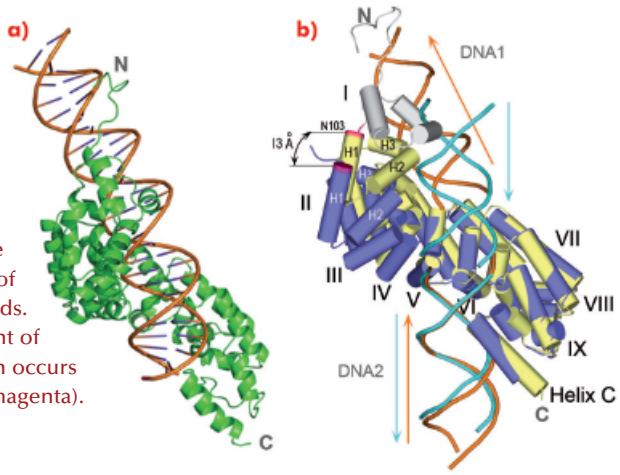

Fig. 103: a) The structural model showing best agreement to the experimental SAXS data. b) Comparison of mTERF (yellow) and mTERF-ΔN (blue) following a superposition of the C-terminal subdomains of their Zurdo solenoids. The maximal displacement of the N-terminal subdomain occurs at Asn103 (magenta).

superhelices have been previously observed only in small helical bundles. The combination of left-handed helical connectivity with tandem propagation is thus unique to mTERF.

Two symmetrically-related 15 bp double-stranded oligonucleotides (DNA1 and DNA2) bind at positively-charged regions of the N- and C-terminal subdomains of the TERF repeats (repeats I to VI, and VIII to IX plus helix C, respectively) of a single protein molecule (Figure 102a). DNA1 and DNA2 do not contact each other and are oriented at an angle of 36°. Eighteen residues are engaged in non-specific interactions with both dsDNA backbone phosphates. In addition, Glu165, Arg169 and Arg202 at the N-terminal subdomain contact three conserved guanines; Arg387 from C-terminal helix C interacts with three bases of DNA2. Additional contacts contribute to stabilising the termini of DNA1 and DNA2. In general, the mTERF residues that contact the DNA are conserved throughout the vertebrate MTERF1 subfamily, suggesting similar modes of protein-DNA interaction for this class of protein.

We also obtained full-length mTERF in complex with longer dsDNA oligonucleotides. However, these did not crystallise. To assess how a continuous dsDNA oligonucleotide containing both DNA1 and DNA2 could be bound by mTERF, we analysed the structure of the protein in complex with a DNA oligonucleotide of 28 bp in solution using SAXS. The model that best fitted the experimental data showed the concave surface of mTERF wrapping around the major groove of the dsDNA, which is bent (Figure 103a). The model also suggests that the C-terminal subdomain of mTERF slightly rearranges to accommodate the longer DNA. Such flexibility in mTERF is supported by the consistent, slight variation of the angle between repeats when comparing the structures of mTERF and mTERF-ΔN solenoids, whose pitch differ by 13 Å (Figure 103b).

In summary, nine left-handed helical TERF repeats give rise to a twisted solenoid structure that binds a continuous bent dsDNA. The DNA binding mode observed is likely to be similar to that of mTERF binding to the mtDNA termination site *in vivo*. Other TERF family members are also likely to contain zurdo domains but will also have member-specific features in order to accomplish particular functions.

Reference
[1] A.K. Hyvarinen *et al., Nucleic acids research* **35**, 6458-6474 (2007).

Discovery of a marine bacterial porphyranase: from gene to structure and beyond

Principal publication and authors
J.H. Hehemann, G. Correc, T. Barbeyron, W. Helbert, M. Czjzek and G. Michel, *Nature* **464**, 908-912 (2010).
Végétaux Marins et Biomolécules, UMR7139 CNRS-UPMC, Station Biologique de Roscoff, (France)

The recent availability of genomic data on heterotrophic marine bacteria emphasises the crucial role that microbes play in the global carbon cycle. However, the massive presence in these genomes of proteins of unknown function hampers our understanding of the detailed mechanisms by which this carbon cycle is fine-tuned. Moreover, genome data from marine organisms are essentially annotated in light of the biochemical knowledge accumulated on bacteria and fungi decomposing terrestrial plants. But marine algal polysaccharides clearly differ from their terrestrial counterparts [1] and their associated enzymes usually constitute novel protein families, as described in the carbohydrate-active enzyme database (CAZy, http://www.cazy.org).

We have applied a knowledge-based strategy for the structural and biochemical characterisation of candidate 'hypothetical conserved proteins' or members of phylogenetic sub-families to identify new enzyme functions, missing in the metabolic pathways by which marine polysaccharides are degraded in the marine environment. In this way we selected several potential enzymes within the GH16 polyspecific glycoside hydrolase family with the aim of expressing them in *E. coli* and of performing enzymatic activity screening. Two of the enzymes selected displayed high activity, measured through the release of reducing sugars from a specific red algal polysaccharide called porphyran. Their crystal structures, in complex with substrate molecules, were then determined using diffraction data collected at the ESRF (**ID23, ID14-1 and BM30A**). These allowed the unambiguous assignment of residues responsible for the new substrate specificity (Figure 104), the hydrolytic cleavage of porphyran.

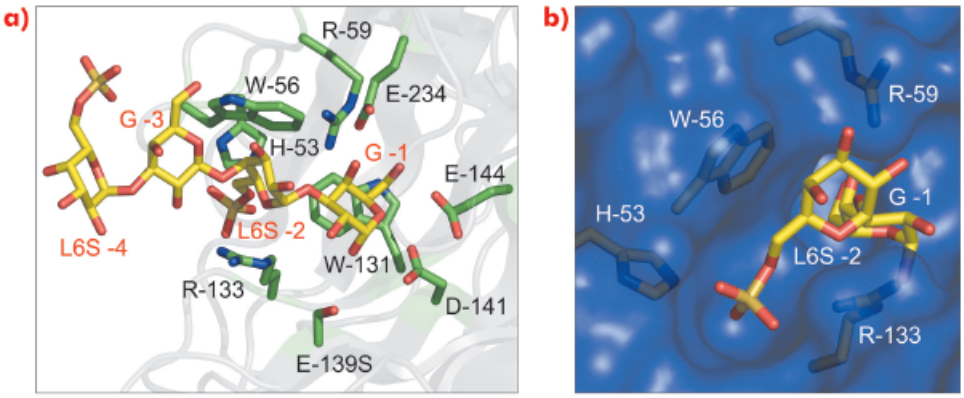

Fig. 104: Crystal structure of porphyranase A (PorA) from *Z. galactanivorans*. a) Ribbon and stick representation of an inactivated PorA mutant in complex with porphyrotetraose. Crucial residues that determine the substrate specificity are labelled. b) Surface representation of mutant PorA in complex with porphyrotetraose highlighting a specific pocket that accommodates the sulphate group on the sugar unit (L6S) in sub-binding site -2.

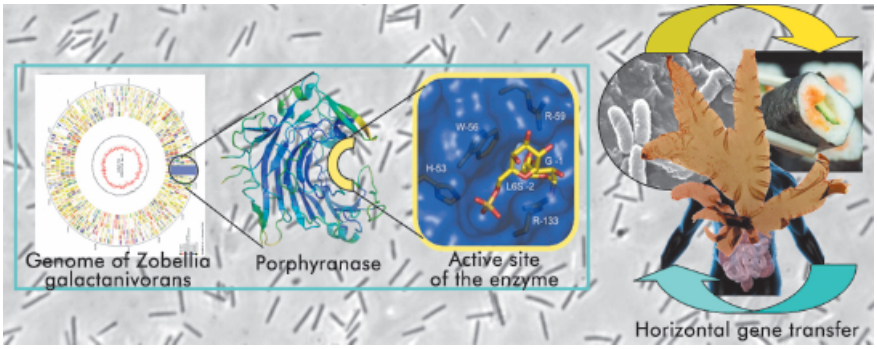

Fig. 105: Schematic representation of our strategy 'from the genome to the structure' and the horizontal gene transfer between marine and Japanese human gut bacteria via the red algae *Porphyra*.

Curious about the distribution of this enzymatic activity in the environment, we screened GenBank using BLAST searches to find homologous proteins having the crucial residues that make them porphyranases. To our surprise, these enzymes were not only present in marine bacteria but also in *B. plebeius*, a human gut bacterium, isolated from Japanese individuals. In depth phylogenetic analyses and pushing our BLAST screening to include recently available metagenomic data collected from soil, 'open ocean' or human gut of North American [2] and Japanese [3] individuals revealed that the presence of these enzymes was currently restricted to coastal marine bacteria – and to a single human gut species!

Where was the link? We know from many other studies that intestinal microorganisms, collectively known as the intestinal 'microbiota' are, to a large extent, specialised in digesting dietary fibres, such as starch and cellulose, for which the human genome does not contain any degradative enzymes. It is likely that significant competition occurs for these substrates. Indeed, genes dedicated to carbohydrate acquisition and degradation, such as those encoding glycoside hydrolase enzymes, are prominent in metagenomic data sets of gut microbiota and are also enriched in the genomes of many species residing in the intestine, including members of the phylum Bacteroidetes [4]. Our work shows that one apparent strategy for success of bacteria in the intestinal ecosystem is to become proficient at using the dietary polysaccharides that the host consumes. This proficiency can be acquired through lateral gene transfer, a strategy known to be at the basis of evolutionary adaptation. In our example, the detailed analyses of the gene context of the porphyranases, present only in marine and gut bacteria, shows that a horizontal gene transfer – from a marine bacterium to a human gut bacterium has most probably occurred. We believe that seaweed, which is prevalent in the Japanese diet – including the *Porphyra*-derived nori, used to wrap sushi – was probably the source of the marine microorganism that introduced the useful genes acquired by the human gut bacterium (Figure 105).

References

[1] B. Kloareg and R.S. Quatrano, *Oceanogr Mar Biol Ann Rev* **26**, 259-315 (1988).

[2] P.J. Turnbaugh, M. Hamady, T. Yatsunenko *et al.* and J.I. Gordon, *Nature* **457**, 480-4 (2009).

[3] K. Kurokawa, T. Itoh, T. Kuwahara *et al.* and M. Hattori, *DNA Research* **14**, 169-81 (2007).

[4] E.C. Martens, N.M. Koropatkin, T.J. Smith and J.I. Gordon, *J. Biol. Chem.* **284**, 24673-24677 (2009).

Principal publication and authors
A. Garcia-Pino (a,b), S. Balasubramanian (c), L. Wyns (a,b), E. Gazit (d), H. De Greve (a,b), R.D. Magnuson (c), D. Charlier (e), N.A.J. Van Nuland (a,b) and R. Loris (a,b), *Cell* **142**, 101-110 (2010).
(a) Dept. of Molecular and cellular Interactions, Flanders Institute for Biotechnology (VIB), Brussels (Belgium)
(b) Structural Biology Brussels, Vrije Universiteit Brussel (Belgium)
(c) Department of Biological Sciences, University of Alabama in Huntsville (USA)
(d) Department of Molecular Microbiology and Biotechnology, Tel Aviv University (Israel)
(e) Erfelijkheidsleer en Microbiologie, Vrije Universiteit Brussel (Belgium)

A prokaryotic transcription regulation mechanism involving allosteric coupling between intrinsically disordered domains

Regulation of transcription is a fundamental process common to all kingdoms of life. Transcription regulation in eukaryotes, however, is generally considered to be significantly more complex than the corresponding mechanisms used by prokaryotes. In particular, eukaryotic transcription regulation makes an abundant use of intrinsic disorder, leading to the concept that eukaryotic transcription regulators are malleable machines that adapt themselves to recognise different targets in response to environmental or temporal cues. The presence of intrinsic disorder in prokaryotes is less well pronounced and was not generally thought to be crucial for transcription regulation. Transcription regulation in prokaryotes is known mostly via a limited number of well-studied examples, such as the choice between a lytic or a lysogenic cycle for phage λ.

Many transcriptional mechanisms in prokaryotes remain unexplored. An interesting example is regulation by conditional co-operativity in toxin-antitoxin (TA) modules. TA modules are stress response elements where a growth regulator or inducer of altruistic cell death (the toxin) is kept under control of a second protein (the antitoxin) which couples toxin neutralisation to transcription regulation (Figure 106). TA modules are auto-regulated. The antitoxin contains a DNA binding domain flanked by an intrinsically disordered toxin-binding domain. DNA binding by the antitoxin is modulated by the toxin. In the absence of the toxin, its affinity for the operator DNA is insufficient for efficient repression. Low ratios of toxin increase this affinity significantly, leading to tight repression. At higher ratios of toxin to antitoxin, the affinity of the repressor complex weakens again and transcription is fired up. This unique mechanism, termed "conditional co-operativity", allows the cell to maintain a delicate balance between toxin and antitoxin without risking accidental toxin activation, which may lead to cell death.

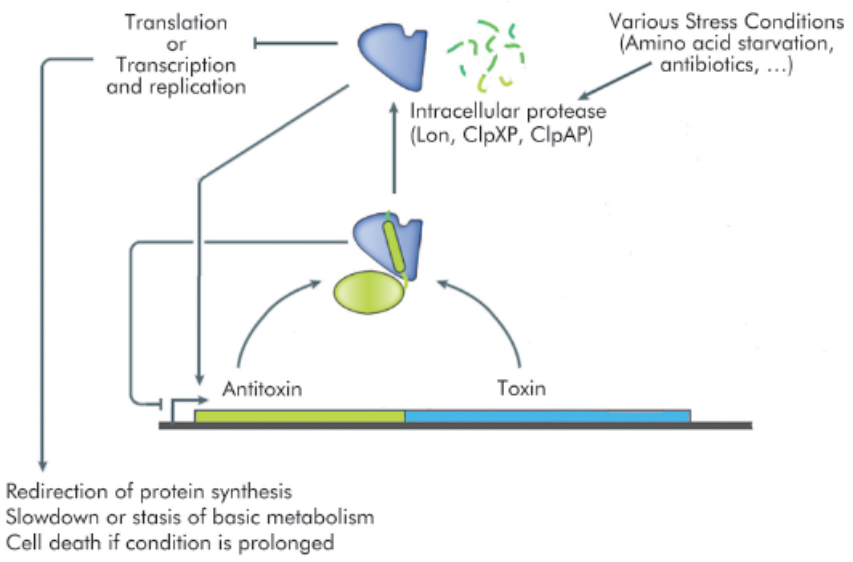

Fig. 106: Schematic diagram of a toxin-antitoxin module. Both toxin and antitoxin genes are transcribed from a single operon. The protein products form a complex that acts as an autorepressor. External stress signals activate intracellular proteases that degrade the antitoxin. This results in release of the toxin, which typically interferes with translation, transcription or replication. Excess of toxin also induces transcription of the TA operon, allowing the balance between toxin and antitoxin to be restored.

Using the *phd/doc* toxin-antitoxin module on bacteriophage P1 as a model system, we were able to propose a consistent molecular model that explains conditional co-operativity (Figure 107). We demonstrated experimentally that the transcription factor Phd contains a significant amount of disorder in both its domains and that this disorder is crucial for the regulation of the operon. Phd exists in an equilibrium between two conformational states: a DNA binding competent state that is highly ordered and an inactive state that contains significant disorder. Binding of Doc to the intrinsically disordered C-terminal domain of Phd structures the N-terminal DNA binding domain of Phd. Thus, allosteric coupling occurs between two disordered biding sites, a phenomenon predicted on theoretical grounds but never before observed experimentally.

The crystal structure of the repressing Phd/Doc complex shows a Doc monomer sandwiched between two Phd dimers. In the non-repressing

complex, a different architecture is observed with a Phd dimer sandwiched between two Doc monomers. The potential to create stoichiometrically different complexes coupled to a switch between a low and a high affinity interaction allowed us to propose a model that explains regulation by conditional co-operativity, where Doc acts as a co-repressor at low Doc to Phd ratios and as a de-repressor at high Doc to Phd ratios.

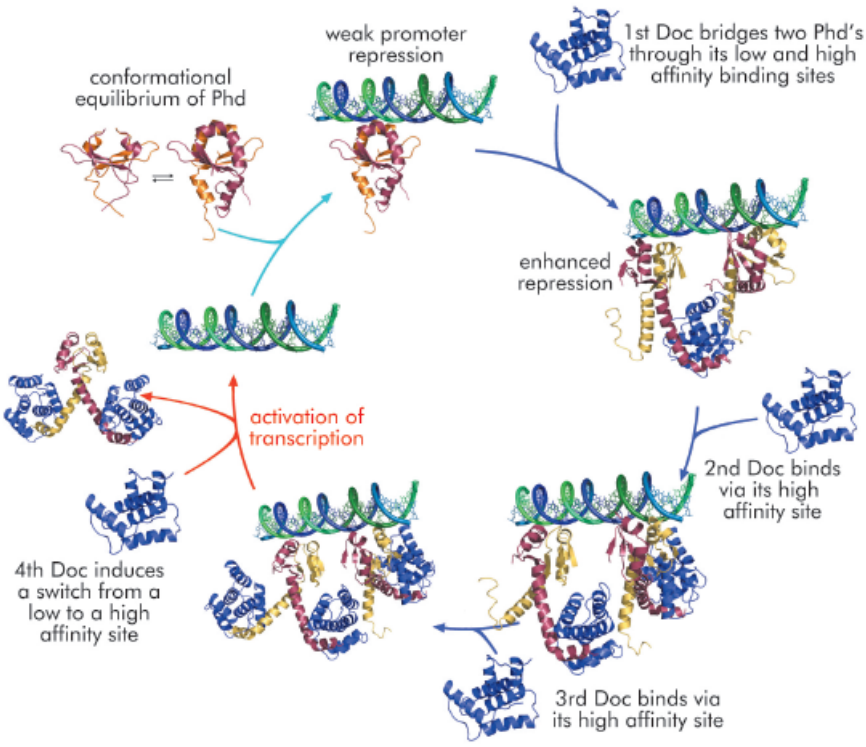

Fig. 107: Schematic diagram of the regulation mechanism of the *phd/doc* operon. Phd exists in two conformational states and binding of Doc drives the equilibrium towards the state that is competent for DNA binding. The operator DNA contains two binding sites for Phd. Bridging of two Phd dimers by Doc increases affinity for DNA at low Doc to Phd ratios. When Doc reaches a certain threshhold, a switch between a low (L) to high (H) affinity interaction creates a complex that loses its DNA interacting capacity, leading to de-repression of the operon.

Activating the AP2 clathrin adaptor complex

Compartmentalisation is a defining characteristic of eukaryotic cells that allows recognition events and chemical reactions to take place in distinct sub-cellular environments that are topographically equivalent to the extracellular space but within a cell's external boundary. All signals, nutrients and pathogens that require access to the cell's cytoplasm must cross a membrane and all contact with other cells and components of the blood and immune system must occur on a membrane's extracellular side.
A membrane's functions and consequently its identity is largely defined by the transmembrane proteins embedded in it. The localisation and movement of transmembrane proteins between the cell's various membranes is carried out by the cell's vesicular transport system.

Coated transport vesicle formation requires the complex interplay of many proteins that are recruited from the cytoplasm, the membrane itself and the many types of transmembrane protein cargo that need to be selected for inclusion into the vesicle. Cargo is typically selected by the binding of short, linear amino acid motifs within the cytosolic portions of cargo to components of vesicle coats. Clathrin-coated vesicles (CCVs) mediate many post-Golgi trafficking routes including internalisation from the plasma membrane, termed clathrin-mediated endocytosis, and can be considered as having a 3-layered structure.
The AP2 adaptor complex is a heterotetramer (subunits named α/β2/μ2/σ2) and is the most abundant endocytic clathrin adaptor [1].
It crosslinks the outer polymeric clathrin scaffold of endocytic CCVs to their inner membrane layer by binding directly both to the membrane phospholipid PtdIns4,5P_2 and to cargo containing YxxΦ or ExxxLL motifs.
In the 'locked' cytosolic form of the AP2 adaptor complex, whose crystal structure was determined from data collected at ESRF in 2002 [2], the binding sites for both YxxΦ motifs (on the C-terminal domain of the μ2 subunit, C-μ2) and [ED]xxxL[LI] motifs (on the σ2 subunit) are blocked by parts of β2 subunit. Thus, away from the membrane AP2 is unable to bind to either of its cognate cargo motifs.

Principal publication and authors
L.P. Jackson (a), B.T. Kelly (a), A.J. McCoy (a), T. Gaffry (b), L.C. James (c), B.M. Collins (d), S. Höning (c), P.R. Evans (b) and D.J. Owen (a), *Cell* **141**, 1220-1229 (2010).
(a) Cambridge Institute for Medical Research, University of Cambridge (UK)
(b) Institute of Biochemistry I, University of Cologne (Germany)
(c) Medical Research Council Laboratory of Molecular Biology, Cambridge (UK)
(d) Institute for Molecular Bioscience, The University of Queensland, Brisbane (Australia)

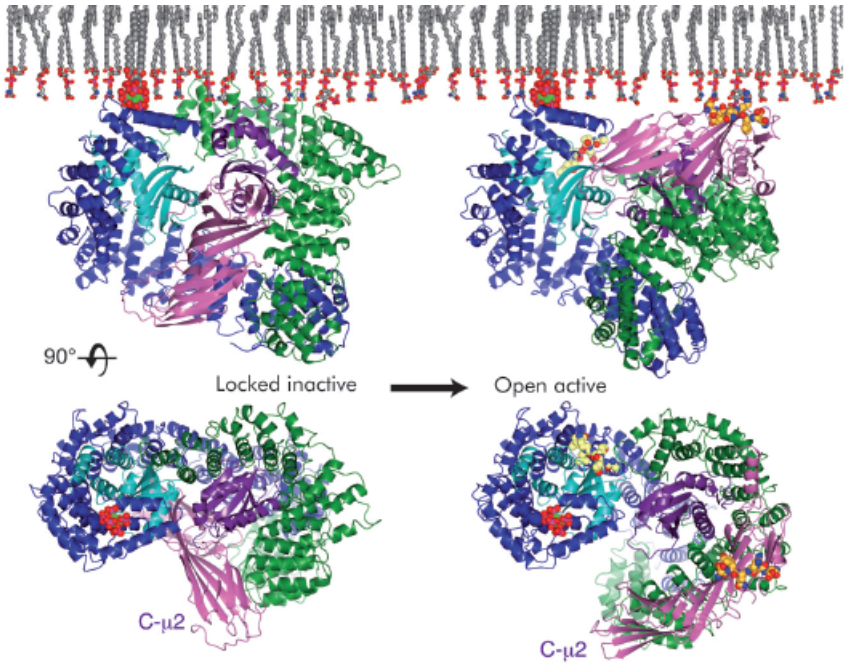

Fig. 108: The conformational changes observed upon activation of AP2 viewed parallel to the membrane (top) and 'through the membrane' (bottom). Subunits are coloured as follows: α (dark blue), β2 (dark green), μ2 (purple) and σ2 (cyan). The endocytic amino acid motifs YxxΦ and ExxxLL are coloured in orange and gold respectively. The membrane is shown in grey.

The crystal structure of the open, motif-liganded form of the AP2 adaptor complex was recently determined from data collected at beamline **ID29**. Here, when compared to the structure of the locked form, C-μ2 undergoes a rotation of 130° and a translation of 40 Å to become relocated to an orthogonal face of the complex (**Figure 108**).
The previously unstructured μ2 linker that connects C-μ2 to the rest of the complex becomes helical and binds back onto the complex.
Four PtdIns4,5P_2 and two endocytic motif-binding sites on AP2 also become co-planar, facilitating their simultaneous interaction with a PtdIns4,5P_2/cargo-containing membrane. The conformational changes observed result in the unblocking of both motif-binding sites allowing them to bind cargo, which can freely diffuse into their binding sites through the plane of the membrane. Polarisation anisotropy measurements show that 99.9% of AP2 exists as the locked inactive form in the cytoplasm and that the structural rearrangements that facilitate cargo binding are driven by the association of AP2 with PtdIns4,5P_2-containing membranes. It therefore appears that AP2 functions as a plasma membrane-activated switch for endocytic cargo recognition. This ensures that AP2 binds only to cargo when YxxΦ or ExxxLL motifs are displayed in the correct membrane, and that AP2 does not bind inappropriately to these rather non-specific short amino acid sequences elsewhere in the cell.

References
[1] M.S. Robinson, *J Cell Biol.* **104**, 887-95 (1987).
[2] B.M. Collins, A.J. McCoy, H.M. Kent, P.R. Evans and D.J. Owen, *Cell* **109**, 523-535 (2002).

How a new class of antibiotic inhibits bacterial type IIA toposiomerases

The increase in antibiotic resistance and the lack of new therapies in development is a cause of medical, public, and governmental concern. The EU and US have established a Transatlantic Task Force to address antimicrobial resistance, and the Infectious Diseases Society of America has announced a call to action for a global commitment to develop 10 novel antibacterial drugs by 2020 [1].

Bacteria have two type IIA topoisomerases, DNA gyrase and topoisomerase IV. These enzymes are challenging targets for crystallography because they are highly flexible molecular machines.

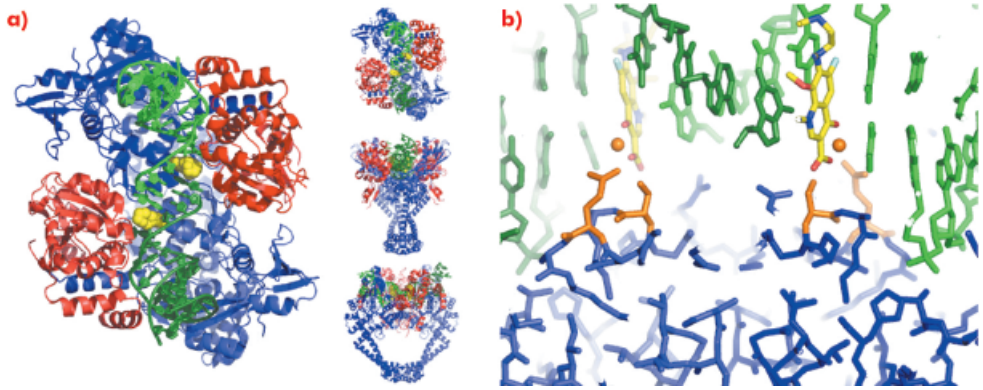

Fig. 109: a) The 3.25 Å crystal structure of *A. baumannii* topoisomerase IV (ParC subunits blue, Par E subunits red), DNA (green) and moxifloxacin (yellow). b) Ser 84 and Glu 88 and the moxifloxacin associated Mg ion(s) are in orange.

Authors
B.D. Bax (a), P.F. Chan (b), D.S. Eggleston (c), A. Fosberry (c), D.R. Gentry (b), F. Gorrec (c), I. Giordano (a), M.M. Hann (a), A. Hennessy (a), M. Hibbs (c), J. Huang (b), E. Jones (c), J. Jones (c), K.K. Brown (b), C.J. Lewis (c), E.W. May (b), M.R. Saunders (a), O. Singh (a), C.E. Spitzfaden (a), C. Shen (b), A. Shillings (c), A.J. Theobald (c), A. Wohlkonig (a), N.D. Pearson (b) and M.N. Gwynn (b).
(a) GlaxoSmithKline, Stevenage (UK)
(b) GlaxoSmithKline, Collegeville, Pennsylvania (USA)
(c) GlaxoSmithKline, Harlow (UK)

Type IIA topoisomerases regulate DNA topology by: (i) creating a four base-pair staggered double-stranded break in one DNA duplex, (ii) passing another DNA duplex through this break, and (iii) resealing the break. Quinolone antibiotics stabilise double-stranded breaks in DNA, killing bacteria. Quinolone antibiotics have been used in the clinic for over 40 years, but resistance has developed. Target mediated resistance to quinolones most frequently occurs through mutation of two residues in the GyrA subunits of DNA Gyrase (and the equivalent residues in the ParC subunit of topoisomerase IV). Dual targeting of the two enzymes by the antibiotic decreases the chance of the development of resistance.

To understand the molecular basis of quinolone action and to investigate new ways of exploiting these clinically validated antibacterial targets [2] we solved the 3.25 Å crystal structure of moxifloxacin in complex with *A. baumannii* topoisomerase IV and DNA [3], using data collected at the ESRF. As expected the structure showed two quinolone molecules binding four base-pairs apart in the cleaved DNA (**Figure 109a**), with the slightly wedge-shaped quinolone seeming to exploit the natural tendency of the enzyme to bend the DNA at the cleavage sites (**Figure 109b**). A magnesium ion, coordinated by two oxygens from moxifloxacin and four water molecules, was seen mediating interactions between the compound and the protein (**Figure 109c**). Two of the water molecules coordinating the magnesium ion were observed to make hydrogen bonds with the side-chains of residues Ser 84 and Glu 88, the two residues most frequently mutated in quinolone resistant bacteria.

A 2.1 Å crystal structure of a novel bacterial topoisomerase inhibitor (NBTI) in complex with DNA and *S. aureus* DNA gyrase [4], showed the compound sitting on the twofold axis of the complex with one end buried in a pocket between the two GyrA subunits and the other end sitting between the central two base-pairs of the un-cleaved DNA (**Figure 110**). Consistent with the good activity of

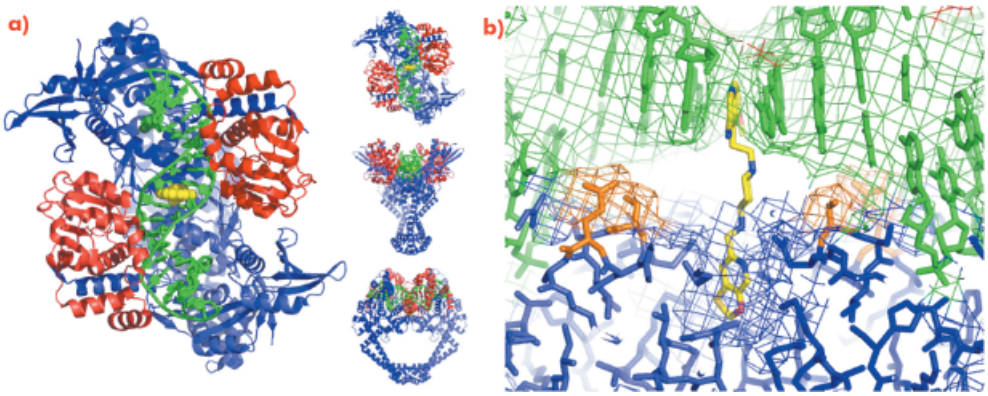

Fig. 110: a) The 2.1 Å crystal structure of *S. aureus* DNA gyrase (GyrA subunits blue, GyrB subunits red), DNA (green) and GSK299423 (yellow). b) Ser 84 and Glu 88 are highlighted in orange.

NBTIs against quinolone resistant strains of bacteria, the NBTI did not interact with either Ser 84 or Glu 88. The NBTI binding site is distinct from the quinolone binding site and the mode of action of NBTIs is different from quinolones [4]. The unprecedentedly high-resolution structure for a complex of a type IIA topoisomerase with DNA also gave new insights into the cleavage mechanism of type IIA topoisomerases [4].

The collection of a 2.1 Å dataset at the ESRF on a weakly diffracting crystal with a 93 x 93 x 412 Å cell led to the determination of a crystal structure which has provided a structural platform to help with the development of a new class of antibacterial agents.

References
[1] http://www.idsociety.org/Content.aspx?id=4810
[2] D.J. Payne, M.N. Gwynn, D.J. Holmes and D.L. Pompliano, *Nature Rev. Drug Discovery* **6**, 29-40 (2007).
[3] A. Wohlkonig, P.F. Chan, P.A. Fosberry, P. Homes, J. Huang, M. Kranz, V.R. Leydon, T.J. Miles, N.D. Pearson, R.L. Perera, A.J. Shillings, M.N. Gwynn and B.D. Bax, *Nature. Struc. Mol. Biol* **17**, 1152-1153 (2010).
[4] B.D. Bax, P.F. Chan, D.S. Eggleston, A. Fosberry, D.R. Gentry, F. Gorrec, I. Giordano, M.M. Hann, A. Hennessy, M. Hibbs, J. Huang, E. Jones, J. Jones, K.K. Brown, C.J. Lewis, E.W. May, M.R. Saunders, O. Singh, C.E. Spitzfaden, C. Shen, A. Shillings, A.J. Theobald, A. Wohlkonig, N.D. Pearson and M.N. Gwynn, *Nature* **466**, 935-940 (2010).

Principal publication and authors
C.Y. Janda (a,b), J. Li (a), C. Oubridge (a), H. Hernandez (c,d), C.V. Robinson (c,d) and K. Nagai (a), *Nature* **465**, 507–510 (2010).
(a) MRC Laboratory of Molecular Biology, Cambridge (UK)
(b) Current address: Howard Hughes Medical Institute, Stanford University School of Medicine (USA)
(c) University of Cambridge Chemical Laboratories, Cambridge (UK)
(d) Current address: Department of Chemistry, University of Oxford (UK)

Binding of the signal peptide to the signal recognition particle

Many proteins are inserted into the cell membrane or secreted from the cell. In 1972, César Milstein, working at the MRC Laboratory of Molecular Biology, discovered that the immunoglobulin light chain is made as a longer precursor; a short sequence at the beginning of the protein is cleaved off when it is secreted. He suspected that this short sequence, now known as the signal peptide, might direct proteins to outside the cell [1]. Signal sequences are divisible into a positively charged n-region, an h-region commonly containing 8–20 hydrophobic residues and a polar c-region, but all regions lack sequence conservation [2]. When the signal sequences (or signal peptide) of secreted proteins emerge from the ribosome they are bound by a signal recognition particle (SRP). SRP directs the ribosome to the endoplasmic reticulum membrane in eukaryotic cells or plasma membrane in prokaryotic cells where the ribosome docks with a protein-conducting channel (translocon). Synthesised proteins are then inserted into the membrane or secreted through a translocon co-translationally [3-5]. It was not known how the signal peptide binding site of SRP54 can recognise highly diverse signal sequences. We have now crystallised SRP54 bound to a signal peptide showing molecular details of recognition.

Signal recognition particles are found in all three domains of life (Eubacteria, Archaea and Eukarya) but their structures differ greatly with only SRP54 (or its homologue Ffh) as the universally conserved protein component [4-5]. SRP54 consists of three domains: the N-terminal four-helix bundle (N domain) and a Ras-like GTPase domain (G domain), which together form the NG domain, and the carboxy-terminal methionine-rich M domain. SRP54 associates with SRP RNA and signal peptide through its M domain. SRP interacts with the ribosome near the peptide-exit site mainly through the N-domain [5] and captures the signal sequence as soon as it emerges from the ribosome. The SRP-ribosome-nascent chain complex (SRP-RNC complex) is then directed to a translocon via a GTP-dependent interaction between the NG domains of SRP54 and a membrane-associated SRP receptor. No structure has been reported that exemplifies SRP54 binding of any signal sequence because

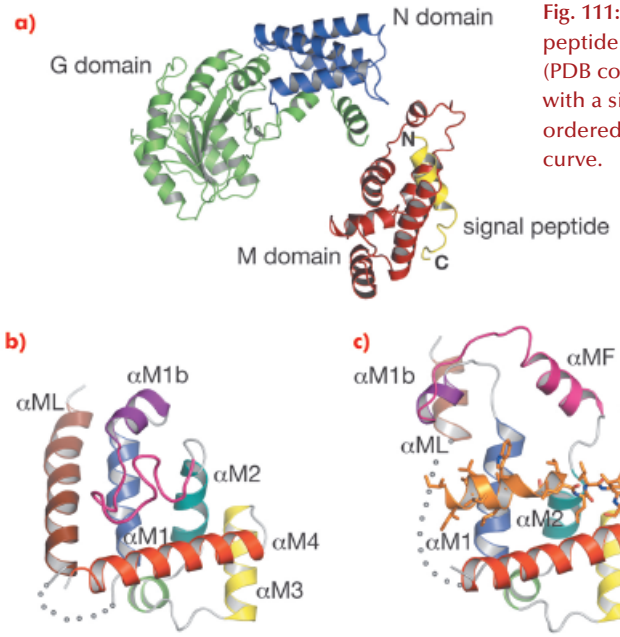

Fig. 111: a) Structure of *Sulfolobus solfataricus* SRP54–signal peptide fusion protein. b) The M domain of free SRP54 (PDB code: 1QZX). c) The M domain of SRP54* in complex with a signal peptide (residues Gly 449B–His 468B). The poorly ordered region (residues 308–326) is represented by a dotted curve.

of the difficulties in producing a complex of SRP54 and hydrophobic signal peptides. We produced SRP54 fused with a signal peptide via a linker peptide. This dimeric form of SRP54* crystallised in space group $P4_12_12$ with one monomer per asymmetric unit. Data were collected at beamlines **ID14-1** and **ID14-4**. The structure was solved by the MAD method using a methylmercury derivative of a single cysteine mutant (N177C) and refined to an R_{free} of 32.3% at 3.5 Å resolution. An unbiased electron density map calculated by combining the Hg MAD phases with molecular replacement phases from a homologous NG domain (PDB code: 1J8M) followed by solvent flattening showed clear density of the signal peptide (PDB code: 3KL4).

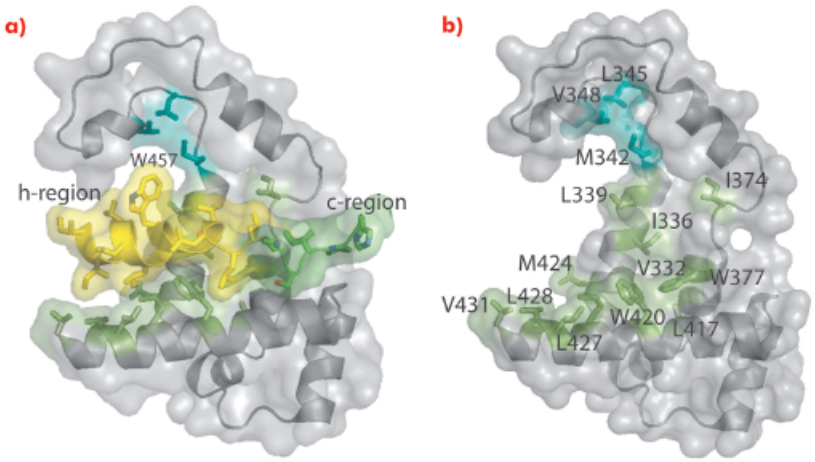

Fig. 112: Interaction of the M domain with a signal peptide. a) Surface representation with the h- and c-regions of the signal sequence coloured yellow and green, respectively. b) Same as (a) but the signal peptide is omitted to reveal the signal-peptide binding groove.

In the M domain of SRP54* helix αM4, and helices αM1 and αM2 oriented perpendicular to αM4, form a hydrophobic groove where the signal peptide in the α-helical conformation is accommodated (**Figure 111**). The indole rings of Trp 377 and Trp 420 cluster together creating a bulge in the groove surface. Eight residues (Ile 450–Trp 457) in the h-region of the signal peptide form an α helix which extends to Leu 461 with a bend at Gly 458 that complements the Trp bulge in the groove floor (**Figure 112**). The signal peptide helix and αM4 interact by the most commonly occurring 4-4 'ridges-into-grooves' helix packing, with a crossing angle of –40° in the Chothia notation [6]. This crossing angle allows the observed extensive interaction between the h-region of the signal peptide and αM4 of the M domain. In addition, the Leu and Met side chains, a conserved hallmark of the M domain, can adopt different rotamers allowing signal peptides with diverse sequences to bind.

The structure of SRP54* has provided a first structural insight into signal peptide binding to SRP. It would be very interesting to crystallise SRP54 with different signal sequences to see how residues in the signal peptide binding groove adopt different conformation to optimise interactions.

References
[1] C. Milstein, G.G. Brownlee, T.M. Harrison and M.B. Mathews, *Nature New Biol.* **239**, 117-120 (1972).
[2] L.M. Gierasch, *Biochemistry* **28**, 923–930 (1989).
[3] P.F. Egea, R.M. Stroud and P. Walter, *Curr. Opin. Struct. Biol.* **15**, 213–220 (2005).
[4] J.A. Doudna and R.T. Batey, *Annu. Rev. Biochem.* **73**, 539–557 (2004).
[5] C. Wild, M. Halic, I. Sinning and R. Beckmann, *Nature Struct. Mol. Biol.* **11**, 1049-1053 (2004).
[6] C. Chothia, M. Levitt and D. Richardson, *J. Mol. Biol.* **145**, 215-250 (1981).

Principal publication and authors
L.K. Lee (a), M.A. Ginsburg (a), C. Crovace (b), M. Donohoe (a) and D. Stock (a), *Nature* **466**, 996-1000 (2010).
(a) Structural and Computational Biology Division, Victor Chang Cardiac Research Institute, Sydney (Australia).
(b) MRC Laboratory of Molecular Biology, Cambridge (UK)

References
[1] T. Minamino, K. Imada and K. Namba, *Curr. Opin. Struct. Biol.* **18**, 693-701 (2008).
[2] P.N. Brown, C.P. Hill and D.F Blair, *EMBO J.* **21**, 3225-3234 (2002).

Structure of the torque ring of the bacterial flagellar motor and the molecular basis for rotational switching

The bacterial flagellar motor is one of the most efficient rotary motors known to man [1]. It utilises proton motive force to drive the rotation of long helical flagellar filaments at up to 1000 revolutions per minute, yet it can reverse its direction in milliseconds. The motor and filament act as a propeller for swimming bacteria, which move in cycles of relatively lengthy forward runs, followed by short tumbles that alter the trajectory of the cell. These cycles are essential for the survival of bacteria as they bias their runs and tumbles such that the net movement is towards a favourable environment and away from unfavourable ones. The mode of swimming is determined by the direction of rotation of the flagellar motor. A run occurs during counter-clockwise (CCW) rotation when all filaments form a helical bundle that propels the cell forward. A tumble occurs when at least some flagella rotate in a clockwise (CW) direction, which causes the bundle to disassemble and results in a somersaulting of the cell. Similar to ATP synthases, the bacterial flagellar motor uses the potential energy from an electrochemical gradient of cations across the cytoplasmic membrane to generate torque. Remarkably, in the flagellar motor both CCW and CW rotation are driven by a flow of cations towards the cytosol, whereas in the reversible bacterial ATP synthases, a switch of rotation is connected to a reversal of cation flow.

A protein known as FliG forms a ring in the motor that is involved in rotational switching and interacts with the cation channel forming stator subunit MotA to generate torque. We determined the crystal structure of the full-length FliG protein from the hyperthermophilic bacterium *Aquifex aeolicus* to 2.4 Å resolution using native data collected at beamline **ID14-1** of the ESRF coupled with single anomalous dispersion data sets from crystals containing selenomethionine-substituted protein collected at beamline 14-ID-B of the Advanced Photon Source (Figure 113).

Structural differences to a previously solved crystal structure of the middle and C-terminal domains of FliG from *Thermotoga maritima* [2] correlated strongly to the location of dozens of mutations that bias the direction in which the motor rotates and revealed two striking conformational changes that are involved in rotational switching. Furthermore, conserved crystal contacts revealed how armadillo repeat motifs on adjacent FliG monomers interact to form a right-handed superhelix and hence define the structural basis for an intermolecular FliG-FliG interaction that mediates the assembly of the FliG ring. This allowed us to derive a model of the FliG ring that is consistent with the size, shape and symmetry of 3D electron microscopy reconstructions and with intermolecular contacts that were defined by mutagenesis and cross-linking studies. Finally, in the context of a fully assembled ring, conformational changes in FliG redistribute the charges involved in torque generation providing a compelling model for rotational switching (Figure 114).

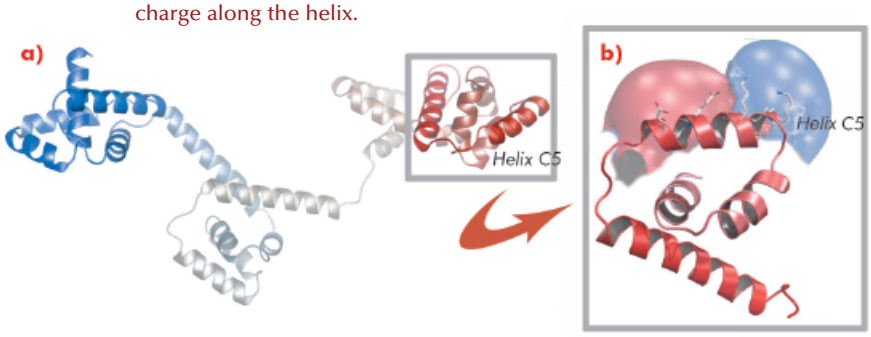

Fig. 113: a) Structure of the full-length *A. aeolicus* FliG monomer. The N-terminus is shown in blue, the C-terminus in red. b) The C-terminal domain containing torque helix C5 is shown enlarged and an electrostatic surface potential map is superimposed to demonstrate the clear distribution of charge along the helix.

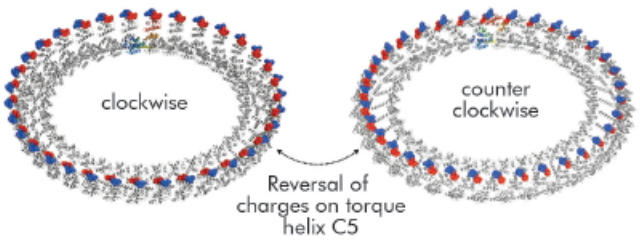

Fig. 114: Model of the FliG ring in CW and CCW conformations. Note that the distinct charge distribution on torque helix C5 is reversed.

Repairing breaks in DNA double strands: the structure of DNA-PKcs

Principal publication and authors
B.L. Sibanda, D.Y. Chirgadze and T.L. Blundell, *Nature* **463**, 118–121 (2010).
Department of Biochemistry, University of Cambridge (UK)

Breaks in both strands of chromosomal DNA occur frequently and constitute a major threat for cells. Left unrepaired or mis-repaired they can result in cell death or cancer. In eukaryotes, two different pathways are used to repair this type of DNA damage, the balance between them varying during the cell cycle [1]. Unlike homologous recombination, which requires a sister chromatid, non-homologous end joining [2] does not copy information lost in double-strand breaks and so can be active throughout the cell cycle. In this process two DNA ends are joined directly, with the help of many proteins that organise, tailor and ligate the broken ends. An important component of this process is DNA-dependent protein kinase (DNA-PK), an enzyme that comprises the DNA-PK catalytic subunit (DNA-PKcs) and the Ku70/Ku80 heterodimer. DNA-PKcs is a protein comprising a single polypeptide chain of 4128 amino acids [3] that belongs to a family of enzymes involved in the sensing and transmission of DNA damage signals initiating cell cycle arrest. Knowledge of its architecture should lead to a better understanding of its role in the events that take place in joining DNA ends. Although electron micrographs have provided images of this large enzyme, crystals have previously been elusive.

Here, we describe the crystal structure of DNA-PKcs in complex with the C-terminal domain of Ku80 at 6.6 Å resolution (Figure 115) in which the overall fold of this enzyme is clearly visible for the first time. The structure was solved using the multi-wavelength anomalous dispersion (MAD) method exploiting a $Ta_6Br_{12}^{2+}$ heavy metal cluster introduced into the crystals and using diffraction data collected on beamline **ID29**. At 6.6 Å resolution the electron density of helical regions is clearly visible indicating that the structure is dominated by α-helices arranged as HEAT repeats. However, the electron density for the loops that link these helices is not visible thus making it difficult to fit the whole molecule reliably. Furthermore, as the Ku80 C-terminal domain also consists of α-helical HEAT repeats it has not yet been possible to locate this moiety in the electron density.

The long polypeptide chain of DNA-PKcs is organised into several distinct domains (Figure 115). From the N-terminus 66 helices are arranged as HEAT repeats and folded into a hollow circular structure, which has a concave shape. Just before the circle is complete, the polypeptide chain changes direction, leaving a gap, and

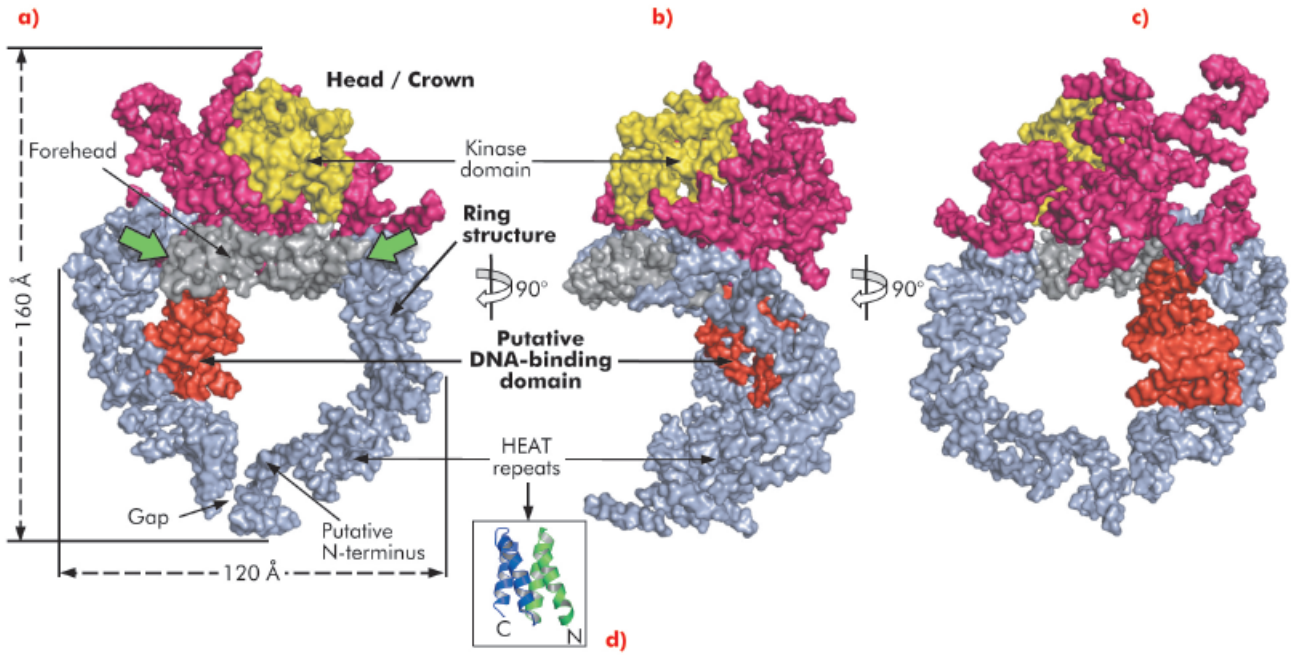

Fig. 115: The molecular surface of DNA-PKcs showing a) front, with the potential conformationally variable regions denoted with green arrows, b) side view, c) back view, d) a HEAT repeat. The colour code of the molecule is as follows: ring structure in grey; the putative DNA binding domain in red; the larger head/crown domain in magenta and (for the kinase sub-domain) yellow.

References
[1] M. Shrivastav, L.P. De Haro and J.A. Nickoloff, *Cell Research* **18**, 93-113 (2008).
[2] S. Critchlow and S.P. Jackson, *Trends Biochem. Sci.* **23**, 394-398 (1998).
[3] K.O. Hartley, D. Gell, G.C. Smith, H. Zhang, N. Divecha, M.A. Connelly, A. Admon, S.P. Lees-Miller, C.W. Anderson and S.P. Jackson, *Cell.* **82**, 849-856 (1995).
[4] M. Yaneva, T. Kowalewski and M.R. Lieber, *EMBO J.* **16**, 5098-5112 (1997).

folds into a much smaller globular domain also organised as HEAT repeats that sits on one side of the circular structure (red in Figure 115a). DNA-PKcs bind directly to DNA [4] and this domain is a good candidate for being the DNA binding domain. After this domain the polypeptide chain then crosses the circular structure and forms the larger C-terminal head/crown domain that is perched on top of the circular structure. This region is also predominantly α-helical and is likely to interact with many other proteins. Contained in this region is the protein kinase domain, involved in both autophosphorylation and the phosphorylation of other proteins.

In summary, the ring structure reflects the role of DNA-PKcs both as an enzyme involved in DNA damage signalling and as a platform for the binding of DNA, Ku and other proteins engaged in the repair of broken DNA. The head/crown kinase domain located at the very top of the circular structure is well placed for easy access to substrates that are phosphorylated by this protein.
There are some irregular regions in the arrangement of the HEAT repeats within the ring structure (Figure 115a, green arrows). These may accommodate conformational changes that widen the gap, shown in Figure 115a, thus providing a way for the molecule to come off DNA at the end of the repair process.

Principal publication and authors
Å.K. Røhr, H.-P. Hersleth and K.K. Andersson, *Angew. Chem. Int. Ed.* **49**, 2324-2327 (2010).
Department of Molecular Biosciences, University of Oslo (Norway)

Consequences of using X-rays when studying redox cofactors

Flavin cofactors are involved in numerous biological processes including light sensing, oxygen activation, electron transfer, and DNA-repair. During these processes the flavin cofactor undergoes subtle conformational changes depending on its state. It is of great importance to understand the connection between flavin conformations and the nature of the chemistry performed.

In the literature, questions regarding flavin structure and function have been addressed many times using spectroscopic methods, theoretical calculations, and X-ray crystallography. The protein data bank (PDB) contains more than 1400 crystal structures containing either a flavin mononucleotide (FMN) or flavin adenine dinucleotide (FAD) cofactor. The redox and protonation states of these cofactors are usually assumed to reflect the situation in the protein crystal prior to X-ray data collection. This is a problematic assumption since redox cofactors are susceptible to react with photoelectrons generated in the crystal by X-rays during data collection. The large distribution of the so-called flavin butterfly bending angle, which is an indicator of flavin red-ox and protonation state, in the PDB-deposited flavoproteins indicate a large diversity of flavin states among these structures [1].

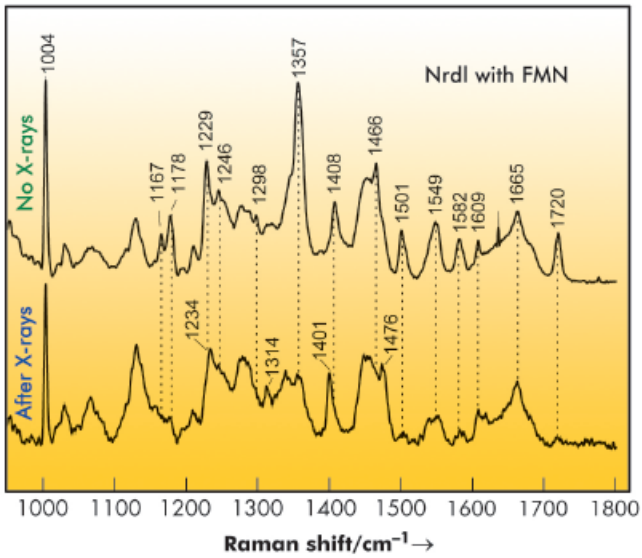

Fig. 116: Single-crystal *in situ* Raman spectra recorded for the flavoprotein NrdI before and after X-ray data collection.

We have solved crystal structures of the flavodoxin-like protein NrdI to 1.12 and 1.15 Å resolution at beamline **BM01** using crystals containing the yellow, oxidised FMN ($NrdI_{ox}$) and the blue, neutral semiquinone FMNH• cofactor ($NrdI_{sq}$), respectively. Before and after X-ray data collection, Raman spectra were collected *in situ* from both crystals. For both crystals, Raman bands confirmed the initial redox states. However, as shown in Figure 116, dramatic changes in the Raman spectra recorded before and after X-ray data

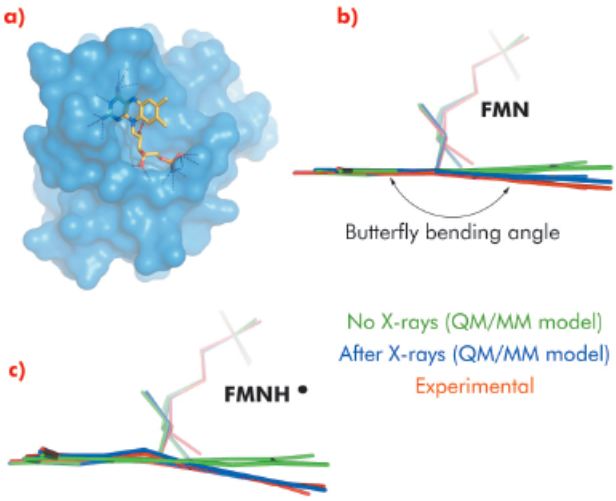

Fig. 117: a) Stick representation of the flavin cofactor bound in a surface pocket of NrdI, b) QM/MM models of flavins in NrdI containing the oxidised FMN cofactor (green), the one-electron reduced ($FMN^{\bullet -}$) cofactor (blue), and the flavin conformation in the crystal structure of $NrdI_{ox}$ (red), c) QM/MM models of flavins in NrdI containing the neutral semiquinone ($FMNH^{\bullet}$) cofactor (green), the one-electron reduced ($FMNH^{-}$) cofactor (blue), and the flavin conformation in the crystal structure of $NrdI_{sq}$ (red). In both b) and c) the QM/MM models confirm a one electron reduction of the flavin during X-ray data collection.

collection were observed. When starting with $NrdI_{ox}$ all flavin Raman bands either shift in energy or disappear after X-ray data collection, indicating a change in the flavin state. For $NrdI_{sq}$ all Raman bands decrease in intensity upon X-ray exposure, indicating a one-electron reduction to the fully reduced anionic form $FMNH^{-}$. These observations coincide with the crystal structures in which the flavin in both models have a butterfly bend deviating from the planarity predicted for FMN and $FMNH^{\bullet}$ (Figure 117).

To shed light on our experimental observations, which indicate that the state of the flavin cofactor is influenced by exposure to X-rays, QM/MM models of possible flavin redox and protonation states were built and their geometry optimised. Of the different models containing FMN, $FMN^{\bullet -}$, $FMNH^{\bullet}$, $FMNH^{-}$, or $FMNH_2$, the one-electron reduced forms of the initial states in the crystals, $FMN^{\bullet -}$ and $FMNH^{-}$, corresponded to the experimentally determined ($NrdI_{ox}$) and ($NrdI_{sq}$) crystal structures respectively.

The combination of single-crystal *in situ* Raman crystallography with QM/MM calculations demonstrate the importance of monitoring active site cofactors during X-ray data collection in order to track and characterise eventual radiation damage, which, if unaccounted for, can result in erroneous interpretation of crystal structures [2-5].

References
[1] T. Senda, M. Senda, S. Kimura and T. Ishida, *Antioxid. Redox Signaling* **11**, 1741-1766 (2009).
[2] H.-P. Hersleth, T. Uchida, Å.K. Røhr, T. Teschner, V. Shünemann, C.H. Görbitz, T. Kitagawa, A.X. Trautwein and K.K. Andersson, *J. Biol. Chem.* **278**, 23372 – 23386 (2007).
[3] H.-P. Hersleth, Y.-W. Hsiao, U. Ryde, C.H. Görbitz and K.K. Andersson, *Biochem. J.* **412**, 257–264 (2008).
[4] H.-P. Hersleth, Y.-W. Hsiao, U. Ryde, C.H. Görbitz and K.K. Andersson, *Chem. Biodiversity* **5**, 2067-2089 (2008).
[5] H.-P. Hersleth and K.K. Andersson, *Biochem. Biophys. Acta* (2010) (in press doi:10.1016/j.bbapap.2010.07.019).

An original Cu(I)-coordination shell in a small bacterial metalloprotein identified by XAS and NMR spectroscopy

Living organisms are continuously exposed to environmental stress from sources such as toxic compounds, radiation, and high temperatures. During evolution, they have adapted to the specific environment in which they live and have learned to protect themselves against sources of stress by developing resistance mechanisms. One well-known class of toxic products is heavy metals that, although naturally occurring in the environment, may be released in huge quantities through anthropogenic processes.

Cupriavidus metallidurans CH34 is a bacterium that is resistant to high concentrations of many heavy metals and is a model for studying metal resistance mechanisms in microorganisms. Copper resistance of *C. metallidurans* CH34 involves more than 19 proteins. One of these is the metallochaperone CopK, a small periplasmic protein that is found in significant amounts under copper stress. We have previously determined the solution structure of *apo*-CopK [1] which has been shown to bind Cu(I)

Principal publication and authors
G. Sarret (a), A. Favier (b), J. Covès (b), J.-L. Hazemann (c), M. Mergeay (d) and B. Bersch (b), *J. Am. Chem. Soc.* **132**, 3770–3777 (2010).
(a) LGIT, Grenoble (France).
(b) Institut de Biologie Structurale, Grenoble (France).
(c) Institut Néel, Grenoble (France).
(d) SCK-CEN, Mol (Belgium)

and Cu(II) in a cooperative way [2]. Recently, we determined the solution structure of the Cu(I)-bound CopK protein and characterised its Cu(I) binding site. A thus far unique Cu(I) ligand sphere, formed by four thioether groups belonging to four methionines from the same protein chain, was discovered.

The three-dimensional structure of CopK was determined from NMR data (Figure 118). However, the Cu(I) ion is NMR-silent and no geometric information on the metal site could be obtained. A cryo-cooled protein solution containing Cu(I)-CopK was therefore studied by XAS, and spectra around the Cu K-absorption edge collected on the **BM30B** (FAME) beamline. The resulting XANES and EXAFS spectra were in accordance with a coordination sphere formed by four sulphur atoms and the fit of the EXAFS data suggested a Cu(I)-S distance of 2.31 Å, a value typical for tetragonal sites. This result was surprising as in most small periplasmic bacterial Cu(I)-binding metallochaperones, Cu(I) is bound in trigonal sites by a combination of sulphur and nitrogen ligands. In addition, a tetrathioether Cu(I) site has so far only been observed in a single protein in which the Cu(I) ion belongs to a copper-molybdenum (MoS_2CuS_2Mo) cluster. Our findings were further corroborated by the observation of chemical shift differences in ^{1}H-^{13}C correlation NMR spectra occurring upon Cu(I)-binding. Four peaks, corresponding to methionine methyl groups were significantly affected by the addition of Cu(I) to the protein. This observation suggests that the chemical shift of these carbons allows the detection of methionine-bound Cu(I) and thus the sequence-specific identification of the Cu(I) ligands.

The structure of Cu(I)-CopK bridges the gap between what was previously known on the Cu(I)/Cu(II)-binding cooperativity and the structures of CopK previously reported. Accommodation of Cu(I) in the tetrathioether site is associated with an important conformational change of the C-terminal region of CopK. We propose that this reorientation is also required for the formation of the Cu(II)-specific site, a hypothesis consistent with the much higher Cu(II) affinity of Cu(I)-CopK compared to *apo*-CopK.

References
[1] B. Bersch *et al., J. Mol. Biol.* **380**, 386-403 (2008).
[2] L.X. Chong *et al., J. Am. Chem. Soc.* **131**, 3549-3564 (2009).

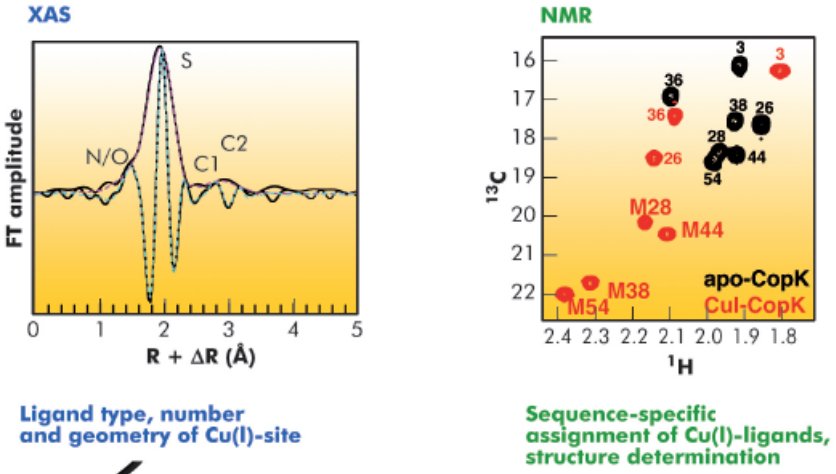

Fig. 118: Solution structure of Cu(I)-CopK. The four methionines forming the Cu(I)-site are shown in detail, with the sulphur atoms and the Cu(I) ion depicted as yellow and green spheres respectively. The structure of *apo*-CopK is shown in light grey for comparison. XAS data: EXAFS Fourier transform of Cu(I)-CopK. Experimental data are shown in black, continuous lines, and simulations in magenta (modulus part) and cyan (imaginary part). NMR data: Comparison of the methionine-CH_3 region of ^{1}H,^{13}C-HSQC spectra acquired on the *apo* protein (black) and Cu(I)-CopK (red). Peaks are annotated with the residue numbers. M28, M38, M44 and M54 form the Cu(I)-site.

The structure of the nuclease domain of human cytomegalovirus DNA packaging terminase

Principal publication and authors
M. Nadal (a,b), P.J. Mas (c), A.G. Blanco (a,b), C. Arnan (a,b), M. Solà (b), D.J. Hart (c) and M. Coll (a,b), *Proc Natl Acad Sci USA* **107**, 16078-16083 (2010).
(a) Institute for Research in Biomedicine (IRB Barcelona) (Spain)
(b) Institut de Biologia Molecular de Barcelona (CSIC) (Spain)
(c) EMBL Grenoble (France)

Human cytomegalovirus (HCMV), one of the eight human herpesviruses, has a high prevalence around the world. In healthy hosts, infection is usually silent but it has life-threatening consequences in immunocompromised individuals. The main groups at risk of HCMV infection are newborn and young children, organ-transplant receivers, patients treated for cancer and people co-infected with HIV. In these risk groups, symptoms can entail loss of hearing and vision, mental retardation and cerebral palsy.

HCMV replicates its DNA via concatamers, a long molecule of DNA containing several copies of the genome. This DNA has to be cut into single genomes and packaged inside the viral capsid. This packaging process is performed by the terminase complex, which in HCMV includes at least, two proteins UL89 and UL56. The observation that DNA packaging processes do not occur in mammalian cells implies that the viral proteins involved might be specific targets for antiviral therapy. However, despite interest in herpes virus terminases as drug targets, no structural information is available for these proteins. Here we focussed on the structural and functional analysis of one component of the HCMV terminase complex, the UL89 protein.

First, we attempted, without success, to express the full-length UL89 in several hosts. In all the cases, the level of expression was very low and the protein expressed was insoluble. Next, to find a soluble fragment of UL89, we predicted domain boundaries using a number of bioinformatic tools; however, all the fragments found were again insoluble. At this point, we attempted a high throughput expression method, ESPRIT, which entails the search for expression of soluble protein fragments by random incremental truncation [1]. Using this approach to test 18432 different gene constructs, we found a soluble domain of UL89, corresponding to the last 257 amino acids of the protein, which we termed UL89-C.

UL89-C was subsequently purified and crystallised, and its crystal structure solved using X-ray diffraction data collected at beamlines **ID14-2** and **BM16**. The structure of UL89-C is composed of a central eight-stranded β-sheet surrounded by six α-helices (Figure 119). Although there are some extra decorations, the fold of UL89-C corresponds to that of RNAse H, an enzyme that removes RNA primers from Okazaki fragments. Other proteins with this fold are *E. coli* Ruv-C resolvase, HIV and ASV integrases, some transposases and other nucleases [2]. All these proteins share a basic fold of a five-stranded β-sheet surrounded by α-helices on both sides. The order and orientation of the strands within the β-sheet is conserved: 3, 2, 1, 4 and 5, one of them being anti-parallel to the other four. An anomalous difference Fourier map, calculated with diffraction data collected at the Mn-K absorption edge at beamline **ID29**, confirmed that the active site of UL89-C contains two Mn^{2+} ions approximately 4 Å apart. The first Mn^{2+} is coordinated by Asp463 and Glu534 and the second by Asp463 and Asp 651 (Figure 120). These residues are fully conserved in all human herpes virus terminases.

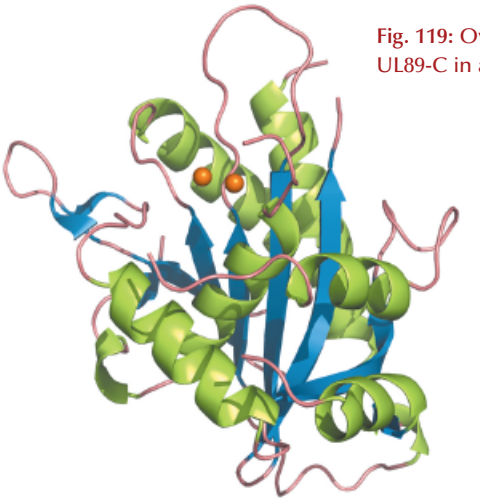

Fig. 119: Overall structure of UL89-C in a ribbon representation.

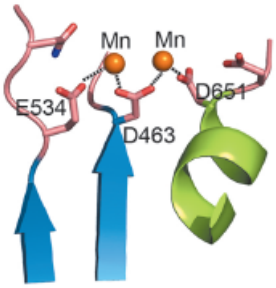

Fig. 120: Detailed view of the active site area of UL89-C.

To demonstrate that UL89-C encodes the nuclease activity of the terminase, we performed a nuclease assay using plasmidic DNA. We tested the reaction in the presence of various divalent ions. Only with Mn^{2+} was total degradation of DNA observed. This finding indicates that nuclease activity is strongly dependent on this cation.
We also checked the nuclease activity with mutants of the residues that coordinate the Mn^{2+} ions and confirmed that they are essential for the function of the protein.

HIV integrase, which is a validated anti-HIV drug target, shares its basic fold with UL89-C and has a similar active site. Prompted by this structural similarity, we tested the inhibitory properties towards UL89-C of a number of known HIV integrase inhibitors. Raltegravir [3], an anti-HIV drug approved by the FDA in October 2007 and widely used in antiretroviral therapy for AIDS patients, was active against the UL89-C terminase domain at low micromolar levels. This observation opens the way for the development of antiviral molecules against herpesviruses using the nuclease domain of the terminase as a target.

References
[1] H. Yumerefendi, F. Tarendeau, P.J. Mas and D.J. Hart, *J Struct Biol* **172**, 66-74 (2010).
[2] W. Yang and T.A. Steitz, *Structure* **3**, 131-134 (1995).
[3] V. Summa *et al., J. Med. Chem* **51**, 5843-5855 (2008).

How the quorum-quenching N-acyl homoserine lactone acylase PvdQ disrupts bacterial virulence

Principal publication and authors
M. Bokhove (a), P. Nadal Jimenez (b), W.J. Quax (b) and B.W. Dijkstra (a), *PNAS* **107**, 686–691 (2010).
(a) Laboratory of Biophysical Chemistry, University of Groningen (The Netherlands)
(b) Department of Pharmaceutical Biology, University of Groningen (The Netherlands)

In many Gram-negative bacterial pathogens, virulent behaviour is activated by quorum sensing, a process in which bacteria become aware of each other by the action of diffusible *N*-acyl homoserine lactone (AHL) messaging compounds. To stop or disrupt quorum sensing, bacteria produce enzymes that break down these AHLs, such that they can no longer be used as signalling molecules. This process, called quorum quenching, can be achieved by the hydrolysis of either the ester bond in the homoserine lactone core of the AHL (performed by lactonases) or of the peptide bond that connects the acyl-chain and the homoserine lactone core (performed by acylases). In view of the increase in bacterial drug resistance, quorum quenching has gained interest as a potential tool in the development of novel antimicrobial strategies.

While AHL lactonases have been structurally characterised [1], no data is available for acylases. To gain insights into the mechanism and substrate specificity of AHL acylases, we solved the crystal structure of the AHL acylase PvdQ from *Pseudomonas aeruginosa* at 1.8 Å resolution, using data collected at **ID14-2**. PvdQ appears to be an N-terminal nucleophile (Ntn) hydrolase [2] with a heart-shaped

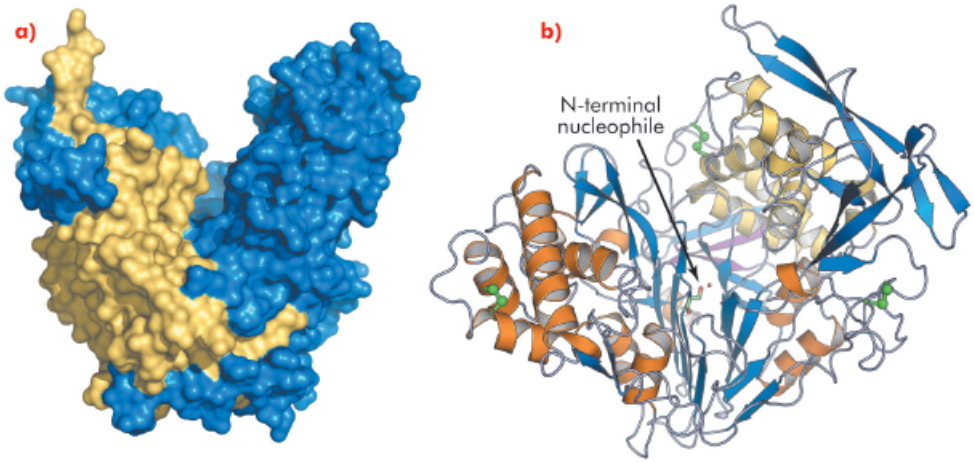

Fig. 121: Overall structure of PvdQ. a) The solvent accessible surface area shows the heart-shaped structure of PvdQ, α-chain in yellow, β-chain in blue. b) Secondary structure representation, α-chain with magenta strands and yellow helices, β-chain with blue strands and orange helices, disulfide bridges are represented by green spheres, the catalytic serine is shown in ball and sticks.

structure and a deep crevice in the centre (Figure 121a). The enzyme consists of two peptide chains, with the N-terminal serine of the β-chain, which is located at the bottom of the crevice, forming the catalytic centre (Figure 121b). Near the catalytic centre an extended hydrophobic pocket is buried inside the enzyme core (Figure 122a).

Detailed information on the mechanism behind substrate recognition and catalysis was obtained from PvdQ crystals soaked briefly with C_{12}-homoserine lactone at pH 5.5. This procedure resulted in the formation of an acyl-enzyme intermediate, as revealed by a 2.1 Å resolution crystal structure obtained with data collected at **ID14-2** (Figure 122c).
To accommodate the substrate, the hydrophobic substrate-binding pocket has opened up to solvent (Figure 122b) and the residues lining the pocket have adapted to specifically recognise the long apolar C_{12} acyl chain of AHL (Figure 122c). This binding mode is in contrast to the AHL lactonases, which specifically recognise the polar homoserine lactone moiety of the AHL. The binding mode of the covalently bound dodecanoic acid indicates a catalytic mechanism of AHL degradation, in which Serβ1 is the nucleophile, Hisβ23 stabilises the reactive state of the nucleophile and Valβ70 and Asnβ269 form the oxyanion hole (Figure 122c).

A BLAST search revealed other Ntn-hydrolases that are homologous to PvdQ, some of which also prefer substrates with long acyl-chain substitutions. PvdQ is the first structurally characterised Ntn-hydrolase that can accommodate such large acyl-chains, and therefore its crystal structure may serve as a paradigm for other Ntn-hydrolases with a similar substrate preference. Moreover, its structure may be used as a template for site-directed mutagenesis to alter the substrate specificity towards short-chain AHLs. This could make the enzyme capable of disrupting quorum sensing-regulated virulence in pathogens that utilise C_6-C_8 substituted homoserine lactones, for which PvdQ shows only weak activity.

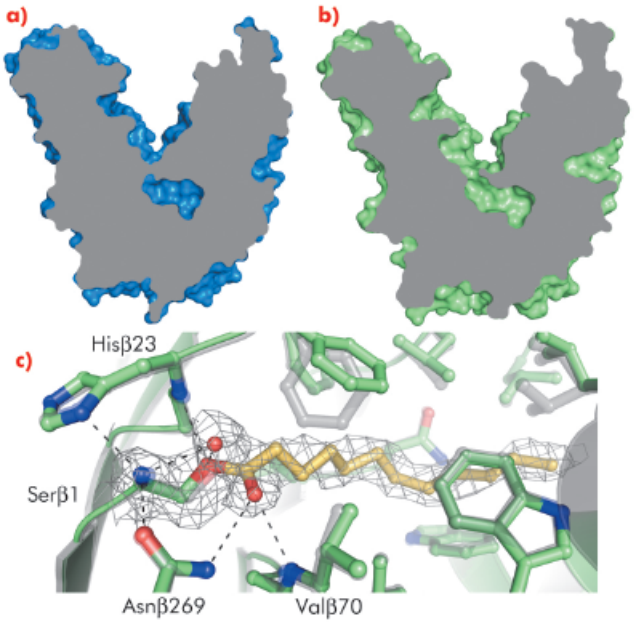

Fig. 122: a) The substrate binding pocket of PvdQ is closed off from the solvent in the unliganded structure; b) it is open when ligand is bound. c) Substrate binding induces subtle conformational changes; the unliganded state is shown in grey, while the structure of the covalently bound dodecanoic acid (yellow) is indicated in green. The important catalytic residues are labelled.

The role of PvdQ in quorum quenching is well established. However, PvdQ is also important for pyoverdine biosynthesis, since *pvdQ*-gene deletion abrogates production of pyoverdine [3], a siderophore involved in iron homeostasis, which is important for *P. aeruginosa* survival and virulence. Although the precise role of PvdQ in this latter pathway is not known, Visca *et al.* have proposed the need for an enzyme that removes a long acyl chain from a pyoverdine precursor [4].
The crystal structures of PvdQ suggest that the distinct binding pocket for long acyl chains might be able to accommodate the acyl chain of a pyoverdine precursor. Whether this specialised acyl-chain binding pocket was initially acquired for AHL hydrolysis or pyoverdine maturation requires further investigation.

References
[1] D. Liu *et al.*, *Proc. Natl. Acad. Sci. USA* **102**, 11882-11887 (2005).
[2] J.A. Brannigan *et al.*, *Nature* **378**, 416-419 (1995).
[3] P. Nadal Jimenez *et al.*, *Microbiology* **156**, 49-59 (2010).
[4] P. Visca, F. Imperi and I.L. Lamont, *Trends Microbiol.* **15**, 22-30 (2007).

X-ray imaging

Synchrotron-based X-ray imaging techniques use a broad range of physical and chemical contrast mechanisms. Their 'resolution' can be seen in three dimensions: spatial, temporal and compositional/structural. Synchrotron radiation-based high resolution X-ray imaging is an invaluable tool for the study of complex systems, leading to substantial scientific progress. The highlights published in the present chapter show the wide variety of topics studied at the ESRF.

Imaging at the ESRF is now approaching spatial resolutions in the few tens of nm range, well below the cell dimensions, and chemical sensitivities allowing the detection within the cell of a single nanoparticle consisting of only a few thousand atoms (ID22). In the first section on biology and biomedical applications, this is highlighted by the contribution on new opportunities for bioimaging and biodelivery, which have potential applications in diagnostics and therapy of diseases such as cancer. Two phase-contrast imaging developments are also presented; both aim to improve medical diagnosis. Grating interferometry tomography allows discrimination between soft tissues such as white and grey matter in a human cerebellum sample (ID19), and phase contrast analyser-based tomography permits differentiation between osteoarthritic and healthy human cartilage samples (ID17). The last paper of this section deals with the tolerance of arteries to microplanar X-ray beams, a study that is required before the new "micro-radiation therapy" (MRT) protocol can be applied to the treatment of cancerous tumours.

High resolution is also important for materials science applications, where "local" diffraction maps are collected at the micrometre level. Two examples are presented here. The growth process of quantum-well based devices for optoelectronics can be improved using the information gained from their imaging (ID22), and superconductivity is associated with the connectivity over large distances within the nanostructure for oxide-based superconductors (ID13).

Works for the upgrade beamline UPBL4 NINA (Nano Imaging and Nano-Analysis) officially started at the end of 2010. This two-branch beamline will provide complementary techniques at the nano-scale for the study of both biological and materials science samples. Nano-imaging covers new application areas and has been pioneered by the pilot project ID22NI. This is exemplified by the study of the growth of grain boundary voids during the high-temperature creep of metals. The usual model considers this process similar to the growth of a hole in a nonlinearly viscous solid. Fast high-energy tomography shows that the real growth rates in copper are higher than the prediction of this model by a factor of about 40. Nano-tomography reveals that voids have a spherical shape in the initial undeformed state and they become facetted during creep (Figure 123). This observation and the large scatter of growth rates suggest that dislocation glide significantly contributes to void growth [1].

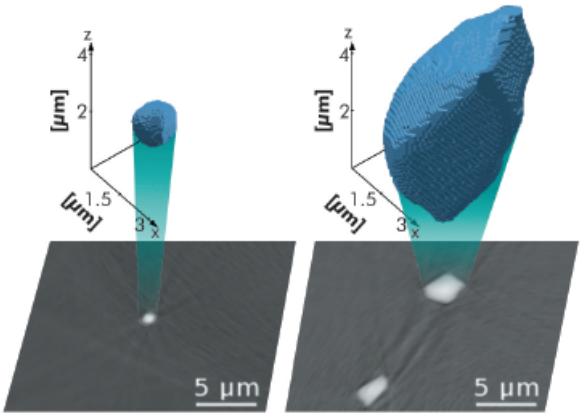

Fig. 123: Submicrometre resolution reconstructions of void shape. a) A spherical shape is characteristic of the initial, recrystallised state. b) Larger voids become faceted after 4% of creep deformation at 723 K (Image copyright 2010, reprinted from [1] with permission from Elsevier).

X-ray imaging is increasingly being used for Cultural Heritage investigations. A combination of fluorescence (µXRF) and absorption (µ-XANES) on ID21 allowed characterisation of the opacification processes in Egyptian and Roman glass. This study highlighted the remarkable know-how of the craftsmen of those periods. Synchrotron radiation based imaging makes it possible to reach elusive information that can completely change our understanding of a palaeontological subject. One study shows that differences existed between the Neanderthal dental development and our own, and that a long childhood is specific to the evolution of our own species (ID19). This investigation is an example of the kind of research carried out in the "Palaeontology Facility", which aims to provide the palaeontological community with specially designed facilities. It will involve the refurbishing of long imaging beamlines and a specialised computing centre. The Palaeontology Facility will involve collaboration among many internationally renowned groups, and it will reinforce the leading role of the ESRF for this scientific activity. Already this effort is producing important new results, such as the very recent evidence about the diet of one of the most important group of ammonites, distant relatives of squids, octopuses and cuttlefish, which sheds a new light on why they became extinct 65.5 million years ago [2].

New science often relies on technical developments: the ESRF staff devote a substantial part of their research to achieving these improvements, as exemplified by two contributions to the present highlights. The first account describes a newly developed wavelength-dispersive spectrometer (ID21) with performance that significantly surpasses that of a solid state detector. In the second article, real-time characterisation is achieved for the evolution of the roughness of silicon surfaces upon ion erosion, this being important for the production of X-ray optical elements.

High-resolution synchrotron X-ray imaging (and in particular microtomography) is increasingly being required for industrial, proprietary studies. This very positive feature raises the issue of the beamtime/personnel for these highly oversubscribed beamlines, and the need to integrate this aspect in the X-ray imaging development strategy at the ESRF.

J. Baruchel

References
[1] K. Dzieciol, A. Borbély, F. Sket, A. Isaac, M. Di Michiel, P. Cloetens, Th. Buslaps and A.R. Pyzalla, Void growth in copper during high-temperature power-law creep, *Acta Materiala* **59**, 671-677 (2011).
[2] I. Kruta, N. Landman, I. Rouget, F. Cecca and P. Tafforeau, The Role of Ammonites in the Mesozoic Marine Food Web Revealed by Jaw Preservation, *Science* **331**, 70-72 (2011).

Biology and biomedical applications

Functionalised nanoparticles in human cells by X-ray nano-imaging

Biomedical applications of gold have a long history stretching back almost five thousand years. The dawn of the 'nano-age' has further broadened the potential of gold and other precious metals in medical applications, and today gold and platinum nanoparticles are being employed in entirely novel ways for improved diagnostics and therapy. In cancer treatment there is a delicate balance between attacking and killing the cancer cells and minimising harm to non-cancerous tissues. To minimise or even eliminate this "collateral" damage, the development of new nanodevices where one nanoparticle can specifically deliver therapeutic payloads, including small drug molecules or large biomolecules, to the targeted cancer cell, have become increasingly appealing for the future treatment of cancer. Gold and platinum nanoparticles have recently emerged as attractive candidates for

Principal publication and authors
D.J. Lewis (a), C. Bruce (b), S. Bohic (c,d), P. Cloetens (d), S.P. Hammond (a), D. Arbon (b), S. Blair-Reid (b), Z. Pikramenou (a) and B. Kysela (b), *Nanomedicine* **5**, 1547-1557 (2010).
(a) School of Chemistry, University of Birmingham (UK)
(b) School of Clinical and Experimental Medicine, University of Birmingham (UK)
(c) Institut des Neurosciences Grenoble (GIN), Université Joseph Fourier, Grenoble (France)
(d) ESRF

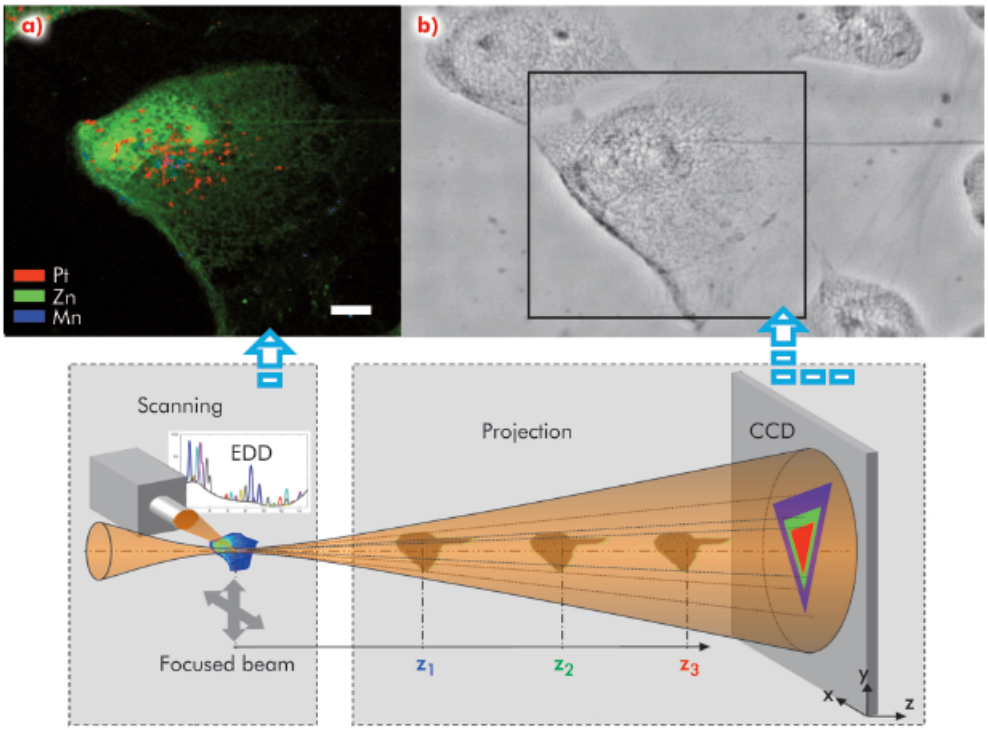

Fig. 124: Synchrotron nano-imaging of internalised lanthanide nanoparticles. Bottom panel: Schematic view of the experimental setup. a) the fluorescence map of the cell transfected with [CeL]+ coated platinum nanoparticles is reconstructed after spectral deconvolution (white size bar represents the distance of 5 µm). The scanning capabilities of the system are combined with projection microscopy that uses the partial coherence of the beams. b) A relative phase map can be generated by applying a numerical phase retrieval procedure. This map is equivalent to the projection of the electron density of the corresponding cell and provides essential complementary microstructural information.

delivery of therapeutic payloads [1]. The noble metal cores are chemically inert and non-toxic and therapeutic payloads including small drug molecules and/or large biomolecules (*e.g.* plasmid DNA or proteins for gene and protein therapy and targeting applications) can be attached *via* thiol linkages yielding stable nanovectors. For these reasons we are actively pursuing development of nanovectors with multiple functionalities. For many intended therapeutic applications, very few nanovectors delivered to the targeted cells and/or cellular compartment (*e.g.* cell nucleus), might be sufficient to achieve the desired effect. It is unlikely that any targeting strategy will be 100% target specific. This will result in at least some nanoparticles being internalised by healthy, non-targeted cells in low numbers. The imaging and detection of such low presence in cells represents a difficult problem and visualising where exactly the nanovectors go and in what numbers is extremely important.

We have developed a new highly-sensitive synchrotron-based X-ray fluorescence microscopy (SR-XFM) technique to image the intracellular distribution of internalised noble metal nanoparticles.

SR-XFM has sufficient sensitivity to detect a single nanoparticle in the cell (few thousand atoms) in cryofixed and lyophilised cells. The nano-imaging end-station **ID22NI** with spatial resolution of 60 nm allows elemental imaging of whole cells (Figure 124). To mimic the targeted nuclear delivery, the CeL gold nanoparticles (CeL-AuNP) and CeL-platinum nanoparticles (CeL-PtNP) were transfected to MRC5VA normal human cells. The fluorescence map panel (Figure 124a) of the selected area from the relative phase map (Figure 124b) shows intracellular distribution of CeL-PtNP (with average diameter of 6 nm) with clear localisation predominantly in the nucleus (red pixels). Although no absorption contrast can be obtained from cells at the incident energy used, a relative phase map of a complete cell was acquired in the hard X-ray regime through projection microscopy using the partial coherence of the X-ray beam. The numerical phase retrieval procedure we have developed shows that a quantitative phase map with high spatial resolution and high sensitivity can be obtained highlighting very thin cellular structures (Figure 124b). This provides essential microstructural information from which the nucleus can be easily located and corroborates with the most intense zinc X-ray fluorescence signal (Figure 124a). Our new approach makes it possible to merge the information that will potentially provide a means to determine cellular volume and consequently an improved chemical quantification of intracellular metal-based nanovectors concomitantly to the level and sub-cellular distribution of physiologically essential metals. The nanofocus X-ray beam allows us to achieve detailed elemental maps with platinum single pixel hotspots likely to represent very small clusters of nanoparticles. Similarly, the technique proved to be very successful in intracellular localisation of CeL-gold nanoparticles in relation to other elements.

In summary, we have demonstrated the unprecedented potential of SR-XFM nano-imaging for the development of new nanoparticles as platforms for bioimaging and biodelivery applications. This technique has the potential to revolutionise the development of targeted nanoparticles.

Reference
[1] P. Ghosh, G. Han, M. De, C.K. Kim and V.M. Rotello, *Adv. Drug Deliv. Rev.* **60,** 1307-1315 (2008).

Cellular insight into the human cerebellum by X-ray grating interferometry

The human brain has a complicated and fascinating micro-structure that requires adequate imaging modes. The established techniques of magnetic resonance imaging (MRI) and X-ray computed tomography (CT) are each subject to limitations. Whereas MRI provides superb contrast between the different components of brain tissue, such as white and grey matter, the

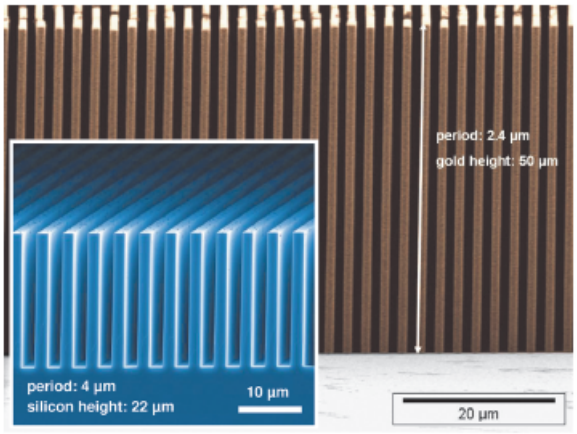

Fig. 125: Deep microstructured transmission gratings used in X-ray grating interferometers. Main picture: gold absorption grating made at KIT; Inset: silicon phase grating made at PSI.

Principal publication and authors
G. Schulz (a), T. Weitkamp (b), I. Zanette (b), F. Pfeiffer (c), F. Beckmann (d), C. David (e), S. Rutishauser (e), E. Reznikova (f) and B. Müller (a), *J. R. Soc. Interface* 7, 1665-1676 (2010).
(a) Biomaterials Science Center, University of Basel (Switzerland)
(b) ESRF
(c) Department of Physics/Biophysics (E17), Technische Universität München, Garching (Germany)
(d) Institute for Materials Research, Helmholtz-Zentrum Geesthacht (Germany)
(e) Laboratory for Micro- and Nanotechnology, Paul Scherrer Institut, Villigen (Switzerland)
(f) Institute for Microstructure Technology, Karlsruhe Institute for Technology (Germany)

spatial resolution of this technique prevents investigations on the cellular level. Whereas, conventional absorption micro-CT has the required spatial resolution but its contrast is limited for soft tissues.

A promising alternative is X-ray phase contrast microtomography, which is known to give superior contrast for light materials. Here we report on phase contrast tomography obtained by X-ray grating interferometry [1,2], a technique originally developed by researchers of the Paul Scherrer Institut, Switzerland, with the ESRF involved since the beginning. We applied the method in a comparative study of synchrotron-based absorption and phase microtomography of the human cerebellum.

Phase tomography as used here yields the real part of the X-ray refractive index. This quantity is essentially proportional to the three-dimensional electron density distribution of the object. Contrast in the radiographs is generated by refraction of the X-ray beam in the specimen. In X-ray grating interferometry, the refraction signal is detected through an arrangement of deep transmission grid structures with micrometre-sized pitch, made using dedicated microstructuring processes (Figure 125). The gratings modulate the phase and/or amplitude profile of the X-ray wavefront.

The interferometric tomography of a human cerebellum was carried out at beamline **ID19** with 23-keV X-rays. The interferometer consisted of a silicon phase grating with a line width of 2.4 µm and a structure height of 29 µm and an absorption grating with gold lines of width 1.2 µm (grating pitch 2.4 µm) and a structure height of 50 µm – *i.e.* an aspect ratio of more than 40. The two gratings were placed between the specimen and the detector, and separated by a propagation space of 480 mm length. During the

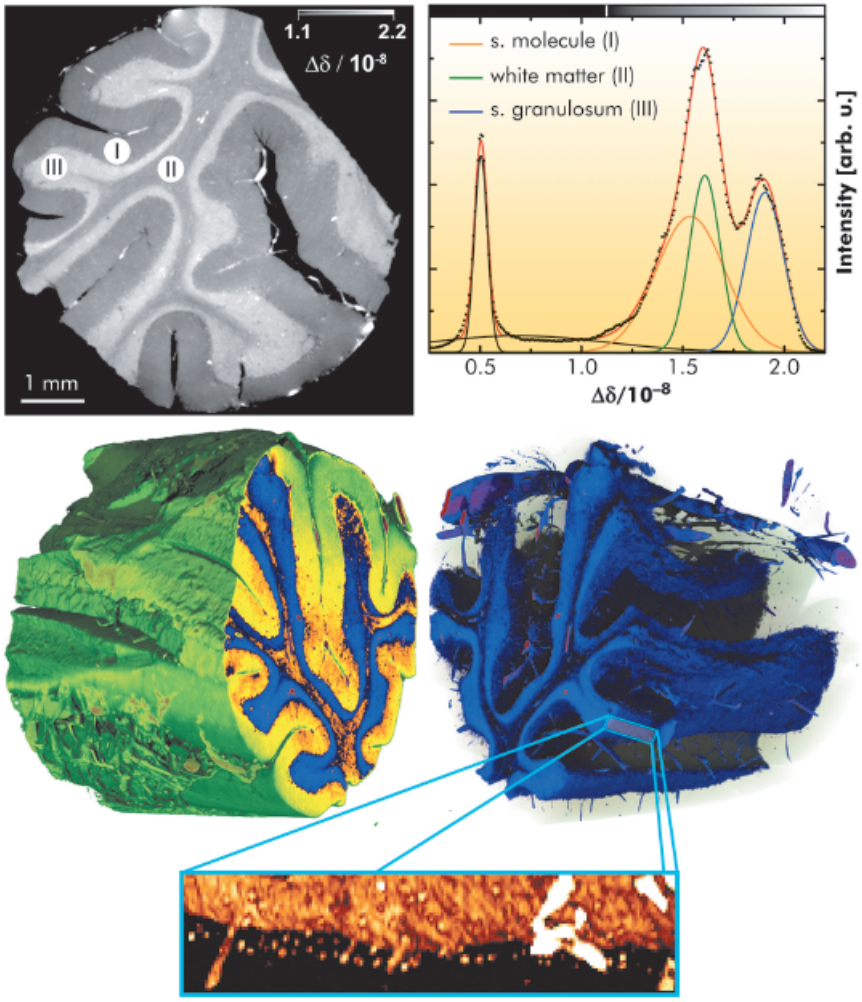

Fig. 126: Upper: A single tomographic slice from the phase tomography dataset and a multi-Gaussian fit to the corresponding histogram. Lower: Three-dimensional false-colour renderings of a human cerebellum, obtained with X-ray grating interferometric phase tomography. White matter (orange) can be distinguished from two types of grey matter (blue: *stratum granulosum*; yellow: *stratum moleculare*). The data also show blood vessels and individual cells identified as Purkinje cells (inset at bottom of figure).

measurements, the cerebellum, fixed in formalin, was immersed in a water tank with parallel acrylic glass plates.

The reconstructed tomograms (Figure 126, top left) show distinct contrast between three different layers: *stratum moleculare* (I) and *stratum granulosum* (III), which both belong to grey matter, plus the white matter (II). Using a multi-Gaussian fit to the corresponding histogram (Figure 126, top right), we quantified the value of refractive index relative to the immersion medium (water), $\Delta\delta(x,y,z)$. The standard deviation of the retrieved values of beam deflection angle α in the unstructured background around the object was $\sigma_\alpha = 17$ nrad. This value is a figure of merit for the measurement sensitivity of the refraction angle. The precision of the refractive index in the tomograms was identified by the width of the water peak in the histogram, $\sigma_\delta(H_2O) = 2.3 \times 10^{-10}$. This corresponds to an electron density resolution of 0.15 electrons per nm^3 and a mass density sensitivity of 0.25 mg cm^{-3}.

With a voxel size of 5 µm, the spatial resolution of the data is good enough to discriminate individual cells in the volume data. Thus, the dot-like structures near the bottom of the inset in Figure 126 are believed to be Purkinje cells, a type of large neuron in the brain. The tissue surrounding the cells has been made transparent in this 3D rendering.

These results clearly demonstrate that the spatial resolution and the sensitivity of this method are well suited for the discrimination between soft tissues such as white and grey matter and even for the visualisation of individual cells surrounded by tissue, without the use of any contrast agent.

References
[1] T. Weitkamp, A. Diaz, C. David, F. Pfeiffer, M. Stampanoni, P. Cloetens and E. Ziegler, *Opt. Expr.* **13**, 6296–6304 (2005).
[2] F. Pfeiffer, O. Bunk, C. David, M. Bech, G. Le Duc, A. Bravin and P. Cloetens, *Phys. Med. Biol.* **52**, 6923–6930 (2007).

Characterisation of human cartilage by phase-contrast imaging

Principal publication and authors
P. Coan (a, b), F. Bamberg (a), P.C. Diemoz (b), A. Bravin (b), K. Timpert (a), E. Mützel (c), J. Raya (a), S. Adam-Neumair (d), M.F. Reiser (a) and C. Glaser (a), *Investigative Radiology* **45**, 437-444 (2010).
(a) Ludwig-Maximilians University, Faculty of Medicine and Institute of Clinical Radiology, Munich (Germany)
(b) ESRF
(c) Ludwig-Maximilians University, Institute of Forensic Medicine, Munich (Germany)
(d) Ludwig-Maximilians University, Institute of Anatomy, Munich (Germany)

Quasi-coherent X-rays have been proven capable of visualising the architecture of articular cartilage, which is invisible in conventional clinical radiographs. A novel X-ray imaging approach, phase contrast imaging (PCI), has been applied to study the fine structure of human cartilage in normal and pathologic conditions. The experiments were performed at **ID17**, the Biomedical beamline, where a particular PCI method, analyser-based imaging (ABI), was utilised [1]. This method exploits the properties of X-ray diffraction with a high quality crystal to generate images where contrast is due to a combination of X-ray absorption, refraction and ultra-small angle scattering. As a result, image contrast can be improved over conventional radiography.

Phase contrast analyser-based tomograms (ABI-CT) showed excellent depiction of the complete cartilage volume and of its 3D architecture in all samples imaged in this study. In Figures 127 and 128, reconstructed ABI-CT slices of a normal and an osteoarthritic sample are provided. The edges and interfaces between cartilage and calcified cartilage/subchondral bone and between the formalin and the cartilage surface (as indicated by the yellow arrow) are clearly discernible. These are attributable to refraction of the beam occurring at the edges between tissues with different refraction indexes. In the ABI images, low intensity oval shaped structures with an extent from 10–40 µm are detectable within the cartilage

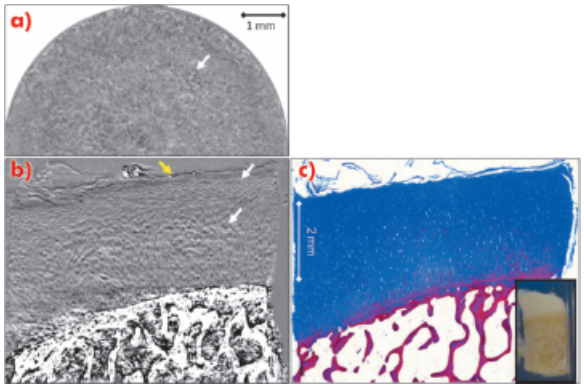

Fig. 127: ABI-CT of a normal cartilage sample at an X-ray energy of 26 keV with a detector pixel size of 8^2 µm^2. a) Portion of an axial ABI-CT acquired at the level of the radial zone of the cartilage. b) Coronal plane extracted from the reconstructed ABI-CT volume. c) Histologic section (Azan staining) and photo of the original osteochondral cylinder (inset).

matrix. Comparison with the corresponding histology sections (Figures 127c, 128b) identifies these structures as chondrocytes and/or chondrons (the synthetically active elements in cartilage). In all ABI data, the tide mark (*i.e.* the interface between calcified and uncalcified cartilage), the subchondral bone plate (calcified cartilage + solid subchondral bone proper) and trabecular detail from within the spongiform bone can be appreciated. In particular, Figure 127a displays the above-mentioned dark oval dots (arrow), chondrocytes, against the brighter background of the cartilage matrix in an axial slice approximately at 75% depth from the surface (at the level of the radial zone). We can appreciate that chondrocytes are aligned perpendicular to the tide mark/surface, thus their cross sections in axial slices appear as circles (Figure 127a). Coronal reformats in both ABI (Figure 127b) and histology (Figure 127c) impressively demonstrate the typical pattern of chondrocyte alignment and distribution across the cartilage. The central portions of Figure 127b display Benninghoff's 'arch' or 'arcade' like alignment of the chondrocytes/chondrons (*i.e.* clusters of chondrocytes): they initially rise vertically upwards from the tide mark but soon diverge laterally when approaching the cartilage surface following a curved trajectory. Figure 128 shows an osteoarthritic cartilage-on-bone sample. Areas of still intact, smooth appearing, cartilage surface (right aspect and mid portion of sample) alternate with subtle (right half of sample) and distinct (left half) surface erosions/defects (Figures 128a,b). A comparison based on histopathological parameters performed by two independent, blinded observers on the ABI-CT images clearly determined differences between the two groups of samples (normal and pathologic). A distinct zonal pattern in the cartilage matrix could consistently be visualised. The osteoarthritic samples showed significantly lower chondrocyte distribution homogeneity, less chondrocyte alignment, lower height of tangential, transitional, and radial zones and a higher prevalence of superficial cartilage damage.

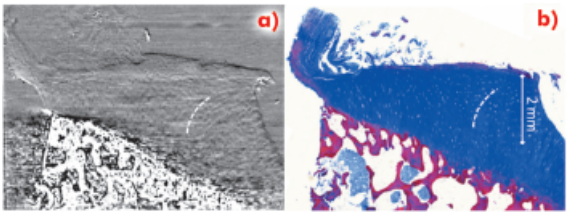

Fig. 128: a) Coronal plane from the ABI-CT volume of osteoarthritic cartilage. b) Corresponding (to the extent that is possible practically) section from histology. ABI-images acquired at an X-ray energy of 26 keV with a detector pixel size of 8^2 µm^2.

The results of this proof-of-concept study indicate that the phase contrast ABI-CT technique is capable of providing soft-tissue contrast at a histopathologic level, useful to differentiate osteoarthritic and healthy cartilage samples. We were able to show that fine structural details of the cartilage matrix as well as its degeneration in early and advanced stages of osteoarthritis can be visualised by ABI-CT in relatively large samples.

References
[1] A. Bravin. *Journal of Physics D: Applied Physics* **vol. 36** (2003).
[2] P. Coan, F. Gruener, C. Glaser, T. Schneider, A. Bravin, M. Reiser and D. Habs, *Nuclear Instruments and Methods in Physics Research A* **vol. 608** (2009).

Tolerance of arteries to microplanar X-ray beams

Radiation-induced damage to healthy tissues limits the maximum dose in the treatment of tumours. It has to be avoided especially for arteries, capillaries and veins because an impaired blood circulation might cause organ dysfunction. The artery wall is a complex structure of multiple layers of elastic fibres, vascular smooth muscle cells (VSMC) and collagen fibres that regulate blood pressure and blood perfusion in organs.

A new radiotherapy protocol micro-beam radiation therapy (MRT) has been developed to spare healthy tissues. X-rays are confined to very thin slices of planar beams of 50 µm arranged in parallel arrays with a interspacing of about 400 µm [1]. As a result, the X-rays irradiate only 20% of a tissue volume, and the areas between the beam slices (valleys) receive less radiation. The microplanar beam arrays are normally cross-fired at the tumour to increase the dose in the valley regions. This therapy has shown in living mice that the cerebral vasculature and the blood brain barrier tolerated high single peak doses (< 1000 Gy) without hemorrhage and loss of blood perfusion [2]. Only at a high peak dose of 1000 Gy, a transient blood brain barrier leakage of 12 days was observed without severe consequences to normal brain function.

Principal publication and authors
B. van der Sanden (a), E. Bräuer-Krisch (b), E. Albert Siegbahn (c), C. Ricard (a), J.-C. Vial (d) and J. Laissue (e), *Int. J. Radiation Oncology Biol. Phys.* 77, 1545-1552 (2010).
(a) INSERM U836, Institute of Neuroscience, Grenoble (France)
(b) ESRF
(c) Department of Oncology and Pathology, Karolinska Institutet, Stockholm (Sweden)
(d) CNRS UMR 5588, Physical Spectroscopy, Grenoble (France)
(e) Institute of Pathology, University of Bern (Switzerland)

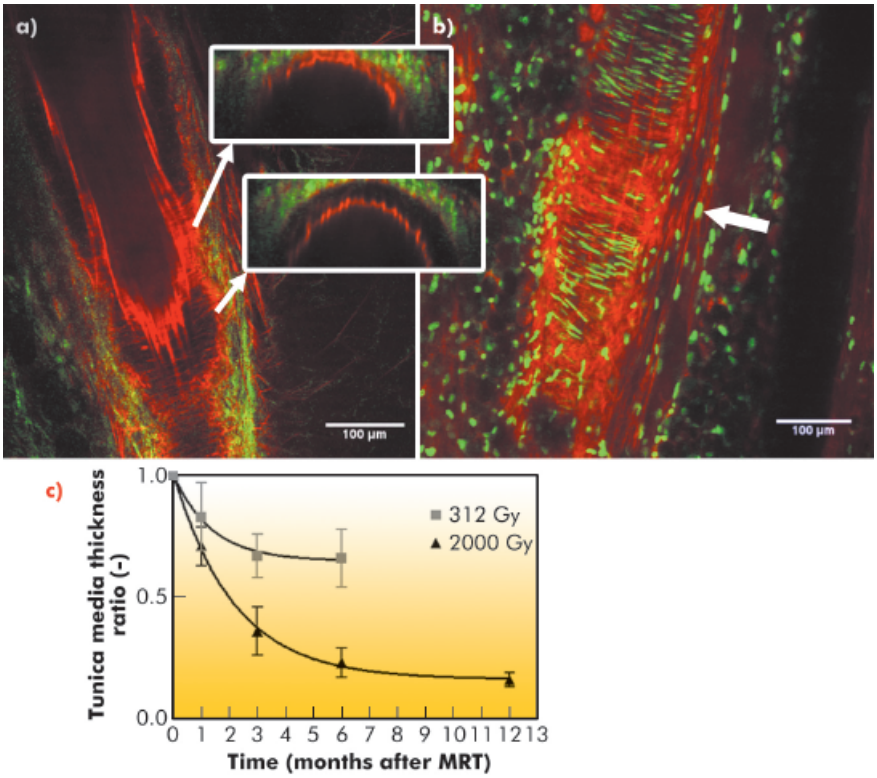

Fig. 129: Longitudinal sections taken three months after microplanar irradiation (2000 Gy). a) Elastic fibres (red) and collagen fibres type I and III (SHG, green) 26 µm below the external surface of the artery. Inserts: Cross sections at the level of the beam path and the valley; the (dark) TM in the beam path is thinner than in the valley region. b) Image 16 µm below the external surface of the artery. Elastic fibres (red) are diffusely stained in the beam path. The density of the green, elongated-shaped VSMC nuclei is higher in the valleys than in the darker beam path. c) Mean tunica media thickness ratio (microbeam path/valley, ± one standard deviation) versus time after irradiation, 312 Gy (■) and 2000 Gy (▲) dose groups.

We have evaluated the effect of MRT on the artery wall of living mice using intravital microscopic techniques: two-photon microscopy (2PM) and second harmonic generation imaging (SHGI) [3]. A new two-photon imaging protocol was used for a more sensitive and deeper detection of elastic fibres in the artery wall using sulforhodamin-B [4]. In parallel, VSMC in the artery wall were detected after nuclei staining with Hoechst 33342.

The left hind leg of healthy mice including the saphenous artery was irradiated by an array of 26 microbeams of synchrotron X-rays (50 µm-wide, spaced 400 µm on centre) with peak entrance doses of 312 Gy and 2000 Gy. During 12 months after irradiation, the artery remained patent, but narrow VSMC segments in the tunica media that were in the microplanar beams paths became atrophic and fibrotic in a dose-dependent pattern (Figure 129). The wide tunica media segments between the microbeam paths hypertrophied.

Mice hind leg arteries tolerate microbeam peak doses of up to 2000 Gy delivered by spatially fractioned micro planar beams in a single session without developing occlusions within 1 year, in contrast to the deleterious consequences of comparable doses delivered by broad-beam X-rays. The permanent sequelae of microplanar irradiation appear to be confined to microscopic segments of the tunica media (layer with VSMC) and tunica adventia (outermost collagen layer of the artery that showed fibrosis). Clinical risks of long-delayed disruption or occlusion of non-targeted arteries from microbeam radiation therapy will prove less than corresponding risks from broad-beam radiosurgery, especially if peak doses are kept below 3 hectogray.

References

[1] D.N. Slatkin, P. Spanne, F.A. Dilmanian and M. Sandborg, *Med Phys* **19**, 1395-1400 (1992).

[2] R. Serduc, P. Verant, J.C. Vial, R. Farion, L. Rocas, C. Remy, T. Fadlallah, E. Brauer, A. Bravin, J. Laissue, H. Blattmann and B. van der Sanden, *Int J Radiat Oncol Biol Phys* **64**, 1519-1527 (2006).

[3] W. Denk, J.H. Strickler and W.W. Webb, *Science* **248**, 73-76 (1990).

[4] C. Ricard, J.C. Vial, J. Douady and B. van der Sanden, *J Biomed Opt* **12**, 064017 (2007).

Materials science

Structure of multi-quantum wells in electroabsorption-modulated lasers for optoelectronics

Multi-quantum well (MQW) structures based on quaternary III-V semiconductor alloys are widely used in optical communication systems. Optoelectronic devices often require the integration of two different functions in the same chip. The selective area growth (SAG) technique gives excellent results for such monolithic integration [1]. SAG exploits

the perturbation of the growth fluxes induced by a dielectric mask. When the metallorganic precursors collide with the dielectric mask, they are deflected and migrate through the unmasked semiconductor where the growth starts. In this way, the reactive species coming from the gas phase are enriched by those deflected by the mask and the result is a variation in composition and thickness of semiconductors grown near (SAG region) and far (field region) from the mask.

The electroabsorption modulated laser (EML), obtained by monolithic integration of an electroabsorption modulator (EAM) with a distributed feedback laser (DFB), is one of the most promising applications of SAG. A voltage modulation applied to the EAM switches it between an opaque and a transparent state by means of the Stark effect and ensures the modulation of the DFB laser emission, allowing long-distance communication (up to 80 km) at high frequency (10 Gb/s). The SAG EML device investigated here is an $Al_{xw}Ga_{yw}In_{1-xw-yw}As/Al_{xb}Ga_{yb}In_{1-xb-yb}As$ (compressive-strained well/tensile-strained barrier) MQW structure grown on InP by metallorganic vapour phase epitaxy. The mask used for the growth (Figure 130a) featured 20 µm wide SiO_2 stripes with a 30 µm opening width between them.

X-ray fluorescence (XRF) maps (Figure 130b) reveal that Ga K_α and As K_β counts are higher in the SAG region owing to material enrichment caused by the SiO_2 stripes. The effectiveness of the SAG technique in modulating the chemical composition of the quaternary alloy is proven by the map reporting the ratio between Ga and As counts in which a gradient in the average well/barrier chemical composition is clearly visible. Since the Ga/As ratio is lower in the SAG region than in the field, we can assert that the average Ga content of the MQW structure progressively increases by moving from the SAG to the field (along the Y-line showed in Figure 130a).

Principal publication and authors
L. Mino (a), D. Gianolio (a), G. Agostini (a), A. Piovano (a), M. Truccato (b), A. Agostino (c), S. Cagliero (c), G. Martinez Criado (d), S. Codato (e) and C. Lamberti (a), *Adv. Mater.* **22**, 2050-2054 (2010).
(a) Department of Inorganic, Materials and Physical Chemistry, University of Turin (Italy)
(b) Department of Experimental Physics, University of Turin (Italy)
(c) Department of General and Organic Chemistry, University of Turin (Italy)
(d) ESRF
(e) Avago Technologies Italy S.r.l., Turin (Italy)

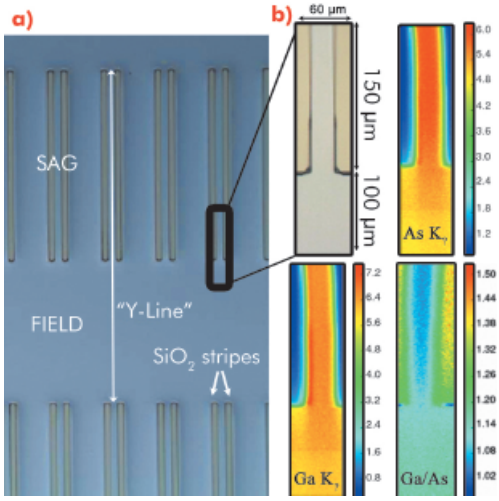

Fig. 130: a) Optical micrograph of the SiO_2 stripes-patterned InP substrate allowing SAG growth. The black rectangle, magnified in part (b), shows the region sampled in the XRF maps. b) Spatial maps of the fluorescence counts of the principal element's lines.

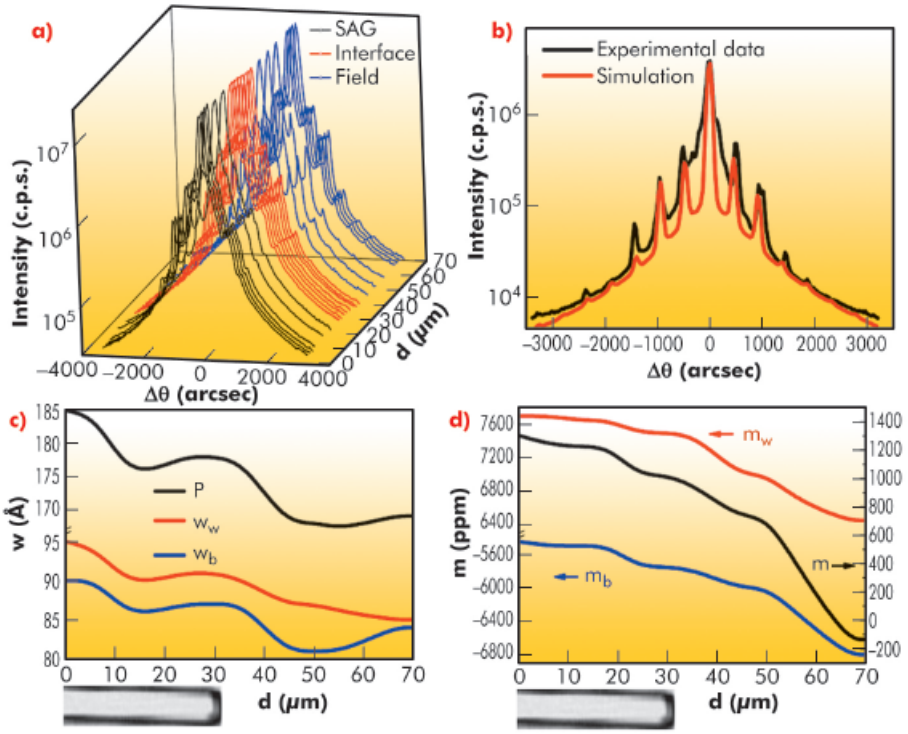

Fig. 131: a) XRD patterns collected along the Y-line starting 30 µm before the end of the stripes in the SAG region. b) Experimental and simulated XRD patterns in the field region. c) Barrier and well widths and period as a function of the position along the Y-line, obtained by simulation of the 35 experimental XRD patterns. d) As part c) for the well, barrier and overall mismatches.

References
[1] M.E. Coltrin and C.C. Mitchell, *J. Crystal Growth* **254**, 35–45 (2003).
[2] C. Ferrari and C. Bocchi, in: *Characterization of Semiconductor Heterostructures and Nanostructures*; C. Lamberti, Ed.; Elsevier: Amsterdam, 93–132 (2008).
[3] L. Mino, A. Agostino, S. Codato and C. Lamberti, *J. Anal. At. Spectrom.* **25**, 831-836 (2010).
[4] L. Mino, D. Gianolio, G. Agostini, A. Piovano, M. Truccato, A. Agostino, S. Cagliero, G. Martinez-Criado, F. d'Acapito, S. Codato and C. Lamberti, Small 7, in press, DOI: 10.1002/smll.201001229 (2011).

The structural parameters of the sample were investigated by μ-X-ray diffraction (XRD): 35 different spatial points were sampled along the Y-line (**Figure 131a**). With such data, it is possible to obtain the widths (w_b, w_w, **Figure 131c**) and the mismatches (m_b, m_w, **Figure 131d**) of the barrier and of the well by fitting the observed patterns (**Figure 131b**) [2]. Both w_b and w_w undergo a modulated increase moving from field to SAG regions: this is the direct measure of the material enrichment in the SAG region. Moreover, both m_b and m_w values increase almost monotonically moving from the field to the SAG reflecting the expected modulation of the $Al_xGa_yIn_{1-x-y}As$ composition of barrier and well layers.

This key information, coupled with the μm-determination of the energy gap by photoluminescence, led to a characterisation of the structural gradient of the MQW structure along the Y-line from the field to the SAG region.

In summary, we determined the composition and the structure of the SAG EML device with a spatial resolution of 2 μm. This unprecedented characterisation allowed us to understand the structure and thus it gave the appropriate feedback needed to improve the growth process; such development was previously based only on a trial and error approach. A new generation of devices may be produced by extending this method to other SAG growths with different stripes and opening sizes [3,4].

Principal publication and authors
M. Fratini (a,b), N. Poccia (a), A. Ricci (a), G Campi (a,c), M. Burghammer (d), G. Aeppli (e) and A. Bianconi (a), *Nature* **466**, 841-844 (2010).
(a) Physics Department, Sapienza University of Rome (Italy)
(b) Current address: Institute for Photonic and Nanotechnologies, CNR, Roma (Italy)
(c) Institute of Crystallography, CNR, Roma (Italy)
(d) ESRF
(e) London Centre for Nanotechnology and Department of Physics and Astronomy, University College London (UK)

Imaging scale-free structural organisation of oxygen interstitial atoms favouring high temperature superconductivity

A new experiment using a focussed micro X-ray beam has found a surprising pattern lurking in a high temperature superconductor showing that high temperature superconductivity belongs to the class of collective "Quantum Phenomena in Complex Matter". The experiment was performed at beamline **ID13.** We studied a layered oxide of copper belonging to the class of metallic ceramics that held the record for operating at the highest temperature when researchers discovered the superconductivity of this material. Oxide-based superconductors are very difficult to study owing to their extra (interstitial) or missing (vacancy) oxygen atoms, called dopants, which are known to roam around in the skeleton of the material, formed by other elements, and that may freeze in ordered or random patterns when the samples are cooled. The reason for this material's elevated high-temperature conductivity was, until now, not known. For many years scientists assumed that it was because of a homogeneous distribution of dopants, which made researchers concentrate on the nanometre arrangement of these dopants to find the answer to the superconductivity. We have focussed on structure at the nanometre scale as the determinant of the unusually strong superconductivity of the oxides of copper. We used the new technique of X-ray microscopy to examine a copper oxide superconductor whose internal structure could be changed via simple heat treatments – an approach employed by ceramicists over millennia to modify oxide materials. We discovered that the best superconductivity was obtained when the microstructure was most 'connected', meaning that it is possible to trace a path with the same nanostructure (exhibited by oxygen atoms) over a large distance. The microstructure in this case was 'fractal': if we were to zoom in on the material's structure at increasing levels of magnification, its appearance would remain the same (see **Figure 132**).

To see whether the fractal pattern was important, we interfered with it by heating and then quickly cooling the superconductor. Crystals with stronger fractal patterns performed better as a superconductor at higher temperatures than those with weaker fractal patterns. The high temperature conductivity was

promoted by oxygen-crystal defects that form geometrical patterns that look the same on different scales, ranging from a micrometre up to fractions of a millimetre (see Figure 132). Figuring out why the fractal pattern forms in these copper-oxide crystals and how it influences the superconductivity are the next challenges.

Once the details are uncovered, researchers could control the arrangement of oxygen atoms to design better copper-oxide superconductors — perhaps even those that operate at room temperature.

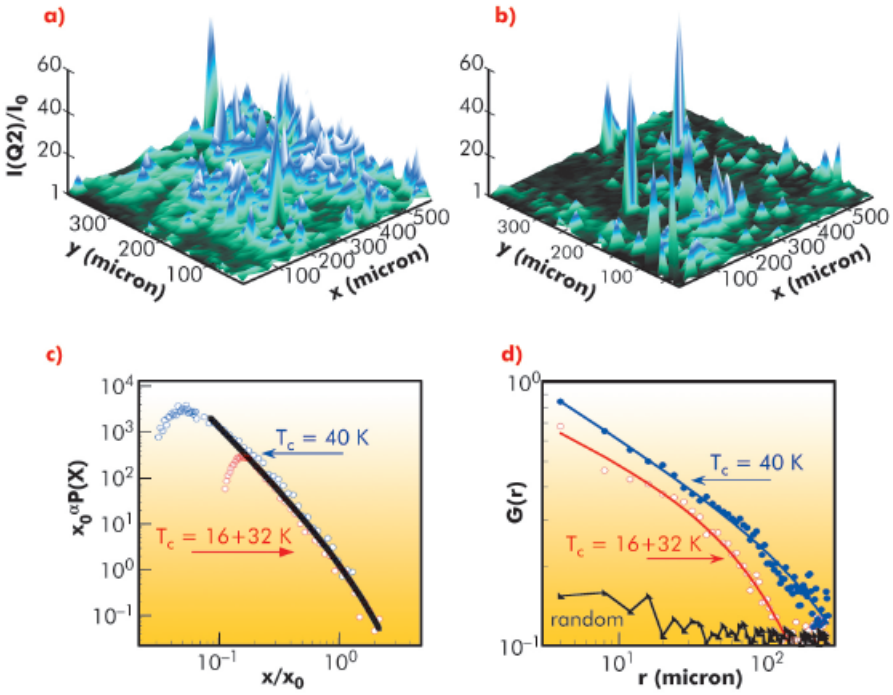

Fig. 132: a) and b) The position dependence of the Q2 superstructure intensity $I(Q2)/I_0$ for two typical samples obtained by following different annealing–quenching protocols, resulting in T_c = 40 K (a) and T_c = 16+32 K (b) phases. Visual inspection of (a) and (b) shows that the spikes corresponding to ordered microdomains are more isolated for the more disordered sample with lower T_c than for the high-T_c sample, indicating that the nucleation and growth of Q2 regions proceeds to smaller length scales for shorter annealing times. c) The probability distribution $P(x)$, of the Q2 XRD intensity. d) Spatial correlation function, $G(r)$. The data are fitted by the functions described in the principal publication.

Cultural heritage

Opacification of Egyptian and Roman glass

During the Egyptian 18th dynasty and the Roman period, opaque coloured glass was extensively used to produce artifacts such as precious jewels or mosaic tesserae (Figure 133). These white, blue or turquoise glasses were opacified by white calcium antimonate crystals dispersed in a vitreous soda-lime-silica matrix. The difference in refractive index between the two phases prevents light from being completely transmitted and leads to the opacification of the glass.

Glass opacification generally relies on two main processes. The first involves the addition of natural or *ex situ* synthesised crystals to a translucent glass. The second relies on the introduction of antimony as an oxide or a sulphide into glass. This leads to the *in situ* crystallisation of opacifying agents through the separation from the melt of calcium antimonate crystals.

The common assumption is that calcium antimonates ($CaSb_2O_6$ and/or $Ca_2Sb_2O_7$) were obtained by *in situ* crystallisation in both Egyptian and Roman glass. However, questions still remain on the technology and provenance of the opacifiers. Contributing to an in-depth knowledge of ancient glass opacification process was the key objective of this study.

Our study focussed on the investigation of the crystals and the vitreous matrices. The oxidation state of antimony in the vitreous matrices and the opacifiers was measured for the first time in opaque Egyptian glass from

Principal publications and authors
S. Lahlil (a), I. Biron (a), M. Cotte (a, b), J. Susini (b) and N. Menguy (c), *Applied Physics A* **98**, 1-8 (2010);
S. Lahlil (a), I. Biron (a), M. Cotte (a, b) and J. Susini (b), *Applied Physics A* **100**, 683-692 (2010).
(a) C2RMF Centre of Research and Restoration of the French Museums –UMR 171 CNRS, Paris (France)
(b) ESRF
(c) IMPMC Institut de Minéralogie et de Physique des Milieux Condensés - UMR 7590 CNRS,

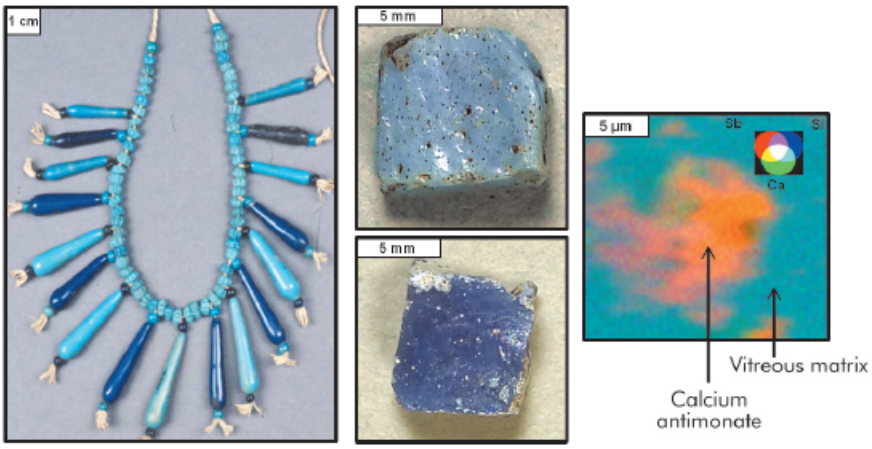

Fig. 133: Left: Blue and turquoise necklace (Louvre Museum E2341 ©C2RMF/D. Bagault). Centre: Opaque blue mosaic Roman tesserae from Aquilea and Rome (1st cent. B.C.- 6th cent. A.D.). Right: µ-XRF cartography showing a calcium antimonate crystal in the vitreous matrix.

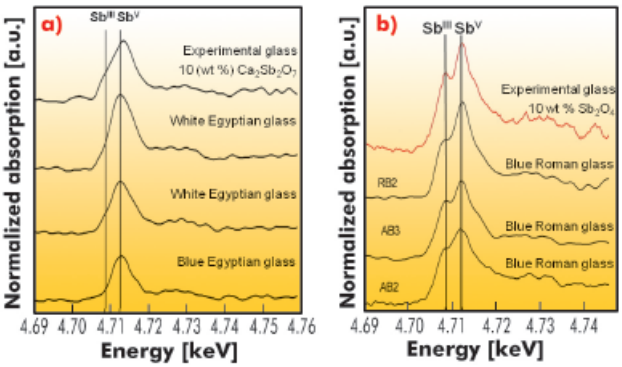

Fig. 134: µ-XANES spectra performed at the Sb L_I edge (average of five measurements) on the vitreous matrices. a) Egyptian white and blue glasses from the 18th dynasty (1570-1292 B.C.) and experimental glass opacified by addition of 10 wt% $Ca_2Sb_2O_7$ to a translucent glass; b) Blue opaque Roman mosaic tesserae from Aquilea and Rome (1st cent. B.C.- 6th cent. A.D.).

the 18th dynasty (1592-1270 B.C.) and in Roman mosaic tesserae from Aquilea and Rome (1st cent. B.C.- 6th cent. A.D.). Additionally, opaque glasses with a composition close to archaeological glasses were synthesised under controlled conditions in the laboratory. These synthetic glasses were compared to ancient glasses using appropriate micro-analytical techniques that have never been used before on this type of material: micro X-ray fluorescence mapping (µ-XRF) and micro X-ray absorption near edge spectroscopy (µ-XANES), carried out at beamline **ID21**. The synchrotron-based sub-micrometric measurements proved to be very well suited to measuring selectively the antimony oxidation state in the vitreous matrix (Figure 133). The latter, when combined with the microstructural observations and the crystalline phases identification, is one of the key parameters for the determination of the opacification process and the source of antimony employed.

Contrary to existing beliefs, it was demonstrated that Egyptian glassmakers were able to synthesise *ex situ* calcium antimonate compounds that do not exist in nature, which were subsequently added to the glass as opacifiers (Figure 134a). Egyptian blue and green pigments were the only high temperature compounds known to have been synthesised in Ancient Egypt. Our results show that calcium antimonate glass opacifiers were also synthetic compounds, providing further evidence for the sophisticated chemistry of this civilisation.

In Roman glasses, not only the *in situ* crystallisation process was confirmed but also the ratio Sb^{III}/Sb^{V} measured in the vitreous matrices indicates that Sb_2O_4 could have been used as an antimony source (Figure 134b). This finding suggests that a first step of roasting natural stibnite (Sb_2S_3) or metallic antimony was made on antimony containing raw materials before introducing them into the glass, and it provides further evidence of the remarkable know-how of Roman craftsmen.

This work demonstrates that µ-XANES measurements provide invaluable information about glass opacification processes. This new approach exploiting the high spatial resolution, low detection limit and high chemical sensitivity provided at the ID21 X-ray microscope is the starting point for new discoveries on ancient glass technology.

Synchrotron reveals human children outpaced Neanderthals by slowing down

Principal publication and authors
T.M. Smith (a,b), P. Tafforeau (c), D.J. Reid (d), J. Pouech (b,c), V. Lazzari (b,c,e), J.P. Zermeno (a), D. Guatelli-Steinberg (f), A.J. Olejniczak (b), A. Hoffman (g), J. Radovcic (h), M. Masrour (i), M. Toussaint (j), C. Stringer (k) and J-J. Hublin (b), *Proc. Natl. Acad. Sci. USA* **107**, 20923-20928 (2010).
(a) Harvard University (USA)
(b) Max Planck Institute for Evolutionary Anthropology (Germany)
(c) ESRF
(d) Newcastle University (UK)
(e) Université de Poitiers (France)
(f) Ohio State University (USA)
(g) Museum für Vor- und Frühgeschichte (Germany)
(h) Croatian Natural History Museum (Croatia)
(i) University Bordeaux II (France)
(j) Service Public de Wallonie (Belgium)
(k) The Natural History Museum (UK)

Reconstructing the evolution of human development from a severely limited fossil record is a fundamental challenge. While is it well established that humans are developmentally unique among living primates, weaning earlier and reproducing later than expected, the adaptive significance and evolutionary origins of our prolonged childhood are unresolved. Tooth histology, involving quantification of microscopic growth, is the most effective means of determining developmental rates, eruption ages, and age at death in juvenile hominins [1]. Studies of daily and near-weekly biological rhythms in teeth have revealed that Pliocene to Early Pleistocene hominin dental development was more rapid than that of recent humans. However, scientists have been debating for more than 80 years over whether Neanderthals, our evolutionary cousins, grew differently from modern humans. Recent studies have reached contradictory conclusions as methodological limitations have led to incomplete data, and population-level variation has been poorly understood in living and fossil hominins. Here we overcome these limitations by characterising dental development and age at death in several fossil juveniles via non-destructive synchrotron virtual histology [2] (Figure 135).

Although traditional histological methods are destructive, generally prohibiting comprehensive studies of rare fossil material, recent advances in synchrotron imaging now permit accurate three-dimensional virtual histology in a fully non-destructive way. We performed a multiscale microtomographic study on the beamline **ID19** using both phase and absorption contrast to assess tooth formation and calculate age at death in a diverse sample of fossil hominins from the past 160,000 years. Our sample includes several invaluable European Neanderthal juveniles, such as the first hominin fossil to be discovered (Figure 135), as well as some of the earliest fossil *Homo sapiens* populations to have left Africa 90-100,000 years ago. We found that most Neanderthal tooth crowns grew more rapidly than modern human teeth, resulting in significantly faster dental maturation (Figure 136).

Fig. 135: Synchrotron imaging of the upper jaw of the Engis 2 Neanderthal allows virtual isolation of the permanent teeth (upper image), quantification of tiny growth lines inside the first molar teeth (lower image), identification of its birth line, and determination that it died at age 3. Fossil courtesy of the Université de Liège and Michel Toussaint. Image credits Paul Tafforeau (ESRF) and Tanya Smith (Harvard University and MPI-EVA). To view a 3D animation of the determination of the individual's age, visit: http://www.heb.fas.harvard.edu/Press

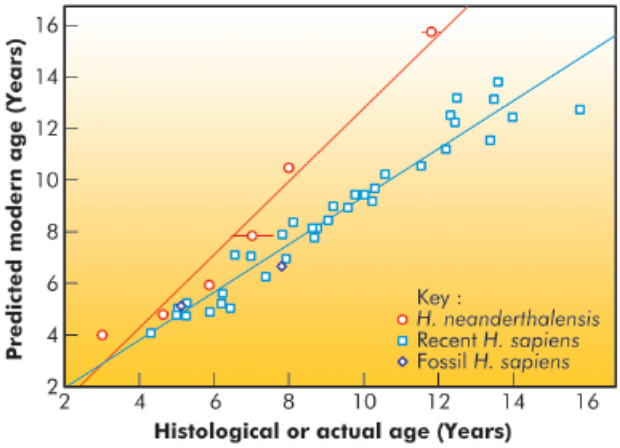

Fig. 136: Regression of predicted versus actual age for eight fossil juveniles and 36 living humans. Predicted ages are derived from human radiographic calcification standards. Actual ages are calculated from counts and measurements of incremental growth lines in permanent tooth crowns and roots. Fossil *Homo sapiens* (dark blue diamonds) are represented by Qafzeh 10 and Irhoud 3; *Homo neanderthalensis* (orange circles) are represented by Engis 2, Gibraltar 2, Krapina Maxilla B, Obi-Rakhmat 1, Scladina, and Le Moustier 1 (from left to right). The comparative recent human sample (blue squares) are western European children of known sex and age.

In contrast, fossil *H. sapiens* juveniles show greater similarity to recent humans. These findings are adding to the growing body of evidence that subtle developmental differences exist between us and our Neanderthal cousins, including cranial and post-cranial growth. Furthermore, the recent sequencing of the Neanderthals genome has provided tantalising genetic clues that point to differences in cranial and skeletal development between Neanderthals and modern humans.

Neanderthal dental development appears to be intermediate between early members of our genus (*e.g. Homo erectus*) and living people, suggesting that the characteristically slow development and long childhood is a recent condition unique to our own species. This extended period of maturation may facilitate additional learning and complex cognition, possibly giving early *Homo sapiens* a competitive advantage over their contemporary Neanderthal cousins.

References
[1] T.M. Smith, *J. Hum. Evol.* **54**, 205-224 (2008).
[2] P. Tafforeau and T.M. Smith, *J. Hum. Evol.* **54**, 272-278 (2008).

Improvement of techniques

Wavelength-dispersive spectrometer for X-ray micro-fluorescence analysis

Principal publication and authors
J. Szlachetko (a,b,c), M. Cotte (a,d), J. Morse (a), M. Salomé (a), P. Jagodzinski (e), J.-Cl. Dousse (f), J. Hoszowska (f), Y. Kayser (f) and J. Susini (a), *J. Sync. Rad.* **17**, 400-408 (2010).
(a) ESRF
(b) Institute of Physics, Jan Kochanowski University, Kielce (Poland)
(c) currently at: Paul Scherrer Institut, Swiss Light Source (Switzerland)
(d) Centre of Research and Restoration of French Museums, UMR171, Paris (France)
(e) Technology University, Kielce (Poland)
(f) Department of Physics, University of Fribourg (Switzerland)

Beamline **ID21** is dedicated to micro-X-ray fluorescence (μXRF) and micro X-ray absorption spectroscopy (μ-XANES) in the X-ray energy domain between 2 keV and 9 keV. The scanning X-ray microscope enables the localisation and speciation of trace elements down to the ppm range with a submicrometre beam size. It provides access to the absorption edges of a wide range of elements of interest in the areas of Environmental Sciences, Earth and Planetary Sciences, Life Sciences and Cultural Heritage [1]. The beamline relies on several solid-state detectors, which are complementary in terms of count rate throughput and solid angle collection efficiency. However, the attainable energy resolution (120-180 eV) of such energy dispersive detectors is often inadequate to permit unequivocal elemental and chemical speciation. To improve the energy resolution of fluorescence detection of the X-ray microscope, a wavelength dispersive spectrometer has been developed.

Since 1912, when the Bragg law was formulated [2], wavelength dispersive spectroscopy has become one of the most important tools in X-ray fluorescence analysis. In contrast to energy dispersive detectors, wavelength-dispersive spectrometers (WDS) can provide a much better energy resolution of the detected X-rays. Their X-ray detection takes place through the diffraction process on the crystal. The spectrometer can be based on a flat or curved crystal geometry that has to be adapted to the particular experimental setup. The geometry of the WDS configuration is shown in Figure 137. It uses a polycapillary optics placed at a distance of a few millimetres from the sample. This optics converts the divergent X-ray fluorescence emitted from the sample into a quasi-parallel beam, which is then directed onto the flat crystal at the required Bragg theta angle. The X-rays diffracted by the crystal are counted by a detector placed at the 2-theta angle.

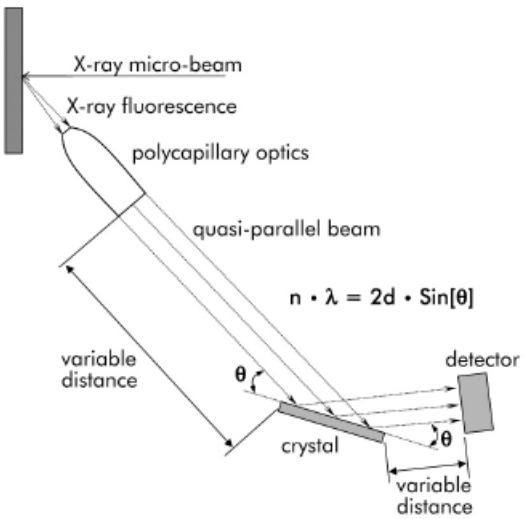

Fig. 137: Schematic drawing of the parallel beam wavelength-dispersive arrangement employing polycapillary optics for X-ray fluorescence collection.

The polycapillary-based-WDS configuration results in a simple alignment of both crystal and detector. Moreover, the distances polycapillary-to-crystal and crystal-to-detector are not critical and thus can be easily adapted to specific experimental constraints. This arrangement also permits a very compact geometry, a necessary prerequisite for the installation of a high-resolution X-ray micro-fluorescence analysis system at the ID21 beamline.

The newly developed spectrometer was applied to study historical samples such as ancient glasses and paintings. For such samples, not only spectral resolution was necessary but also spatial resolution as the pigments and opacifiers are usually present as micrometric particles dispersed in a matrix. Accordingly, a sub-micrometric probe is crucial to selectively probe the different constituents. This point is illustrated in the following example whose objective was to identify the composition of a brown alteration spreading on the surface of a painting entitled "Bateaux de Pêche", executed by J.A. Noel in 1867 and conserved in the Musée de Picardie, Amiens, France. A sample fragment was taken in an altered area and prepared as a cross-section to reveal its entire stratigraphy. The altered brown layer was only 5 µm over the original blue layer, and the main composition of both layers was lead. The X-ray fluorescence spectra measured with a solid-state detector showed very small differences between the two layers. In the broad unresolved Pb M-emission lines only a shoulder on the low energy side could be seen (Figure 138b). When acquiring the X-ray fluorescence spectra with the WDS, this shoulder can be unequivocally shown to contain the sulphur K_α emission lines (Figure 138a). The energy resolution of the spectrometer was crucial in this case to establish the presence of sulphur in the brown layer. Spatial micro-mapping of sulphur and lead show that they are both present in the brown layer, while sulphur was absent in the original blue layer (Figure 138, top panels). Lead sulphates were subsequently identified using µXANES. This analysis showed that the brown alteration observed on the surface of the painting may have resulted from the reaction of the original lead white pigment with exogenous SO_2.

Many other complex materials from the Cultural Heritage field will probably benefit from the new capabilities offered by the ID21 WDS.

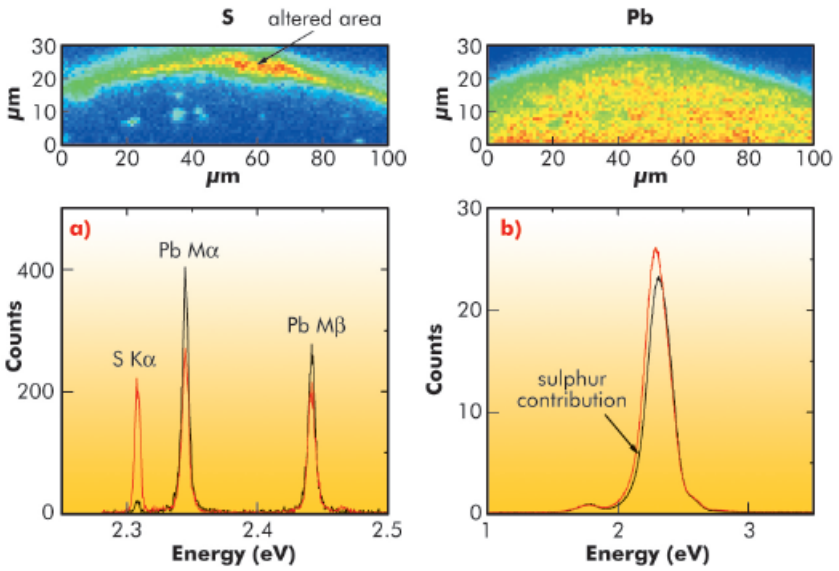

Fig. 138: Top panels, The X-ray fluorescence map of S and Pb in the painting cross-section containing the altered area. Bottom, XRF spectra acquired in the altered (red) and safe (black) areas a) with the polycapillary-based-WDS X-ray fluorescence spectrum, b) with a SDD detector.

References
[1] J. Susini, M. Salome, B. Fayard, R. Ortega and B. Kaulich, *Surf. Rev. Lett.* **9**, 203- 211 (2002).
[2] W.H. Bragg and W.L. Bragg, *Proceedings of the Royal Society of London, Series A* **88**, 428-438 (1913).

Real-time study of roughness evolution of Si surfaces upon ion erosion

The analysis of the Si surface roughness evolution under ion treatment and the determination of parameters to preserve or improve the surface smoothness are increasingly important for advanced reflective X-ray/extreme ultraviolet (EUV) optics. Ion etching is used during the fabrication of such optics to figure a macroscopic Si substrate with sub-nanometre accuracy while maintaining the microscopic roughness at an atomic level.

The evolution of the surface topography upon etching is determined by competing roughening and smoothening mechanisms with different spatial-frequency and time

Principal publication and authors
V.I.T.A. de Rooij-Lohmann (a), I.V. Kozhevnikov (b), L. Peverini (c), E. Ziegler (c), R. Cuerno (d), F. Bijkerk (a,e) and A.E. Yakshin (a), *Applied Surface Science* **256**, 5011–5014 (2010).
(a) FOM Institute for Plasma Physics Rijnhuizen, Nieuwegein (The Netherlands)
(b) Institute of Crystallography, Moscow (Russia)
(c) ESRF
(d) Universidad Carlos III Madrid, Leganes (Spain)
(e) MESA+ Institute for Nanotechnology, University of Twente, Enschede (The Netherlands)

dependencies. A growing or eroding surface can often be described within the theoretical framework of surface dynamic scaling, where the scaling exponents α and β are the signatures in space and time of the growth or etch processes. By comparing the experimental scaling exponent values to the theoretical predictions, one can establish a differential equation describing the growth or erosion. Being a universal description of the ion erosion of Si surfaces, such an equation would contribute tremendously to the understanding of the dynamics for ion-eroded surfaces, and provide the ultimate tool for the selection of etch settings that lead to the best smoothening results.

In situ, real-time information about the roughness evolution of Si surfaces upon Ar ion erosion was obtained from X-ray scattering (XRS) measurements. Diffuse scatter patterns (scattering diagrams) were recorded with a CCD camera at the grazing incidence X-ray reflectometry setup at the **BM05** beamline. A microwave electron cyclotron resonance plasma source provided Ar ions for sample erosion. The angle of incidence was 55° with respect to the sample surface (a Si wafer). In two experiments the sample surface was roughened beforehand, so that the effect of the initial roughness on the roughness evolution could be studied.

According to first order perturbation theory, the scattering diagram as a function of the scattering angle is proportional to the power spectral density (PSD) function of the surface roughness as a function of the spatial frequency ν. At high spatial frequencies, the PSD-function behaves as $\mathrm{PSD}(\nu) \sim 1/\nu^{1+2\alpha}$. This asymptotic behaviour was used to determine the static scaling exponent α, which characterises the saturated roughness. For the previously roughened samples etched at 300 and 1000 eV, we found $\alpha = 0.30 \pm 0.05$ and $\alpha = 0.23 \pm 0.08$, respectively. Therefore, within the experimental error we conclude that α is independent of the ion energy. For the not-roughened sample, α is not clearly defined in the spatial frequency range measured in this experiment.

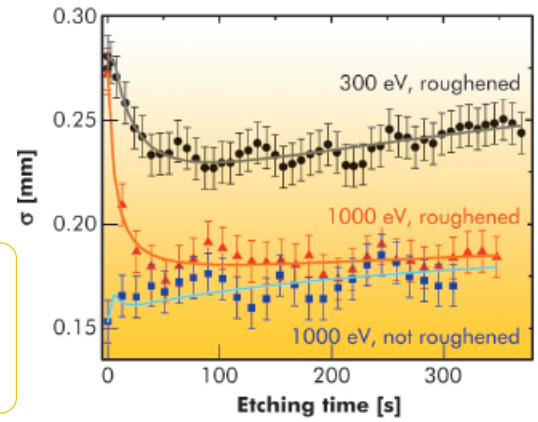

Fig. 139: The evolution of the root-mean-square roughness σ upon etching, for three samples. The solid lines represent the best fits to Equation (1).

Figure 139 shows the evolution of the root-mean-square roughness σ for three samples, as obtained by integration of the PSD over the measured spatial frequency range. To take into account both the initial roughness of the substrate σ_S disappearing with the erosion time, and the etching induced roughness σ_E following the scaling law $\sigma_E(t) \sim t^{\beta}$, Majaniemi *et al.* suggested the following formula in Ref. [1]:

$$\sigma^2(t) = \sigma^2_S(t) + \sigma^2_E(t) = \frac{\sigma^2_S(0)}{(1+t/t_S)^{2\beta/\alpha}} + A \cdot t^{2\beta} \quad (1)$$

where β is the dynamic scaling exponent, and A and t_S are fitting parameters.

The solid curves in **Figure 139** are the result of fitting $\sigma^2(t)$ according to Equation (1). The evolution of the rms roughness of all samples is described properly with this equation. The same set of fitting parameters, with $\beta = 0.07 \pm 0.01$ is used for both the roughened and the not-roughened sample etched at 1000 eV. This shows that the Majaniemi model explains smoothening as well as roughening, depending on the initial roughness of the substrate. In contrast to α, the dynamic scaling exponent β was found to be energy-dependent, as $\beta = 0.14 \pm 0.02$ at 300 eV.

In summary, we analysed the roughness evolution of Si substrates upon Ar ion etching. Both smoothening and roughening have been observed, depending on the initial substrate roughness. The scaling exponents α and β, important parameters for the determination of a comprehensive theory of ion erosion of (Si) surfaces, have been determined.

Reference
[1] S. Majaniemi, T. Ala-Nissila and J. Krug, *Phys. Rev. B* 53, 8071-8082 (1996).

Enabling Technologies

The Upgrade Programme is now running at full speed and, despite some uncertainties related to the economic situation, many projects have started in the ESRF's two service divisions, Instrumentation Services and Development Division (ISDD) and Technical Infrastructure Division (TID).

The instrumentation activities are dedicated to providing state-of-the-art instrumentation for the new beamlines and, equally importantly, to initiating several mid and long-term R&D projects to anticipate future needs which will be decisive in maintaining the ESRF at the forefront of synchrotron instrumentation. This chapter will focus on a few select topics from the many instrumentation-related activities.

The performance of all of the upgrade beamlines will rely on mechanical and thermal stability and the quality of beamline components. ISDD has consequently been providing wide-ranging mechanical engineering expertise from modelling to drafting for slab design, high stability white beam mirrors and high-power gas absorbers, to mention but a few.

The high quality of optical components is equally crucial to the new beamlines and the ISDD Optics Group has been deeply involved in many critical projects such as high reflectivity X-ray multilayers, sub-100 nm KB mirrors and diamond monochromators and beam splitters. Two of the following articles highlight the very successful use of compound reflective lenses in routine operations and in innovative imaging methods, respectively.

2010 also saw the maturation of several technologies pioneered and developed at the ESRF, such as the 2D detectors MaxiPIX and FreLon, and the generic motor controller IcePAP, which is now in use on many of the beamlines.

The detector programme was identified as one of the core drivers of the upgrade and is still in a definition stage. Nevertheless, the implementation of a liquid phase epitaxy laboratory was identified as a strategic choice to secure the procurement of high quality scintillators. Initiated in 2009, this lab is now fully operational and has produced the first light converters to equip 2D detectors, which also benefit from a new software framework, LiMA, (Library for IMage Acquisition). LiMA offers new, fully-standardised interfaces with enhanced capabilities that are being developed in collaboration with other synchrotron facilities to ensure compatibility with a wide range of 2D detectors. A first version of an integrated TANGO-based software application for the control of vacuum equipment was also tested successfully on one beamline. Development of GPU accelerated data processing was successfully implemented for tomography reconstruction and will be further developed for other scientific applications.

The collaborative projects XNAP, NanoFOX and HiZPAD serve as illustrations of the ESRF's coordination of pan-European initiatives and its role in the European synchrotron community.

The two newly created service divisions have helped along all of these projects by gathering together staff from particular domains and encouraging collaboration in projects bridging many disciplines. After one year of operation, ISDD has demonstrated an efficient transverse coordination between the various areas of expertise, higher standardisation where applicable, and a better response to new technological challenges.

The newly created TID continues to maintain the existing infrastructure at the highest possible standard and, in parallel, aims to foster the development of key infrastructure components that contribute to enhancing the scientific life at the ESRF.

The EX2 building programme is now well underway with construction starting in September 2011 and delivery of the buildings extending from the end of 2012 to May 2013. Although this project had to be downscaled, which led to the suppression of the Vercors extension, the most significant part of the project remains unaffected. The new premises will provide floor space for the phase-1 upgrade beamlines as well as some additional laboratory and office space. Please refer to the

Upgrade Section for more information on the EX2 project. The CPER programme also underwent careful scrutiny to make sure that future equipment and running costs would be compatible with the new financial context of the ILL and ESRF. The revised project outline has yet to be approved by the local funding authorities.

In this chapter of the Highlights you can read about the extension of the Central Building data centre, which will be completed in spring 2011. The data centre will provide space, power and cooling for additional storage and data analysis computers. The new data centre caters for data archiving and affords a significant increase in data analysis capacity; both issues are core to European collaborations undertaken with colleagues in the Neutron and Photon Science Community. This chapter also provides an insight into some specific aspects of the Alignment & Geodesy and Vacuum Groups' activities. We hope you enjoy reading the articles.

R. Dimper and J. Susini

Principal publication and authors
A. Bosak (a), I. Snigireva (a), K. Napolskii (b) and A. Snigirev (a), *Adv. Mater.* **22**, 3256-3259 (2010).
(a) ESRF
(b) Moscow State University (Russia)

Coherent high resolution X-ray microscopy: a new tool for mesoscopic materials

Structural studies of mesoscopic materials at the submicrometre scale are limited by the available techniques. Surfaces and ultrathin slices can be imaged by scanning electron microscopy and transmission electron microscopy, respectively. Whereas information on the average structure is provided by diffraction methods such as visible light diffraction and small-angle X-ray scattering. The gap corresponding to the volume-specific study of mesoscopic structures can now be filled by high-resolution X-ray microscopy (HRXRM). We developed HRTXM, based on parabolic refractive lenses [1]. The immediate benefit of using lens-based methodology is the possibility to retrieve both the high-resolution diffraction pattern and real-space images in the same experimental setup [2,3]. Methodologically the approach is similar to the traditional method of studying crystalline samples with high-resolution transmission electron microscopy (HRTEM). Here, we demonstrate the applicability of the HRXRM technique for studies of a wide variety of mesoscopically-structured materials. HRXRM will become an invaluable tool for the investigation of self-assembling systems such as photonic crystals.

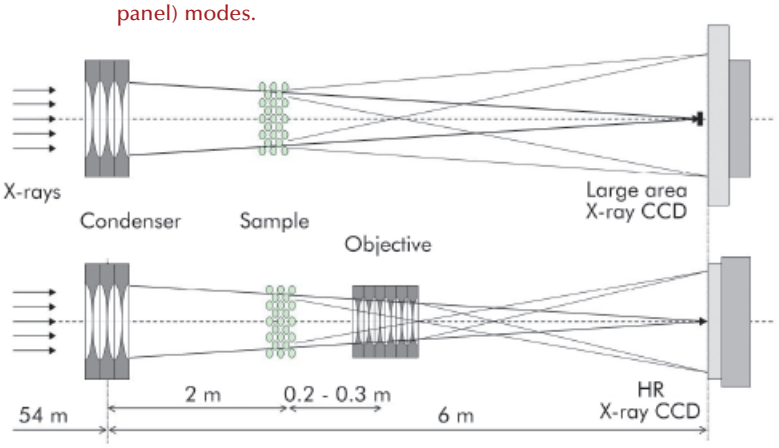

Fig. 140: Conceptual layout of the X-ray microscope. Diffraction (upper panel) and imaging (lower panel) modes.

The HRTXM experiment was set up at the micro-optics test bench of beamline **ID06** using X-rays from 10 to 20 keV. It makes use of a condenser for sample illumination in imaging mode and as Fourier transformer in diffraction mode. The condenser is comprised of 11 Be parabolic lenses with 300 micrometre radius of parabola apex giving a focal length of ~6 m. The objective lens assembly of 45-62 individual Be parabolic lenses with 50 micrometre radius of parabola apex was located at 2.3 m from the condenser. Two X-ray 2D cameras were used: (i) large area Photonics science CCD detector with 9 µm pixel size for diffraction experiments and (ii) high resolution Sensicam CCD detector with 0.645 µm pixel size. In diffraction mode the direct focussed beam was intercepted in front of the camera by a tungsten beamstop. Switching from the diffraction mode to the imaging mode was achieved by placing the objective lens into the beam, and the chosen camera (**Figure 140**). The tuneable objective lens provides a magnification between 10 and 25. At maximum magnification a resolution of ~100 nm

was achieved. For this benchmark study, a ~70 µm thick single domain grain of Australian gem opal as a prototypical photonic crystal was used.

Figure 141 shows a diffraction pattern taken with the X-ray beam parallel to <1-20> zone and the corresponding enlarged X-ray image. Reflections not satisfying the condition $H = 3n$ transform from a well-defined round shape to modulated diffuse rods (see Figure 141a), they are a signature of structural imperfections. The behaviour observed for opal is well known for a close-packed structure with stacking faults, but the surprising feature is the absence of a six-fold axis which must exist for the so-called "growth faults". The apparent reduction of symmetry of Australian opals to a three-fold symmetry is an indication of unequal probabilities to meet A/B and B/A stackings in the structure. A stripe-like contrast variation with the stripes perpendicular to the *c* axis is due to a change of the packing sequence (Figure 141b). The orientation of the stripes coincides with striations observable with visible light.
Figure 141d shows a filtered HRTXM image, superposed with simulated patterns of a face-centred cubic structure fragment containing a single stacking fault (…ABCABCBCABCABC… sequence) with satisfactory agreement. The most widespread packing mode is obviously f.c.c., but it is not absolutely dominant. A variety of longer-period stacking sequences can be identified, but not being repetitive, they cannot be treated as separate "polytypes" of "phases".

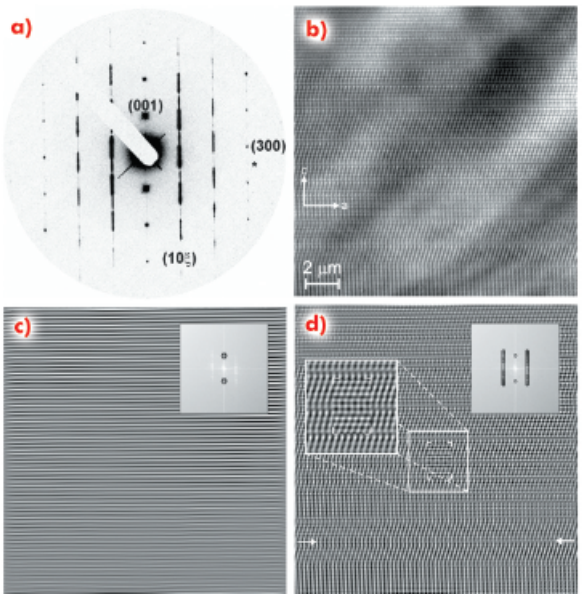

Fig. 141: a) diffraction pattern in <1-20> zone and b) corresponding enlarged high resolution X-ray image. c) and d) Fourier-filtered images, power spectrum with superposed mask sketch is shown as insert. Simulated patterns are given in panel d (see text). Arrows indicate the layer with laterally changing contrast.

The HRTXM technique, combining high-resolution diffraction and full-field imaging in one setup, provides the tools for efficiently studying the real structure of mesoscopic materials. In structural studies of inverted photonic crystals a resolution in the order of 100 nm was achieved for a wide X-ray energy range from 10 to 50 keV. Short acquisition times with modern area detectors allow the method to be extended to time-resolved studies and combined 3-D real/reciprocal space mapping. The HRTXM method can easily be implemented on existing beamlines. As immediate practical application we mention the characterisation of the real crystal structure during photonic crystal growth.

References
[1] A. Snigirev, V. Kohn, I. Snigireva and B. Lengeler, *Nature* **384**, 49-51 (1996).
[2] V. Kohn, I. Snigireva and A. Snigirev, *Opt. Comm.* **216**, 247-260 (2003).
[3] M. Drakopoulos, A. Snigirev, I. Snigireva and J. Schilling, *Appl. Phys. Lett.* **86**, 014102 (2005).

X-ray transfocators: tuneable focussing devices based on compound refractive lenses

Authors
A. Snigirev, G.B.M. Vaughan, J.P. Wright, V. Honkimaki and I. Snigireva
ESRF

Since their development almost 15 years ago, X-ray refractive lenses have rapidly gained renown and they are now in common use on synchrotron beamlines. Compared to other focussing elements, refractive lenses present several attractive features, being simple to align and relatively insensitive to misorientations. Since refractive lenses are in-line optics, they are more stable with respect to angular vibrations in comparison to deflecting optics. They can be adapted to very high X-ray energies by modifying their composition and number, and can be inserted and removed from the beam to allow fast switching of the beam size. As the index of refraction for refractive lenses is extremely close to 1 and energy dependent, a substantial, well-defined number of lenses are necessary to focus X-rays of a given energy at a given distance. For this reason,

References
[1] A. Snigirev, I. Snigireva, G.B.M. Vaughan, J. Wright, M. Rossat, A. Bytchkov and C. Curfs, *Journal of Physics, Conference Series*, **186**, 012073 (2009).
[2] G.B.M. Vaughan, J.P. Wright, A. Bytchkov, M. Rossat, H. Gleyzolle, I. Snigireva and A. Snigirev, *J. of Synchrotron Rad.*, accepted (2011), doi:10.1107/S0909049510044365.

transfocators – systems with a tuneable number of lenses – have been proposed to provide permanent energy and focal length tunability [1-2]. The transfocators are comprised of several cartridges containing different numbers of lenses, such that the focal distance can be continuously adjusted by insertion or retraction of one or more of the lens cartridges.

An in-air transfocator (IAT) [1] has been in operation at the **ID11** beamline for almost 3 years (Figure 142a). Based on the success of the IAT, in-vacuum transfocators (IVT) have now been installed at ID11 and ID15 (Figure 142b). The IVTs are water cooled to allow use in the white beam. They are installed closer to the X-ray source (~30 m) where they capture a larger proportion of the diverging X-ray beam (Figure 143). The variable focal length of the transfocator focussed beam means that it can be exploited at all of the beamline experimental stations leading to enormous flux gains (up to 10^5) with respect to an unfocussed beam.

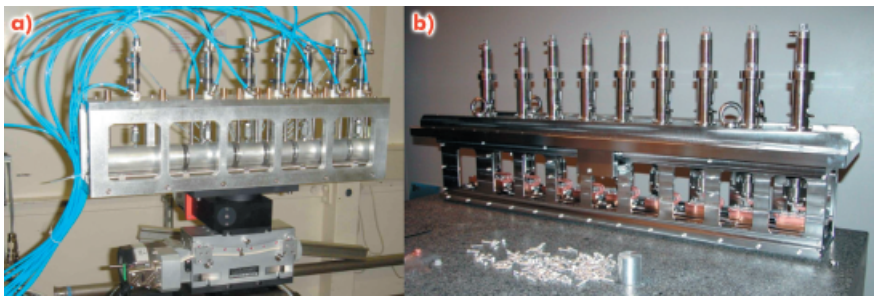

Fig. 142: a) The IAT installed on the ID11 beamline and b) the IVT during construction (right).

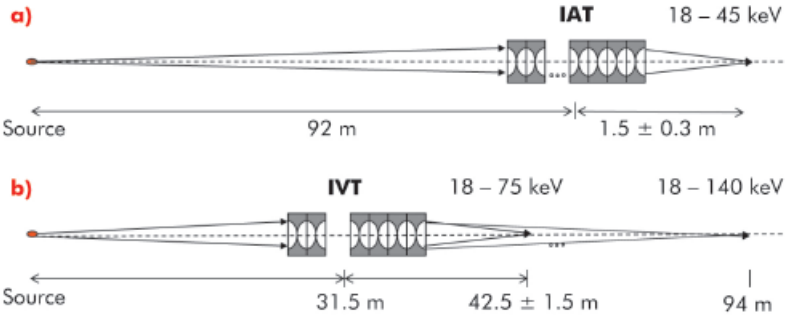

Fig. 143: Implantation at ID11 of a) the IAT and b) the IVT. The IAT is configured to give an ~1:15 focussing of the source, whereas the IVT operates in either a 3:1 or 1:2 configuration. Other beamline optics are not shown in the figure.

Transfocators are very flexible and have been used in several different configurations. They can be used as standalone focussing devices in the monochromatic beam, giving micrometre spot sizes. Also the transfocators can act as pre-focussing devices to be used in conjunction with a downstream micro- or nano-focussing element. As a single optical device in the white beam, the IVT can act as a fundamentally new kind of monochromator, delivering impressive flux in a ~1% band pass beam (a factor of 75 with respect to the ~10^{-3} band pass beam when used in conjunction with a double Laue monochromator) (Figure 144). The energy selectivity of the IVT comes from the chromatic nature of the focussing; with a relatively short focal length the depth of focus is sufficiently short that only a narrow band pass is focussed at a given longitudinal point. At the focal point, this leads to an increase in the flux of 2 orders of magnitude at the selected energy with respect to the rest of the spectrum. Such ultra intense, stable and focussed beams with moderate band pass can be useful for several applications in which high energy resolution is not necessary, such as scattering from liquids or poorly crystalline materials. The band pass of this monochromator is well matched to exploit the spectrum of the harmonic peaks of an undulator insertion device at a third generation storage ring.

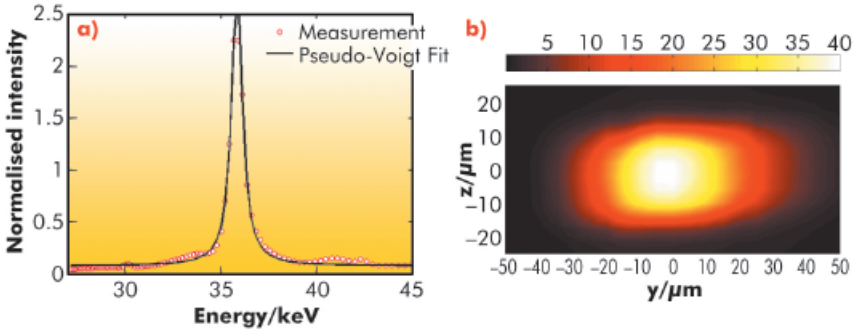

Fig. 144: a) Measured spectrum through a 10 × 10 µm² pinhole of the beam optimised for 35.5 keV.
b) Spatial distribution of the flux at 35.500 ± 0.005 keV perpendicular to the beam at the focus.

Liquid phase epitaxy facility for single crystal film scintillators

Authors
T. Martin, P.-A. Douissard and E. Mathieu.
ESRF

2D X-ray detectors for synchrotron sources have become a standard for almost all applications including radiography and tomography. High-resolution detectors are able to provide volumetric data of samples during non-destructive experiments for biology, medicine and material sciences. They can also be used as diagnostic tools for the X-ray beam. A detector that is able to provide sub-micrometre spatial resolution consists of a scintillator, light microscopy optics and an image sensing device (CCD or CMOS). The scintillator converts the X-rays into visible light which is projected onto the image sensor through the optics. Sub-micrometre resolution requires a thin layer, in the micrometre thickness range, with a high optical grade for the sensitive layer. The thinner the scintillator film, the better the spatial resolution and image contrast. Thin film layer growth requires the use of several advanced techniques: sputtering, chemical solution deposition, liquid phase epitaxy (LPE), laser ablation, etc. As such single crystal film (SCF) scintillators are not commercially available, the ESRF has constructed its own scintillator production facility with LPE capability. LPE is a versatile technique for the development of miniature optical components, such as lasers, amplifiers and scintillators, in single crystal structures [1]. This technique was chosen owing to its high reproducibility, simplicity and homogeneous distribution of the activator ions within the film.

The 40 m^2 laboratory has been operational since April 2010 and is divided into three main sectors: Chemistry room for powder and substrate preparation, a "lead oxide" room for the manipulation of micro-nano toxic powders and a furnace room.

We have already produced some europium-doped gadolinium gallium garnet ($Gd_3Ga_5O_{12}$:Eu; GGG) films for the ESRF beamlines. The constituents of the solution are melted in a platinum crucible at about 1000°C. Before growth, the melt is stirred at about 1100°C. The substrate is mounted horizontally on a platinum holder and preheated in the furnace.

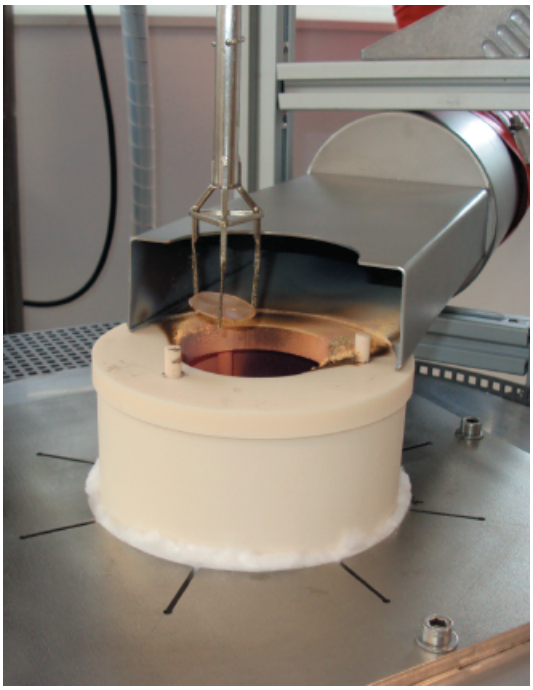

Fig. 145: SCF scintillator, after growth and melt characterisation, fixed on its platinum holder.

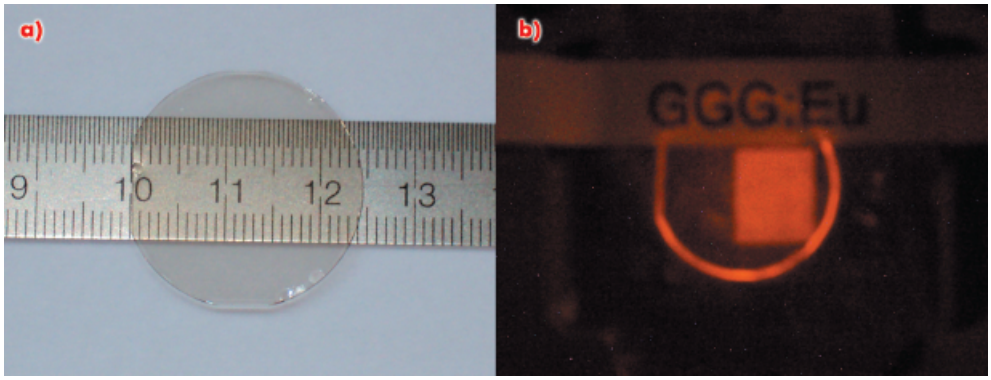

Fig. 146: An ESRF GGG:Eu scintillator. a) 16 µm thick GGG:Eu on 500 µm undoped GGG, 25.4 mm diameter. b) Digital camera picture of visible light emitted by the scintillator under irradiation from a laboratory X-ray generator (40 kV, 40 mA).

The growth is then performed at constant temperature by dipping the substrate in the supersaturated melt solution (Figure 145). The single-crystal films from 2 µm to 120 µm that have been manufactured show high optical quality (Figure 146) and have the same level of performance as layers developed previously in the now-defunct laboratory of a partner institute.

Today the thin scintillators that are the most promising to reach spatial resolution in the micrometre range suffer from inadequate detection efficiency. There is therefore a need to develop more efficient SCF scintillators made from materials of high density and high effective atomic number. In a first step, we have chosen candidate materials that are garnet and silicate based. At a later stage, we may try materials based on peroskite, hafnate, tantalate and lutetium. In particular, gadolinium and lutetium oxide are more promising host materials than GGG because of their high density. Lutetium oxide could boost the absorption efficiency by a factor of 2 or 3 when compared to GGG and YAG, respectively. These materials could provide even higher absorption efficiency than the garnet and silicate based materials, but today they are much less well known because of the lack of substrates and/or temperature of growth. We successfully developed a scintillator based on GGG:Tb at the end of 2010, which provided a better wavelength emission that matches interline and back-illuminated CCD chips. Optical quality and light yield are promising for the future production of GGG:Tb in 2011. An investigation of dense garnet materials was also launched in 2010: pure LuGG substrates are under development and the first LuGG:Eu layer is expected in the first half of 2011. For LuGG co-doped with a weak concentration of terbium, the sensitivity of detectors coupled to back-illuminated CCD will be improved by a factor of 4 in comparison with GGG:Eu. While we are able to perform significant development work in-house, international collaborations would be welcomed concerning substrates and the growth of exotic materials.

To conclude, the LPE facility is operational for production and development. The SCF scintillators that we have produced provide sub-micrometre resolution with high contrast. The alternative materials tested so far, such as YAG, LuAG, GGG and LSO, show complementary performance. This new facility aims to be of great benefit to the synchrotron community and will ensure continuous production, innovation and development for X-ray imaging and other applications. Our scintillators are available for the ESRF beamlines and are also commercially available [3].

References
[1] B. Ferrand, B. Chambaz and M. Couchaud, *Optical Materials* **11**, 101-114 (1999).
[2] P.A. Douissard, A. Cecilia, T. Martin, V. Chevalier, M. Couchaud, T. Baumbach, K. Dupré, M. Kühbacher and A. Rack, *J. Synchrotron Rad.* **17**, 571-583 (2010).
[3] For details please contact: industry@esrf.fr.

Acknowledgement
The authors thank the CEA/LETI and especially M. Couchaud, A. Million and J.L. Santailler for their help and advices in the LPE laboratory installation. We also thank the ESRF Technical Service and Safety Group for their work and support.

Status of NEG coating at the ESRF

Authors
M. Hahn and H. Pedroso Marques.
ESRF

Non-evaporable getters (NEG) are materials that exhibit particular behaviour within a vacuum such as a pumping action (gettering) and low molecular desorption yield under electron or photon irradiation.
NEG coating is attractive because it can be used for volumes that are difficult to evacuate.

NEG coated insertion device (ID) vacuum chambers have been installed on all available straight sections of the ESRF storage ring. The NEG coating helps to overcome the conductance limitations of these flat vessels by providing distributed pumping across its length as well as lowering its photo desorption yield. These effects induce reduced levels of Bremsstrahlung radiation and permit faster vacuum recovery after maintenance or shut downs.

Since 2002, following collaboration and the purchase of a license from CERN, which holds the TiZrV NEG coating technology patent, the ESRF has been producing NEG coated vacuum chambers using DC magnetron enhanced physical vapour deposition (PVD) in a dedicated coating facility. Initially, two independent coating systems were constructed to coat

vacuum chambers up to 5 m in length. Within the ongoing ESRF Upgrade Programme one of these systems was modified to allow the coating of 6.2 m chambers (Figure 147).

During production and testing of the first 6.2 m long ID vacuum chambers in 2009 it became apparent that the optimisation of the experimental setup for finer control of the overall coating process was necessary. All steps of the production, quality check, installation and commissioning were reviewed in order to obtain reproducible results with these chambers.

We discovered that the cathode target required guiding inside the chamber to ensure the correct centring over the full length due to the flexibility of their 6-metre long flat extruded profile. The cathodes were positioned with ceramic spacers, which proved determinant to avoid short-circuits and to guarantee a better distribution of the plasma along the chamber.

To monitor quality, scanning electron microscopy (SEM) and energy-dispersive X-ray spectroscopy (EDX) were performed on samples taken from the extremities of the coated chamber (Figure 148). A recent improvement has been the systematic use of non-destructive analysis of the coating using X-ray fluorescence through the chamber walls. The presence of the film is verified by looking through the aluminium substrate for the fluorescence peak of the zirconium (one of the three metals forming the NEG alloy).

After installation of the chamber in the storage ring it is necessary to follow a rigorous bake-out procedure to obtain a full *in situ* activation of the NEG film. The initial exposure to synchrotron radiation was found to be crucial to the outcome of the newly coated chamber. If the gas load resulting from photo desorption is too high the coating will be saturated quickly, which disables further gettering. In such cases, the accelerator needs to be stopped until the NEG is baked and activated again or a pre-conditioned replacement chamber has been installed.

A sputtering ion pump was installed in the centre of the first generation of the 6.2 metre vessels. This pump assists the pumping of the initial pressure burst after first exposure to the beam and serves as an additional vacuum gauge. As the presence of this pump is not compatible with all possible configurations of ID equipment, a second-generation chamber without a middle pumping port is soon going to be tested. The challenge will be to obtain the same initial low Bremsstrahlung levels and quick conditioning.

For the 6.2 metre long ID chambers there is a dedicated sector of the storage ring available for radiation measurement and pre-conditioning.

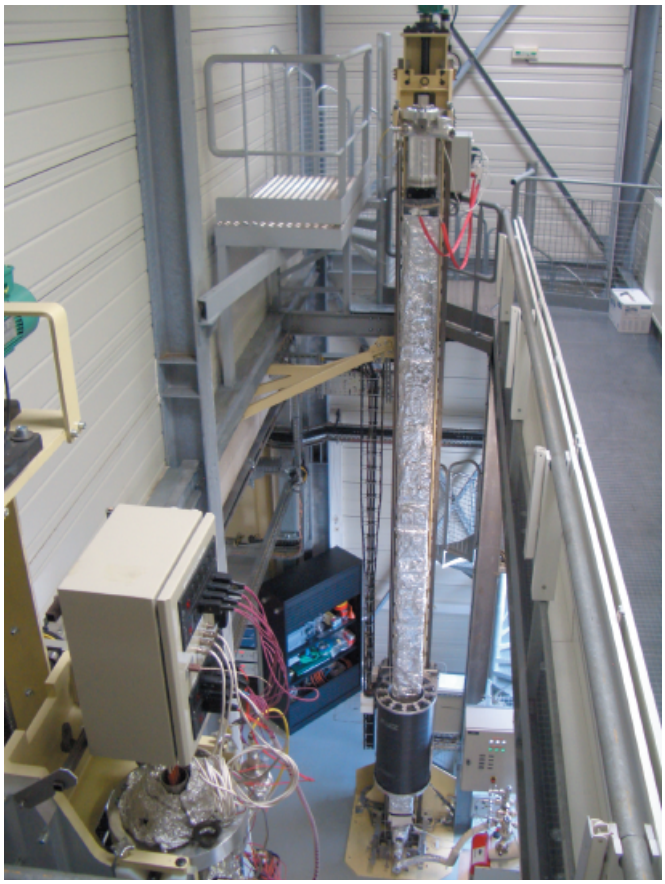

Fig. 147: NEG coating system for 6.2 m vacuum chambers.

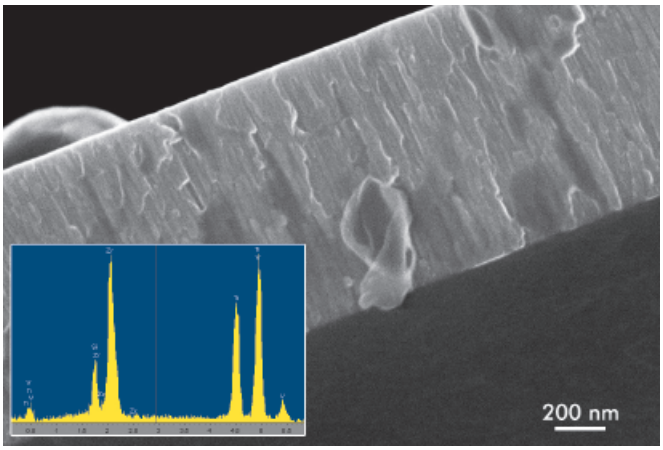

Fig. 148: NEG coating quality control by SEM and EDX (*credit: I. Snigireva*).

Some coated chambers for the Upgrade Programme, however, cannot be tested *in situ* before use due to their different lengths and interface geometries. Therefore, the use of the photo desorption test bench on D31 will play an important role. It enables chambers to be studied when exposed to synchrotron radiation without compromising the performance of the storage ring (**Figure 149**).

Fig. 149: Photodesorption measurements at D31: results from an ESRF 2m NEG coated chamber.

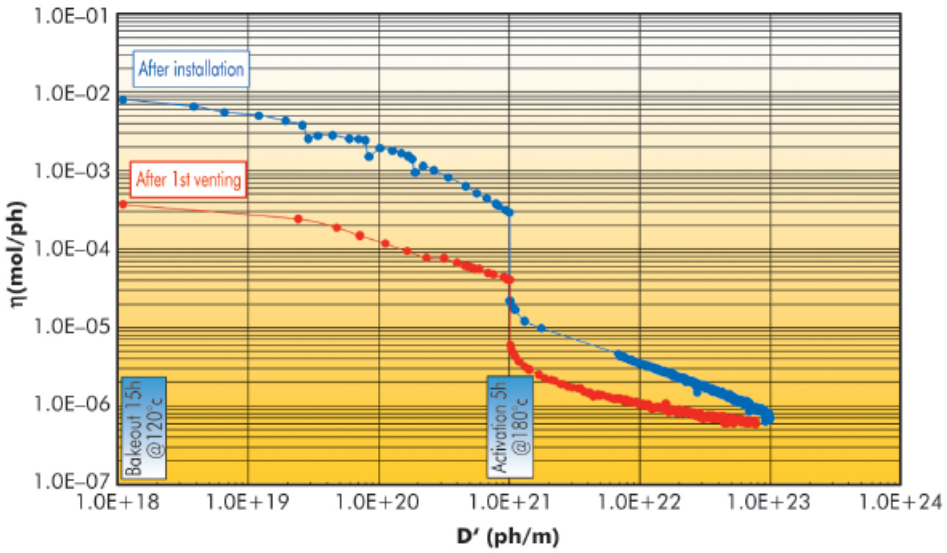

In the presence of many conductance limited ID chambers (about 114 metres in total), the NEG coating has made a significant contribution towards reducing the vacuum related losses of the electron beam in the storage ring. The challenge now lies in consolidating and optimising all processes and to check that the available *in situ* data allows an accurate measure of the performance of the chambers. New coatings can be tested, such as a protective layer on the TiZrV to prevent it from ageing. This may be of interest for other UHV systems that have to be opened frequently. Specific coatings can be deposited on vacuum construction materials to reduce their thermal and photon-induced desorption yields without having to go through an activation cycle by *in situ* baking. The ESRF is expanding its coating activities to be able to provide interesting options for accelerator, beamline and sample environment vacuum designs.

Author
D. Martin.
ESRF

References
[1] D. Martin, Some Design Considerations for the ESRF Upgrade Program Experimental Hall Slab, 11th International Workshop on Accelerator Alignment, 2010, DESY, Hamburg (Germany).

Design considerations for the ESRF Upgrade Programme EX2 slab

Expected probe sizes on the ESRF upgrade beamlines will range between 20 and 50 nm. With a probe size of 50 nm and an acceptable 10% drift, translational and rotational stability tolerances are 15 μm and 100 nrad. These tolerances must be respected for the duration of a scan which taken to be a maximum of 30 minutes.

Although vibrational stability of the new EX2 experimental hall slab is a key element in its design, measurements and simulations indicate that movements driven by temperature variations may be the dominant stability constraint. The ESRF has made high precision levelling and hydrostatic levelling system (HLS) measurements to characterise these and other site movements.

Several systematic ground movement signatures have been identified at the ESRF. These long-term movements do not directly influence experiments, but they do have to be considered in the design of a beamline. Beamlines can be subjected to millimetres of vertical uplift or subsidence with respect to the X-ray beam over their lifetime. So sufficient alignment stroke should be designed into instrument supports.

Recent tests using HLS on BM18 show large deformations at the support columns due to the passage of the overhead crane. This is not surprising; however, deformation reaches right across the slab. Indeed movement between 3 and 5 μm is even measured on the X-ray beam. This indicates that the ground deforms and the slab – regardless of thickness – follows the deformation. Although these deformations are only a nuisance,

maximum measured inclinations along the beamline 0 mrad axis vary between 200 and 500 nrad. These movements are substantially outside of desired EX2 tolerances (Figure 150a).

Figure 150b shows variability in vertical movements on four ESRF long beamlines ID11, ID13, ID17 and ID19. Although movements are within desired EX2 tolerances, normalising the data to beamline length and extrapolating to a 250 m long beamline gives uncertainty estimates that reach 15 µm in less than 3 days. This demonstrates the necessity for frequent re-alignment and reflection in appropriate design.

Rotational stability is far more challenging. Slabs curl non-linearly as a function of temperature (and/or humidity) gradient through them. Considering the temperature under the slab is essentially stable over several days, the main parameter driving the curling is the temperature variation in the experimental hall and hutches. Curling at the edge of the existing slab is 50 µm/°C. Figure 150c shows rotational uncertainty growth on the ESRF slab. Results are much better in an air-conditioned optical hutch (Figure 150d), but only just at the EX2 tolerance limit. The thermal uncertainty for the two cases is shown in Figure 150e.

The overhead crane results have led us to recommend restrictions on its use during USM. Indeed at the micrometre level, the slab and experiments are extremely sensitive to groups of people walking and forklifts circulating in the corridor. Although vertical movement tolerances are respected on the existing floor slab, measurements show that the 100 nrad rotational tolerance is largely exceeded in the experimental hall and is only just respected in an air-conditioned optical hutch. Because the curling effect is theoretically exacerbated in thicker slabs, one of the real design challenges for EX2 is to optimise potentially conflicting parameters such as mechanical rigidity with thermal performance. The measurements discussed here have helped to advance this challenge.

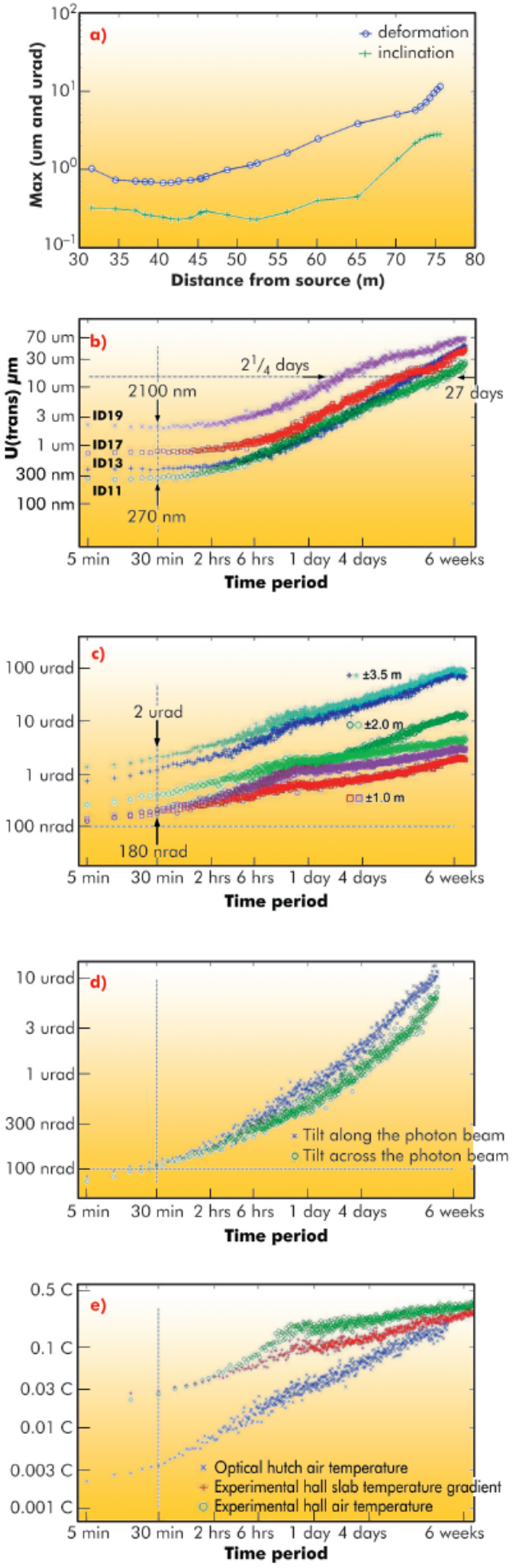

Fig. 150: a) Maximum deformation and inclination along the 0 mrad line from the source point due to the passage of the overhead crane charged with a 5.7 T load.
b) Vertical movement uncertainty growth on ID11, ID13, ID17 and ID19.
c) Slab curling as a function of time and position.
d) Slab tilt uncertainty growth along and across the X-ray beam in an air conditioned optical hutch.
e) Uncertainty growth in the optical hutch, experimental hall air temperature and temperature gradient through the existing slab.

Authors
B. Lebayle, T. Marchial and R. Dimper.
ESRF

Construction of the new data centre in the central building

For many years the ESRF has been reliant on two data centres, one in central building and the other in the control room building. The basic principle is to ensure that the fast and expensive disk storage systems are kept separate from the tape-based backup systems. Similarly, several critical IT services have been installed using both data centres for additional safety in case of a failure of one of them. For years it has been apparent that the central building data centre would need to be upgraded or complemented by a new room; the increasing influx of experimental data requires substantial additional space, power, and cooling. This is why a new data centre was defined within the scope of the ESRF Upgrade Programme, and initially planned in the new premises of the experimental hall extensions. However, as the experimental hall extensions will not be available before 2013, it was decided instead to opt for a complete overhaul of the central building data centre scheduled to be operational at the beginning of 2011.

The new data centre is designed to improve three key parameters by increasing:
• electrical power from 75 kW to 370 kW,
• cooling power proportioned appropriately for the electrical power with a target temperature of 23°C ± 1°C,
• floor space from 120 m^2 to 300 m^2 with a load resistance of 1000 kg/m^2 instead of the existing 500 kg/m^2.

Detailed specifications were drafted to incorporate state-of-the-art techniques, with the aim of improving both efficiency and reliability.

Bearing in mind that the IT infrastructure must run non-stop, the electrical network specifications include two separate circuits for each device in the computer room. The overall electrical supply will be composed of a 500 kVA uninterruptable power supply (UPS) with a 20 minute autonomous run time and two separate input sources from the mains network. All electrical supplies will be fed in

Fig. 151: Installation of the heat exchangers on the roof of the ESRF central building.

through the ceiling, thus avoiding installing any equipment in the raised floor. The cooling systems will be based on two different supplies; direct chilled water for water-cooled racks and chilled water for air cooling. The chilled water production will rely on two independent production circuits (Figure 151). The new data centre will be equipped with fire detection and a powerful smoke extraction system; it also features fire-resistant walls. A state-of-the-art building management system will enable remote monitoring and surveillance.

The future rack distribution will orient the racks to create hot and cold aisles; computers take cold air from the front side of the racks and reject hot air through the rear side to the hot aisle where the extraction of the hot air is optimised. High power computing equipment will be concentrated in water-cooled racks located in a confined area of 22 m^2. Last, but not least, the network cabling will be organised for optimal cable length and flexibility with the network electronics located in the middle of each row of racks.

It should be noted that keeping the data centre within the central building reduces the total construction cost and consequently the associated carbon foot print.

Works started in 2009 with a preparatory phase consisting of the modification of many adjacent rooms on the ground floor of the central building. Several storage rooms and laboratories have been moved, a few offices have been freed up to accommodate the future technical rooms, and two new corridors have been created to comply with safety regulations. Major works started in summer 2010 and the project is progressing on schedule.

The entire project will cost 2 M€ with a delivery foreseen in March 2011.

Accelerator and X-ray Source

Throughout 2010, the Accelerator and Source Division has continued its efforts to ensure reliable operation as well as upgrading a number of systems. Some new developments have been carried out and many of these are described hereafter.

Beam parameters of the storage ring

Table 1 presents a summary of the characteristics of the storage ring electron beam.

Table 2 gives the main optic functions, electron beam sizes and divergences at various source points. For insertion device source points, the beta functions, dispersion, sizes and divergences are calculated in the middle of the straight section.

Two representative source points for each type of bending magnet (even or odd number) have been selected, corresponding to observation angles of 3 and 9 mrad from the extremity. The bending magnets are such that the magnetic field is 0.4 T and 0.85 T at the tangent point when the radiation is extracted at 3 and 9 mrad angles, respectively. Electron beam profiles are Gaussian and the size and divergence are presented in terms of rms quantities. The associated full width half maximum sizes and divergences are 2.35 times higher. Horizontal electron beam sizes and divergences are given for the uniform filling mode and apply to almost all filling patterns except for single bunch, for which a slightly larger size and divergence are attained because of the increased energy spread of the electron beam. Vertical electron beam sizes and divergences apply to 2 x 1/3 and 7/8+1 filling modes only. The vertical sizes and divergences are about 1.4 times larger in uniform filling mode (due to ion effects). To increase the lifetime of the stored beam, the vertical beam sizes and divergences are deliberately increased by about 3 in the 16 and 4 bunch filling patterns.

The lifetime, bunch length and energy spread mainly depend on the filling pattern. These are given in Table 3 for a few representative patterns. Note that in both 16-bunch and 4-bunch filling patterns, the energy spread and bunch

Table 1: Principal characteristics of the electron beam.

Energy	[GeV]	6.03
Maximum current	[mA]	200
Horizontal emittance	[nm]	4
Vertical emittance (minimum achieved)	[nm]	0.005
Revolution frequency	[kHz]	355
Number of bunches		1 to 992
Time between bunches	[ns]	2.82 to 2816

		Even ID (ID02, ID06...)	Odd ID (ID01, ID03...)	Even BM (BM02, 04,...) 3 mrad	Even BM (BM02, 4,...) 9 mrad	Odd BM (BM01, 03,...) 3 mrad	Odd BM (BM01, 03,...) 9 mrad
Magnetid Field	[T]	Variable	Variable	0.4	0.85	0.4	0.85
Horiz. beta functions	[m]	37.6	0.35	1.34	0.96	2.13	1.77
Horiz. dispersion	[m]	0.134	0.031	0.063	0.046	0.090	0.079
Horiz. rms e- beam size	[µm]	413	50	99	79	133	113
Horiz. rms e- divergence	[µrad]	10	107	116	112	194	99
Vert. beta functions	[m]	2.95	2.97	41.7	42.2	32.1	32.2
Vert. rms e- beam size	[µm]	3.8	3.9	14.4	14.5	12.7	12.7
Vert. rms e- divergence	[µrad]	1.3	1.3	0.6	0.5	0.4	0.4

Table 2: Beta functions, dispersion, rms beam size and divergence for the various source points.

length decay with the current (the value indicated in the table corresponds to the maximum current). The bunch lengths are given for the usual radio frequency accelerating voltage of 9 MV (8 MV for 16-bunch and 4-bunch).

Filling pattern		Uniform	7/8 +1	Hybrid	16-bunch	4-bunch
Number of bunches		992	870	24x8+1	16	4
Maximum current	[mA]	200	200	200	90	40
Lifetime	[h]	50	40	30	16	9
Rms energy spread	[%]	0.11	0.11	0.11	0.12	0.16
Rms bunch length	[ps]	20	20	25	48	55

Table 3: Current, lifetime, bunch length and energy spread for a selection of filling modes.

Summary of accelerator operation

In 2010, 701 shifts (5607 hours) of beam were initially scheduled. Of these 5607 hours, 5538 were effectively delivered (including 48.5 hours of refill). This represents a beam availability of 98.78%, which is an excellent figure, barely lower than last year's record of 99.04%. Dead time due to failures accounts for the remaining 1.22%. The number of failures was slightly higher compared to 2009 due to more repetitive and complicated failures originating from the storage ring radio-frequency system. However, The mean time between failures remains at a high level: 67.5 hours (75.8 hours in 2009). Table 4 presents an overview of operation in 2010.

In 2010, the shutdowns continued to be busy with the upgrade of ID straight sections, replacement of water flowmeters to increase the reliability whilst decreasing the maintenance costs.

RUN NUMBER	TOTAL 2009	2010-01	2010-02	2010-03	2010-04	2010-05	TOTAL 2010
Start		15/01/10	26/03/10	04/06/10	20/08/10	15/10/10	
End		17/03/10	26/05/10	28/07/10	06/10/10	20/12/10	
Total number of shifts	867	183	183	162	141	198	867
Number of USM shifts	701.5	146.1	150	130.4	113.1	161.1	700.813
Beam available for users (h)	5510.1	1148.7	1176.4	1023.6	882.2	1258.9	5489.8
Availability	99.04%	99.19%	98.89%	98.66%	98.50%	98.62%	98.78%
Dead time for failures	1%	0.8%	1.1%	1.3%	1.5%	1.4%	1.2%
Dead time for refills	0.9%	0.9%	0.9%	0.6%	1%	1%	0.9%
Average intensity (mA)	115	152	133	178	121	147	146.6
Number of failures	74	13	18	18	12	22	83
Mean time between failures (h)	75.8	89.9	66.7	58	75.4	58.6	67.5
Mean duration of a failure (h)	0.73	0.7	0.7	0.8	1.1	0.8	0.82

Table 4: Overview of storage ring operation in 2010.

Eighteen long delivery periods (*i.e.* more than 100 hours) without a single interruption took place in 2010, in particular during the second run when the beam was delivered continuously for 13.25 days interrupted only by the two scheduled machine dedicated days (Figure 152).

During the last months of the year, the beam has been regularly delivered with a very low vertical emittance in multibunch modes (see below).

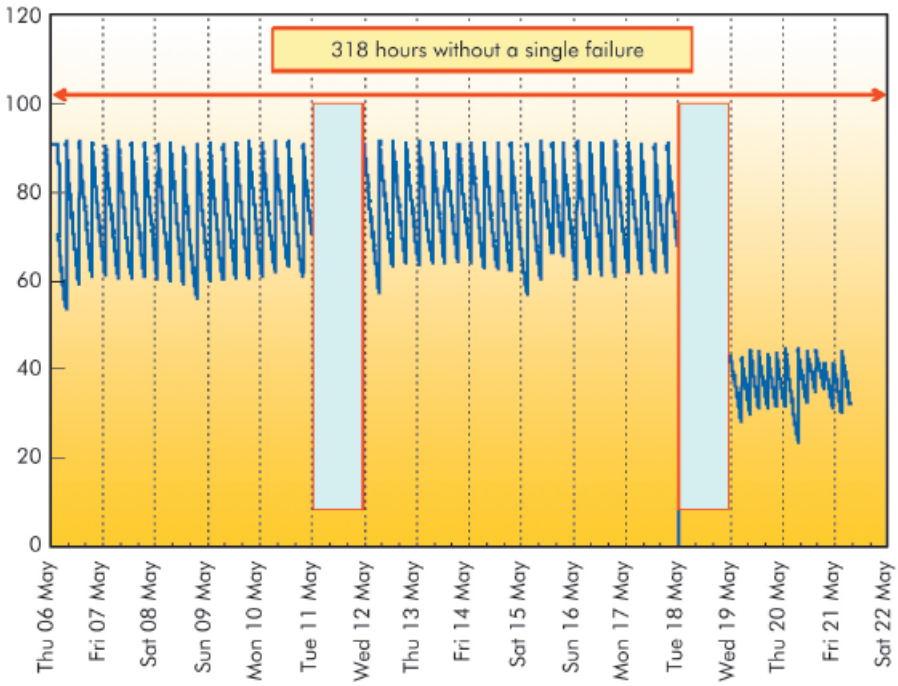

Fig. 152: An example of two weeks delivery without a single failure, interrupted only by 2 scheduled machine dedicated days.

Filling Patterns

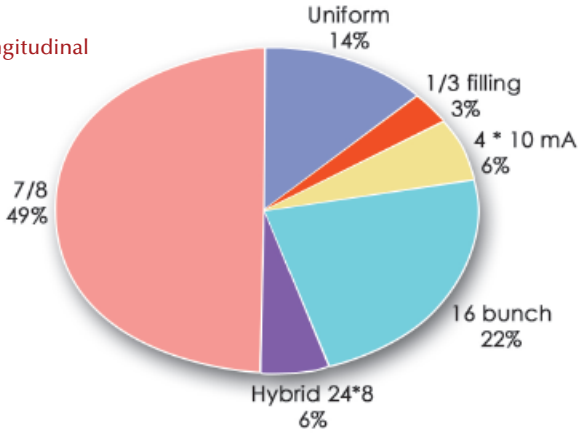

Fig. 153: Distribution of longitudinal filling modes in 2010.

Figure 153 presents the distribution of filling modes delivered in 2010. There are no changes with respect to 2009. The filling mode labelled "7/8 + 1" remains the standard multibunch mode with almost 50% of the total shifts. Thanks to the vertical bunch-by-bunch feedback, the intensity of the single bunch present in the empty 1/8th gap has been increased from 2 mA to 4 mA compared to 2009.

6 m insertion device straight sections

The ESRF lattice designed in the late 1980s is a 32 double bend achromat lattice with 32 cells designed with triple quadrupoles on both sides of the insertion device (ID) segments. Several years ago, a new setting of the quadrupole (linear lattice) was implemented with no current in the quadrupole adjacent to the insertion devices. The advantage of this is a longer length available for IDs. Such an advantage is now entering into effect with the Upgrade Programme.

As the beamlines are being refurbished, new IDs are being designed and built which make use of the 6 m length available for undulator magnets. Since December 2010, ID18 and ID30 have been extended from 5 to 6 m with a 6 m long narrow aperture (8 mm) fixed gap NEG coated ID chamber. Further transitions that involve significant vacuum work are planned during each long shutdown (summer and winter) with no disruption to the user programme.

Reduction of the vertical emittance

Third-generation light sources are characterised by low transverse beam emittances. The largest contribution to the vertical emittance comes from undesired vertical dispersion and coupling between the two transverse planes, both originating from small residual magnetic and alignment errors in the storage ring. The interest of coupling correction is three-fold. Firstly, smaller vertical beam sizes (proportional to the square root of the vertical emittance) allow the reduction of the magnetic gap of insertion devices, making it possible to reach higher magnetic fields, and hence photon flux. Secondly, any reduction of the vertical emittance induces higher photon brilliance from the undulators. Thirdly, large horizontal oscillations during injection experienced by the incoming off-axis beamlet would have limited impact on the vertical clearance, hence reducing the radiation dose during injection.

During 2010, a new correction algorithm developed at the ESRF was successfully implemented. It was possible to correct coupling and vertical dispersion of the bare machine (*i.e.* at open ID gaps) with the available 32 corrector skew quadrupoles at unprecedented levels, yielding the lowest vertical emittance ever measured at the ESRF, 4.4 ± 0.7 pm (see Figure 154). With closed (fixed) gaps, values between 5 and 7 pm are routinely achieved. To preserve low emittance against ID gap movements,

two additional correction schemes were also conceived. The first consists of cabling the two steerers placed at the ends of a few straight sections as skew quadrupoles and to power them in order to compensate ID gap-dependent skew quadrupole errors by means of look-up tables. The red curve of Figure 155 shows the vertical emittance growth when the gap of the in-vacuum ID06 undulator decreases, while the blue curve demonstrates how effective this correction can be in preserving low emittance. This correction scheme has been applied to a single undulator segment and will be applied to a few more in 2011. Fortunately, the majority of the 70 ID segments in operation produce negligible residual coupling at all gap values. A further development was a separate coupling feedback to modulate the power of the 32 correctors in such a way as to correct the nearest coupling resonance in the tune diagram. Figure 156 shows a comparison between two USM weeks with and without the coupling feedback: while large variations between 6 and 30 pm are observed in the later case, a rather stable vertical emittance between 6 and 7 pm was achieved during that week when the coupling feedback was on.

In the wake of these successful results, a study was carried out to assess whether a larger number of corrector skew quadrupoles might lead to even smaller emittance. Simulations indicate that 2 pm may be achieved with 32 additional correctors. The latter are already installed (but not yet used) in the storage ring. During 2011 it is foreseen to power them and to include them in the coupling correction.

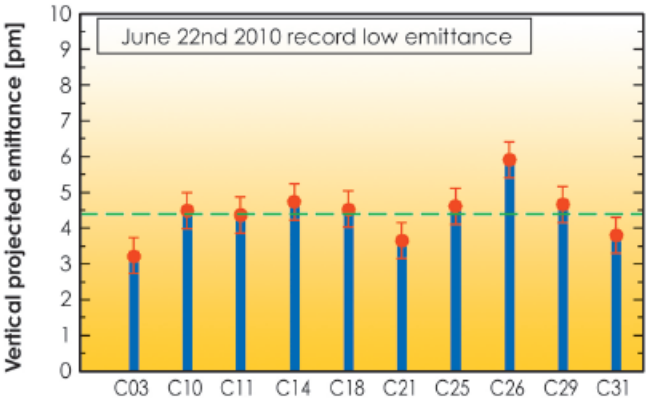

Fig. 154: Record vertical emittance at open ID gaps measured using the 10 in-air X-ray monitors located around the ring circumference.

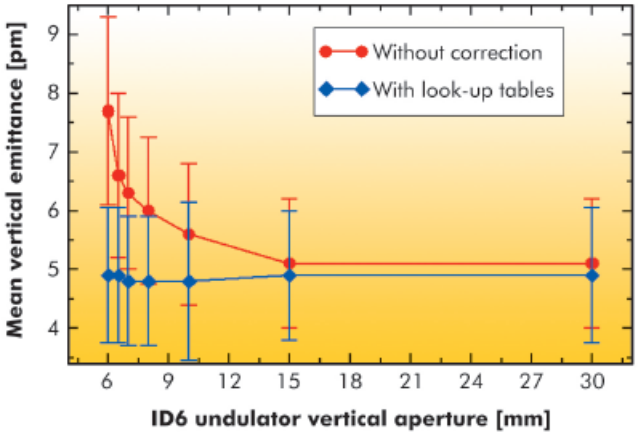

Fig. 155: Vertical emittance measured with and without coupling look-up tables.

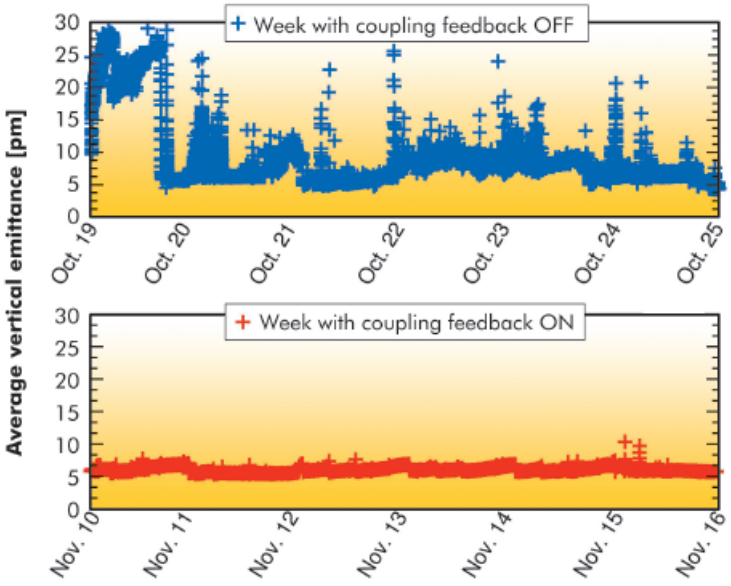

Fig. 156: Comparison between the vertical emittance measured during an USM week without (top) and with (bottom) coupling feedback correcting the closest sum resonance in the tune diagram.

References

A. Franchi, L. Farvacque, J. Chavanne, F. Ewald, B. Nash and K. Scheidt, submitted to *Physical Review Special Topics in Accelerators and Beams.*

Upgrade of the electron beam position monitoring system

The most essential diagnostic in the storage ring of a third-generation light source is the beam position monitoring system and its associated orbit correction system. The quality of such systems largely determines the final beam stability, which is of utmost importance for many beamlines.
The ESRF storage ring is equipped with 224 (32 cells x 7) beam position monitors (BPMs) located at regular intervals along the ring circumference. Each BPM station is constituted of 4 insulated buttons that capture weak radio frequency (RF) signals when the electron beam is passing through. The relative amplitudes of these weak signals depends on the position of the beam. The electronics processing these signals were replaced in 2009 with new units based on digital electronics (Libera Brilliance). This has already had far reaching and beneficial consequences for the beam quality, and further improvements can be expected in 2011. Indeed, the much lower noise in the beam position measurement has resulted in a greatly improved precision in the modelling of the linear lattice as obtained through transfer matrix measurements. The higher accuracy in the measurement of the lattice has resulted in a more effective coupling correction (less than 5 pm vertical emittance in USM as described above). A number of other applications of these electronics has been made or identified. The so-called sum signal of these 4 signals is proportional to the circulating beam current. Such a signal is only of real use if the whole chain of analogue and digital signal detection is of excellent stability. This appears to be the case of the Libera-Brillance units, if operated in a suitable way to maintain such stability. Averaging over the 224 BPMs results in a further reduction of the noise level by 15. This very low noise current monitor has resulted in a number of improvements in the monitoring of the beam in the storage ring. We have developed an improved lifetime measurement of the stored beam (see **Figure 157**), the capacity to diagnose instant micro-beam losses (see **Figure 158**) as well as an improved injection efficiency of the booster beam into the storage ring. Many other uses of the Libera electronics are under development, one of the most important being the fully renovated orbit correction system operating with all 96 steerers which will operate continuously from DC to 150 Hz.

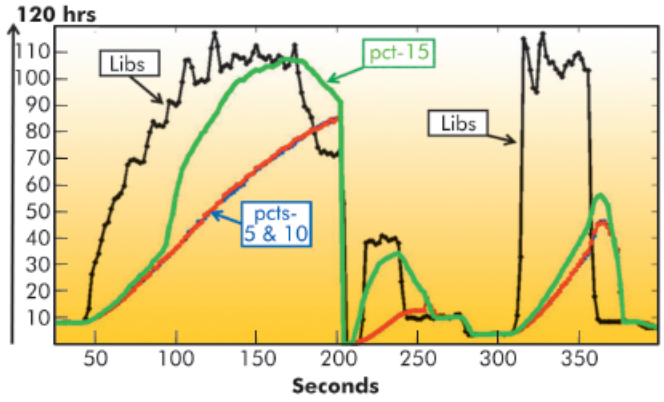

Fig. 157: Comparison of lifetime measurements made over a Machine Dedicated Time experiment during which the beam emittances were varied considerably. The measurement made from the sum signals from the Liberas is capable of diagnosing a 120 h lifetime over a few seconds while the conventional Parametric Current Transformers need several minutes of averaging to deliver a stable lifetime diagnostic.

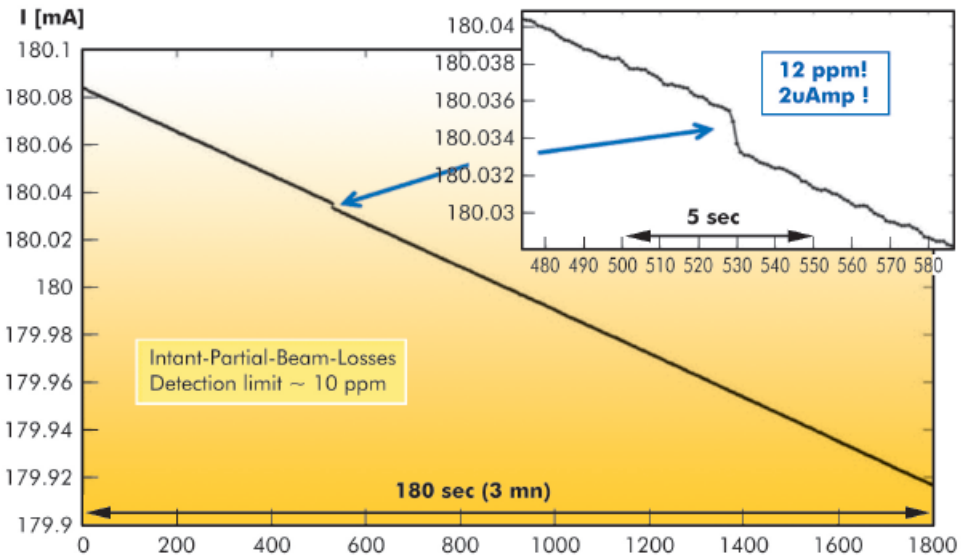

Fig. 158: Micro-beam loss of 2 micro-amps taking place over a second diagnosed by the sum signal of the Libera electronics.

A versatile stretched wire bench for magnetic measurements of accelerator magnets

A number of accelerator magnets (high gradient quadrupoles and new short sextupoles) are needed for the upgrade of the accelerator. These magnets need to be fully magnetically characterised. In such measurements, the field integral inside the aperture of the magnet is analysed in terms of integrated multipoles (harmonic analysis); the main integrated multipole must be resolved with a relative accuracy better than 10^{-4}. An accurate determination of the magnetic axis of the magnet is also important. This must coincide with the electron beam axis with an error lower than 50 micrometres when installed in the accelerator. This needs dedicated fiducialisation tasks to transfer the magnetic axis to survey monument installed on the magnet.
A well-established technique is based on long rigid rotating coils inserted in the aperture of the magnets.
A large majority of quadrupole and sextupole magnets have been characterised with this method. However, in the case of magnets with small internal bore or long devices, the method becomes impractical due to the reduced rigidity of the coil.

Another approach has been developed at the ESRF. It is based on a Cu-Be or Ti-Al wire stretched between two synchronised XZ stages (Figure 159). This concept is not new, but is re-examined here on the basis of modern motion controls and instrumentation. The movable wire and a fix return part form a loop connected to a low noise voltmeter. This is moved at a constant speed (10 to 40 mm/s) along various paths built up from successive straight and circular segments while triggering the voltmeter at constant path length intervals.
The circular motion as used with a conventional coil for harmonic analysis has become a particular case. The first tests carried out in this mode on a quadrupole magnet (Figure 159) show that the stretched wire concept is fully usable for the accurate characterisation of conventional accelerator magnets.

All linear stages involve DC motors operated in closed loop with encoders. From laser interferometer measurements, a correction grid is implemented in the motor controller to achieve a positioning accuracy smaller than 5 µm in a circle with a radius of 5 cm. As the design of the measuring bench allows it to be adapted to any magnet aperture, it was recently used for the accurate field adjustment of permanent magnet steerers to be installed in future canted undulator sections. It also offers new opportunities for the field integral magnetic measurements of undulators. In particular, compared to benches based on solid coils that are commonly used, it provides measurements with higher spatial resolution that should allow more efficient corrections on small gap devices such as in-vacuum undulators.

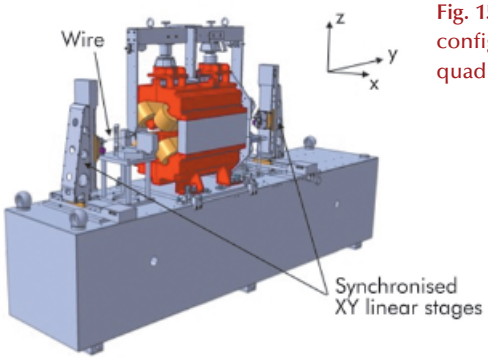

Fig. 159: ESRF stretched wire bench configured for the measurement of a quadrupole magnet.

Facts and Figures

Members and associate countries

(as of January 2011)

Members' shares:

27.5%	*France*
25.5%	*Germany*
15%	*Italy*
14%	*United Kingdom*
4%	*Spain*
4%	*Switzerland*
6%	*Benesync (Belgium, The Netherlands)*
4%	*Nordsync (Denmark, Finland, Norway, Sweden)*

Additional contributions

1%	*Portugal*
1%	*Israel*
1%	*Austria*
1%	*Poland*
1,05%	*Centralsync (Czech Republic 0,55%, Hungary 0,25%, Slovakia 0,25%)*

The beamlines

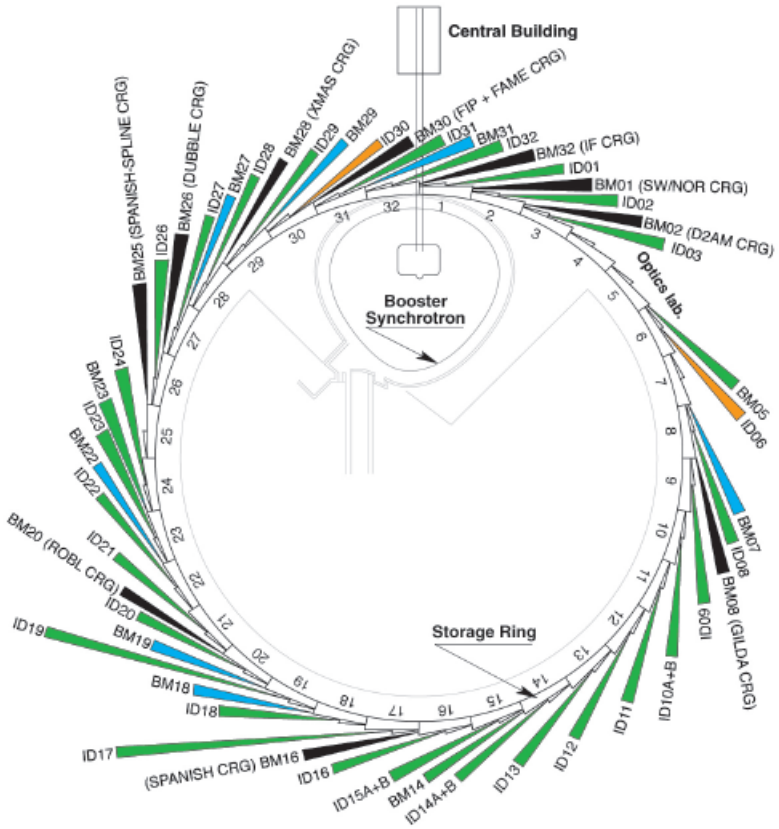

Details of the public ESRF beamlines as well as those operated by Collaborating Research Groups (CRG) are given in Tables 5 and 6. Figure 160 shows the location of the beamlines in the experimental hall.

- Public beamlines
- Instrumentation test and development beamlines
- CRG beamlines
- Free bending magnet ports

Fig. 160: Experimental hall showing location of the beamlines (public and CRG beamlines).

SOURCE POSITION	NUMBER OF INDEPENDENT END-STATIONS	BEAMLINE NAME	STATUS
ID01	1	Anomalous scattering	Operational since 07/97
ID02	1	High brilliance	Operational since 09/94
ID03	1	Surface diffraction	Operational since 09/94
ID08	1	Dragon	Operational since 02/00
ID09	1	White beam	Operational since 09/94
ID10A	1	Troika I + III	Operational since 09/94
ID10B	1	Troika II	Operational since 04/98
ID11	1	Materials science	Operational since 09/94
ID12	1	Circular polarisation	Operational since 01/95
ID13	1	Microfocus	Operational since 09/94
ID14A	2	Protein crystallography EH 1	Operational since 07/99
		Protein crystallography EH 2	Operational since 12/97
ID14B	2	Protein solution small-angle scattering EH 3	Operational since 12/98
		Protein crystallography EH 4	Operational since 07/99
ID15A	1	High energy diffraction	Operational since 09/94
ID15B	1	High energy inelastic scattering	Operational since 09/94
ID16	1	Inelastic scattering I	Operational since 09/95
ID17	1	Medical	Operational since 05/97
ID18	1	Nuclear scattering	Operational since 01/96
ID19	1	Topography and tomography	Operational since 06/96
ID20	1	Magnetic scattering	Operational since 05/96
ID21	1	X-ray microscopy	Operational since 12/97
ID22	1	Microfluorescence	Operational since 12/97
ID23	2	Macromolecular crystallography MAD	Operational since 06/04
		Macromolecular crystallography microfocus	Operational since 09/05
ID24	1	Dispersive EXAFS	Operational since 02/96
ID26	1	X-ray absorption and emission	Operational since 11/97
ID27	1	High pressure	Operational since 02/05
ID28	1	Inelastic scattering II	Operational since 12/98
ID29	1	Multiwavelength anomalous diffraction	Operational since 01/00
ID31	1	Powder diffraction	Operational since 05/96
ID32	1	X-ray standing wave and surface diffraction	Operational since 11/95
BM14	1	Macromolecular crystallography (MAD)	Operational since 01/10
BM23	1	X-ray absorption spectroscopy	Operational since 03/11

Table 5: List of the ESRF public beamlines.

SOURCE POSITION	NUMBER OF INDEPENDENT END-STATIONS	BEAMLINE NAME	FIELD OF RESEARCH	STATUS
BM01	2	Swiss-Norwegian BL	X-ray absorption & diffraction	Operational since 01/95
BM02	1	D2AM (French)	Materials science	Operational since 09/94
BM08	1	Gilda (Italian)	X-ray absorption & diffraction	Operational since 09/94
BM16	1	SPANISH CRG	Structural biology (MAD, SAX)	Operational since 01/03
BM20	1	ROBL (German)	Radiochemistry & ion beam physics	Operational since 09/98
BM25	2	SPLINE (Spanish)	X-ray absorption & diffraction	Operational since 04/05
BM26	2	DUBBLE (Dutch/Belgian)	Small-angle scattering & interface diffraction Protein crystallography + EXAFS	Operational since 12/98 Operational since 06/01
BM28	1	XMAS (British)	Magnetic scattering	Operational since 04/98
BM30	2	FIP (French) FAME (French)	Protein crystallography EXAFS	Operational since 02/99 Operational since 08/02
BM32	1	IF (French)	Interfaces	Operational since 09/94

Table 6: List of the Collaborating Research Group beamlines.

User operation

After 16 years of successful operation of the facility for scientific Users, we look back on user operation over the last year 2010. For the first time since midway through 2005, the full complement of 32 public beamlines (now including BM14), together with 10 additional beamlines operated by Collaborating Research Groups (CRGs), were not available in their entirety for experiments by visiting research teams. The EXAFS beamlines ID24 and BM29, along with the Macromolecular Crystallography station ID14-2, were either partially or fully unavailable during the year due to reconstruction or commissioning work undertaken within the framework of the Upgrade Programme. Figure 161 shows the ever-increasing number of applications for beamtime received since 2004. As expected, following announcements to the user community of the closure to the public of the two EXAFs beamlines during the year 2010, the number of applications received during that year did not follow the usual trend. Since the decrease is only very slight, one can extrapolate that, had the full complement of beamlines been open for proposals, an increase in number of applications would once again have been seen.

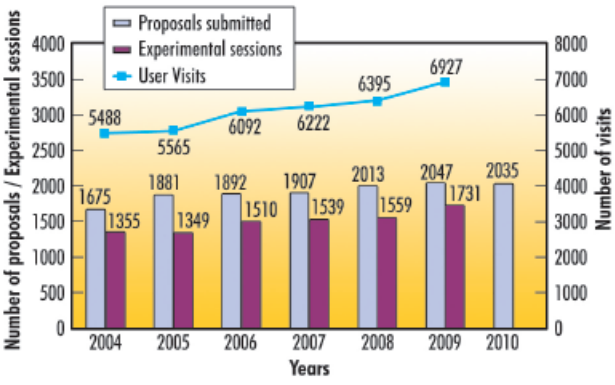

Fig. 161: Numbers of applications for beamtime, experimental sessions and user visits, 2004 to 2010. N.B. Final numbers of experimental sessions and user visits for 2010 were not available at the time of going to press.

Table 7: Number of shifts of beamtime requested and allocated for user experiments, year 2010.

Scientific field	Total shifts requested	Total shifts allocated
Chemistry	3 242	1 306
Hard condensed matter:		
• Electronic and magnetic prop.	4 596	2 195
• Crystals and ordered structures	3 721	1 536
• Disordered systems	1 334	609
Applied materials and engineering	3 471	1 493
Environmental and cultural heritage matters	2 410	945
Macromolecular crystallography	3 417	2 571
Medicine	1 278	595
Methods and instrumentation	860	429
Soft condensed matter	2 954	1 368
Surfaces and interfaces	3 320	1 227
Totals	30 603	14 274

Proposals for experiments are selected and beamtime allocations are made through peer review. Review Committees of specialists, for the most part from European countries and Israel, have been set up in the following scientific areas:

- chemistry
- hard condensed matter: electronic and magnetic properties
- hard condensed matter: crystals and ordered systems
- hard condensed matter: disordered systems and liquids
- applied materials and engineering
- environmental and cultural heritage matters
- macromolecular crystallography
- medicine
- methods and instrumentation
- soft condensed matter
- surfaces and interfaces.

The Review Committees met twice during the year, around six weeks after the deadlines for submission of proposals (1 March and 1 September). They reviewed 2035 applications for beamtime, and selected 974 (47.9 %), which were then scheduled for experiments.

Features of this period:

- the April meeting was seriously disrupted due to travel difficulties resulting from the Icelandic volcano eruption and, as a result, the Review Committees met for the very first time via telephone conference to the ESRF from their home laboratories. Whilst the meetings under this format went very smoothly and successfully, most parties involved felt that physical meetings onsite were still the best way of thoroughly evaluating the large number of proposals for beam time.
- the imaging beamlines were once again highly oversubscribed. Such beamlines are widely requested over the majority of the eleven Review Committees due to the applicability of the imaging techniques to many scientific areas.

Requests for beamtime, which is scheduled in shifts of 8 hours, totalled 30 603 shifts or 244 824 hours in 2010, of which 14 274 shifts or 114 192 hours (46.6 %) were allocated. The distribution of shifts requested and allocated, by scientific area, is shown in Table 7.

The breakdown of shifts scheduled for experiments by scientific area in the first half of 2010 is shown in Figure 162. This same period saw 3045 visits by scientists to the ESRF under the user programme, to carry out 729 experiments. Overall, the number of users in each experimental team averaged 4 persons as in 2009, and the average duration of an experimental session was 10.0 shifts compared with 9.7 shifts in 2009. This can be further broken down to show an average duration of 3.3 shifts for MX experiments and 14.4 shifts for non-MX experiments. Experiments have tended to become shorter thanks to many factors including higher automation and increased flux from state-of-the-art optics. This is reflected in the constant rise in the annual number of experimental sessions and user visits since 2004 as shown in Figure 161. The particularly high number of experiments and user visits in the full year 2009 is also due to the fact that an extra week of beam time was made available to users during that year; this was to compensate partly for the anticipated reduction in beam time available in 2010 following the start of the reconstruction work of the Upgrade Programme.

One of the principle measurable output parameters of the ESRF is the number and quality of publications accepted in peer-reviewed journals. Figure 163 shows how this number has been rising continuously over the past years, with a publication output systematically on a level of one publication per experimental session and reaching a record number of more than 1800 for the year 2009. The year 2010 promises to be even more fruitful, with 1641 publications already registered so far in the ILL/ESRF Library database. Since ESRF began user operation back in 1994, a total of 17495 publications have been accepted in peer-reviewed journals. Of these, more than 200 every year are published in high impact factor journals.

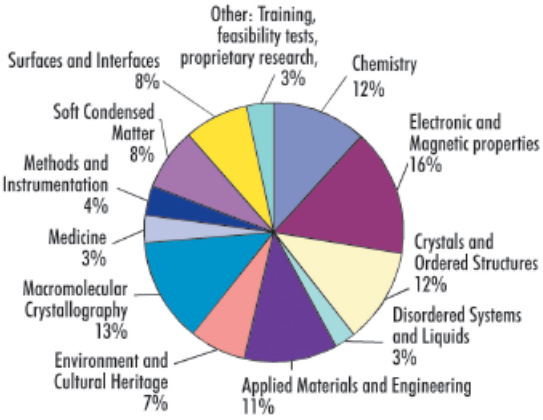

Fig. 162: Shifts scheduled for experiments, March to July 2010, by scientific area.

User responses to questionnaires show once again that the ESRF continues to maintain its excellent reputation concerning the assistance and service given by scientists and support staff on beamlines, and travel and administrative arrangements, in addition to the quality both of the beam and of the experimental stations. Facilities on site, such as preparation laboratories, the Guesthouse and a canteen open 7 days a week, also make an important contribution to the quality of user support.

J. McCarthy

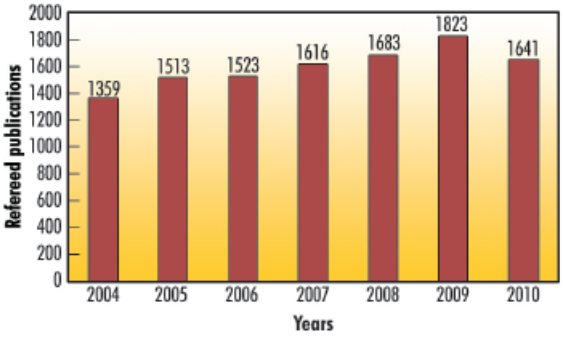

Fig. 163: Numbers of publications appearing in refereed journals reporting on data collected either partially or totally at ESRF, 2004 to 2010.

Administration and finance

Expenditure and income 2009

Expenditure		kEuro
Accelerator and Source		
Personnel		5 324.5
Recurrent		2 191.8
Operating costs	*1 487.7*	
Other recurrent costs	*704.1*	
Capital		7 559.7
Accelerator and Source developments	*7 559.7*	
Beamlines, experiments and in-house research		
Personnel		20 814.2
Recurrent		7 116.7
Operating costs	*3 969.7*	
Other Recurrent costs	*3 147*	
Capital		5 944.6
Beamline developments	*4 463*	
Beamline refurbishment	*1 481.6*	
Technical and administrative supports		
Personnel		24 904.4
Recurrent		12 114.8
Capital		6 764.6
Unexpended committed funds		
Funds carried forward to 2010		915
Total		**93 650.3**

Income	kEuro
2009 Members' contributions	81 685.7
Funds carried forward from 2008	117.2
Other income	
Scientific Associates	4 643.9
Sale of beam time	1 798.9
Compensatory funds	0
Scientific collaboration and Special projects	5 404.5
Total	**93 650.3**

Revised expenditure and income budget for 2010

Expenditure		kEuro
Accelerator and Source		
Personnel		5 550
Recurrent		1 710
Operating costs	*1 500*	
Other recurrent costs	*210*	
Capital		6 987
Accelerator and Source developments	*6 987*	
Beamlines, experiments and in-house research		
Personnel		18 205
Recurrent		6 100
Operating costs	*2 950*	
Other Recurrent costs	*3 150*	
Capital		9 551
Beamline developments	*6 422*	
Beamline refurbishment	*3 129*	
Technical and administrative supports		
Personnel		27 080
Recurrent		12 305
Capital		10 861
Industrial and commercial activity		
Personnel		405
Recurrent		95
Personnel costs provision		
Total		**98 849**

Income	kEuro
2010 Members' contributions	87 274
Funds carried forward from 2009	915
Other income	
Scientific Associates	4 960
Sale of beam time	1 600
Compensatory funds	0
Scientific collaboration and Special projects	4 100
Total	**98 849**

The budget for 2010 includes additional contributions from Members and Scientific Associates of 15 385 kEuro dedicated to the Upgrade Programme. The Upgrade expenditure budget amounts to a total of 18 334 kEuro including 2299 kEuro of ESRF operating budget (and 650 kE from other sources).

Expenditure 2009 by nature of expenditure

	kEuro
PERSONNEL	
ESRF staff	48 786.1
External temporary staff	182.5
Other personnel costs	2 074.6
RECURRENT	
Consumables	8 265.0
Services	10 459.5
Other recurrent costs	2 698.7
CAPITAL	
Buildings, infrastructure	2 069.0
Lab. and Workshops	735.2
Accelerator and Source incl. ID's and Fes	7 559.7
Beamlines, Experiments	7 170.5
Computing Infrastructure	2 547.7
Other Capital costs	186.8
Unexpended committed funds	
Funds carried forward to 2010	915
Total	**93 650.3**

Revised budget for 2010 by nature of expenditure

	kEuro
PERSONNEL	
ESRF staff	49 045
External temporary staff	85
Other personnel costs	2 110
RECURRENT	
Consumables	8 200
Services	9 505
Other recurrent costs	2 505
CAPITAL	
Buildings, infrastructure	5 331
Lab. and Workshops	256
Accelerator and Source incl. ID's and Fes	6 981
Beamlines, Experiments	11 816
Computing Infrastructure	2 950
Other Capital costs	65
Total	**98 849**

Financial resources in 2008, 2009, 2010 and 2011, by major programme

(current prices in MEuro for the respective years)

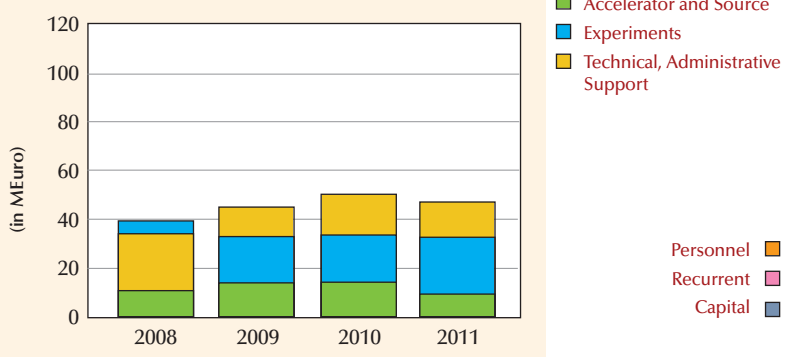

Financial resources in 2008, 2009, 2010 and 2011, by nature of expenditure

(current prices in MEuro for the respective years)

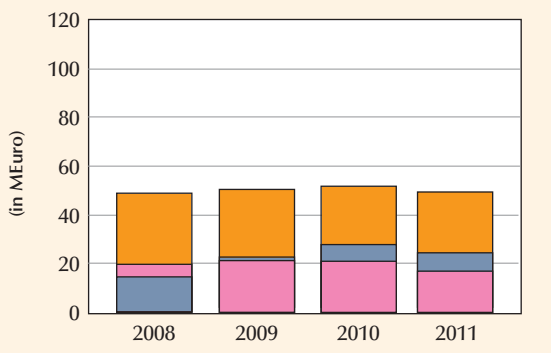

2010 manpower *(posts filled on 31/12/2010)*

	Scientists, Engineers, Senior Administrators	Technicians and Administrative Staff	PhD students	Total
Staff on regular positions				
Accelerator and Source	30	37.4		67.4
Beamlines, instruments and experiments*	229	88.2	27.5	344.7
General technical services	28.6	51		79.6
Directorate, administration and central services	35.6	52.2		87.8
Sub-total	*323.1*	*228.8*	*27.5*	*579.4*
Other positions				
Short term contracts	6.8	12		18.8
Staff under "contrats de professionnalisation" (apprentices)		20		20
European Union grants				0
Temporary workers				0
Total	**329.9**	**260.8**	**27.5**	**618.2**
Absences of staff (equivalent full time posts)				23.6
Total with absences				*594.6*
Scientific collaborators and consultants	*9*			*9*
External funded research fellows	*3*		*24*	*27*

** Including scientific staff on time limited contract.*

Organisation chart of the ESRF
(as of January 2011)

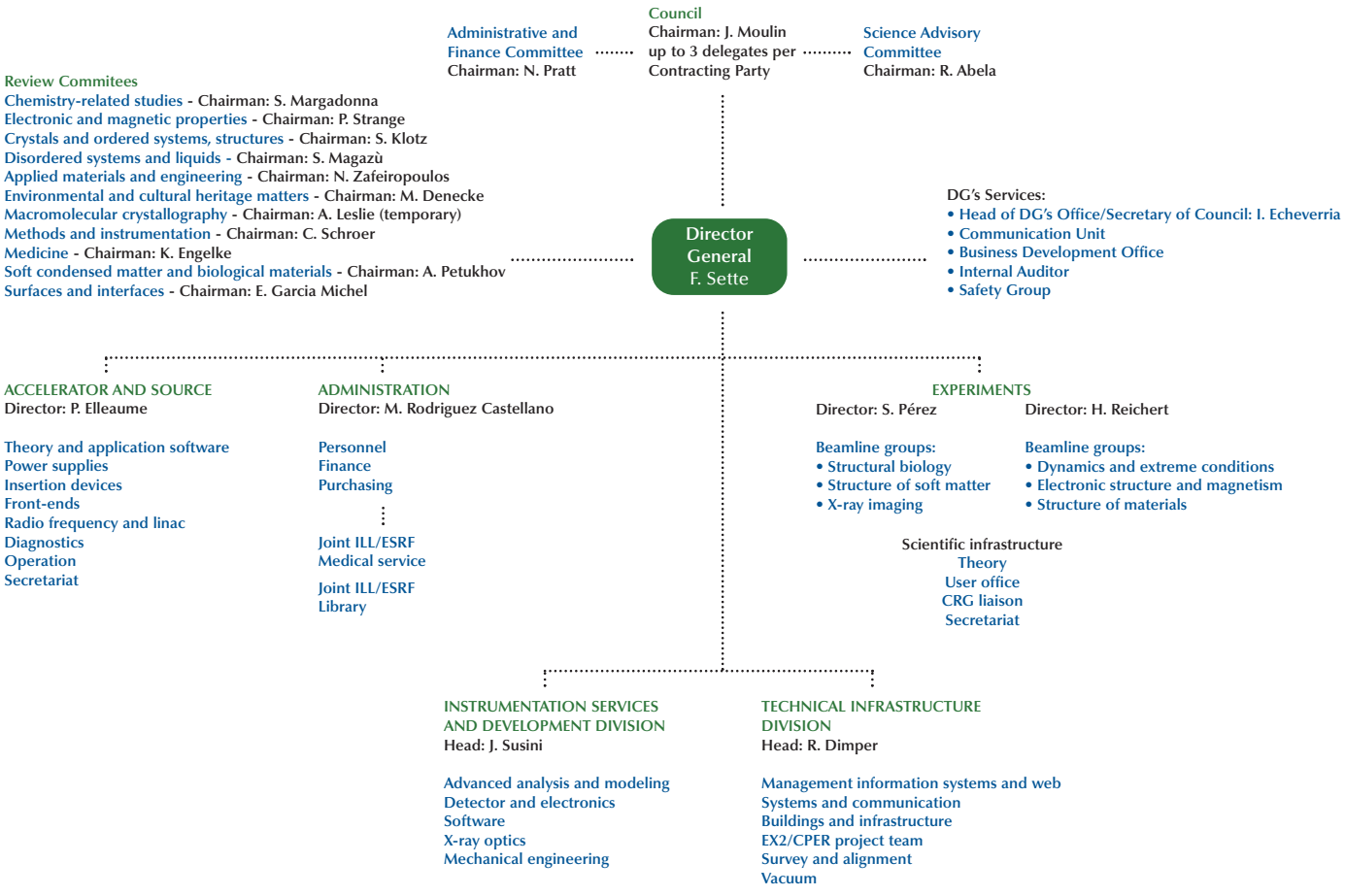

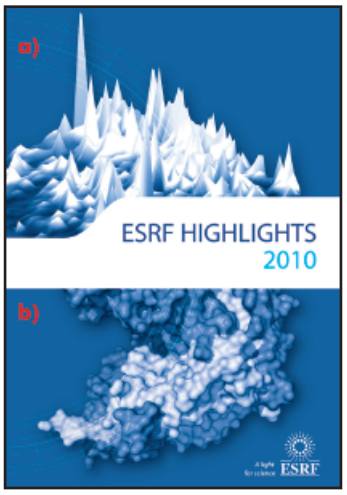

Cover

Design by M. Collignon. Featured images:
a) Imaging scale-free structural organisation of oxygen interstitial atoms in a high temperature superconductor, M. Fratini *et al.*, page 114 *(Credit: N. Poccia)*.
b) Crystal structure of the AHL acylase PvdQ from *Pseudomonas aeruginosa*, M. Bokhove *et al.*, page 104 *(Credit. M. Bokhove)*.

We gratefully acknowledge the help of:

C. Argoud, J. Baruchel, S. Gerlier, B. Boulanger, N.B. Brookes, K. Clugnet, M. Collignon, E. Dancer, R. Dimper, P. Elleaume, A. Fitch, P. Gaget, C. Habfast, E.S. Jean-Baptiste, A. Kaprolat, M. Krisch, G. Leonard, C. Mary, J. McCarthy, T. Narayanan, M. Newton, S. Pascarelli, S. Pérez, F. Perrin, H. Reichert, S. Rio, M. Rodriguez Castellano, F. Sette, C. Stuck, J. Susini, S. McSweeney, K. Wong and all the users and staff who have contributed to this edition of the Highlights.

Editor
G. Admans
Layout
Pixel Project
Printing
Imprimerie du Pont de Claix

Communication Group
ESRF
BP220 • 38043 Grenoble • France
Tel. +33 (0)4 76 88 20 56 • Fax. +33 (0)4 76 88 25 42
http://www.esrf.eu

www.esrf.eu

European Synchrotron Radiation Facility
BP220 - F38043 Grenoble Cedex, France